

DISSERTATION

UNDERSTANDING THE MOLECULAR-LEVEL CHEMISTRY OF H<sub>2</sub>O PLASMAS  
AND THE EFFECTS OF SURFACE MODIFICATION AND DEPOSITION ON A  
SELECTION OF OXIDE SUBSTRATES

Submitted by

Kristina J. Trevino

Department of Chemistry

In partial fulfillment of the requirements

For the Degree of Doctor of Philosophy

Colorado State University

Fort Collins, Colorado

Summer 2011

Doctoral Committee:

Advisor: Ellen R. Fisher

C. Michael Elliott

Charles S. Henry

Amy L. Prieto

Travis S. Bailey

## ABSTRACT

### UNDERSTANDING THE MOLECULAR-LEVEL CHEMISTRY OF H<sub>2</sub>O PLASMAS AND THE EFFECTS OF SURFACE MODIFICATION AND DEPOSITION ON A SELECTION OF OXIDE SUBSTRATES

This dissertation first examines electrical discharges used to study wastewater samples for contaminant detection and abatement. The abatement process of contaminants in liquid discharges is relatively unstable; thus, to help elucidate the sources of instability, the gas phase constituents of plasmas formed from artificially-contaminated water samples were examined using optical emission spectroscopy (OES) and mass spectrometry (MS). Two different water samples contaminated with differing concentrations of either methanol (MeOH) or methyl *tert*-butyl ether (MTBE) were used to follow breakdown mechanisms. Emission from CO\* was used to monitor the contaminant and for molecular breakdown confirmation through actinometric OES as it can only arise from the carbon-based contaminant in either system. Detection limits for each compound were as low as 0.01 ppm at a range of varying plasma parameters. MS data revealed plasma molecular breakdown and little evidence for fragment recombination to form larger molecules. MS data for the two contaminated H<sub>2</sub>O samples suggest the primary plasma species are CH<sub>x</sub>, C<sub>2</sub>H<sub>x</sub>, CH<sub>2</sub>O, CO, C<sub>4</sub>H<sub>x</sub>, and C<sub>3</sub>H<sub>x</sub>O and

their corresponding ions. From this study, the detection and decomposition of organic molecules in water was accomplished for the first time with an ICP system. Detection was achieved at concentrations as low as 0.01 ppm, and molecular decomposition was seen at a variety of plasma parameters.

This dissertation also explores the vibrational ( $\theta_v$ ), rotational ( $\theta_R$ ) and translational ( $\theta_T$ ) temperatures for a range of diatomic species in different plasma systems. Specifically we have investigated four molecules; OH in plasmas formed from H<sub>2</sub>O (g), tetraethyl orthosilicate (TEOS), NH<sub>3</sub>/O<sub>2</sub> mixtures, and CH<sub>3</sub>OH; NH formed in plasmas created from NH<sub>3</sub> and NH<sub>3</sub>/O<sub>2</sub> mixtures; SiH radicals in SiH<sub>4</sub>, SiH<sub>4</sub>/Ar, Si<sub>2</sub>H<sub>6</sub> and Si<sub>2</sub>H<sub>6</sub>/Ar plasmas; and CH in plasmas formed from mixtures of CH<sub>4</sub>/Ar. These species were probed with both laser induced fluorescence (LIF) and OES. For the majority of the plasma species studied,  $\theta_v$  are much higher than  $\theta_R$  and  $\theta_T$ . This suggests that more energy is partitioned into the vibrational degrees of freedom in our plasmas. The  $\theta_R$  reported are significantly lower in all the plasma systems studied and this is a result of radical equilibration to the plasma gas temperature.  $\theta_T$  values show two characteristics; (1) they are less than the  $\theta_v$  and higher than the  $\theta_R$  and (2) show varying trends with plasma parameters. Radical energetics were examined through comparison of  $\theta_R$ ,  $\theta_T$ , and  $\theta_v$ , yielding significant insight on the partitioning of internal and kinetic energies in plasmas. Correlations between energy partitioning results and corresponding radical surface scattering coefficients obtained using our imaging of radicals interacting with surfaces (IRIS) technique are also presented.

Another aspect of plasma process chemistry, namely surface modification via plasma treatment, was investigated through characterization of metal oxides (SiO<sub>x</sub>N<sub>y</sub>, nat-SiO<sub>2</sub>,

and dep-SiO<sub>2</sub>) following their exposure to a range of plasma discharges. Here, emphasis was placed on the surface wettability, surface charge, and isoelectric point (IEP). The results demonstrate that 100% Ar, H<sub>2</sub>O, and NH<sub>3</sub> plasma treatments cause changes in surface charge, wettability, and IEP values for all treated surfaces. Observed variations in these values depend primarily on the specific mechanism for surface functionalization with each plasma treatment. Ar plasmas tend to create surface radical sites, H<sub>2</sub>O plasmas yield surface-bound OH, and NH<sub>3</sub> plasmas lead to the incorporation of nitrate functional groups. The wettability, surface charge, IEP values, chemical composition, and surface damage of the substrates were analyzed using contact angle goniometry (CA), x-ray photoelectron spectroscopy (XPS), and scanning electron microscopy (SEM). Although the permanence of these modifications varied with substrate, lasting between one week and one month, these results highlight the utility of IEP measurements for characterizing plasma treated surfaces and suggest the possibility that plasmas may provide a valuable means of controlling surface charge and wettability of metal oxides.

The incorporation of functional groups on the surface of Zeolite X was also examined as an additional form of plasma surface modification. The intention of these studies was to (1) alter the surface functionality by simple plasmas treatments, as characterized by XPS data; (2) change the hydrophilic nature of the zeolite to be more hydrophobic with fluoro-carbon plasmas; (3) gain total surface area functionality with our new rotating drum reactor; and (4) ensure that damage was not occurring to the zeolite structure, as evidenced by SEM images. Results showed the incorporation of different surface functionality was accomplished with all plasma systems studied (CF<sub>4</sub>, C<sub>2</sub>F<sub>6</sub>, C<sub>3</sub>F<sub>8</sub>), the

zeolite structure was not damaged by the plasma, and the potential for altering the entire surface area of these porous materials exists.

The final portion of this dissertation addresses aspects of work designed to understand the adhesion behavior of amorphous carbon nitride ( $a\text{-CN}_x$ ) films deposited from a  $\text{CH}_3\text{CN}$  and  $\text{BrCN}$  plasmas. In particular, films obtained from  $\text{CH}_3\text{CH}$  plasmas stayed intact whereas  $\text{BrCN}$  plasmas produced films that delaminated upon their exposure to atmosphere. These results have been attributed to humidity, film stress, hydrocarbon species, and the Br content in the film. The major contributions to this work made here center on the chemical composition and binding environments of the deposited films as measured by XPS, which are shown to be critical in understanding the mechanical properties of  $a\text{-CN}_x$  films.

## TABLE OF CONTENTS

<b>ABSTRACT OF DISSERTATION</b> .....	ii
<b>TABLE OF CONTENTS</b> .....	vi
<b>LIST OF FIGURES</b> .....	ix
<b>LIST OF TABLES</b> .....	xii
<b>CHAPTER 1. Introduction</b>	
1.1 Plasma Chemistry .....	2
1.2 Gas-Phase Diagnostics.....	3
1.3 Plasma Surface Modification.....	7
1.4 Plasma Enhanced Chemical Vapor Deposition .....	10
1.5 References.....	12
<b>CHAPTER 2. Experimental Methods</b>	
2.1 Reactor Design and Plasma Systems .....	14
2.2 Instrumentation .....	28
2.3 Analysis Techniques .....	33
2.4 References.....	40
<b>CHAPTER 3. Detection Limits and Decomposition Mechanisms for Organic Contaminants in Water using Optical Emission Spectroscopy</b>	
3.1 Introduction.....	43
3.2 Results.....	47
3.3 Discussion .....	61
3.4 Summary .....	66
3.5 References.....	67
<b>CHAPTER 4. Energy Partitioning in Diatomic Radicals II: CH, SiH, OH, and NH in Inductively Coupled Plasmas</b>	

4.1 Introduction.....	70
4.2 Results.....	72
4.3 Discussion.....	83
4.4 Summary.....	94
4.5 References.....	96

**CHAPTER 5.** Isoelectric Points of Plasma Modified and Aged Silicon Oxynitride Surfaces Measured Using Contact Angle Titrations

5.1 Introduction.....	98
5.2 Results.....	100
5.3 Discussion.....	120
5.4 Summary.....	127
5.5 References.....	129

**CHAPTER 6.** Comparing Isoelectric Point and Surface Composition of Plasma Modified Native and Deposited SiO<sub>2</sub> Films Using Contact Angle Titrations and X-Ray Photoelectron Spectroscopy

6.1 Introduction.....	132
6.2 Results.....	134
6.3 Discussion.....	152
6.4 Summary.....	157
6.5 References.....	158

**CHAPTER 7.** Surface Characterization of rf plasma Treated Zeolite X

7.1 Introduction.....	161
7.2 Reactor Design.....	164
7.3 Results/Discussion.....	164
7.4 Summary and Future Work.....	179
7.5 References.....	182

**CHAPTER 8.** Deposition of a-CN<sub>x</sub> Materials in BrCN Plasmas: Film Characterization in Support of Mechanisms for Adhesion Behavior

8.1 Introduction.....	184
8.2 Results/Discussion .....	186
8.3 Summary .....	200
8.4 References.....	201

**CHAPTER 9.** Research Summary and Perspectives

9.1 Research Summary .....	203
9.2 Future Work.....	206
9.3 References.....	208

**APPENDIX A.** Sample Cleaning Methods for SiO<sub>x</sub>N<sub>y</sub> and nat-SiO<sub>2</sub> Substrates .....209

## LIST OF FIGURES

<b><u>FIGURE</u></b>	<b><u>PAGE</u></b>
2.1 Inductively coupled reactor schematic .....	15
2.2 IRIS apparatus schematic .....	19
2.3 Rotating drum reactor schematic .....	27
2.4 Deposition reactor schematic .....	29
2.5 Mass spectrometer schematic .....	31
2.6 High-resolution XPS spectra for untreated $\text{SiO}_x\text{N}_y$ .....	37
3.1 Optical emission spectra of 100% $\text{H}_2\text{O}$ , 100% $\text{CH}_3\text{OH}$ , and 100% MTBE plasmas ..	48
3.2 Optical emission spectra of 0.01 ppm $\text{CH}_3\text{OH}$ and 0.01 ppm MTBE plasmas .....	52
3.3 Actinometric results for CO as a function of rf power .....	54
3.4 Calibration curves for CO in $\text{CH}_3\text{OH}$ and MTBE plasmas .....	57
3.5 Mass spectrometry data in + ion SIMS mode for $\text{CH}_3\text{OH}$ and MTBE plasmas.....	58
3.6 Mass spectrometry data for 0.01 ppm $\text{CH}_3\text{OH}$ and 0.01 ppm MTBE plasmas .....	60
4.1 Raw OES spectra of CH, SiH, OH and NH.....	74
4.2 Simulated and experimental OES spectra for CH.....	75
4.3 LIF images of OH in a 100% $\text{H}_2\text{O}$ plasma .....	76
4.4 $\theta_R$ , $\theta_T$ , $\theta_V$ and S for CH in $\text{CH}_4/\text{Ar}$ and 100% $\text{CH}_4$ plasmas.....	78
4.5 $\theta_R$ , $\theta_T$ , and $\theta_V$ for SiH in $\text{SiH}_4/\text{Ar}$ and $\text{Si}_2\text{H}_6/\text{Ar}$ plasmas.....	79
4.6 $\theta_R$ , $\theta_T$ , and $\theta_V$ for OH in 100% $\text{H}_2\text{O}$ plasmas.....	81
4.7 $\theta_R$ , $\theta_T$ , and $\theta_V$ for OH in 50:50 and 20:80 $\text{NH}_3/\text{O}_2$ plasmas.....	82
4.8 $\theta_R$ , $\theta_V$ , and S for NH in a 100% $\text{NH}_3$ plasma.....	84
4.9 $\theta_R$ , $\theta_T$ , and $\theta_V$ for NH in 50:50 and 20:80 $\text{NH}_3/\text{O}_2$ plasmas.....	85
5.1 High-resolution XPS spectra for untreated $\text{SiO}_x\text{N}_y$ substrates .....	102
5.2 CA titration data for untreated and Ar plasma treated $\text{SiO}_x\text{N}_y$ .....	103
5.3 High-resolution XPS spectra for Ar plasma treated $\text{SiO}_x\text{N}_y$ substrates.....	107

5.4 CA titration data and high-resolution XPS spectra of SiO <sub>x</sub> N <sub>y</sub> substrates treated with a H <sub>2</sub> O plasma .....	109
5.5 CA titration data and high-resolution XPS spectra of SiO <sub>x</sub> N <sub>y</sub> substrates treated with an NH <sub>3</sub> plasma .....	113
5.6 High-resolution XPS spectra for NH <sub>3</sub> plasma treated SiO <sub>x</sub> N <sub>y</sub> substrates .....	116
5.7 SEM images of an untreated and an NH <sub>3</sub> plasma treated SiO <sub>x</sub> N <sub>y</sub> substrate .....	118
5.8 OES spectra of a H <sub>2</sub> O plasma with a SiO <sub>x</sub> N <sub>y</sub> substrate .....	119
6.1 CA titration data for untreated and Ar plasma treated nat-SiO <sub>2</sub> substrates .....	135
6.2 SEM and AFM images for untreated and Ar plasma treated nat-SiO <sub>2</sub> and dep-SiO <sub>2</sub> .....	138
6.3 High-resolution XPS spectra for untreated and Ar plasma treated nat-SiO <sub>2</sub> .....	139
6.4 CA titration data and corresponding high-resolution XPS spectra for dep-SiO <sub>2</sub> and Ar plasma treated dep-SiO <sub>2</sub> .....	142
6.5 CA titration data for untreated and H <sub>2</sub> O plasma treated nat-SiO <sub>2</sub> substrates .....	146
6.6 High-resolution XPS spectra for untreated and H <sub>2</sub> O plasma treated nat-SiO <sub>2</sub> .....	149
6.7 High-resolution XPS spectra for dep-SiO <sub>2</sub> and H <sub>2</sub> O plasma treated dep-SiO <sub>2</sub> .....	150
6.8 FTIR spectra for untreated, plasma treated (Ar and H <sub>2</sub> O), and aged dep-SiO <sub>2</sub> substrates.....	151
7.1 Rotating drum reactor schematic .....	165
7.2 SEM and high-resolution XPS spectra for untreated Zeolite X.....	166
7.3 SEM and high-resolution C <sub>1s</sub> XPS spectra for CF <sub>4</sub> plasma treated Zeolite X.....	169
7.4 High-resolution F <sub>1s</sub> XPS spectra for CF <sub>4</sub> plasma treated Zeolite X.....	170
7.5 SEM and high-resolution C <sub>1s</sub> XPS spectra for C <sub>2</sub> F <sub>6</sub> plasma treated Zeolite X.....	173
7.6 High-resolution F <sup>1s</sup> XPS spectra for C <sub>2</sub> F <sub>6</sub> plasma treated Zeolite X .....	175
7.7 SEM and high-resolution C <sub>1s</sub> XPS spectra for C <sub>3</sub> F <sub>8</sub> plasma treated Zeolite X.....	176
7.8 High-resolution XPS spectra for C <sub>3</sub> F <sub>8</sub> plasma treated Si wafers .....	178
8.1 Phase contrast microscope images of 100% CH <sub>3</sub> CN and 100% BrCN plasma deposited films .....	187
8.2 FTIR spectra of 100% CH <sub>3</sub> CN and 100% BrCN plasma deposited films.....	188

8.3 High-resolution XPS spectra for 100% BrCN and 100% CH <sub>3</sub> CN plasma deposited films .....	190
8.4 High-resolution XPS spectrum for a 100% BrCN plasma deposited film.....	193
8.5 High-resolution XPS spectrum for a 50:50 BrCN/CH <sub>4</sub> plasma deposited film.....	195
8.6 Phase contrast microscope image of a 50:50 BrCN/CH <sub>4</sub> plasma deposited film .....	196
8.7 High-resolution XPS spectra for a 100% BrCN, 100% CH <sub>3</sub> CN, and 50:50 BrCN/CH <sub>4</sub> plasma deposited films.....	198
8.8 High-resolution XPS spectra for films deposited in 1:1:1, 14:43:43, and 3:1:1 CH <sub>3</sub> CN/BrCN/CH <sub>4</sub> plasmas .....	199
A.1 High-resolution XPS spectra of untreated and cleaned SiO <sub>x</sub> N <sub>y</sub> substrates .....	213
A.2 High-resolution XPS spectra of untreated and cleaned nat-SiO <sub>2</sub> substrates .....	214

## LIST OF TABLES

<u>TABLE</u>	<u>PAGE</u>
2.1 Plasma radical conditions for IRIS an LIF experiments.....	20
2.2 IRIS conditions for surface reactivity values.....	22
2.3 LIF conditions for $\theta_R$ and $\theta_T$ values.....	24
2.4 OES conditions for $\theta_V$ values.....	26
3.1 CH <sub>3</sub> OH decomposition pathways .....	49
3.2 MTBE decomposition pathways.....	50
4.1 Spectroscopic transitions used in calculations of $\Theta_V$ from OES spectra, and of $\Theta_R$ and $\Theta_T$ from LIF spectra.....	73
4.2 $T_e$ (in eV) for selected plasma systems .....	86
5.1 XPS elemental composition, IEP, and CA values for Ar plasma treated SiO <sub>x</sub> N <sub>y</sub> substrates.....	106
5.2 XPS elemental compositions, IEP, and CA values for H <sub>2</sub> O plasma treated SiO <sub>x</sub> N <sub>y</sub> substrates.....	112
5.3 XPS elemental compositions, IEP, and CA values for NH <sub>3</sub> plasma treated SiO <sub>x</sub> N <sub>y</sub> substrates.....	114
6.1 Atomic concentrations, IEP, and CA for Ar plasma treated nat-SiO <sub>2</sub> .....	137
6.2 Atomic concentrations, IEP, and CA for Ar and H <sub>2</sub> O plasma treated dep-SiO <sub>2</sub> .....	144
6.3 Atomic concentrations, IEP, and CA for H <sub>2</sub> O plasma treated nat-SiO <sub>2</sub> .....	147
7.1 XPS percent composition of untreated and plasma treated Zeolite X .....	167
8.1 XPS percent composition and C/N ratios for freshly treated and aged sample .....	192
A.1 XPS elemental compositions, IEP, and CA values for cleaned SiO <sub>x</sub> N <sub>y</sub> substrates ..	210
A.2 XPS elemental compositions, IEP, and CA values for cleaned nat-SiO <sub>2</sub> substrates.	211

## **CHAPTER 1**

### **INTRODUCTION**

This chapter provides an introduction to the fundamentals of plasma chemistry along with the discussion of three aspects of plasma technology explored in this dissertation: gas-phase diagnostics, surface modification, and chemical vapor deposition. The idea of plasma-surface interaction studies for advancing these technologies is also incorporated, with special emphasis on issues associated with wastewater remediation, energetics of diatomic molecules, IEP determination of metal oxides, surface modification of zeolites, and deposition of amorphous carbon nitride films. This chapter is concluded with a summary of the research discussed in subsequent chapters.

## 1.1 Plasma Chemistry

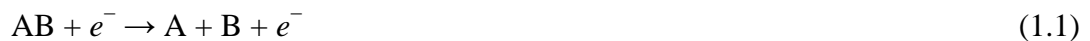
Plasma discharges create an abundance of energetic gas phase species, including ions, electrons, excited state species, photons, and reactive neutrals. The presence of such reactive components makes these systems extremely useful, but very complex and difficult to understand at the same time. Plasmas can occur naturally as lightning, flames, and auroras. They can also be created under both simple and complex laboratory conditions, and can be very useful for commercial applications, including those requiring surface modification, film deposition, or etching. There are two main categories for plasmas based on their characteristic temperatures; thermal and cold plasmas.<sup>1</sup> Thermal plasmas (e.g. the sun), are characterized by equivalent gas and charged particle temperatures, whereas cold plasmas are not at local thermodynamic equilibrium (LTE). A non-LTE results in an electron temperature,  $T_e$ , up to two orders of magnitude greater than the ion temperature,  $T_i$ , and the neutral gas temperature,  $T_g$ , in the plasma bulk.<sup>1</sup> Cold plasmas are of particular use in industry because of their ability to promote specific types of gas-phase reactions and species that can modify bulk materials. The research in this dissertation focuses on the use of cold plasmas ignited and maintained electrically using radio frequency (rf) only at 13.56 MHz.

This dissertation intends to propel the improvement of plasma chemistry by understanding the reactions that are occurring in the gas-phase of rf plasma discharges and at the plasma-surface interface of different substrates. In the plasma systems used in this research, optical diagnostics along with surface characterization techniques will be presented, details on the specifics of these plasma discharges are given below and descriptions of the different reactor systems and techniques can be found in Chapter 2.

## 1.2 Gas-Phase Diagnostics

**Wastewater Remediation.** The Environmental Protection Agency (EPA) places strict regulations on the amount of contaminants that are allowed in drinking water and natural environments. So the remediation of contaminated water is a significant concern for industries that have to comply with these regulations. Specifically, those contaminants associated with fuel oxygenate additives such as methyl *tert*-butyl ether (MTBE), ethyl *tert*-butyl ether (ETBE), ethanol (C<sub>2</sub>H<sub>5</sub>OH), *tert*-butyl alcohol (TBA) and methanol (CH<sub>3</sub>OH) are of enormous concern as they partition readily into the water phase.<sup>2,3</sup> Here, the remediation of artificially contaminated water samples with either CH<sub>3</sub>OH or MTBE as the organic contaminant in the gas phase of an rf plasma was analyzed by optical emission spectroscopy (OES) and mass spectrometry (MS). Plasma remediation of wastewater is not a traditional plasma application. The gas-phase properties plasmas possess are ideal for this application.

The plasmas in the Fisher lab are cold rf plasma discharges and are generated and sustained when a free electron is accelerated across an applied electric potential and a collision occurs with another species, often a molecule. During a collision, electron energy is transferred to the collision partner, thereby allowing a variety of gas-phase reactions to follow that we can study. Potential reactions of interest include:



where, AB is an OH molecule and the asterisk indicates an excited state species. Reactions 1.1-1.4 describe the processes of electron impact dissociation, excitation, dissociative excitation, and ionization, respectively. Dissociation of a molecule (reaction 1.1) occurs when a molecule is excited above its given threshold and is important to the wastewater project because breakdown of the organic parent molecule to a less toxic species is necessary to achieve remediation. Excitation (reaction 1.2) is the production of an excited state species from the collision of an electron and a molecule or atom. Formation of excited state species through excitation processes was also essential in the wastewater remediation study, because OES was used to follow the species of interest. Dissociative excitation (reaction 1.3) occurs when a product of a dissociation reaction is promoted to an excited state. This reaction was found to be the most crucial to the wastewater remediation study because the excitation of the dissociated parent molecule allowed for its relative concentration to be tracked through a selected species of interest. Ionization (reaction 1.4) produces positive or negative atomic or molecular ions. This process occurred in the wastewater remediation plasmas and ionized species were identified with MS.

We have studied these reactions in particular for the artificially contaminated water samples with OES and MS. Because plasmas are an inexpensive and reliable way to breakdown organic contaminants in water, they provide an alternative to expensive and time-consuming techniques that are currently being used. Chapter 3 presents the study of the plasma remediation of artificially contaminated wastewater samples containing CH<sub>3</sub>OH and MTBE. These organic contaminants were found to exhibit different dissociation trends in the OES spectra at all rf powers. MS data revealed that oxidation

of the dissociated parent molecule species was also occurring in the plasma further reducing the toxic nature of the contaminants.

**Energetics of Diatomic Species.** The reactions occurring in the gas-phase of a plasma tend to be very complex, but the unraveling of these reactions can lead to a better understanding of why some reactions are favored over others. Distribution of energy in a plasma complicates our understanding of plasma reactions and thus represents a largely untapped area for exploration. To evaluate the contributions from a variety of parameters, and to address issues associated with radical formation mechanisms in the plasma, both single source precursors and mixed precursor systems were used for the study of energy partitioning in the main group hydrides CH, SiH, OH, and NH radicals. Internal (vibrational and rotational) and translational temperatures along with surface reactivity data for these radicals has been collected in our lab with OES, laser induced fluorescence (LIF), and our imaging of radicals interacting with surfaces technique (IRIS). These analyses provided insight into gas-phase properties for radicals in their ground state as well as their excited state. The correlation of the collected internal energies with their corresponding behavior when interacting with a specific substrate represents an extension of ongoing research that seeks to correlate and understand the impact of radical energy on surface reactivity.

Gas-phase radicals can be characterized by three different types of energies, expressed as temperatures, namely rotational ( $\theta_R$ ), translational ( $\theta_T$ ), and vibrational ( $\theta_V$ ) temperatures. Rotational temperatures represent the measurement of rotational  $J$  states within a single vibrational state. From the intensity of the spectral distribution of a selected radical species,  $\theta_R$  can be measured by comparison to simulated spectra.  $\theta_T$

represents the measurement of the kinetic motion of radical species along a specific axis of travel.  $\theta_V$  provides a measure of the distribution of vibrational states of a radical species. A fourth characteristic plasma temperature is  $T_e$ . In many systems, the electron temperature is related to both  $\theta_V$  and the electron density.

Radical interactions with a surface are thought to depend on the amount of energy the radical contains. Clearly, this energy could be in many forms (i.e. internal vs. kinetic); thus, the measurement of all three characteristic temperatures described above could be invaluable in understanding radical-surface reactions. One method for measuring surface interactions employs our unique imaging of radicals interacting with surfaces (IRIS) technique. IRIS provides surface scattering coefficients ( $S$ ), which can be acquired as a function of a range of plasma parameters. Having  $S$  and  $\theta_R$ ,  $\theta_V$ , and  $\theta_T$  values allows the determination of the effects of different types of energy on radical-surface interactions.

In Chapter 4, a detailed analysis of the internal energies of CH, SiH, OH and NH radicals is presented. Reported energies include the  $\theta_R$ ,  $\theta_T$ , and  $\theta_V$  temperatures all measured by OES and LIF. The relationship of these temperatures to their corresponding surface scatter coefficients measured by IRIS is also examined. It should be noted that the surface scatter coefficients used for these correlations were measured previously by other students and postdoctoral associates in the Fisher group. At the time those measurements were made, however, extensive information on both internal and kinetic temperature were not available. Thus, the contributions made by this work include (1) the measurement of  $\theta_V$  for all of the species; (2) measurement of many of the  $\theta_R$  and  $\theta_T$  values; and, perhaps most importantly, (3) derivation of the relationships that exist between characteristic plasma ( $T_e$ ) and molecular ( $\theta_R, \theta_V$  and  $\theta_T$ ) temperatures, and (4) our

ability to control plasma parameters resulted in trends that elucidated the fundamental behavior of these gas-phase species.

### **1.3 Plasma Surface Modification**

**Surface Modification of Metal Oxides.** Plasma surface modification can be examined on a molecular level with our IRIS technique, but for the characterization of plasma treated metal oxides, the surface functionality must also be explored. Surface modification of  $\text{SiO}_x\text{N}_y$ , native  $\text{SiO}_2$  (nat- $\text{SiO}_2$ ), and plasma-deposited  $\text{SiO}_2$  (dep- $\text{SiO}_2$ ) with a range of plasmas has been successfully employed in our lab to alter the surface isoelectric point (IEP) and surface charge. Plasma discharges are well suited for this application because of their ease of use, high degree of process control, minimal generation of waste, and the wide selection of gaseous precursors that can be used. Their primary advantage over wet chemical treatments is that they can be tailored to only treat the outermost layer of non-porous materials leaving the bulk properties of the material largely unchanged.<sup>4</sup> The studies presented in this dissertation found that the alteration of these materials rely on the chemistry occurring at the surface during treatment in combination with the age time after treatment. Plasma surface treatment of materials incorporates different functional groups on the surface that can in turn change characteristics of the surface, including the hydrophobic/hydrophilic character of the surface,<sup>5</sup> the IEP,<sup>6</sup> and the chemical functionality of the surface.<sup>7</sup> The analysis of the treated metal oxides was investigated with contact angle goniometry (CA), x-ray photoelectron spectroscopy (XPS), scanning electron microscopy (SEM), and Fourier transform infrared spectroscopy (FTIR).

The incorporation of chemical functionality on the surfaces of the different metal oxides occurs through the interaction of energetic particles with the surface. This forms surface radical sites that can react with active gas-phase plasma species to form functional groups on the surface. For the Ar plasma treated metal oxides, radical sites are created in the plasma and upon exposure to atmosphere they react with atmospheric species. The H<sub>2</sub>O plasma treatments introduce polar groups on the surface and amine groups are implanted with the NH<sub>3</sub> plasma treatments.

The hydrophilicity or hydrophobicity of the metal oxide surfaces are affected by the surface functionality, which can be assessed by contact angle goniometry.. CA values can be measured for a variety of liquids, including ultra pure water, non-polar solutions, and with solutions having different pH. When the latter of these are used, a plot of the CA as a function of the solution pH yields parabolic dependence that can be fit with a second order polynomial. The vertex of the polynomial fit provides the CA<sub>max</sub> value and a measure of the surface IEP.<sup>8</sup> From this, the surface charge can be determined, an acidic IEP means an overall net negative charge and a basic IEP has a net positive charge.

Here, we have explored the plasma treatment of metal oxides with plasmas which were effective in shifting CA<sub>max</sub> and IEP values. Specifically, studies of SiO<sub>x</sub>N<sub>y</sub> plasma treated substrates with Ar, H<sub>2</sub>O, and NH<sub>3</sub> are presented in Chapter 5. The Ar plasma treatment resulted in the creation of radical sites on the surface and lasted up to one week, a non-permanent modification. The H<sub>2</sub>O and NH<sub>3</sub> plasma treatments were found to permanently treat the SiO<sub>x</sub>N<sub>y</sub> surfaces and implant OH and NH<sub>x</sub> groups respectively. CA measurements were used to determine wettability, surface charge, and IEP values. Chemical composition was analyzed by XPS and images of the surface were collected

with SEM. To extend the studies of Chapter 5, the research in Chapter 6 focuses specifically on the plasma treatment of two different substrates: nat-SiO<sub>2</sub> and dep-SiO<sub>2</sub> treated with 100% Ar and 100% H<sub>2</sub>O vapor plasmas. The Ar plasma induced radical sites on the surface and the H<sub>2</sub>O plasma implanted OH functionality. The results showed that dep-SiO<sub>2</sub> substrates were less susceptible to aging effects after plasma treatment than the native oxide layers. The stability of these surfaces is attributed to their relative thickness, embedding of surface species, and mild annealing experienced during film formation.

**Surface Modification of Zeolite X.** The surface functionality of natural materials, such as zeolites can also be modified with rf plasmas. Zeolites are currently being used industrially as adsorbents, for catalysis, and in ion-exchange systems. Literature studies focused on treating Zeolite Y with fluorocarbon plasmas to chemically alter the surface of the zeolites by replacing -OH functional groups with -F plasma species.<sup>9,10</sup> This functional group replacement would change the properties of the zeolites and allow them to be used for a wider range of applications. Zeolites possess a net negative surface charge and the ability to chemically change this property by implanting different functionality on the surface and in the pores would also increase the number of uses for zeolites. Currently, zeolites are treated in wet chemical baths and the use of plasmas for these treatments would allow for less waste production, larger selection of surface treatments, and little to no structural damage.

One outcome of the incorporation of functional groups on the surface of zeolites is rearrangement of the crystal structure. The bombardment of ions on the surface can result in desorption of these functional groups, ultimately breaking chemical bonds and thereby causing further crystal structure damage. Under the optimal plasma conditions,

incorporation of chemical functionality to the zeolite surfaces over etching or crystal damage can be achieved. The resulting surface modified zeolites will provide the basis for establishment of a better understanding of plasma interactions with zeolites based on their changed hydrophilicity, surface charge, and surface functionality.

In Chapter 7, preliminary data for total area surface modification of zeolite X with  $\text{CF}_4$ ,  $\text{C}_2\text{F}_6$ , and  $\text{C}_3\text{F}_8$  plasma discharges in a new rotating drum reactor are presented. Zeolite surface functionality with these different plasma discharges was analyzed by XPS and results showed significant promise for the use of such systems to create tailored zeolite materials. The effects of plasma exposure on surface morphology was also examined using SEM and little to no damage was incurred in these experiments.

#### **1.4 Plasma Enhanced Chemical Vapor Deposition**

**Deposition of a-CN<sub>x</sub> Films.** Plasma enhanced chemical vapor deposition (PECVD) is currently used in industry for the deposition of thin films such as amorphous materials, oxides, nitrides, metal alloys, and doped materials.<sup>11-16</sup> PECVD allows for film formation over large areas and on fragile materials such as polymers. Film deposition from plasmas is the result of creating active or energetic species that are nonvolatile products from gas phase and gas-surface interface reactions. Neutral particles deposit as a layer or layers on the surface. Surface reactions can be the result of the dissociation of adsorbed species or the reaction of adsorbed radicals with the substrate to form a product. Because the thickness of deposited films can be controlled by changing plasma parameters such as rf power, chamber pressure, deposition time, and feed gas composition, understanding how these films are created/deposited is not a simple task.

Amorphous carbon nitride films produced in our laboratory delaminated when deposited from BrCN plasmas, but stayed intact when formed from CH<sub>3</sub>CN plasmas. Mixed precursor systems were also investigated and delamination occurred in most instances. Delamination was attributed to atmospheric humidity, film stress, hydrocarbon species, and Br content in the film. With the aid of XPS, further insight into previously collected data allowed for a better understanding of the incorporation of CN and additional chemical functionalities in these films after deposition prior to delamination. Thus, Chapter 8 describes efforts to understand the delamination of a-CN<sub>x</sub> films deposited on silicon wafers from single source precursor systems, namely CH<sub>3</sub>CN and BrCN. Mixed precursor systems of BrCN/CH<sub>4</sub> and three different ratios of CH<sub>3</sub>CN/BrCN/CH<sub>4</sub> were also explored to help unravel the delamination effects seen in 100% CH<sub>3</sub>CN and 100% BrCN plasma systems. Chemical composition of the deposited films analyzed with XPS found that surface species exist that promote delamination where delamination occurs.

Chapter 9 provides a summary of this dissertation work along with suggested future directions for selected projects described in this dissertation.

## 1.6 References

- <sup>1</sup>A. Grill, *Cold Plasma in Materials Fabrication From Fundamentals to Applications* (IEEE PRESS, New York, 1994).
- <sup>2</sup>C. Baus, H.-W. Hung, F. Sacher, M. Fleig, and H.-J. Brauch, *Acta Hydrochim. Hydrobiol.* **33**, 118 (2005).
- <sup>3</sup>D. A. Cassada, Y. Zhang, D. D. Snow, and R. F. Spalding, *Anal. Chem.*, 4654 (2000).
- <sup>4</sup>J. M. Grace and L. J. Gerenser, *J. Dispersion Sci. Technol.* **24**, 305 (2003).
- <sup>5</sup>M. L. Steen, L. Hymas, E. D. Havey, N. E. Capps, D. G. Castner, and E. R. Fisher, *J. Membr. Sci.* **188**, 97 (2001).
- <sup>6</sup>L. Tusek, M. Nitschke, C. Werner, K. Stana-Kleinschek, and V. Ribitsch, *Colloids Surfaces A* **195**, 81 (2001).
- <sup>7</sup>P. Favia, N. De Vietro, R. Di Mundo, F. Fracassi, and R. d'Agostino, *Plasma Process. Polym.* **3**, 66 (2006).
- <sup>8</sup>L. Chau and M. D. Porter, *Journal of Colloid and Interface Science* **145**, 283 (1991).
- <sup>9</sup>K. Nishihara, K. Furukawa, H. Ijiri, and S. Yamazaki, *Transactions of the Materials Research Society of Japan* **26**, 1201 (2001).
- <sup>10</sup>S. Yamazaki, T. Nishimura, K. Furukawa, H. Ijiri, and K. Tsutsumi, *Zeolites* **135**, 1718 (2001).
- <sup>11</sup>G. Cicala, G. Bruno, and P. Capezzuto, *journal of vacuum science & technology A-vacuum surfaces and films* **16**, 2762 (1998).
- <sup>12</sup>G. Bruno, P. Capezzuto, and G. Cicala, *journal of Applied physics* **69**, 7256 (1991).
- <sup>13</sup>K. H. A. Bogart, S. K. Ramirez, L. A. Gonzales, G. R. Bogart, and E. R. Fisher, *journal of vacuum science & technology A-vacuum surfaces and films* **16**, 3175 (1998).
- <sup>14</sup>K. M. Byun and W. J. Lee, *Metals and Materials-Korea* **6**, 155 (2000).
- <sup>15</sup>P. Favia, G. Caporiccio, and R. d'Agostino, *journal of polymer science part a-polymer chemistry* **32**, 121 (1994).
- <sup>16</sup>T. Gungor and H. Tolunay, *J. Phys.* **26**, 269 (2002).

## **CHAPTER 2**

### **EXPERIMENTAL METHODS**

This chapter provides a detailed description of the experimental apparatus, reagents, instruments, and methods used to analyze data discussed throughout this dissertation. Section 2.1 gives a description of the different reactor designs and their corresponding plasma systems. Section 2.2 discusses instrumentation used for plasma gas-phase diagnostics and surface characterization of plasma treated substrates. Section 2.3 examines specific techniques used to analyze data collected from Section 2.2.

## 2.1 Reactor Design and Plasma System

**Inductively coupled plasma (ICP) reactor.** The experimental apparatus used for gas phase analysis of artificially contaminated water samples is schematically illustrated in Figure 2.1 and has been described in detail previously.<sup>1</sup> The reactor consists of two glass tubes (50 mm i.d.) joined by an o-ring (58 mm i.d., 3.5 mm cross-section) to allow access to the interior of the reactor. The main barrel of the reactor is ~380 mm long. Feed gases enter the reactor through a 6 mm i.d. inlet stem and unreacted gases are pumped away by a two-stage rotary vane mechanical pump (2 L/s). The pressure in the chamber was monitored with an MKS Baratron capacitance manometer, which is insensitive to differing gas composition, and was allowed to stabilize for ~20 min prior to plasma ignition. For all artificially contaminated H<sub>2</sub>O experiments, the total system pressure in the plasma reactor was 100 mTorr ( $\pm 5\%$ ), and the applied rf power ( $P$ ) was varied from 20 to 100 W. For this study, samples were produced from ACS grade methanol, HPLC grade MTBE, and deionized water distilled by passing it through a Bardstead Nanopure water treatment system with a final resistivity of 18 M $\Omega$ -cm. Aqueous CH<sub>3</sub>OH (Fisher Scientific, 99.9%) and MTBE (B & J, 99.9%) solutions were prepared with concentrations ranging from 100.0 to 0.01 ppm (100.0 - 0.01  $\mu\text{g/L}$ ). Each water sample was subjected to several freeze-pump-thaw cycles to remove trapped atmospheric gases prior to use and was introduced into the reactor from a 50 mL Pyrex sidearm vacuum flask with a Teflon stopcock. The vapor pressure of the water samples was controlled (within  $\pm 2\%$ ) using a Nupro bellows-sealed metering valve. Argon (General Air, 99.985%) was added to the system as an actinometer and controlled with an MKS mass

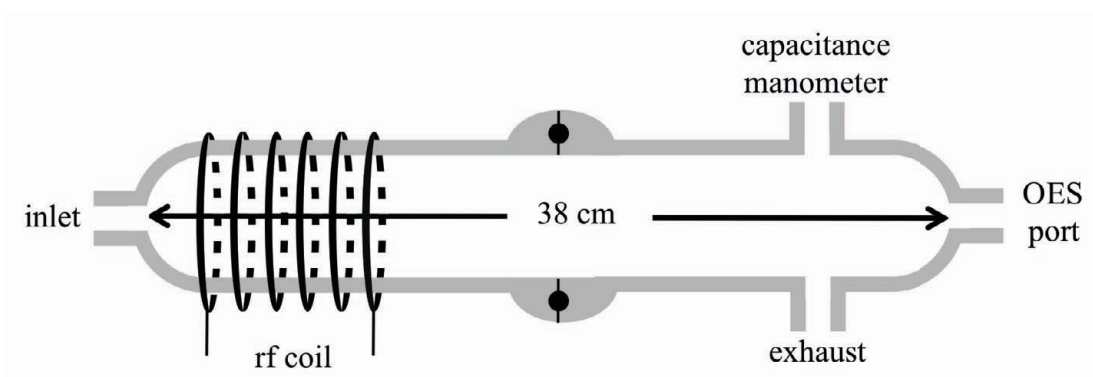


**Figure 2.1** Cross sectional schematic of the ICP reactor.

flow controller. The sample vapor and Ar percentages were calculated from the partial pressures of each gas. The Ar fraction was maintained at 3-5% for all experiments.

**Surface Modification Reactor.** All metal oxide substrate plasma treatments were performed in the same tubular reactor described above, Figure 2.1. Thermally grown  $\text{SiO}_x\text{N}_y$  substrates (BioStar, Inc), Si wafers with a native oxide (nat- $\text{SiO}_2$ ) (N-type Si, Wacker), and  $\text{SiO}_2$  films deposited from hexamethyldisiloxane (HMDSO) plasmas, described below (dep- $\text{SiO}_2$ ) were used in this set of experiments. Sample cleaning for these substrates is discussed in Appendix A. Substrates were placed on glass slides positioned at three different locations in the reactor: directly in the coil region, 5 cm downstream from the end of the coil, and 14 cm downstream from the end of the coil. Processing parameters used were  $P = 50$  and 150 W, a total system pressure of 1.0 Torr and 100 mTorr, a treatment time of 10 min, and the three substrate positions listed above. Although all three substrate locations were employed for all sets of conditions, only the data from the “in the coil region” and “5 cm downstream” locations are reported here. Substrates placed at 14 cm downstream displayed little evidence of plasma treatment (i.e. analyses showed very little change in composition or physical properties). Three precursor gases were used in these experiments: 100% Ar, 100% deionized (DI)  $\text{H}_2\text{O}$  vapor (distilled with the process described above), and 100%  $\text{NH}_3$  (Airgas, 99.99%). Aging of the substrates was followed by measuring both contact angle and surface composition within 24 hours of the plasma treatment (generally within 4 hours of initial treatment, designated as “fresh”); ~1 week after the initial treatment (designated as “1 week aged”); and at least 1 month (designated as “1 month aged”) after treatment. Between measurements, samples were stored under ambient laboratory conditions in

closed petri dishes to prevent excess dust from accumulating on the samples. For the 100% H<sub>2</sub>O vapor plasma, DI H<sub>2</sub>O was subjected to a minimum of three freeze-pump-thaw cycles as described above and was introduced to the plasma chamber as described above. For the 100% Ar and 100% NH<sub>3</sub> systems, the pressure and flow were controlled with MKS mass flow controllers and the total system pressure was monitored with an MKS Baratron capacitance manometer.

A plasma generated from a 10:90 mixture of HMDSO and O<sub>2</sub> was used to create the dep-SiO<sub>2</sub> substrates. The HMDSO (Fluka, 99.5%) was placed in a 50 mL Pyrex sidearm vacuum flask with a Teflon stopcock and subjected to three freeze-pump-thaw cycles prior to use. The HMDSO was introduced into the reactor and the flow rate controlled (within  $\pm 2\%$ ) using a Nupro bellows sealed metering valve. The HMDSO pressure was allowed to stabilize for  $\sim 10$  min before addition of O<sub>2</sub> (Airgas, 99.99%) to the gas feed using an MKS mass flow controller. Upon addition of O<sub>2</sub>, the gas ratio was calculated using the partial pressures of the gases in the reactor. SiO<sub>2</sub> depositions were performed with a total system pressure of 400 mTorr,  $P = 50$  W, and a deposition time of 10 min.

**IRIS/LIF Reactor.** Surface scatter coefficients, rotational ( $\theta_R$ ), and translational ( $\theta_T$ ) temperatures were measured using our imaging of radicals interacting with surfaces (IRIS) technique, which has been described in detail previously.<sup>2</sup> IRIS experiments combine molecular beam techniques and laser induced fluorescence (LIF) to investigate the steady-state surface reactivity of gas phase species with a substrate, as well as the gas phase energetics of plasma species as a function of different parameters including  $P$ , total system pressure, and gas composition. In a typical experiment, Figure 2.2, feed gases enter at the rear of the tubular glass reactor used as the source for the molecular beam and

a plasma is produced via the induction of rf power applied to an Ni-plated Cr coil wrapped around the back end of the reactor. The plasma is expanded through a set of collimating slits into the differentially pumped high vacuum interaction chamber. In this manner, a near-effusive molecular beam is formed consisting of virtually all species present in the plasma. The working pressure in the interaction chamber of the apparatus, is  $\sim 1 \times 10^{-5}$  Torr.

A variety of precursors, single source and mixtures of gases were used to investigate surface scatter coefficients and internal energies of all molecules presented in this study, Table 1. All liquid precursors; DI H<sub>2</sub>O (as described above), CH<sub>3</sub>OH, and tetraethoxysilane (TEOS) were subjected to three freeze-pump-thaw cycles prior to use. In all experiments, precursors (listed in Table 1) were admitted to the reactor using MKS mass-flow controllers. The total system pressure in each system was monitored with an MKS Baratron capacitance manometer. The total system pressure and  $P$  for each plasma system are also listed in Table 1. The plasma molecular beam in these experiments was collimated by two slits 12 mm apart. As noted in Table 2, the slit widths varied for each set of experiments, as required for each molecule. A tunable excimer-pumped dye laser system (Lambda Physik LPX210i, XECl, 180 mJ/pulse, 25 Hz) was used in all LIF experiments. Specific dye systems used for each molecule are shown in Table 1. A quartz lens is used to focus the laser at the position of the molecular beam, yielding a well-defined laser spot, <1 mm in diameter. The laser radiation intersects the plasma molecular beam at a 45° angle for  $\theta_R$  and reactivity data or at a 90° angle for  $\theta_T$  data, exciting a specific spectroscopic transition in the molecule under study. The specific transitions probed for each diatomic species are listed in Table 2. All LIF experiments

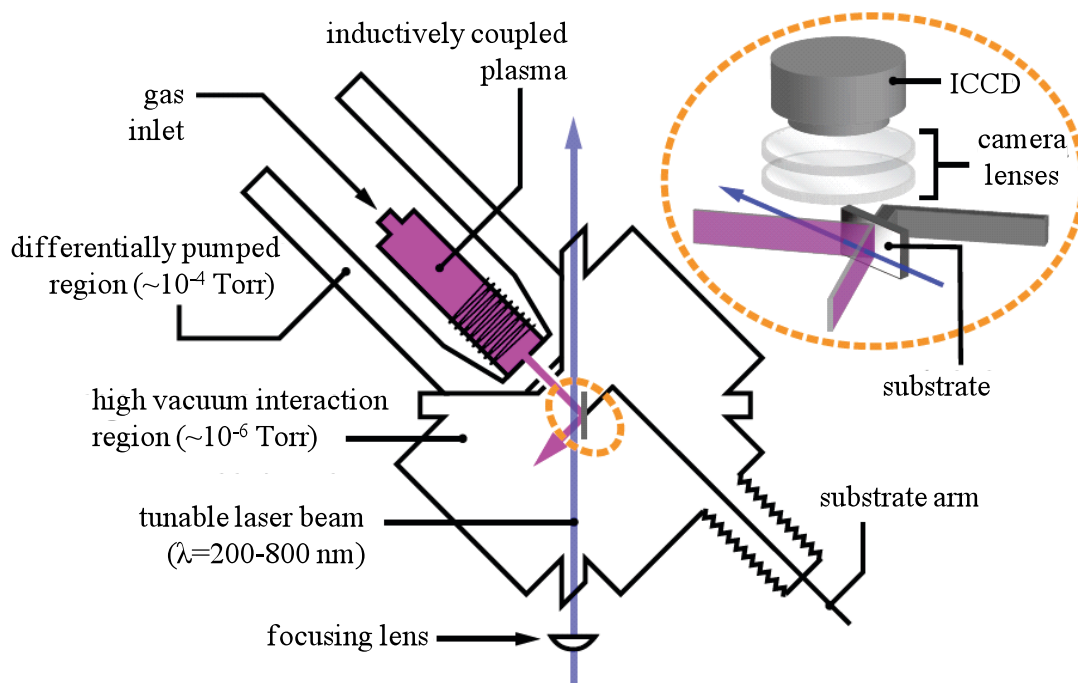


**Figure 2.2** Schematic of imaging of radicals interacting with surfaces (IRIS) apparatus. Details of the interaction region show the spatial orientation of the optics and detector relative to the molecular and laser beam.

**Table 2.1** Plasma radical conditions used for IRIS and LIF experiments.

Radical	Plasma System	Pressure (mTorr)	Rf Power (W)	Laser Dye	Filter	Radiative Lifetime (ns)	Dipole Moment (D)	EA(eV)
OH	100% H <sub>2</sub> O	50, 100, 150	50	Rhodamine B or 610*	340 nm cutoff	686	1.80	1.764
	80:20 TEOS <sup>a</sup> /O <sub>2</sub> <sup>b</sup>	50	55 and 70					
	50:50 NH <sub>3</sub> <sup>b</sup> /O <sub>2</sub>	50	100-200 (every 25)					
	20:80 NH <sub>3</sub> /O <sub>2</sub>							
100% CH <sub>3</sub> OH <sup>c</sup>	50, 100, 150	30-80						
NH	100% NH <sub>3</sub>	65	25-150 (every 25)	p-Terphenyl*	-	440	1.39	0.38
	50:50 NH <sub>3</sub> /O <sub>2</sub>	50	100-200 (every 25)					
	20:80 NH <sub>3</sub> /O <sub>2</sub>							
SiH	100% SiH <sub>4</sub> <sup>b</sup>	25, 30, 40, 45, 50	10, 20, 40, 60, 80	Excalite 417*	IR cutoff (>800 nm)	534	0.14	1.46
	SiH <sub>4</sub> /Ar <sup>b</sup>							
	100% Si <sub>2</sub> H <sub>6</sub> <sup>d</sup>							
	Si <sub>2</sub> H <sub>6</sub> /Ar							
CH	CH <sub>4</sub> <sup>b</sup> /Ar	50 and 110	20, 60, 100, 140, 180	Coumarin 440*	-	537	0.55	1.61

<sup>a</sup>Purchased from Aldrich (>97%)<sup>b</sup>Purchased from Airgas (99.7%)<sup>c</sup>Purchased from Fisher (99.9%)<sup>d</sup>Purchased from Volaix (99.99%)

were performed at laser energies in the optical saturation regime; thus the measurements are not affected by small fluctuations in laser power. LIF signals are collected for 100-750 laser shots per step, with the exact number dictated by the amount of signal present in each experiment. Spatially and temporally resolved LIF signals are collected by an electronically gated, intensified charge-coupled device (ICCD) located perpendicular to both the molecular and laser beams, directly above the interaction region. Fluorescence is collected by a set of two lenses, with focal lengths of 300 and 75 mm, imaging a 2630 mm<sup>2</sup> area onto the 512 x 512 pixel array of the ICCD. A filter can be placed between the ICCD camera and the vacuum chamber to reduce spurious signals from scattered laser light and plasma emission. Filters used in individual experiments are listed in Table 1. ICCD pixels were 4 x 4 binned, the ICCD gate widths and gate delays for all molecules are shown in Tables 2 and 3.

For surface interaction measurements, the laser radiation is directed into the main chamber of the IRIS apparatus, such that it intersects the molecular beam at a 45° angle, as shown in the enlarged region of Figure 2.2. A substrate, Table 2, can be rotated into the path of the molecular beam with its surface parallel to the laser beam. Laser-surface distances ranged from 3.0 to 4.0 mm for all systems. LIF signals are collected with the surface out of and in the path of the molecular beam. Comparisons between the spatial distributions of scattered and incident molecules are used to determine the surface reactivity of all molecules. Background images were acquired with the laser tuned to an off-resonance wavelength and subtracted from each image, Table 2. To obtain signal resulting from molecules desorbing from the substrate surface, the image acquired without the substrate is subtracted from the image with the substrate. One-dimensional

**Table 2.2** IRIS conditions for the determination of surface reactivity values.

Radical	Plasma System	Scatter	Substrate	Transition	Slit: 1/2	Gate Width/ Delay ( $\mu$ s)	On/Off Res. $\lambda$ (nm)
OH	100% H <sub>2</sub> O	0.45 $\pm$ 0.10	SiO <sub>2</sub>	A <sup>2</sup> $\Sigma^+$ $\leftarrow$ X <sup>2</sup> $\Pi$	1.2/1.3	1.3/1.5	307.848/ 307.836
	80:20 TEOS/O <sub>2</sub>	0.43 $\pm$ 0.05	Si <sub>3</sub> N <sub>4</sub>				
	50:50 NH <sub>3</sub> /O <sub>2</sub>	-	-				
	20:80 NH <sub>3</sub> /O <sub>2</sub>	0.58 $\pm$ 0.08	Polyethylene				
	100% CH <sub>3</sub> OH	-	-				
NH	100% NH <sub>3</sub>	2.59 $\pm$ 0.12	Polyimide	A <sup>3</sup> $\Pi$ $\leftarrow$ X <sup>3</sup> $\Sigma^-$	1.5/1.6	1.0/1.6	336.072/ 336.050
		0.85 $\pm$ 0.10	Polyimide				
		0.98 $\pm$ 0.07	Pt				
		1.30 $\pm$ 0.20	Pt				
	100%	Si <sub>3</sub> N <sub>4</sub>					
	50:50 NH <sub>3</sub> /O <sub>2</sub>	-	-				
20:80 NH <sub>3</sub> /O <sub>2</sub>	-	-					
SiH	100% SiH <sub>4</sub>	0.05 $\pm$ 0.05	Si wafer	A <sup>2</sup> $\Delta$ $\leftarrow$ X <sup>2</sup> $\Pi$	1.0/1.0	2.0/1.6	413.418/ 413.440
	SiH <sub>4</sub> /Ar	-	-				
	100% Si <sub>2</sub> H <sub>6</sub>	0.05 $\pm$ 0.03	Si wafer				
	Si <sub>2</sub> H <sub>6</sub> /Ar	-	-				
CH	CH <sub>4</sub> /Ar	0.00 $\pm$ 0.05	a-C:H	A <sup>2</sup> $\Delta$ $\leftarrow$ X <sup>2</sup> $\Pi$	1.6/1.7	2.0/1.6	430.402/ 430.200
		0.01 $\pm$ 0.04	a-C:H				
		0.04 $\pm$ 0.07	a-C:H				
		0.01 $\pm$ 0.05	a-C:H				

cross sections were formed by averaging 20 pixel-wide columns along the laser axis and plotting signal intensity as a function of distance along the laser path, where zero is arbitrarily selected as the center of the molecular beam. Spatially-resolved LIF data are interpreted using a quantitative model of the experiment that produces the surface reactivity of the radical of interest. The simulation procedure, described in detail previously,<sup>2</sup> is based on the known geometry of the experiment and calculates the spatial distribution of the radical number density in the molecular beam at the interaction region and of molecules scattering from the substrate surface. The surface scattering coefficient,  $S$ , defined as the ratio of the flux of the scattered molecules to that of the incident beam, is adjusted to best fit the experimental data. The surface reactivity,  $R$ , is defined as  $1-S$ . Plasma parameters for the reactivity measurements of the molecules studied here are listed in Table 2 and have been discussed in detail previously, OH,<sup>2-6</sup> NH,<sup>5,7</sup> SiH,<sup>3,8</sup> and CH.<sup>9,10</sup>

We have collected LIF excitation spectra for OH,<sup>2,4</sup> NH,<sup>5</sup> SiH,<sup>8,14</sup> and CH<sup>9,10</sup> and have measured the  $\theta_R$  using multiple lines from each spectral region. Wavelengths used for each molecule are listed in Table 3. Final rotational temperatures were determined from simulating the individual spectrum for each molecule using the LIFBASE program,<sup>3</sup> and optimizing  $\theta_R$  values to match the experimental spectra.<sup>15</sup> The measurement of  $\theta_R$  is most easily accomplished by measuring the intensity of spectral lines that represent significantly different rotational quantum states. Step sizes and number of laser pulses for molecules are listed in Table 3.

We have scanned individual rotational lines from different vibrational bands where they occupy the same spectral region and compared these experimental data to spectra

**Table 2.3** LIF conditions for the determination of  $\theta_R$  and  $\theta_T$  values.

Radical	Plasma System	$\lambda$ Range/Step Size	Transition	$\Delta$ Gate Delay	Gates per exposure
OH	100% H <sub>2</sub> O	306.5-307.5 nm/ 0.001 nm	$A^2\Sigma^+ \leftarrow X^2\Pi$	500 nm	250
	80:20 TEOS/O <sub>2</sub>				
	50:50 NH <sub>3</sub> /O <sub>2</sub>				
	20:80 NH <sub>3</sub> /O <sub>2</sub>				
	100% CH <sub>3</sub> OH				
NH	100% NH <sub>3</sub>	335.25-335.6 nm/ 0.001 nm	$A^3\Pi \leftarrow X^3\Sigma^-$	1686 ns	200
	50:50 NH <sub>3</sub> /O <sub>2</sub>				
	20:80 NH <sub>3</sub> /O <sub>2</sub>				
SiH	100% SiH <sub>4</sub>	413.40-413.45 nm/ 0.001 nm	$A^2\Delta \leftarrow X^2\Pi$	300 ns	10,000
	SiH <sub>4</sub> /Ar				
	100% Si <sub>2</sub> H <sub>6</sub>				
	Si <sub>2</sub> H <sub>6</sub> /Ar				
CH	CH <sub>4</sub> /Ar	429.6-430.5 nm/ 0.001 nm	$A^2\Delta \leftarrow X^2\Pi$	205 nm	1,000

simulated in LIFBASE to obtain an estimate of  $\theta_T$  in the plasma systems listed in Table 3. The LIFBASE program allows for spectra to be fit assuming linear, full, or partial saturation behavior. Although we operate in the optical saturation regime, the best fits to the experimental excitation spectra were found assuming a linear saturation in the simulation. This type of behavior has been seen previously and results when a laser beam interacts with a volume of gas that exceeds the focal volume of the laser.<sup>16</sup> Specific conditions for OH, NH, SiH, and CH have described in detail previously and are shown in Table 3.<sup>8,9,14</sup>

The vibrational temperature,  $\theta_v$ , for each molecule has also been measured using multiple lines from each spectral region obtained by optical emission spectroscopy (OES), Table 4. OES spectra was used to determine  $\theta_v$  by simulating the individual spectrum for each molecule using the LIFBASE program, and optimizing  $\theta_v$  values to match the experimental spectra as described for  $\theta_R$ .

**Rotating Drum Reactor.** Zeolite modification experiments were performed on zeolite X (Sigma Aldrich) in a home-built ICP rotating drum reactor, Figure 2.3. This reactor is described in detail in Chapter 7, section 7.2. Zeolites were not cleaned prior to plasma modification, treatment times were 30 minutes in either the still or rotating mode with a total system pressure of 75 mtorr and an applied rf power of 50 W. Plasma systems included 100%  $\text{CF}_4$  (Airgas, semiconductor grade), 100%  $\text{C}_2\text{F}_6$  (Airgas, semiconductor grade) and 100%  $\text{C}_3\text{F}_8$  (Airgas, semiconductor grade). All gases were controlled with an MKS mass flow controllers. The total system pressure of these gases was allowed to stabilize for at least 20 min before treatment and was monitored with an MKS capacitance manometer.

**Table 2.4** Plasma conditions, parameters, and transitions used to determine  $\theta_v$  with OES.

Radical	Plasma System	Emitted $\lambda$ (nm)	Transition
OH	100% H <sub>2</sub> O	308	A <sup>2</sup> $\Sigma^+$ → X <sup>2</sup> $\Pi$
	80:20 TEOS/O <sub>2</sub>		
	50:50 NH <sub>3</sub> /O <sub>2</sub>		
	20:80 NH <sub>3</sub> /O <sub>2</sub>		
	100% CH <sub>3</sub> OH		
NH	100% NH <sub>3</sub>	335.8	A <sup>3</sup> $\Pi$ → X <sup>3</sup> $\Sigma^-$
	50:50 NH <sub>3</sub> /O <sub>2</sub>		
	20:80 NH <sub>3</sub> /O <sub>2</sub>		
SiH	100% SiH <sub>4</sub>	411.0	A <sup>2</sup> $\Delta$ → X <sup>2</sup> $\Pi$
	SiH <sub>4</sub> /Ar		
	100% Si <sub>2</sub> H <sub>6</sub>		
	Si <sub>2</sub> H <sub>6</sub> /Ar		
CH	CH <sub>4</sub> /Ar	389	A <sup>2</sup> $\Delta$ → X <sup>2</sup> $\Pi$

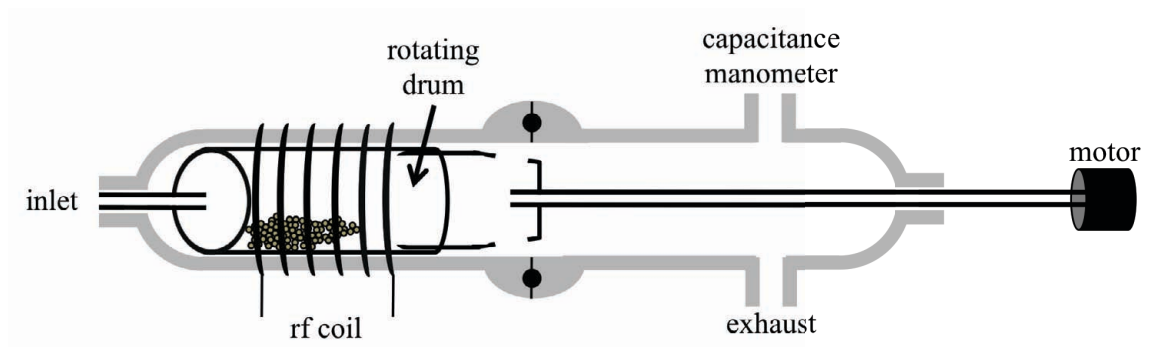


**Figure 2.3** Cross-sectional schematic of the rotating drum reactor used for zeolite modification.

**Deposition Reactor.** The experimental apparatus used for film deposition is schematically illustrated in Figure 2.4 and been described in detail previously.<sup>12,13</sup> The pressure in the chamber was monitored with an MKS Baratron capacitance manometer and was allowed to stabilize before initiating the plasma discharge. For all depositions, the pressure was maintained at  $100 \pm 2$  mTorr and  $P = 50 \pm 2$  W. Deposition times ranged from 10 to 40 minutes. Following deposition, the plasma discharge was stopped, and the flow of precursor was continued for 20 minutes to minimize the effect of oxidation upon exposure to atmosphere.

## 2.2 Instrumentation

**Gas Phase Analysis.** OES spectra were acquired in the ICP reactor described in Section 2.1 fitted with a replaceable fused quartz window at the downstream end of the reactor, allowing for the coaxial collection of plasma emission for maximum signal intensities. Plasma emission was imaged onto a 10  $\mu\text{m}$  entrance slit of an Avantes multichannel spectrometer fitted with four optical fibers fused into one cable. The spectrometer houses four fiber gratings yielding a 0.1 nm resolution, four 3648 pixel charged coupled device (CCD) array detectors, and a wavelength detection range from 187 to 1016 nm. Emission signal integration times ranged between 2 and 2000 ms. OES data was acquired for all plasma remediation of wastewater experiments and the plasma systems studied with the IRIS/LIF reactor, Table 2.4.

Mass spectrometry (MS) data were collected using a previously described<sup>17</sup> independent apparatus equipped with an ICP source nearly identical to that used for the OES measurements and a Hiden PSM003 mass spectrometer capable of detecting both

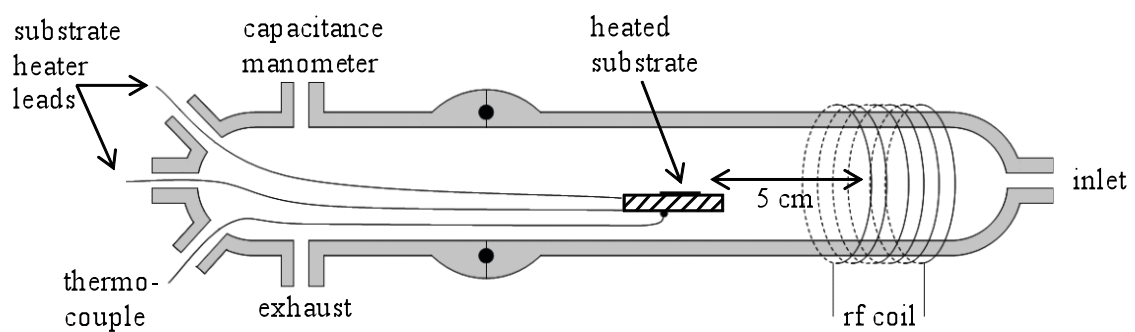


**Figure 2.4** Cross-sectional schematic of the experimental apparatus used for deposition studies.

neutral and ionic species in the plasma, Figure 2.5. Neutral species can be detected with the ionizer on (RGA mode), wherein the neutral species are ionized by electron impact. Nascent ions created by the plasma are detected with the ionizer off (positive ion mode). Although energy analysis was performed to determine ion energy distributions of the positive ions present in the plasma, they are not presented here. MS data were collected only for the plasma remediation of wastewater experiments.

**Surface Characterization.** Static contact angles (CA) were measured by the sessile drop method with a CA goniometer (Krüss DSA 10) equipped with video capture. The automatic dosing feature of the DSA 10 dispenses a water drop (~2  $\mu\text{L}$ , DI water) on a surface and the needle is manually withdrawn. An image was taken within 2 seconds of the placement of the drop on the surface. CA measurements are analyzed by one of six CA profiles available with the DSA 10 imaging software. In general, our CA values were fit with the circle fitting profile, unless otherwise noted. Three separate measurements were made on each substrate at different locations randomly varying the order in which the pH solutions were utilized. Reported  $CA_{\text{max}}$  (the maximum in CA measurements) values were calculated using a Labview<sup>TM</sup> (Labview 8.6, National Instruments) program that iteratively removed a single data point from a complete CA vs. pH data set to give a modified data set of a minimum of two separate substrates. Samples were stored under ambient laboratory conditions in closed petri dishes between measurements to prevent excess dust from accumulating on the samples.

For all isoelectric point (IEP) measurements, CA data were collected using ten solutions with different pH, ranging from 0.9 to 13.0, created using 0.1 N solutions of NaOH and

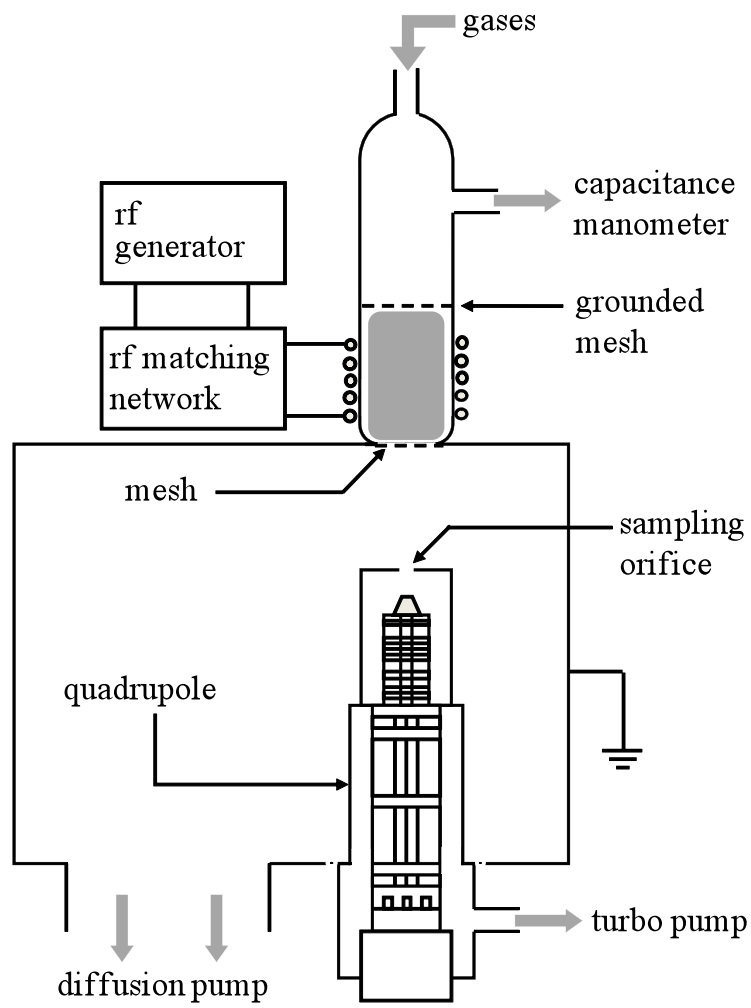


**Figure 2.5** Cross-sectional schematic of the experimental apparatus used for mass spectrometry.

0.2 N HCl to adjust the pH. The solution pH values were monitored weekly with an Accurnet excel dual channel pH/ion/conductivity meter (Fisher Scientific) and were adjusted as needed. CA titrations were performed on all metal oxide surfaces studied:  $\text{SiO}_x\text{N}_y$ , nat- $\text{SiO}_2$ , and dep- $\text{SiO}_2$ .

Surface morphology, including the possibility of damage from the plasma treatments was monitored with conventional scanning electron microscopy (SEM). Images were obtained using a field emission JEOL, JSM-6500F microscope with an accelerating voltage of 15 keV. Prior to SEM analysis, the substrates were affixed to a standard SEM stub by double-sided Cu tape (3M brand). To prevent charge excess on the surface of the substrate during analysis, ~5 nm of Au was sputtered onto the surface by an Anatech sputter coater prior to imaging. SEM images were collected for all metal oxide plasma treated substrates and all zeolite modifications.

Survey and high-resolution x-ray photoelectron spectroscopy (XPS) spectra were collected on samples using a Physical Electronics PHI-5800 ESCA/AES system. The monochromatic Al  $K_\alpha$  X-ray source (1486.6 eV) at 350 W and 15 kV was used for all data sets with a photoelectron take-off angle of 45°. Survey scans were collected with a pass energy of 93.90 eV and high-resolution spectra were acquired with a pass energy of 23.50 eV. Charge correction for all spectra were referenced to the  $\text{C}_{1s}$  peak at 284.8 eV.<sup>18</sup> Elemental compositions were calculated from high-resolution spectra and all values reported are the mean and standard deviation of a minimum of three measurements on at least two samples (i.e.  $\geq 6$  measurements). XPS data were collected for all metal oxide plasma treated substrates, all zeolite modifications, and all BrCN depositions.

Surface composition/functionality of plasma treated substrates was examined using a Nicolet Magna 760 Fourier-transform infrared (FTIR) spectrophotometer (resolution of  $1\text{ cm}^{-1}$  and averaging over 1024 scans). Spectra for all samples were acquired immediately after treatment upon removal from the reactor. Aged samples were kept in closed petri dishes for 1 month and spectra were collected as needed. FTIR data was collected on nat-SiO<sub>2</sub> and dep-SiO<sub>2</sub> plasma treated substrates.

### 2.3 Analysis Techniques

**Actinometric OES.** Actinometry was used to provide quantitative data on the species present in the plasma. Actinometric OES has been used extensively<sup>19-24</sup> to determine the relative density of ground state species. In its simplest form, the ratio of the emission intensity from the excited state species of interest ( $I_x$ ) to that of an actinometer ( $I_{act}$ ) is taken as the relative number density for the ground state species of interest.<sup>24</sup> The noble gases make suitable actinometers, based on their inert properties and direct electron excitation processes.<sup>21</sup> Here, small amounts (3-5%) of Ar (actinometric signal for Ar\* at 750 nm) were added to the plasmas because it is relatively inexpensive and has been shown to provide reliable actinometry for a wide range of systems.<sup>19-21,25</sup> Note that for wastewater remediation studies OES experiments labeled as 100% H<sub>2</sub>O, 100% CH<sub>3</sub>OH, and 100% MTBE are data taken with undiluted monomer, but still contain 3-5% Ar in the feed to allow for actinometric analysis of the data. Thus, the “100%” identifier is intended to indicate the concentration of the monomer, and not the concentration of the monomer in the feed.

**Isoelectric Point (IEP) Determination.** The acid-base properties of the metal oxide substrates were determined by the method of Chau and Porter.<sup>26</sup> Their model used the

Young relationship to examine the compositional changes of the surface by monitoring solid and liquid surface tensions in equilibrium with the saturated liquid vapor,  $\gamma^{\circ}_{LV}$  and  $\gamma^{\circ}_{SV}$ , respectively, by the change in pH. Systematically varying the pH of the contact angle liquid reveals changes in the ionization of oxide surfaces. Employing test solutions with different pH also allows the IEP of a surface to be determined as changes in surface charge density control the contact angle of a surface. As previously discussed,<sup>26-31</sup> a maximum in contact angle occurs at the point of zero surface charge. Here, we plotted the measured contact angle as a function of the pH of the test liquid, and fit the data with a second order polynomial to determine the maximum contact angle, and thus the IEP for the untreated and treated surfaces.

The relative magnitude of the error of the CA and IEP values as noted above were measured with a Labview<sup>TM</sup> (Labview 8.6, National Instruments) program that iteratively removed a single data point from a complete CA vs. pH data set to give a modified data set. A polynomial fit was used on the modified data set, yielding the new IEP for the modified set by setting the 1<sup>st</sup> derivative of the polynomial to zero and solving for pH. The value of the maximum CA (i.e., the CA at the IEP, or  $CA_{max}$ ) was calculated by solving the polynomial at the IEP. The reported average IEP,  $CA_{max}$  values, and corresponding errors for each come from compiled sets of IEP and  $CA_{max}$  values calculated from fitting multiple modified data sets. The reported error comes from the fit to the data and thus demonstrates how error in CA measurements affects the calculated IEP and  $CA_{max}$  values.

**XPS analysis for  $SiO_xN_y$ .** All high-resolution XPS spectra were analyzed using XPS Peak v4.1 software. Because the substrates were amorphous silicon oxynitride samples,

the analysis of high resolution spectra was relatively complex. Here some of the specific details on the analysis procedure used to deconstruct the XPS spectra acquired on both untreated and treated  $\text{SiO}_x\text{N}_y$  substrates are explained. High resolution XPS spectra were collected for the  $\text{Si}_{2p}$ ,  $\text{O}_{1s}$ , and  $\text{N}_{1s}$  regions, and were generally fit with 100% Gaussian functions with each full width at half maximum (FWHM)  $\leq 2.0$  eV, based on typical values found for plasma treated and plasma deposited materials,<sup>32</sup> as well as generally accepted rules regarding peak fitting in XPS analyses.<sup>33</sup> Lorentzian distributions were not included because the Lorentzian distribution allows the peaks to have wings that could be masking another binding environment. Thus, the Gaussian function allowed for clear definition of the peaks set in each region.

Given the rather amorphous nature of the original  $\text{SiO}_x\text{N}_y$  samples, it is difficult to make absolute assignments for some of the binding environments. For example, for the  $\text{Si}_{2p}$  spectra, possible binding environments in these materials include  $\text{SiO}_2$ ,  $\text{Si}_3\text{N}_4$ ,  $\text{SiO}_3\text{N}$ , and  $\text{SiON}_3$ . Some studies have reported as many as fifteen different binding environments for the  $\text{Si}_{2p}$  peak of a- $\text{SiO}_x\text{N}_y$ .<sup>34</sup> One issue with trying to fit spectra with this many binding environments is that the peaks have significant overlap, with peak positions differing by only 0.1 eV. Moreover, most XPS fitting programs do not allow more than 10 peaks per region; thus, it is impossible to use the full 15 suggested by some of the literature.<sup>34,35</sup> Thus, rather than describing the bonding unit associated with silicon, all of our analyses are described in terms of the silicon oxide tetrahedral network. The  $\text{Si}(\text{-O})_4$  binding environment describes a pure tetrahedral silicon dioxide network. The deconstructed peaks labeled  $\text{Si}(\text{-O})_3$ ,  $\text{Si}(\text{-O})_2$  and  $\text{Si}(\text{-O})_1$  describe binding environments wherein oxygen has been replaced with another element. Elemental composition data

suggests that for surfaces described in this work the alternate atoms are either nitrogen or carbon.

For high-resolution Si<sub>2p</sub> XPS spectra, Alexander, et al. have assigned the binding energies for Si(-O)<sub>1</sub>, Si(-O)<sub>2</sub>, Si(-O)<sub>3</sub>, and Si(-O)<sub>4</sub> to 101.5, 102.1, 102.8, and 103.4 eV, respectively.<sup>36</sup> Although sample charging was minimized during analysis, significant peak shifts were still observed for some samples. Based on the elemental compositions and the anticipated nature of the SiO<sub>x</sub>N<sub>y</sub> surface, we also have assigned the highest energy peak to the Si(-O)<sub>4</sub> binding environment. The difference ( $\Delta$ ) in binding energies between this peak and subsequent peaks was used to determine what binding environments were present in each sample. For example, Figure 2.6 shows high-resolution Si<sub>2p</sub>, O<sub>1s</sub>, and N<sub>1s</sub> spectra for an untreated SiO<sub>x</sub>N<sub>y</sub> substrate. In the Si<sub>2p</sub> spectrum, the highest energy binding environment appears at 102.8 eV, and is assigned to Si(-O)<sub>3</sub>. The second binding environment is located at 101.7 eV, a difference of 1.1 eV. According to Alexander et al.,<sup>36</sup> the Si(-O)<sub>4</sub> and Si(-O)<sub>3-1</sub> binding environments have energies with  $\Delta = 0.6$  eV, 1.3 eV, and 1.9 eV, respectively, using Si(-O)<sub>4</sub> as the reference. Thus, the most appropriate assignments for the two peaks in the Figure 2.6a spectrum is Si(-O)<sub>3</sub> and Si(-O)<sub>1</sub>. Again, for Si(-O)<sub>x</sub> surfaces (where x = 1-3), C and/or N atoms have replaced O in the silicon dioxide network. The O<sub>1s</sub> spectrum is deconstructed into two peaks, and the N<sub>1s</sub> spectrum contains three binding environments. For the O<sub>1s</sub> spectrum, the majority of the signal arises from the dominant peak at 532.5 eV, with only ~8% in the second peak at 530.9 eV. Similarly, the N<sub>1s</sub> spectrum is dominated by the peak at 397.9 eV (~87%), but contains small contributions from moieties at 396.3 eV (~8%) and 400.8 eV (~5%). Unfortunately, the complexity of the surface makes specific

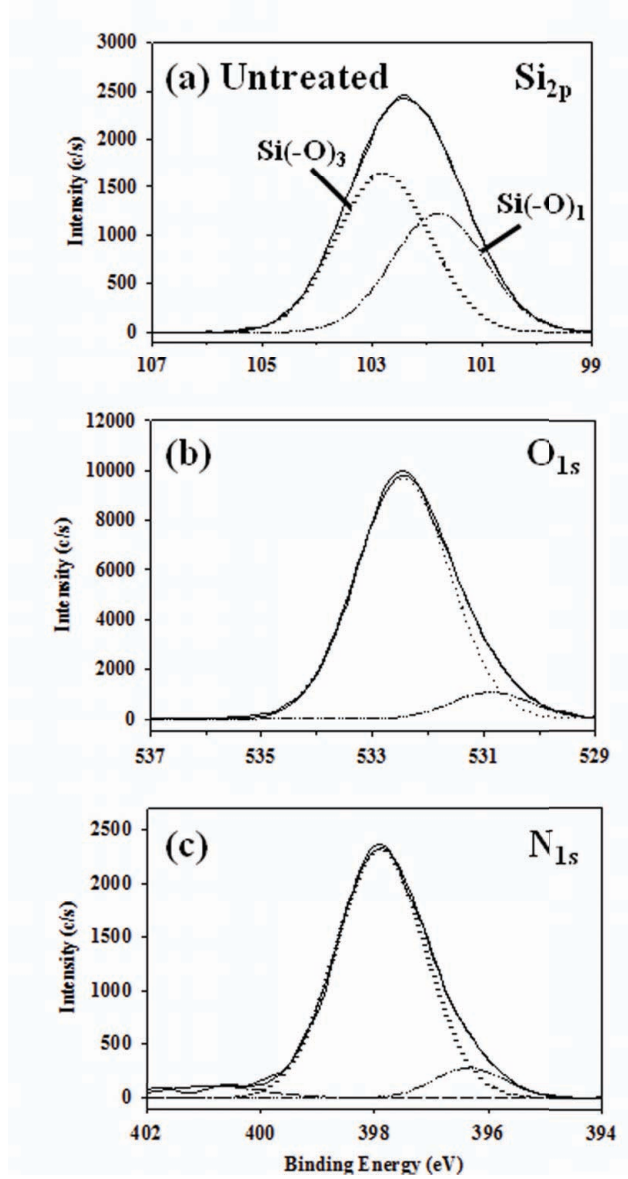


**Figure 2.6** High-resolution (a)  $\text{Si}_{2p}$ , (b)  $\text{O}_{1s}$ , and (c)  $\text{N}_{1s}$  XPS spectra for an untreated, "as received"  $\text{SiO}_x\text{N}_y$  substrate.

assignments problematic, but in general all five peaks in both spectra likely arise from  $\text{SiO}_x\text{N}_y$  environments containing different distributions of oxygen and nitrogen.<sup>34,35</sup>

**XPS analysis for nat-SiO<sub>2</sub> and dep-SiO<sub>2</sub>.** Deconstruction of the  $\text{Si}_{2p}$  and  $\text{O}_{1s}$  spectra was performed on selected nat-SiO<sub>2</sub> samples by fitting high-resolution spectra to peaks with a maximum FWHM of 1.8 eV. In contrast to the method described above for the  $\text{SiO}_x\text{N}_y$  substrates, with the SiO<sub>2</sub> substrates, spectra were fit using a 9:91 Lorentzian to Gaussian peak shape to improve the overall fit quality as determined by  $\chi^2$  analysis. The oxidized silicon binding environments in the  $\text{Si}_{2p}$  region were fit to 1 or 2 peaks to minimize the fitting error; two peaks were generally used when the oxidized peak was asymmetric with a lower energy tail. Shifts in the  $\text{Si}_{2p}$  and  $\text{O}_{1s}$  peak positions were determined explicitly when the  $\text{Si}^0$  peak was within the XPS sampling depth. For samples with a measurable  $\text{Si}^0$  binding environment, the  $\text{Si}_{2p1/2}$  and  $\text{Si}_{2p3/2}$  peaks were deconstructed by maintaining a 1:2 peak area ratio. Charge correction was then performed by shifting the average position of the deconstructed  $\text{Si}_{2p1/2}$  and  $\text{Si}_{2p3/2}$  peaks to 100.0 eV, placing the  $\text{Si}_{2p1/2}$  binding energy at ~99.7 eV. Shifts in the  $\text{Si}(-\text{O})_4$  [corresponding to Si in a tetrahedral SiO<sub>2</sub> binding environment] and  $\text{O}_{1s}$  peak maxima were calculated as the difference in binding energy of a treated sample from the untreated control sample tested at the fresh time point. For simplicity, the  $\text{O}_{1s}$  spectra are not reported here.

Deconstruction of the  $\text{Si}_{2p}$  regions of dep-SiO<sub>2</sub> samples was accomplished by shifting the adventitious carbon  $\text{C}_{1s}$  peak position to 284.6 eV. All peaks were assumed to be 100% Gaussian and FWHM was limited to <1.8 eV. The control dep-SiO<sub>2</sub> sample  $\text{Si}_{2p}$  region was fit based on previously reported silicon oxide binding environments

determined for SiO<sub>2</sub> plasma deposited films consisting of Si(-O)<sub>4</sub> [silicon in a tetrahedral oxide environment], Si(-O)<sub>3</sub> and Si(-O)<sub>2</sub> at 103.4, 102.8 and 102.1eV, respectively.<sup>37,38</sup>

The oxidized silicon binding environments of plasma treated dep-SiO<sub>2</sub> films were fit similarly to the nat-SiO<sub>2</sub> samples where the Si<sub>2p</sub> region was fit to 1 or 2 peaks to minimize the fitting error.

## 2.4 References

- <sup>1</sup>K. H. A. Bogart, N. F. Dalleska, G. R. Bogart, and E. R. Fisher, *J. Vac. Sci. Technol. A* **13**, 476 (1995).
- <sup>2</sup>K. H. A. Bogart, J. P. Cushing, and E. R. Fisher, *J. Phys. Chem. B* **101**, 10016 (1997).
- <sup>3</sup>P. R. McCurdy, K. H. A. Bogart, N. F. Dalleska, and E. R. Fisher, *Rev. Sci. Instrum.* **68**, 1684 (1996).
- <sup>4</sup>E. R. Fisher, P. Ho, B. W. G., and R. J. Buss, *J. Phys. Chem.* **97**, 10287 (1993).
- <sup>5</sup>R. J. Buss, P. Ho, E. R. Fisher, and W. G. Breiland, *Mater. Res. Soc. Symp. Proc.* **334**, 51 (1994).
- <sup>6</sup>K. H. A. Bogart, J. P. Cushing, and E. R. Fisher, *Chem. Phys. Lett.* **267**, 377 (1997).
- <sup>7</sup>E. R. Fisher, P. Ho, W. G. Breiland, and R. J. Buss, *J. Phys. Chem.* **96**, 9855 (1992).
- <sup>8</sup>W. M. M. Kessels, P. R. McCurdy, K. L. Williams, G. R. Barker, V. A. Venturo, and E. R. Fisher, *J. Phys. Chem. B* **106**, 2680 (2002).
- <sup>9</sup>J. Zhou and E. R. Fisher, *J. Phys. Chem. B* **110**, 21911 (2006).
- <sup>10</sup>D. Liu, I. T. Martin, J. Zhou, and E. R. Fisher, *Pure Appl. Chem.* **78**, 1187 (2006).
- <sup>11</sup>D. Liu and E. R. Fisher, *J. Vac. Sci. Technol. A* **25**, 368 (2007).
- <sup>12</sup>J. M. Stillahn and E. R. Fisher, *J. Phys. Chem. C* **113**, 1963 (2009).
- <sup>13</sup>J. M. Stillahn and E. R. Fisher, *J. Phys. Chem. A* **114**, 5287 (2010).
- <sup>14</sup>J. Zhou, J. Zhang, and E. R. Fisher, *J. Phys. Chem. A* **109**, 10521 (2005).
- <sup>15</sup>J. Luque and D. R. Crosley, 2.0.60 ed., edited by S. I. R. MP-99-009 (SRI International, Menola Park, CA, 2008).
- <sup>16</sup>P. Ho, W. G. Breiland, and R. J. Buss, *J. Chem. Phys.* **91**, 2627 (1989).
- <sup>17</sup>J. Zhou, I. T. Martin, R. Ayers, E. Adams, D. Liu, and E. R. Fisher, *Plasma Sources Sci. Technol.* **15**, 714 (2006).
- <sup>18</sup>K. J. Trevino, J. C. Shearer, P. R. McCurdy, S. E. Pease-Dodson, C. C. Okegbe, and E. R. Fisher, *Surf. Interface Anal.* (2010).
- <sup>19</sup>J. W. Coburn and M. Chen, *J. Appl. Phys.* **51**, 3134 (1980).
- <sup>20</sup>R. W. Dreyfus, J. M. Jasinski, R. E. Walkup, and G. S. Selwyn, *Pure Appl. Chem* **57**, 1265 (1985).
- <sup>21</sup>N. C. M. Fuller, M. V. Malyshev, V. M. Donnelly, and I. P. Herman, *Plasma Sources Sci. Technol.* **9**, 116 (2000).
- <sup>22</sup>R. Walkup, K. Saenger, and G. S. Selwyn, *Mater. Res. Soc. Symp. Proc.* **38**, 69 (1985).
- <sup>23</sup>M. V. Malyshev and V. M. Donnelly, *J. Appl. Phys.* **88**, 6207 (2000).
- <sup>24</sup>C. B. Labelle and K. K. Gleason, *J. Appl. Polym.* **88**, 6207 (2001).
- <sup>25</sup>Q. S. Yu, E. Krentsel, and H. K. Yasuda, *J. Polym. Sci.: Part A: Poly. Chem.* **36**, 1583 (1998).
- <sup>26</sup>L. Chau and M. D. Porter, *J. Colloid Interface Sci.* **145**, 283 (1991).
- <sup>27</sup>E. McCafferty, *J. Adhesion Sci. Technol.* **16**, 239 (2002).
- <sup>28</sup>E. McCafferty and J. P. Wightman, *J. Adhesion Sci. Technol.* **13**, 1415 (1999).
- <sup>29</sup>D. Chvedov and E. L. B. Logan, *Colloids and Surfaces A: Physiochem. Eng. Aspects* **240**, 211 (2004).
- <sup>30</sup>E. McCafferty and J. P. Wightman, *J. Colloid Interface Sci.* **194**, 344 (1997).
- <sup>31</sup>C. Vittoz, M. Mantel, and J. C. Joud, *J. Adhesion* **67**, 347 (1998).

- <sup>32</sup>G. M. Ingo, C. Riccucci, G. Bultrini, and G. Chiozzini, *J. Thermal Anal. Calorim.* **66**, 27 (2001).
- <sup>33</sup>M. F. Koenig and J. T. Grant, *J. Electron Spectrosc. Rel. Phenom.* **33**, 9 (1984).
- <sup>34</sup>P. Cova, S. Poulin, and R. A. Masut, *J. Appl. Phys.* **98**, 094903 (2005).
- <sup>35</sup>P. Cova, S. Poulin, O. Grenier, and R. A. Masut, *J. Appl. Phys.* **97**, 073518 (2005).
- <sup>36</sup>M. R. Alexander, R. D. Short, F. R. Jones, W. Michaeli, and C. J. Blomfield, *Appl. Surf. Sci.* **137**, 179 (1999).
- <sup>37</sup>J. C. Shearer, M. J. Fisher, D. Hoogeland, and E. R. Fisher, *Appl. Surf. Sci.* **256**, 2081 (2010).
- <sup>38</sup>D. S. Wavhal, J. Zhang, M. L. Steen, and E. R. Fisher, *Plasma Process. Polym.* **3**, 276 (2006).

## CHAPTER 3

### DETECTION LIMITS AND DECOMPOSITION MECHANISMS FOR ORGANIC CONTAMINANTS IN WATER USING OPTICAL EMISSION SPECTROSCOPY

This chapter contains data from a full paper published in the journal of *Plasma Processes and Polymers*. All of the data were collected and analyzed by Kristina J. Trevino and the manuscript was written by Kristina J. Trevino and Ellen R. Fisher. These studies examine the use of inductively-coupled rf plasmas for the detection and breakdown of organic contaminants (CH<sub>3</sub>OH, MTBE) in water. Parent molecule decomposition was followed using actinometric optical emission spectroscopy (OES) and complementary mass spectrometry data were used to explore decomposition mechanisms.

### 3.1 Introduction

There are numerous places where having clean or even ultrapure water is extremely important for drinking or production purposes. For example, the Environmental Protection Agency (EPA) has placed increasingly strict regulations on the emission of organic compounds into drinking water sources.<sup>1,2</sup> Among the many potential contaminants of drinking wells, those associated with fuel oxygenate additives such as methyl *tert*-butyl ether (MTBE), ethyl *tert*-butyl ether (ETBE), ethanol (C<sub>2</sub>H<sub>5</sub>OH), *tert*-butyl alcohol (TBA) and methanol (CH<sub>3</sub>OH) are of significant concern as they partition readily into the water phase.<sup>3,4</sup> Of these, MTBE has received extensive attention in the last decade as its concentration in some drinking water supply wells in California has exceeded 600 µg/L,<sup>1,3,5</sup> over an order of magnitude higher than the EPA's limit for drinking water of 20-40 µg/L.<sup>5</sup> Ultimately, this situation led to a 2003 ban on the use of MTBE as a gasoline additive in California.<sup>2,6,7</sup> Because MTBE is now ubiquitous in water sources worldwide, development of methods for both detection and decontamination have been the objective of many scientific studies in the past decade.<sup>1-5,8,9</sup> Another example where ultrapure water is critical is in the microelectronics industry.<sup>10,11</sup> Specifically, ultrapure water sources are used in various steps in the manufacture of microelectronics components and contaminants such as carbon (total organic content), metals, and particles can negatively impact product yield increasing waste and manufacturing costs.

One method that has been explored for the removal of organic pollutants in water, including MTBE, is plasma pollution control. Several different types of plasmas have been employed in the pursuit of organic contaminant removal from both gaseous and

aqueous waste streams, including pulsed streamer corona discharges, spark discharges, dielectric barrier discharges (DBDs) and glow discharge electrolysis.<sup>12-16</sup> Removal of organic contaminants was effective with these systems, but the amount of liquid treated was small (200 mL). Dense medium plasmas (DMPs) have been developed to determine oxidation mechanisms of organic pollutants and potentially to remove contaminants.<sup>9,12,17</sup> DMPs function by creating a discharge within a dense medium such as water, which avoids the need to volatilize the waste stream prior to entering the plasma. In DMP studies, MTBE was used as a model compound for the conversion of organic contaminants to less toxic species such as CO<sub>2</sub>, acetone, and formaldehyde.<sup>9</sup> Concentrations of organic molecules (MTBE as well as aromatic compounds) were determined using gas chromatography and mass spectrometry to monitor the DMP-treated water.<sup>9,12</sup> One advantage to using plasma-based processes (including DMPs) for removal of oxygenates such as MTBE is that OH radicals are formed and appear to be a key factor in the removal of ethers from waste water streams. The major disadvantages to DMPs, however, are that detection times are extremely long and the discharge is difficult to reproducibly sustain for extended periods of time. An additional concern is that large volumes of water may not be treatable with such devices, making their utility in ground water decontamination limited.

Inductively coupled plasmas (ICPs) are alternative plasma systems that avoid the problems associated with DMPs,<sup>18</sup> and have been used for the remediation of gas streams in microelectronics processes.<sup>14</sup> Graves and coworkers used an ICP system to detect fluorinated compounds from an etch chamber, and have also effectively dissociated and recombined the fragments with additive gas fragments to create by-products that are

environmentally benign or scrubbable.<sup>19,20</sup> Evidence for remediation came from Fourier transform infrared (FTIR) spectroscopy, which was coupled to the reactor's exhaust manifold. Likewise, Kushner and coworkers also used an ICP coupled with mass spectrometry and computer modeling to describe the plasma abatement of  $\text{CF}_4$  and  $\text{C}_2\text{F}_6$ .<sup>21</sup> One result of this combined computational and experimental study is that the consumption of the perfluorinated compounds was proportional to the applied rf power in the system, suggesting that input power is an important parameter in plasma abatement of waste streams. Although ICPs have been used for gas stream remediation, they have not been explored for the detection of organic contaminants or for small volume remediation of wastewater, which could find utility in industrial processes, including microelectronics manufacturing.

The initial goals of the work presented in this chapter were (1) to explore the effectiveness of ICPs for removal of organic contaminants from water sources; (2) to determine if optical emission spectroscopy (OES) could be used as a detection method for contaminated water sources; and (3) to determine the detection limit of OES for organic contaminants in these systems, with the intent of potentially incorporating them into microelectronics manufacturing processes. There are primarily two potential advantages of using OES for contaminant detection. First, OES is an in situ technique, eliminating the need for sample preparation and sample run time, which can amount to several minutes to hours, depending on sample size. OES can be run continuously on samples of any size, providing direct, real-time information. Gas-chromatography mass spectrometry (GC-MS) is currently the most commonly used method for detection of contaminants. With GC-MS, sample sizes are limited to the microliter range, severely

restricting the sample size that can be analyzed. Second, OES is much more cost effective than GC-MS with significantly lower capital investment as well as maintenance costs. Another consideration must be the sensitivity of the detection method. With GC-MS, the EPA limit of detection for organic contaminants is 0.02-1 ng/L (0.02-1 ppt) in drinking water. OES has the potential to have comparable detection limits, which is another motivation for the current study.

Previous work in our group has focused on using H<sub>2</sub>O vapor plasmas for the modification of polymeric materials. Included in this work was extensive gas-phase diagnostic studies utilizing both OES and laser-induced fluorescence (LIF), which clearly demonstrated that high levels of OH radicals are formed in H<sub>2</sub>O-based ICPs.<sup>22-24</sup> LIF studies for OH in plasma systems specific to my research will be discussed in detail in Chapter 4. The high levels of OH radicals produced in H<sub>2</sub>O-based ICPs suggests oxidation of MTBE and other organics should be readily achievable in these systems. We have used aqueous solutions of various concentrations of both CH<sub>3</sub>OH and MTBE to determine if OES can be used to detect organic contaminants in water. Through the addition of small amounts of Ar to the plasma, actinometry was used to provide more quantitative information on the relative densities of various plasma species. For both CH<sub>3</sub>OH and MTBE, carbon-containing fragments of the parent gas (i.e. CH and CO) are potential indicators of parent molecule breakdown. Although OES is not capable of providing molecule-specific information for the parent molecules, it does provide information on the presence of organic contaminants via these two carbon-based species. Thus, to complement these results, we have also applied mass spectrometry (MS) to the same plasmas to identify specific fragmentation patterns for both parent molecules.

Applied rf power ( $P$ ) and concentration dependence are discussed along with the potential mechanisms for parent molecule breakdown in the plasma for both CH<sub>3</sub>OH and MTBE.

### 3.2 Results

Figure 3.1 shows raw OES spectra of three different plasma systems generated from 100% H<sub>2</sub>O vapor, 100% CH<sub>3</sub>OH, and 100% MTBE ( $P = 70$  W, 100 mTorr). Figure 3.1a shows the spectrum from the 100% H<sub>2</sub>O plasma, which exhibits three primary peaks at 656, 434, and 308 nm, corresponding to emission from H $_{\alpha}$ , H $_{\beta}$ , and OH, respectively. The observation that a 100% H<sub>2</sub>O vapor system reveals only its natural components is useful for comparison to the more complex systems of 100% CH<sub>3</sub>OH and 100% MTBE plasmas, Figures 3.1b and c, respectively. Spectral features in both hydrocarbon systems reveal emission from CO, CH, and OH radicals along with peaks at 430, 656, 750, and 844 nm, corresponding to emission from H $_{\beta}$ , H $_{\alpha}$ , Ar, and O, respectively. H<sub>2</sub>\* is also observed at wavelengths above 850 nm.<sup>32</sup> The presence of both CO and CH indicate that these species may be potential OES identifiers for organic molecule breakdown. The relatively broad background present in the spectra between 400 and 600 nm is attributable to signal from the swan bands of C<sub>2</sub>.<sup>34</sup> Note that all the species identified in the OES spectra can be explained by considering the logical dissociation pathways for the parent molecules, Tables 3.1 and 3.2. Clearly, there are numerous other pathways to decomposition, but we have limited the discussion to those routes that both yield the products we observed in our OES and MS data and that are energetically feasible as determined by their reaction enthalpies,  $\Delta H_r$ .

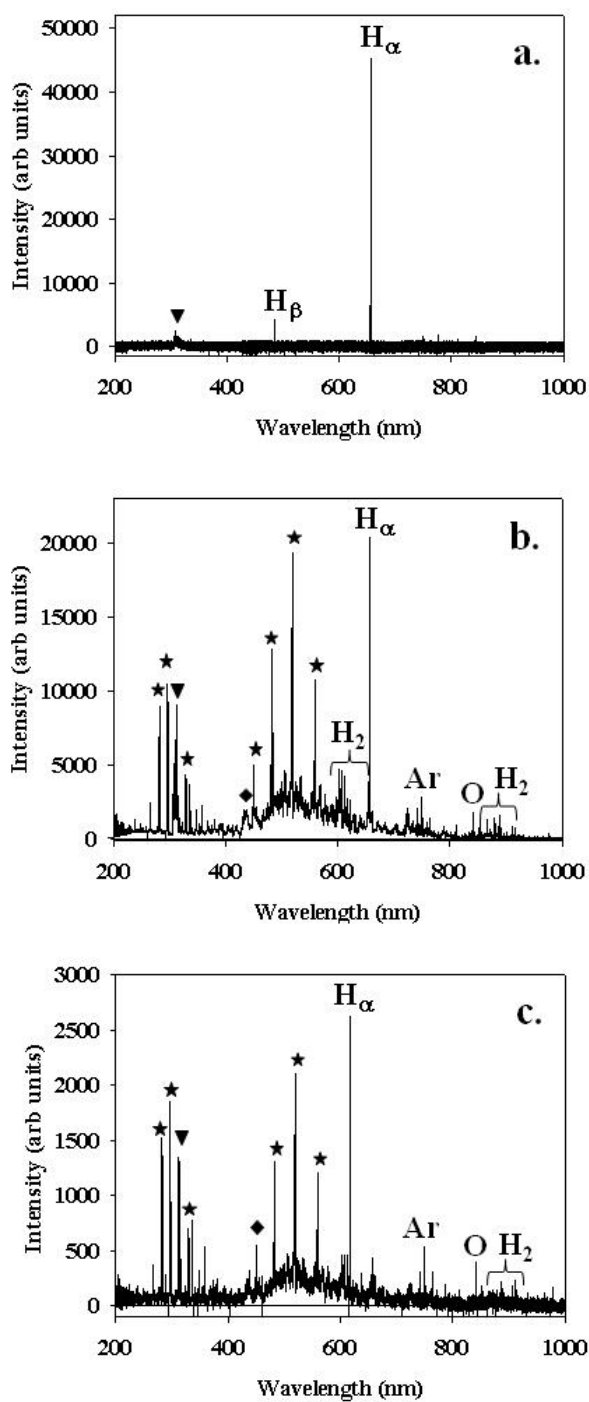


**Figure 3.1** Raw OES spectra of a) 100% H<sub>2</sub>O, b) 100% CH<sub>3</sub>OH, and c) 100% MTBE plasmas. Each spectrum was acquired at a total system pressure of 100 mTorr with  $P = 70$  W. Significant peaks are identified for emission from OH (inverted triangles), CH (diamonds) and CO (stars); other significant peaks are labeled with their atomic and molecular symbols.

**Table 3.1** Selected CH<sub>3</sub>OH decomposition pathways

Reaction	$\Delta H_r^a$ kcal · mol <sup>-1</sup>
CH <sub>3</sub> OH → CO + 2H <sub>2</sub>	21.8 ± 0.1
CH <sub>3</sub> OH → CH <sub>2</sub> O + H <sub>2</sub>	22.2 ± 0.3
CH <sub>3</sub> OH → CH <sub>2</sub> + H <sub>2</sub> O	83.4 ± 0.1
CH <sub>3</sub> OH → CH <sub>3</sub> + OH	92.3 ± 0.6
CH <sub>3</sub> OH → CH <sub>2</sub> OH + H	94.1 ± 1.6
CH <sub>3</sub> OH → CH <sub>3</sub> O + H	104.0 ± 0.8
CH <sub>3</sub> OH → CHO + H <sub>2</sub> + H	111.0 ± 0.1
CH <sub>3</sub> OH → CH + H <sub>2</sub> O + H	184.9 ± 0.1
CH <sub>3</sub> OH → CH + H <sub>3</sub> O	190.6 ± 0.1
CH <sub>3</sub> OH → CH <sub>3</sub> + O + H	194.7 ± 0.4
CH <sub>3</sub> OH → CH + OH + H <sub>2</sub>	199.9 ± 0.3
CH <sub>3</sub> OH → CH <sub>2</sub> + H <sub>2</sub> + O	200.8 ± 0.1
CH <sub>3</sub> OH → CH <sub>2</sub> + OH + H	202.6 ± 0.3

<sup>a</sup>) Calculated from  $\Delta H_r$  values found in ref.<sup>37</sup>

**Table 3.2** Selected MTBE decomposition pathways

Reaction	$\Delta H_r^{a)}$ kcal $\cdot$ mol $^{-1}$
$C_5H_{12}O \rightarrow C_3H_9 + CH_3 + CO$	$70.1 \pm 0.3$
$C_5H_{12}O \rightarrow C_4H_9O + CH_3$	$79.5 \pm 0.3$
$C_5H_{12}O \rightarrow C_2H_4 + C_2H_2 + CH_4 + H_2O$	$88.7 \pm 0.6$
$C_5H_{12}O \rightarrow C_3H_9 + C_2H_2O + H$	$102.4 \pm 0.6$
$C_5H_{12}O \rightarrow C_2H_4 + CH_4 + CH_2 + CH_2O$	$123.2 \pm 0.5$
$C_5H_{12}O \rightarrow C_3H_9 + C_2H_2 + OH$	$125.5 \pm 0.6$
$C_5H_{12}O \rightarrow C_2H_4 + C_2H_2 + CH_2 + H_2O + H_2$	$163.9 \pm 0.5$
$C_5H_{12}O \rightarrow C_2H_4 + C_2H_2 + CH_3 + OH + H_2$	$172.8 \pm 1.1$
$C_5H_{12}O \rightarrow C_3H_9 + CH + H_2 + CO$	$177.7 \pm 0.1$
$C_5H_{12}O \rightarrow C_3H_9 + CH_2 + CO + H$	$180.4 \pm 0.1$
$C_5H_{12}O \rightarrow C_4H_9O + CH + H_2$	$186.9 \pm 0.1$

<sup>a)</sup>Calculated from  $\Delta H_r$  values found in ref.<sup>37</sup>

to CO, OH, H<sub>β</sub>, H<sub>α</sub>, and O respectively. Bands attributable to H<sub>2</sub> emission are also present. Although the absolute intensity of these spectra cannot be directly compared, the peaks in the CH<sub>3</sub>OH spectrum appear to be more intense than those in the MTBE spectrum, with the exception of that attributed to O atom emission. The spectra in Figure 3.2 clearly highlight the similarity between the two systems with respect to dissociation of the parent molecules. Moreover, when compared to the spectra for the 100% CH<sub>3</sub>OH and MTBE plasmas, the spectra for the 0.01 ppm solution plasmas have fewer peaks, all of which are directly attributable to small molecular and atomic fragments of either the solute or the solvent. The most intense peaks from the carbon-containing species CO have not been eliminated. Thus, CO emission peaks were used with actinometry to identify organic species in our system and to determine detection limits in both the CH<sub>3</sub>OH and MTBE systems.

Using actinometry, we have determined the relative densities of the various emitting species in our plasmas. To monitor decomposition of organics, we are primarily interested in the carbon containing fragments present in the OES spectrum as species such as OH, O, and H could arise from decomposition of either the contaminant or water. Thus, CH, CO, and C<sub>2</sub> are all potentially viable species for actinometric studies. As can be seen from Figure 3.2, however, signals arising from both CH and C<sub>2</sub> are negligible at the lowest concentrations; thus, we have chosen to monitor only the CO\* emission for relative density studies.

Figure 3.3a shows the relative density of CO in plasmas formed from solutions containing different concentrations of CH<sub>3</sub>OH (0.9, 0.5, and 0.01 ppm) as a function of *P*.

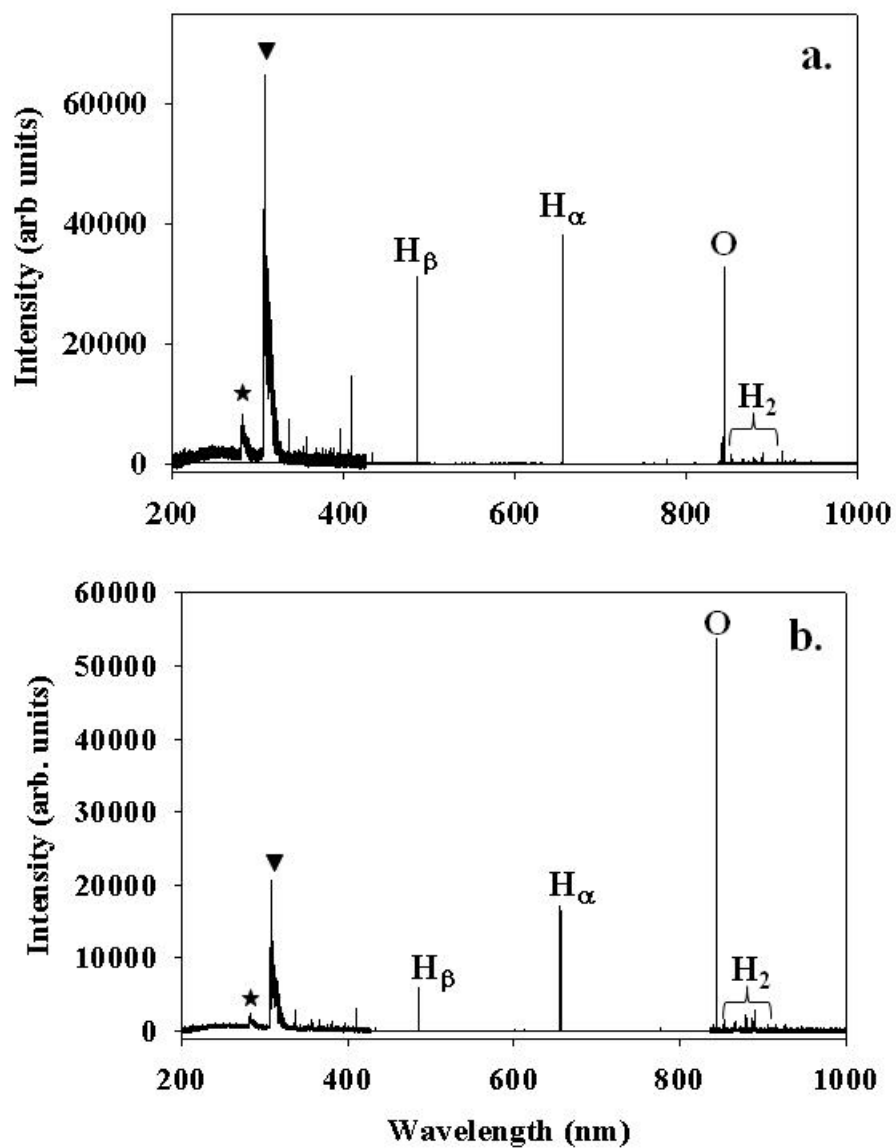


**Figure 3.2** Raw OES spectra of a) 0.01 ppm CH<sub>3</sub>OH, and b) 0.01 ppm MTBE plasmas. Each spectrum was acquired at a total system pressure of 100 mTorr with P = 70 W. Significant peaks are identified for emission from OH (inverted triangles) and CO (stars); other significant peaks are labeled with their atomic and molecular symbols.

At  $P > 50$  W, the intensity of CO decreases with decreasing CH<sub>3</sub>OH concentration, as is expected in our systems. At the lower rf powers, however, the intensity of CO is approximately the same for the 0.9 and 0.5 ppm solutions, whereas that for the 0.01 ppm solution is significantly lower. The data point for the 0.9 ppm solution at  $P = 20$  W does not follow the trend, but this is likely due to instabilities in the plasma under these conditions. At the highest CH<sub>3</sub>OH concentration (0.9 ppm), the intensity of CO increases somewhat with  $P$ , but the intensity does not change appreciably from  $P = 30$  W to  $P = 90$  W. At 0.5 ppm, the intensity of the CO radical decreases linearly as a function of  $P$  [slope, (m) = -0.35]. This behavior is somewhat unusual as we would expect that the CO intensity would increase with  $P$  due to increased fragmentation of the parent molecule at higher applied rf powers. One explanation for the observed behavior is that the CO could be further dissociating at higher  $P$  or recombining to form larger species. At the lowest concentration (0.01 ppm), the CO intensity also decreases somewhat as a function of  $P$ , although the dependence is relatively weak (m = -0.08). This is likely the result of the extremely low concentration of organic material in the plasma such that either detection of CO is limited or there is simply very little to no production of CO from the organic parent molecule.

Interestingly, the same behavior is not observed for the MTBE solutions at all concentrations. Figure 3.3b contains data for the relative density of CO in plasmas formed from solutions containing different concentrations of MTBE (0.7, 0.3, and 0.01 ppm) as a function of  $P$ . At the highest MTBE concentration (0.7 ppm), the CO intensity decreases linearly with  $P$  (m = -0.18), as was observed for the similar CH<sub>3</sub>OH concentration of 0.5 ppm. The observation of very similar trends for both CH<sub>3</sub>OH and

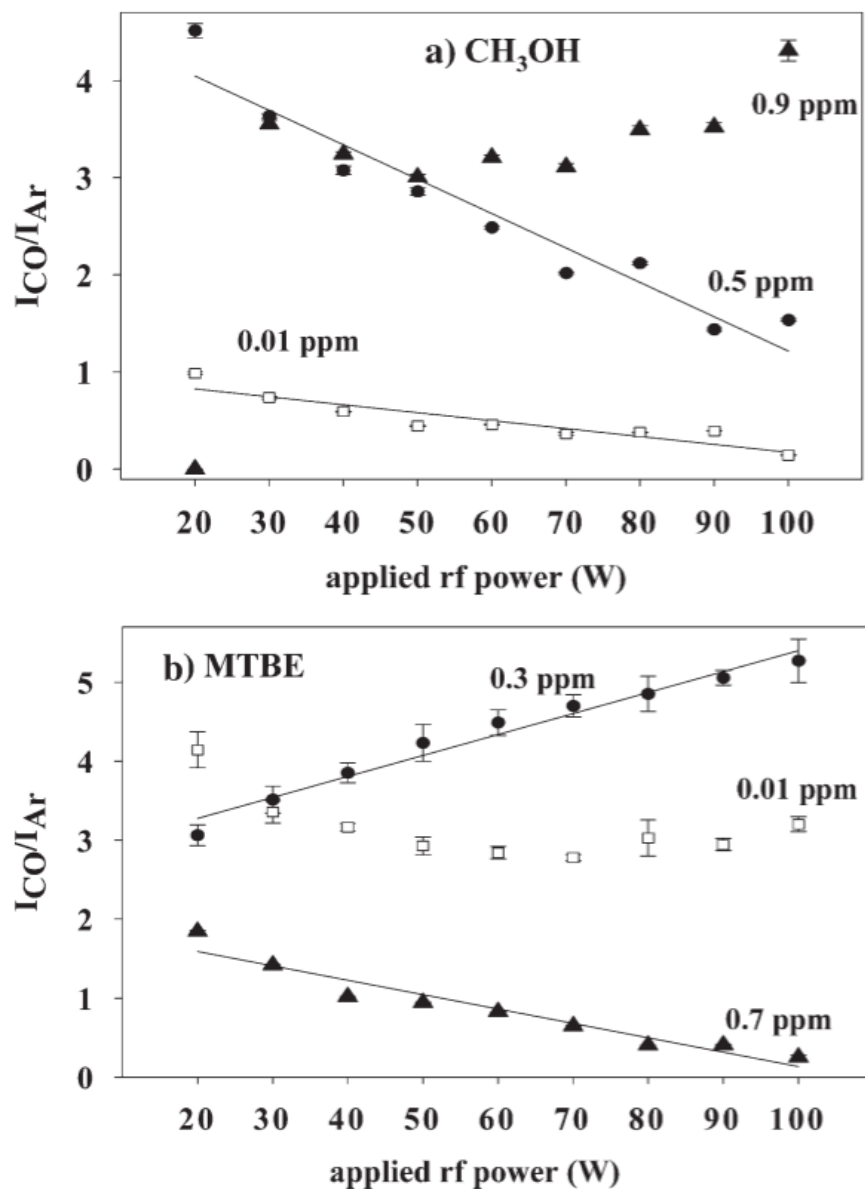


**Figure 3.3** Absolute intensity of CO in CH<sub>3</sub>OH and MTBE plasmas as a function of applied rf power: a) 0.9 (triangles), 0.5 (circles) and 0.01 ppm (open squares) CH<sub>3</sub>OH plasmas. Lines represent a linear regression fit to the data with  $r^2 = 0.93$  and  $0.84$  for the 0.5 and 0.01 ppm systems, respectively. b) shows 0.7 (triangles), 0.3 (circles) and 0.01 ppm (open squares) MTBE plasmas. Lines represent a linear regression fit to the data with  $r^2 = 0.93$  and  $0.92$  for the 0.5 and 0.01 ppm systems, respectively. Error bars represent one standard deviation of the mean of several ( $n = 4$ ) measurements at each  $P$ .

MTBE suggests the same dissociation mechanism and/or formation mechanisms may be occurring in both systems under these conditions. This is discussed further below. Note, however, that the intensity of the CO resulting from the 0.7 ppm MTBE solution is significantly lower than that for the other two, lower concentration, solutions at all  $P$ . This behavior is in direct contrast to the CH<sub>3</sub>OH data, Figure 3.3a, wherein the CO intensity decreased with decreasing concentration. In the MTBE system, this may result from either the lower solubility of MTBE in water (relative to CH<sub>3</sub>OH) or from the thermodynamically favored dissociation pathways for MTBE, Table 3.2. This is also discussed further below.

When the concentration of MTBE is 0.3 ppm, however, the intensity of CO increases with  $P$ , and does so linearly. This suggests that dissociation of the parent molecules is occurring to produce CO radicals, but further dissociation of the CO is not seen under the conditions employed here. At the lowest concentrations of MTBE (0.01 ppm), the CO intensity has very little dependence on  $P$ . As noted above for the CH<sub>3</sub>OH system, this may be the result of the extremely low concentration of organic material in the plasma such that either detection of the CO is limited or there is simply very little to no production of CO from MTBE. Studies on the oxidative dehydrogenation of CH<sub>3</sub>OH have demonstrated that CO is formed selectively in the absence of oxygen, but is not observed with high concentrations of O<sub>2</sub> present.<sup>35</sup> From our OES data we observed a linear increase in O\* with  $P$ , suggesting increased oxidation is possible at higher applied rf powers.

As noted in the Introduction, one of the goals of this research was to explore the possibility of using OES as a reliable detection method for accurately determining low

levels of organic contaminants in water samples. To that end, we have attempted to construct calibration curves for both CH<sub>3</sub>OH and MTBE using the actinometric ratios for CO for the concentration range of 0.1-1.0 ppm, at three different *P*, Figure 3.4. In both systems, the CO intensity decreases linearly as a function of concentration between 0.2 and 0.6 ppm for CH<sub>3</sub>OH and 0.1 and 0.7 ppm for MTBE at all *P*. Above ~0.7 ppm, however, the intensities are not dependent on precursor concentration. Note that this corresponds to the concentration (i.e. 0.7 ppm) at which the intensity of CO is extremely low at all *P*, Figure 3.3b. Although the negative correlation between  $I_{\text{CO}}$  and concentration is somewhat unusual for calibration curves involving optical spectroscopies, the behavior likely results from issues associated with the CO formation mechanisms in the CH<sub>3</sub>OH and MTBE plasmas.

To substantiate our OES data and to further explore the degree of dissociation occurring in the CH<sub>3</sub>OH and MTBE systems, we examined the plasmas using MS. MS analysis also provides additional precursor-specific information, whereas the OES data does not distinguish between organic precursors (i.e. CO arises from both precursors). Figure 3.5 shows mass spectra acquired with the ionizer off (positive ion mode) of 100% H<sub>2</sub>O, 100% CH<sub>3</sub>OH, and 100% MTBE plasmas (*P* = 80 W, 100 mTorr, no Ar added). As expected, for the 100% H<sub>2</sub>O plasma, the most intense peaks are located at  $m/z = 17, 18$  and 19, Figure 3.5a, attributable to OH<sup>+</sup>, H<sub>2</sub>O<sup>+</sup>, and H<sub>3</sub>O<sup>+</sup> ions formed in the plasma. For the 100% CH<sub>3</sub>OH plasma, two dominant sets of peaks are observed in the mass spectrum, Figure 3.5b, centered at  $m/z = 15$  and 28, respectively. These sets of peaks correspond to

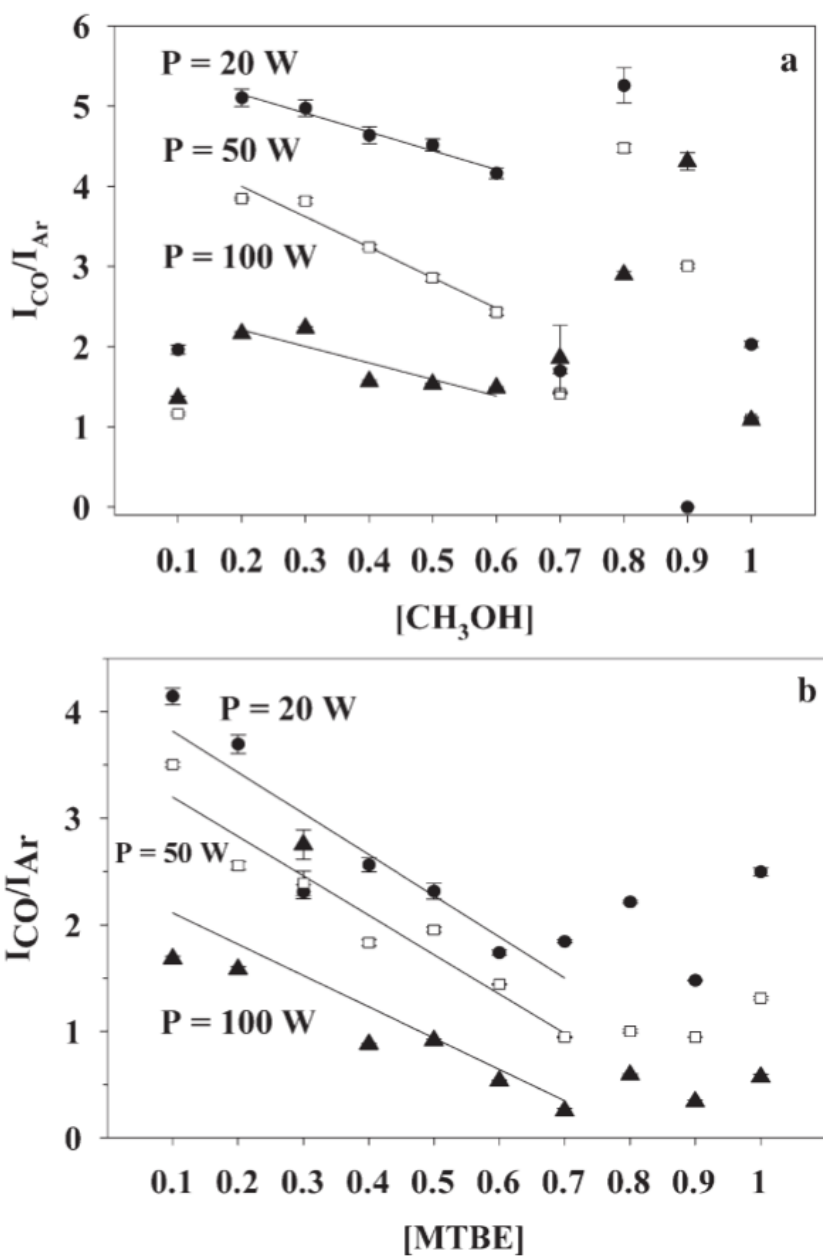


**Figure 3.4** Absolute intensity of CO as a function of organic contaminant concentration for a)  $CH_3OH$  and b) MTBE plasmas with  $P = 20, 50,$  and  $100$  W. The lines represent the linear regression fit to the data between 0.2 and 0.6 ppm with  $r^2 = 0.92, 0.95$  and  $0.77$  for the  $CH_3OH$  plasmas at 20, 50, and 100 W, respectively; linear regressions for the MTBE data between 0.1 and 0.7 ppm are 0.68, 0.93, and 0.31 for the 20, 50 and 100 W plasmas, respectively. Error bars represent one standard deviation of the mean of several ( $n = 4$ ) measurements.

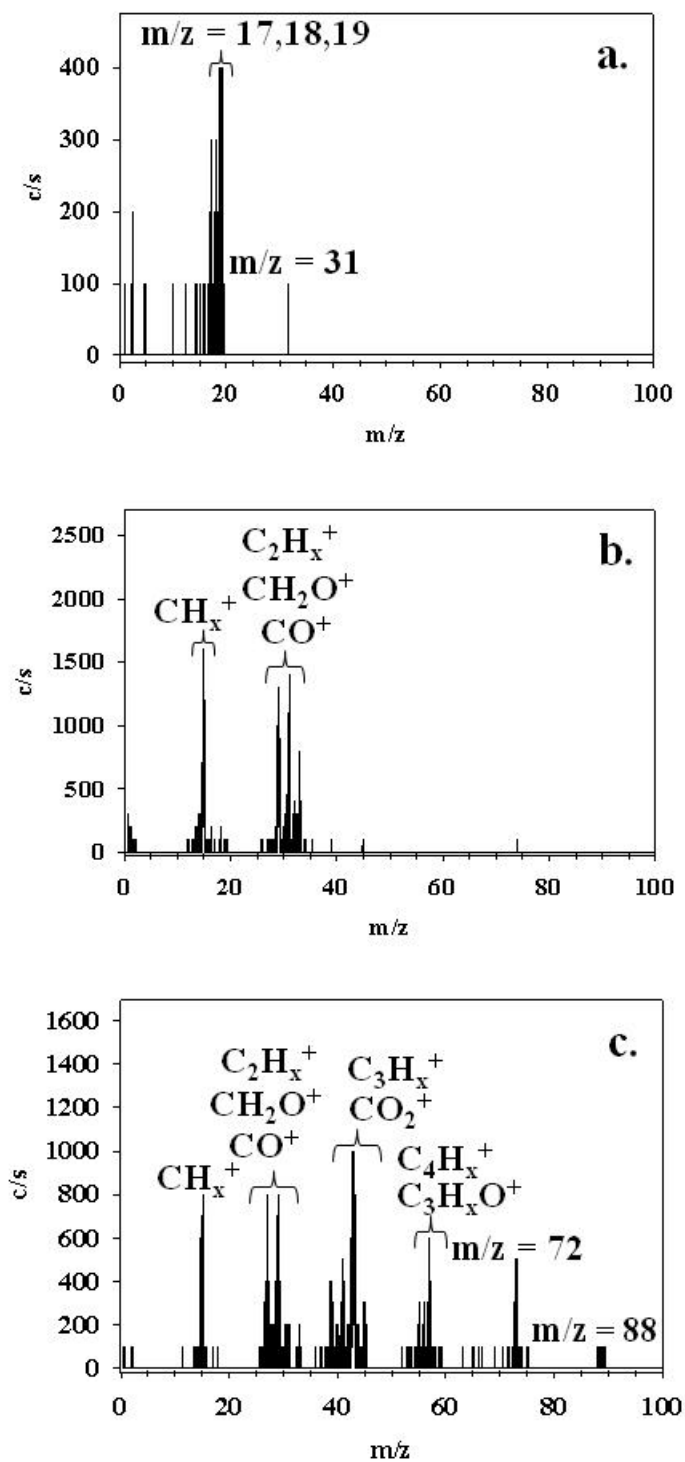


**Figure 3.5** Mass spectra acquired in positive ion SIMS mode of the mass spectrometer (ionizer off) for a) 100% H<sub>2</sub>O, b) 100% CH<sub>3</sub>OH, and c) 100% MTBE plasmas. Each spectrum was acquired at a total system pressure of 100 mTorr,  $P = 80$  W.

$\text{CH}_x^+$  and  $\text{C}_2\text{H}_x^+/\text{CH}_2\text{O}^+/\text{CO}^+$  ions, as expected from the dissociation of  $\text{CH}_3\text{OH}$  molecules. Some of the intensity in the  $m/z = 15-18$  amu range can be attributed to  $\text{OH}_x^+$  ( $x = 1-3$ ) ions. Although this system is somewhat more complicated than the water system, it is relatively easy to decipher.

In contrast, Figure 3.5c shows the spectrum for the 100% MTBE plasma, which contains an abundance of peaks from the dissociation of MTBE molecules in the plasma. The most intense peaks at  $m/z \sim 40-45$  correspond to  $\text{C}_3\text{H}_x^+/\text{CO}_2^+$  ions. A range of other peaks attributable to various hydrocarbon moieties are clearly identifiable in this spectrum up to  $m/z = 89$ , which could be protonated MTBE ( $\text{HMTBE}^+$ ) or tertbutyl formate [ $(\text{CH}_3)_3\text{OCHO}$ ], one of the principle MTBE oxidation products.<sup>9</sup> Johnson and coworkers also identified three other MTBE oxidation products, specifically carbon dioxide, formaldehyde, and acetone [ $\text{CO}_2$  ( $m/z = 44$ ),  $\text{CH}_2\text{O}$  ( $m/z = 30$ ), and  $\text{C}(\text{CH}_3)_2\text{O}$  ( $m/z = 58$ )], all of which are observed in our mass spectrum for the 100% MTBE system. This suggests that MTBE is being oxidized in the plasma. No higher mass ions are observed.

Figure 3.6 contains mass spectra taken in the two different modes of the mass spectrometer using the solutions with the lowest concentrations of organic molecules, 0.01 ppm. Figures 3.6a and b are positive ion mode spectra for the 0.01 ppm  $\text{CH}_3\text{OH}$  and MTBE plasmas, respectively. The corresponding RGA mode spectra are shown in Figures 3.6c and d. Figures 7a and b show similarities with major peaks at  $m/z = 17-19$ , and no peaks at  $m/z > 40$  for the  $\text{CH}_3\text{OH}$  system and  $m/z > 63$  in the MTBE system, which suggests complete dissociation of the parent molecules  $\text{CH}_3\text{OH}$ , MTBE, and  $\text{H}_2\text{O}$  has occurred and recombination reactions have not resulted in formation of larger ionic

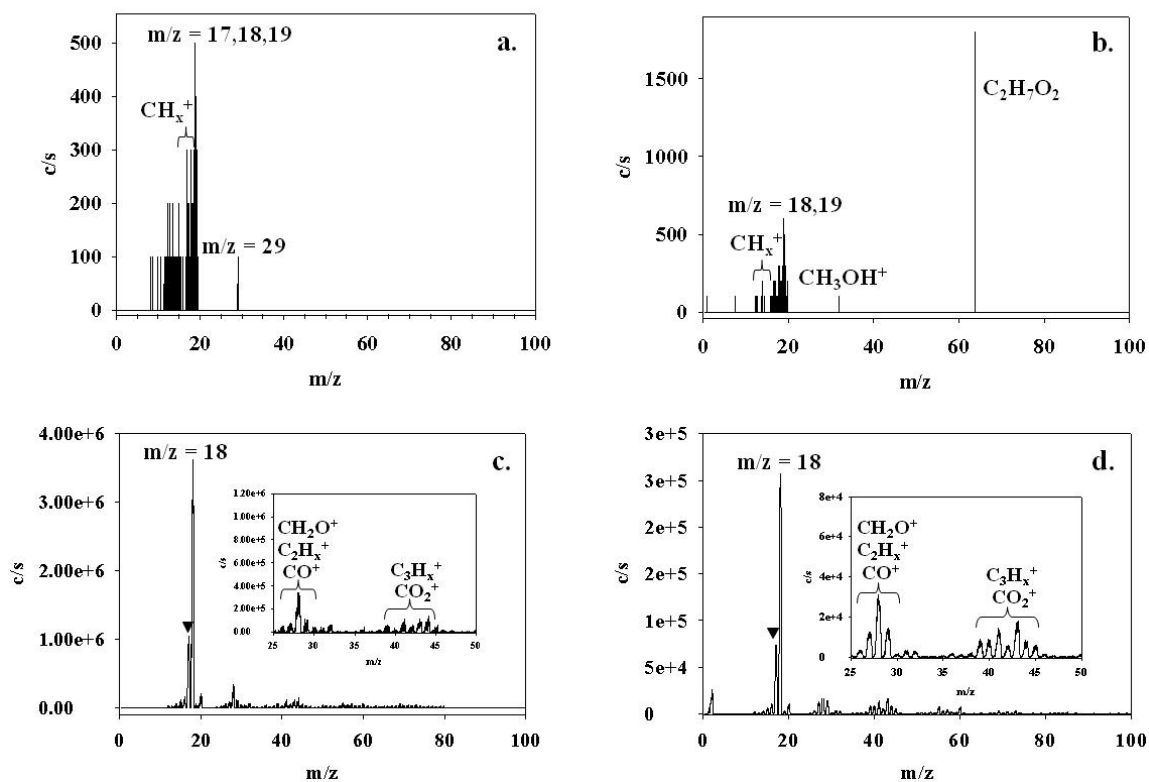


**Figure 3.6** Mass spectra of 0.01 ppm  $\text{CH}_3\text{OH}$  and MTBE plasmas acquired in two different modes of the mass spectrometer. Positive ion SIMS mode (ionizer off) spectra are shown in a)  $\text{CH}_3\text{OH}$  and b) MTBE plasmas and RGA mode (ionizer on) spectra are shown in c)  $\text{CH}_3\text{OH}$  and d) MTBE. Each spectrum was acquired at a total system pressure of 100 mTorr with  $P = 80$  W. The insets in c and d show enlarged views of the  $m/z = 25$ -50 region of the corresponding spectra.

species. When the ionizer is on, however, the resulting mass spectra show there are clearly species present at  $m/z > 40$ , Figures 3.6c and d (insets), demonstrating that although these higher mass fragments are formed, they are not ionized within the plasma.

### 3.3 Discussion

We have used an ICP equipped with an optical emission spectrometer to detect hydrocarbons and oxygenated species formed in plasmas produced from  $\text{CH}_3\text{OH}$  and MTBE solutions at concentrations  $\geq 0.01$  ppm. As noted in the Introduction, the initial goals of this work focused on determining if OES could be used to detect organic contaminants in water sources. The data presented here in Figures 2 and 3 clearly demonstrate that OES is capable of detecting a number of species attributable to the breakdown of organic molecules in artificially contaminated water samples. Through monitoring of the OES signal attributable to  $\text{CO}^*$ , we have obtained effective detection limits of 0.01 ppm for both  $\text{CH}_3\text{OH}$  and MTBE. Although OES can not distinguish between contaminants, it clearly can be used for the detection of organic species in aqueous solutions as no signals arising from CO (or CH) are observed in OES spectra of 100% water vapor plasmas, Figure 3.1a.

Another result from this work is that the ICP plasma is decomposing the organic contaminants in the water, even at very low concentrations. Both OES and MS data show clear evidence of hydrocarbon fragments that must come from the parent organic species in each system. (Although plasmas are not always well behaved with respect to thermodynamics, the most thermodynamically stable products will be formed under most circumstances). Thus, examination of various pathways for the decomposition of both  $\text{CH}_3\text{OH}$  and MTBE also yields insight into decomposition pathways in our ICP system.

Tables 3.1 and 3.2 contain thermodynamic data for various potential decomposition reactions for CH<sub>3</sub>OH and MTBE, respectively. As noted above, the decomposition pathways listed in the two tables are not intended to be a complete list of all possible reactions. Indeed we focused primarily on routes that accounted for the production of breakdown products we observe in the OES and MS data and that are thermodynamically accessible. Moreover, these reactions do not take into consideration the presence of plasma species that could be formed from decomposition of the solvent (H<sub>2</sub>O). For CH<sub>3</sub>OH, Table 3.1 data reveal that the most energetically favorable pathways lead to formation of either CO ( $\Delta H_r = 21.8 \pm 0.3$  kcal/mol) or formaldehyde ( $\Delta H_r = 22.2 \pm 0.3$  kcal/mol). As revealed in the OES data CO is one of the major excited state species we observe in this system and the most intense MS peaks in the 100% CH<sub>3</sub>OH plasma are observed at  $m/z = 28, 30,$  and  $44,$  Figure 3.6b, corresponding to CO, CH<sub>2</sub>O, and CO<sub>2</sub>, respectively. Thus, CH<sub>3</sub>OH decomposition in the ICP proceeds via well known dehydrogenation pathways.<sup>35</sup>

As noted in the Introduction, one advantage to using plasma-based processes for removal of oxygenates such as CH<sub>3</sub>OH and MTBE is that formation of OH radicals appears to be a key factor in removal of ethers from water waste streams. Again, our MS and OES data show clear evidence that OH is being formed in all systems, including those that do not initially contain water (i.e. 100% CH<sub>3</sub>OH and 100% MTBE); thus OH is a decomposition product of the organic species as suggested by the data in Tables 3.1 and 3.2. This indicates that ICPs may have increased efficiency for removal of organic contaminants. Gas-phase LIF studies of OH radicals in CH<sub>3</sub>OH plasmas are presented in Chapter 4, and help clarify energy partitioning in this system.

Johnson and coworkers demonstrated that DMPs effectively oxidize MTBE to less toxic compounds. Interestingly, they found the predominant product of the oxidation process was  $\text{CO}_2$ , with lower concentrations of acetone, tertbutyl formate and formaldehyde also being formed. With MTBE, we see evidence in the MS data for significant fragmentation in the 100% MTBE ICP, Figure 3.5c, to form a variety of species, including the oxidation products identified by Johnson et al. In comparison, the MS data for the lower concentration MTBE solution, Figures 3.6c and d, suggest fragmentation also produces some oxidation products. Indeed, it appears both additional fragmentation pathways have been accessed and more oxidation is occurring. Note that our MS data for solutions containing 0.01-100 ppm clearly demonstrate that 100% abatement of both  $\text{CH}_3\text{OH}$  and MTBE was achieved in our ICP as the MS data only contain signals associated with fragmentation and recombination species. No signals resulting from parent molecules are observed.

When the ionizer of the MS is on (RGA mode), we see formation of both CO ( $m/z = 28$ ) and  $\text{CO}_2$  ( $m/z = 44$ ) for all MTBE and  $\text{CH}_3\text{OH}$  solutions (0.01-100 ppm). This observation clearly indicates both decomposition and oxidation are occurring. Interestingly, similar to the  $\text{CH}_3\text{OH}$  system, formation of CO from MTBE is one of the most energetically favorable pathways to decomposition ( $\Delta H_r = 70.1 \pm 0.3$  kcal/mol). In contrast, formation of CH from MTBE requires significantly more energy ( $\Delta H_r = 177.7 \pm 0.1$  kcal/mol). This helps to explain why we do not observe significant OES signal from CH in most of the plasmas formed from dilute solutions. Additionally, even if CH does form in these plasmas, at higher applied rf powers the CH is much more likely than CO to dissociate as the CH bond energy is more than 2 eV lower than that for CO.

In addition to detecting organic contaminants in water streams, we were also interested in establishing calibration curve data to develop reliable predictions regarding contaminated waters. The data in Figures 3.3 and 3.4 demonstrate the CO\* OES signal does not exhibit a linear response to concentration or power, especially in the MTBE system. When examining the data in Figure 3.3b, we note that the 3 different concentrations exhibit very different behavior as a function  $P$ . At the lowest concentration (0.01 ppm), the CO signal is relatively weak at all  $P$ , indicating not much CO is formed, regardless of the rf power. The different behaviors observed at 0.3 and 0.7 ppm are likely the result of oxidation processes. Specifically, at the higher concentrations, it is likely that additional oxidation pathways as well as reactive collisions between MTBE fragments result in a decrease in the formation of CO at higher  $P$ . At the lower concentration (0.3 ppm), some of these CO loss pathways may disappear (or formation pathways may appear) simply because the number of MTBE fragments have decreased. In Figure 3.4, although we do observe a linear range in the data, at concentrations lower than  $\sim 0.1$  ppm and higher than  $\sim 0.7$  ppm, there is no clear trend in the observed CO OES signal. As noted above, CO is a thermodynamically stable and energetically favorable dissociation product and should be a reasonable indicator of parent molecule breakdown. Thus, the lack of reliable calibration curve data for both the CH<sub>3</sub>OH and MTBE systems is unexpected. As a final note, we have examined the MS data for both CH<sub>3</sub>OH and MTBE and find a similar lack of distinct trend in formation of CO<sup>+</sup> as a function of either  $P$  or concentration.

One potential explanation lies in the use of actinometry as the diagnostic tool. Although actinometry is a powerful technique, there are several requirements that must

be met to produce reliable density data. Specifically, the actinometer and the species of interest must both be excited primarily from the ground state; the excited species decay must occur via optical emission or optical emission accompanied by a parallel de-excitation pathway with a constant branching ratio; and the electron impact cross section for both species must have similar thresholds and shapes as a function of electron energy.<sup>27</sup> In our systems, the first two of these do not hold under all conditions as the formation of CO from the parent species can proceed via several different pathways, Tables 3.1 and 3.2. Moreover, CO can readily be formed via recombination reactions within the plasma itself. Because there are multiple formation mechanisms, there are also likely multiple excitation mechanisms to produce CO\*. CO\* formation could occur via a single step dissociation of the parent molecule, excitation of the parent molecule and subsequent dissociation (with or without recombination), or from product molecules (formed in gas-phase plasma reactions) that contain CO. If CO is first formed via a decomposition pathway and then undergoes an electron impact excitation, it is unclear how much internal excitation of the CO has already occurred during the formation process, prior to excitation. Although it is difficult to explicitly examine this factor, it is well established that excitation processes that lead to formation of emitting species can be inferred from examination of OES spectral line shapes.<sup>27,36</sup> In our spectra, the Ar\* line at 750.4 nm is relatively narrow ( $\Delta\lambda \sim 0.4$  nm), whereas that for the CO\* at 283.7 nm is significantly wider ( $\Delta\lambda \sim 1.5$  nm). The Ar line width is clearly determined by the resolution of the instrument. Likewise, the CO line width is determined by both the spectrometer resolution and by the rotational levels populated in the excitation process. Thus, the discrepancies in line width do not allow us to make a clear distinction on

formation mechanisms as has been performed in other studies. Nonetheless, both the multiple formation mechanisms as well as indirect excitation of CO violate the primary conditions for accurate actinometric measurements. Overall, however, our data clearly demonstrate that ICPs can decompose organic contaminants in water samples and that OES detection of carbon containing fragments is a clear indicator of the presence of contaminants in pure or ultrapure water sources. If OES were to be used with non-purified environmentally-obtained water sources, the presence of dissolved CO<sub>2</sub> would clearly hamper the use of this method for detection of other organic sources of carbon.

### **3.4 Summary**

An ICP system equipped with an optical emission spectrometer has been used for detection and abatement of organic contaminants. Using the model compounds CH<sub>3</sub>OH and MTBE, we have demonstrated that OES can be used to detect contaminants in water with an effective detection limit of 0.01 ppm. Complimentary MS data provided insight into the decomposition pathways, which suggest CH<sub>3</sub>OH abatement is achieved primarily via an oxidative dehydrogenation mechanism, whereas MTBE abatement occurs via both decomposition and oxidation mechanisms. Although accurate calibration data were not obtained for either the CH<sub>3</sub>OH or MTBE systems, we continue to explore the gas-phase as well as gas-surface interface reactions in both systems to further elucidate abatement mechanisms and detection methods for organic species in water sources.

### 3.5 References

- <sup>1</sup>M. Rosell, S. Lacorte, and D. Barcelo, *Trends Anal. Chem.* **25** (2006).
- <sup>2</sup>P. R. D. Williams, C. A. Cushing, and P. J. Sheehan, *Risk Anal.* **23**, 1085 (2003).
- <sup>3</sup>C. Baus, H.-W. Hung, F. Sacher, M. Fleig, and H.-J. Brauch, *Acta Hydrochim. Hydrobiol.* **33**, 118 (2005).
- <sup>4</sup>D. A. Cassada, Y. Zhang, D. D. Snow, and R. F. Spalding, *Anal. Chem.* **72**, 4654 (2000).
- <sup>5</sup>B. P. J. de Lacy Costello, P. S. Sivanand, N. M. Ratcliffe, and D. M. Reynolds, *Water Sci. Technol.* **52**, 117 (2005).
- <sup>6</sup>R. Johnson, J. F. Pankow, D. Bender, C. Price, and J. S. Zogorski, *Environ. Sci. Technol.* **34**, 210A (2000).
- <sup>7</sup>C. Baus, M. Sona, and H.-J. Brauch, *Water Sci. Technol: Water Supply* **7**, 127 (2007).
- <sup>8</sup>J. S. Arey and P. M. Gschwend, *J. Contam. Hydrol.* **76**, 109 (2005).
- <sup>9</sup>D. C. Johnson, V. A. Shamamian, J. H. Callahan, F. S. Denes, S. O. Manolache, and D. S. Dandy, *Environ. Sci. Technol.* **37**, 4804 (2003).
- <sup>10</sup>J. Hutcheson, *Filtr. Sep.* **43**, 22 (2006).
- <sup>11</sup>F. De Smedt, S. De Gendt, M. Claes, M. M. Heyns, H. Vankerckhoven, and C. Vinckier, *Ozone Sci. Eng.* **24**, 379 (2002).
- <sup>12</sup>S. O. Manolache, V. A. Shamamian, and F. S. Denes, *J. Environ. Eng.*, 17 (2004).
- <sup>13</sup>D. M. Angeloni, S. E. Dickson, M. B. Emelko, and J.-S. Chang, *Jpn. J. Appl. Phys.* **45**, 8290 (2006).
- <sup>14</sup>J.-S. Chang, *Sci. Technol. Adv. Mater.* **2**, 571 (2001).
- <sup>15</sup>G. J. Pietsch and A. B. Saveliev, *Plasma Process. Polym.* **4**, 737 (2007).
- <sup>16</sup>H. L. Chen, H.-M. Lee, L. C. Cheng, M. B. Chang, S. J. Yu, and S.-N. Li, *IEEE Trans. Plasma Sci.* **36**, 509 (2008).
- <sup>17</sup>D. C. Johnson, D. S. Dandy, and V. A. Shamamian, *Water Res.* **40**, 311 (2006).
- <sup>18</sup>V. Vartanian, L. Beu, T. Lii, D. Graves, E. J. Tonnis, R. Jewett, B. Wofford, J. Bevan, C. Hartz, and M. Gunn, *Semicon. Internat.*, 191 (2000).
- <sup>19</sup>E. J. Tonnis, D. B. Graves, V. H. Vartanian, L. Beu, T. Lii, and R. Jewett, *J. Vac. Sci. Technol. A* **18**, 393 (2000).
- <sup>20</sup>M. W. Kiehlbach and D. B. Graves, *J. Appl. Phys.* **89**, 2047 (2001).
- <sup>21</sup>X. P. Xu, S. Rauf, and M. J. Kushner, *J. Vac. Sci. Technol. A* **18**, 213 (2000).
- <sup>22</sup>M. L. Steen, C. I. Butoi, and E. R. Fisher, *Langmuir* **17**, 8156 (2001).
- <sup>23</sup>M. L. Steen, L. Hymas, E. D. Havey, N. E. Capps, D. G. Castner, and E. R. Fisher, *J. Membr. Sci.* **188**, 97 (2001).
- <sup>24</sup>M. L. Steen, A. C. Jordan, and E. R. Fisher, *J. Membr. Sci.* **204**, 341 (2002).
- <sup>25</sup>K. H. A. Bogart, N. F. Dalleska, G. R. Bogart, and E. R. Fisher, *J. Vac. Sci. Technol. A* **13**, 476 (1995).
- <sup>26</sup>J. W. Coburn and M. Chen, *J. Appl. Phys.* **51**, 3134 (1980).
- <sup>27</sup>R. W. Dreyfus, J. M. Jasinski, R. E. Walkup, and G. S. Selwyn, *Pure Appl. Chem.* **57**, 1265 (1985).
- <sup>28</sup>N. C. M. Fuller, M. V. Malyshev, V. M. Donnelly, and I. P. Herman, *Plasma Sources Sci. Technol.* **9**, 116 (2000).
- <sup>29</sup>R. Walkup, K. Saenger, and G. S. Selwyn, *Mater. Res. Soc. Symp. Proc.* **38**, 69 (1985).
- <sup>30</sup>M. V. Malyshev and V. M. Donnelly, *J. Appl. Phys.* **88**, 6207 (2000).

- <sup>31</sup>C. B. Labelle and K. K. Gleason, *J. Appl. Polym. Sci.* **80**, 2084 (2001).
- <sup>32</sup>Q. S. Yu, E. Krentsel, and H. K. Yasuda, *J. Polym. Sci.: Part A: Polym. Chem.* **36**, 1583 (1998).
- <sup>33</sup>J. Zhou, I. T. Martin, R. Ayers, E. Adams, D. Liu, and E. R. Fisher, *Plasma Sources Sci. Technol.* **15**, 714 (2006).
- <sup>34</sup>Y. Yamagata, A. Sharma, J. Narayan, R. M. Mayo, J. W. Newman, and K. Ebihara, *J. Appl. Phys.* **88**, 6861 (2000).
- <sup>35</sup>T. Ohtake, T. Mori, and Y. Morikawa, *J. Nat. Gas Chem.* **16**, 1 (2007).
- <sup>36</sup>R. A. Gottscho and V. M. Donnelly, *J. Appl. Phys.* **56**, 245 (1984).
- <sup>37</sup>S. G. Lias, J. E. Bartmess, J. F. Liebman, J. L. Holmes, R. D. Levin, W. G. Mallard, *J. Phys. Chem. Ref. Data* **17**,1 (1988).

## **CHAPTER 4**

### **ENERGY PARTITIONING IN DIATOMIC RADICALS II: CH, OH, NH, AND SiH IN INDUCTIVELY COUPLED PLASMAS**

This chapter contains energy partitioning data along with surface scatter coefficient measurements for radical species from a variety of plasma systems. Data were collected with laser induced fluorescence (LIF), optical emission spectroscopy (OES), and our imaging of radicals interacting with surfaces technique (IRIS). Relationships between scatter coefficients and internal and translational temperatures were observed for all radical species. These correlations provide insight into the partitioning of energy in the gas phase of the plasma as well as the influence of internal and kinetic energy on radical-surface interactions.

## 4.1 Introduction

Plasma chemistry is very complex, one reason being the large collection of energy available and the ease with which energy is transferred from one species to another. This results in a large selection of formation mechanisms for species in plasma systems. The main group hydride species explored here are formed primarily by either unimolecular decomposition reactions or through bimolecular gas-phase collisions. Their production through these formation mechanisms allows for their rotational ( $\theta_R$ ), translational ( $\theta_T$ ), and vibrational ( $\theta_V$ ) temperatures to be measured. Rotational temperatures represent rotational  $J$  states within a single vibrational state and vibrational temperatures provide a measure of the distribution of vibrational states of a radical species. Translational temperatures represent the measurement of the kinetic motion of radical species along a specific axis of travel.

The measured temperatures of the plasma systems in the Fisher group follow the normal relationship where  $\theta_V$  are generally greater than  $\theta_T$  and  $\theta_R$ , but are less than the electron temperature ( $T_e$ ) of the plasma.<sup>1,2</sup> We have found here and in previous studies that  $\theta_T$  and  $\theta_R$  values are similar in some cases, for example OH in tetra-ethoxy-silane (TEOS) /O<sub>2</sub> plasmas,<sup>3</sup> and significantly different in others, for example SiH in SiH<sub>4</sub> plasmas.<sup>4</sup> This suggests that formation mechanisms are a leading source of these differences. Because of the many different combinations of relationships possible between  $\theta_V$ ,  $\theta_T$ , and  $\theta_R$ , knowing how molecules interact with surfaces and relating that to the molecule's characteristic temperatures can lead to further understanding of plasma discharges.

Our unique imaging of radicals interacting with surfaces (IRIS) technique allows for the measurement of a molecule's probability to react at a surface. Previous results in our lab found that the surface scattering coefficient,  $S$ , is dependent on the  $\theta_V$  values for NO, SiF, and CF.<sup>5</sup> Here we have attempted to correlate the reported internal temperatures with a molecule's measured  $S$  value by comparing the four measurements.  $\theta_R$  and  $\theta_T$  values are measured by laser-induced fluorescence (LIF),  $\theta_V$  values by optical emission spectroscopy (OES), and surface scatter coefficients by our IRIS technique. We have investigated four different hydride species formed in multiple plasma systems; specifically CH in CH<sub>4</sub> and CH<sub>4</sub>/Ar plasmas, SiH in SiH<sub>4</sub>, SiH<sub>4</sub>/Ar, Si<sub>2</sub>H<sub>6</sub>, and Si<sub>2</sub>H<sub>6</sub>/Ar plasmas, OH in H<sub>2</sub>O, CH<sub>3</sub>OH, TEOS/O<sub>2</sub>, and NH<sub>3</sub>/O<sub>2</sub> plasmas, and NH in NH<sub>3</sub> and NH<sub>3</sub>/O<sub>2</sub> plasmas. We have also examined different radicals produced in the same plasma systems; specifically OH and NH in NH<sub>3</sub>/O<sub>2</sub> plasmas. These radicals are all covalent hydrides and, as demonstrated here, they exhibit similarities in their internal energies as well as their surface interactions being correlated with their electronic character and formation mechanisms rather than on their internal and translational temperatures. Although these molecules have been studied for a number of years in the Fisher group under an array of plasma conditions,<sup>3,4,6-13</sup> we have yet to collect these studies for direct comparison. Furthermore, the major component that this work adds is the measurement of  $\theta_V$  and  $\theta_T$  values for all four molecules. Thus, two major objectives presented in this chapter are the exploration of (1) the differences and or similarities in radicals from one system to the next and (2) the correlation between internal energy and behavior at surfaces.

## 4.2 Results

**Temperature Determinations.** New data are presented here for  $\theta_V$  for CH, SiH, OH, and NH, along with  $\theta_R$  and  $\theta_T$  for OH. These temperatures are compared to data previously published for  $\theta_R$ ,  $\theta_T$ , and surface scattering coefficients of CH, SiH, and NH. Both OES and LIF spectroscopies were employed to collect these data. The wavelengths and transitions probed for the radicals studied here (both OES and LIF) are listed in Table 4.1.

Representative OES spectra collected from plasmas containing the molecules of interest and used for calculations of  $\theta_V$  are shown in Figure 4.1, illustrating the A—X transition for CH, SiH, OH, and NH. Such OES spectra are fit with optimized simulated lines using the LIFBASE program to estimate  $\theta_V$ .<sup>4</sup> An example is shown in Figure 4.2 for CH produced from a 100% CH<sub>4</sub> plasma fit with a simulated spectrum corresponding to a vibrational temperature of 2700 K.  $\theta_R$  values are likewise determined using LIBASE where simulations are compared to LIF excitation spectra for each molecule.  $\theta_T$  temperatures are calculated from the velocity,  $v$ , of radicals measured by collecting LIF images for a series of ICCD gate delay times, according to equation (4.1), where

$$\Theta_T = \frac{\pi m v^2}{8 k_B} \quad (4.1)$$

$m$  is the mass of the molecule, and  $k_B$  is Boltzmann's constant. Fig. 4.3 contains images of LIF signal produced from OH radicals formed in a 100% H<sub>2</sub>O plasma as the camera gate delay is iteratively increased in 500 ms intervals, thereby depicting the movement of the molecules in time. Molecular velocity is determined by plotting the distance traveled

**Table 4.1** Spectroscopic transitions used in calculations of  $\Theta_V$  from OES spectra, and of  $\Theta_R$  and  $\Theta_T$  from LIF spectra.

Molecule	OES transition, $\lambda$ range	LIF transition, $\lambda$ range	IRIS excitation $\lambda$ (nm)	IRIS background $\lambda$ (nm)
OH	$A^2\Sigma^+ \rightarrow X^2\Pi$ , 307.0-310.0 nm	$A^2\Sigma^+ \leftarrow X^2\Pi$ , 306.5-307.5 nm	307.848	307.836
CH	$A^2\Delta \rightarrow X^2\Pi$ , 425.0-433.0 nm	$A^2\Delta \leftarrow X^2\Pi$ , 429.6-430.5 nm	430.402	430.200
SiH	$A^2\Delta \rightarrow X^2\Pi$ , 413.0-415.0 nm	$A^2\Delta \leftarrow X^2\Pi$ , 413.40-413.45 nm	413.418	413.440
NH	$A^3\Pi \rightarrow X^3\Sigma^-$ , 334.0-338.0 nm	$A^3\Pi \leftarrow X^3\Sigma^-$ , 335.25-335.6 nm	336.072	336.050

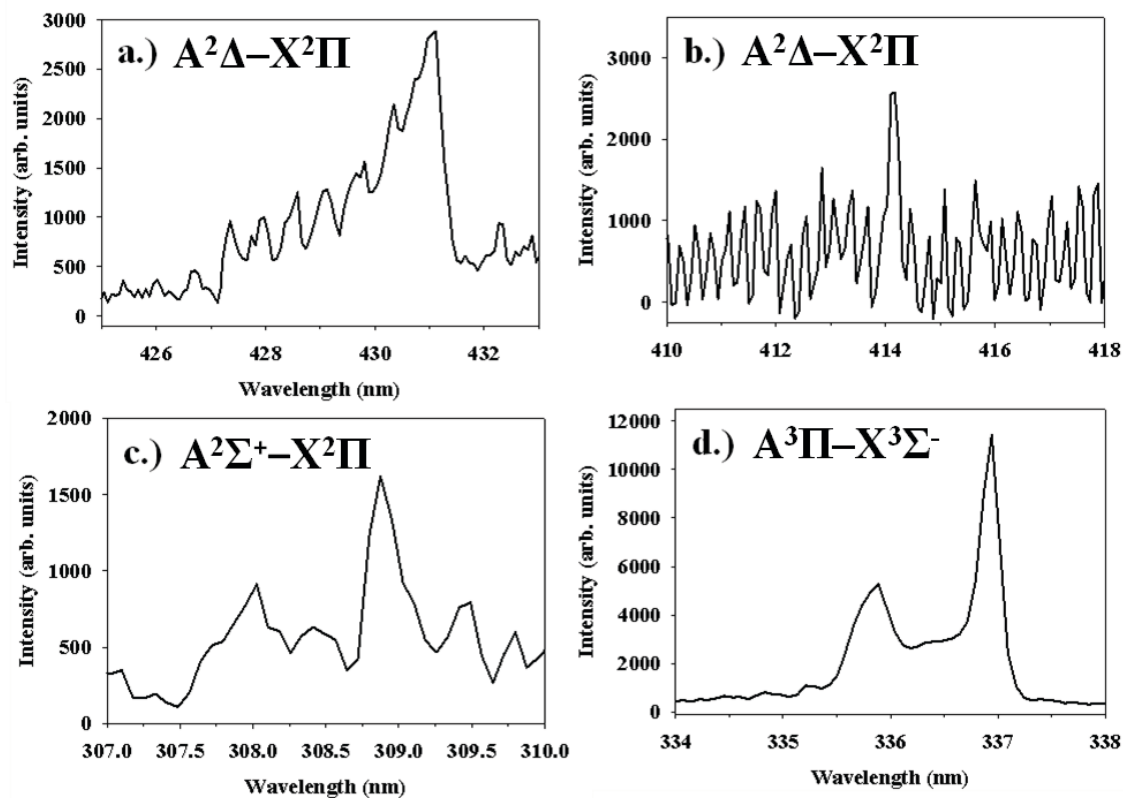


**Figure 4.1** Raw OES spectra of (a) CH in a 100% CH<sub>4</sub> plasma, (b) SiH in a 90:10 SiH/Ar plasma, (c) OH in a 100% H<sub>2</sub>O vapor plasma, and (d) NH in a 100% NH<sub>3</sub> plasma. Spectra were collected at 110, 50, 100, and 50 mTorr, respectively and P = 100 W with the exception of SiH at 80 W.

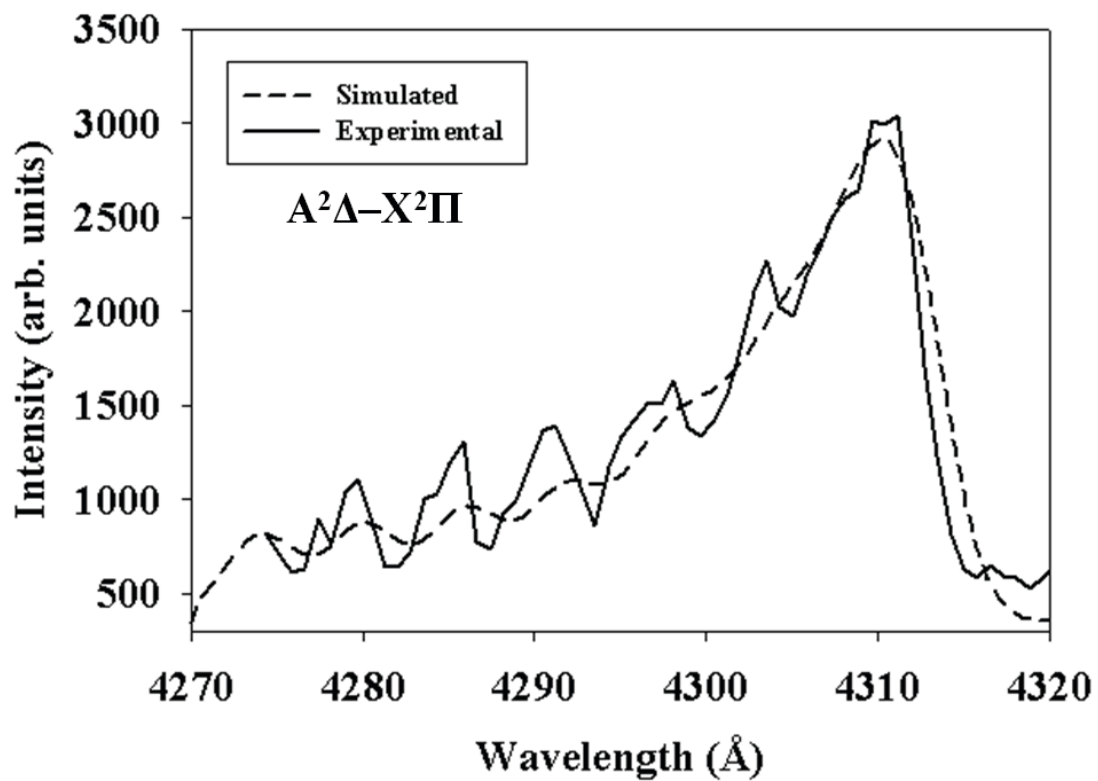


**Figure 4.2** Raw OES spectrum (solid black line) for CH from a 100% CH<sub>4</sub> plasma at 110 mTorr and  $P = 100$  W and a simulated LIFBASE spectrum (dashed line) with  $\Theta_v = 2700$  K.

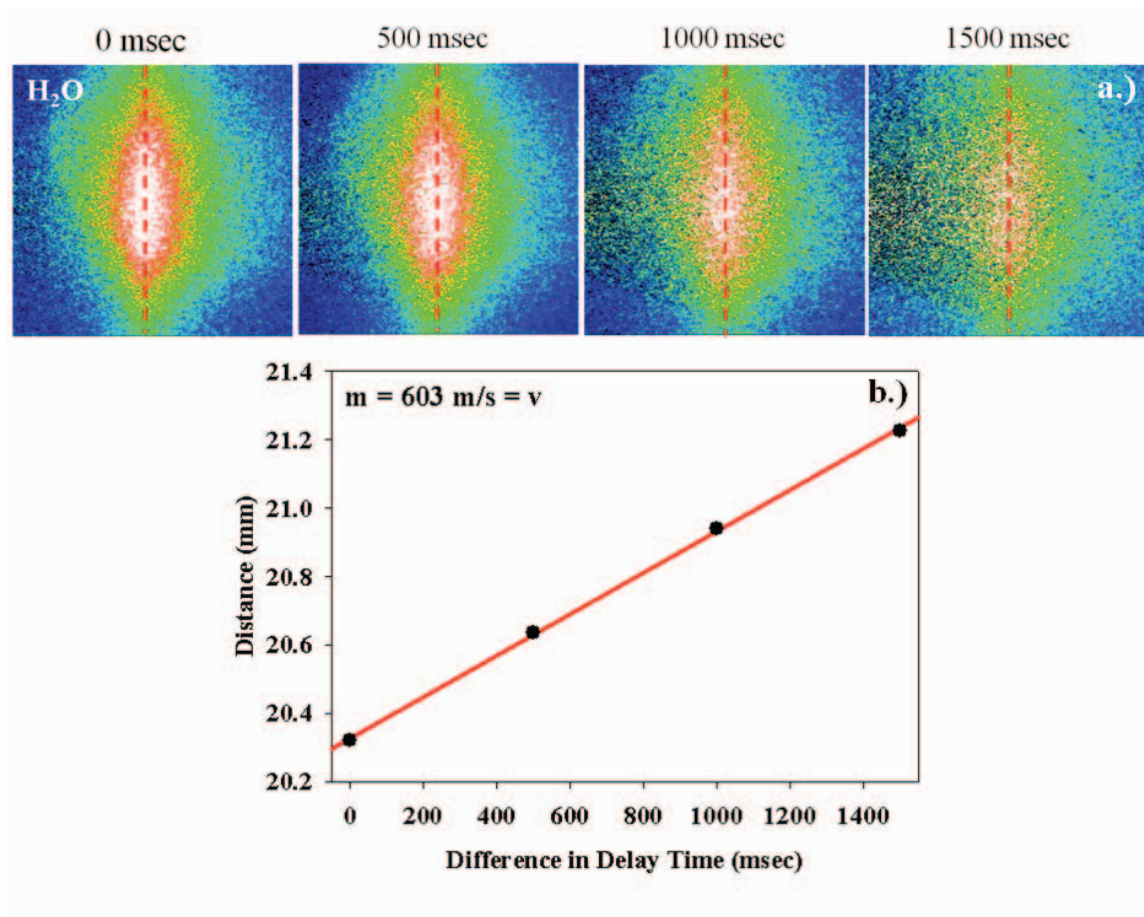


**Figure 4.3** LIF images of OH radicals seen in a (a) 100% H<sub>2</sub>O vapor plasma at 150 mTorr, 80 W. Images are taken at 500 ms intervals to determine  $\theta_T(\text{OH})$ . Graph (b) shows the corresponding distance changes in the LIF images in (a) as a function of delay time.

as a function of the gate delay time; the slope of the linear regression fit to the data provides the molecule's velocity, Fig. 4.3b.

**CH.** Internal and translational temperatures for CH formed in a CH<sub>4</sub>/Ar mixture are plotted in Figure 4.4a as a function of the percentage of Ar in the plasma feed. With increasing %Ar,  $\theta_V$  increases slightly from 2300 K at 0% Ar to 2800 K at 20% Ar.  $\theta_T$  values are the same within experimental error, and  $\theta_R$  remain constant for all %Ar. The clear trend between the three temperatures is that  $\theta_V > \theta_T > \theta_R$ . Surface scatter coefficient data suggest the reactivity of CH is independent of Ar concentration.  $S(\text{CH})$  values are ~0.05 under all conditions, indicating that the molecule is highly reactive at surfaces. Figure 4.4b shows complementary data for CH in a 100% CH<sub>4</sub> plasma as a function of applied rf power ( $P$ ).  $\theta_V$  are constant with respect to increasing  $P$ , whereas  $\theta_T$  are high (~2500 K) for  $P < 100$  W and plateau at  $P \geq 100$  W.  $\theta_R$  is constant at ~1800 K. We also see that the  $\theta_V$  and  $\theta_T$  are essentially the same at  $P = 100$  W. In further comparing the temperatures and  $S(\text{CH})$  in Figures 4.4a and 4.4b the all temperatures and scatter values are similar with respect to their collection parameters on the x-axis. This suggests that regardless of the plasma parameters these values will remain constant.

**SiH.** The  $\theta_V$ ,  $\theta_T$ , and  $\theta_R$  values for SiH formed in two different plasma systems, SiH<sub>4</sub>/Ar and Si<sub>2</sub>H<sub>6</sub>/Ar, are shown in Figure 4.5 as a function of %Ar in the feed gas. Data for SiH molecules in the silane systems show a decrease in  $\theta_V$ , constant  $\theta_T$  values within experimental error, and constant  $\theta_R$  values with increasing %Ar, Figure 4.5a. Both  $\theta_V$  and  $\theta_T$  are significantly greater than the previously reported  $\theta_R$  values.<sup>4</sup> SiH species in disilane systems, Figure 4.5b, show constant  $\theta_V$  and  $\theta_R$  temperatures regardless of the amount of Ar added to the system.  $\theta_T$  decreases as the % Ar is increased, and similar to

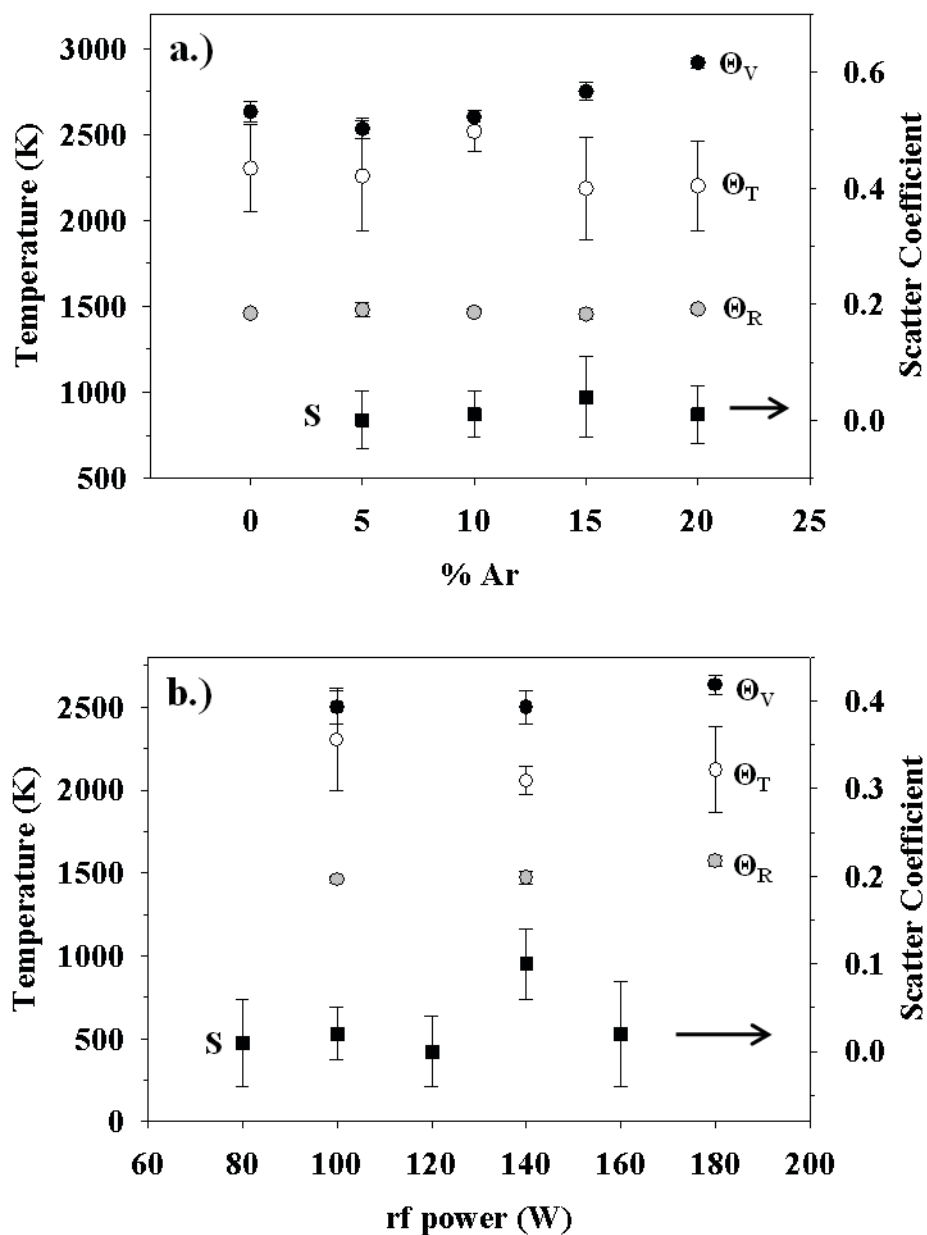


**Figure 4.4**  $\theta_V$  (solid black circles),  $\theta_T$  (open circles),  $\theta_R$  (solid grey circles) and scatter coefficients (solid black squares) for CH radicals from (a) CH<sub>4</sub>/Ar plasmas at 50 mTorr  $P = 180$  W and (b) a 100% CH<sub>4</sub> plasma at 50 mTorr and a range of applied rf powers. Scatter coefficient values correspond to the right-hand side y-axis and temperatures are to the left.

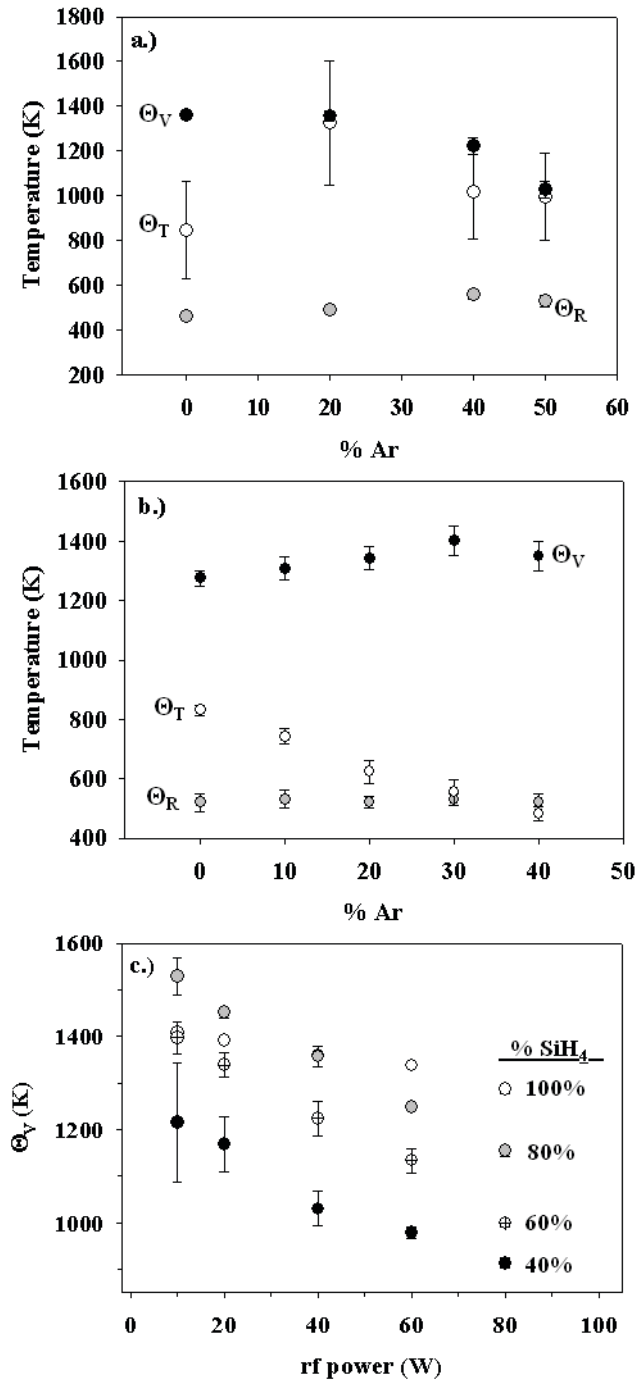


**Figure 4.5**  $\theta_V$  (black),  $\theta_T$  (white), and  $\theta_R$  (grey) for SiH from (a) a SiH<sub>4</sub>/Ar plasma and (b) a Si<sub>2</sub>H<sub>6</sub>/Ar plasma at 60 W and a total system pressure of 50 mTorr.  $\theta_V$  data for SiH<sub>4</sub>/Ar plasma systems are shown in (c) as a function of applied rf powers, with a total system pressure of 50.

CH in the CH<sub>4</sub>/Ar systems, it follows the relationship whereby  $\theta_V > \theta_T > \theta_R$ . In both the SiH<sub>4</sub>/Ar and Si<sub>2</sub>H<sub>6</sub>/Ar systems,  $\theta_T$  are identical at 0% Ar, but increases in %Ar affect  $\theta_T$  in contradictory ways in the two systems.  $\theta_T$  values tend to increase with increased Ar concentration in the silane system, but decrease in the disilane system.  $\theta_V$  values are generally higher in the disilane plasma, but this difference becomes insignificant as %SiH<sub>4</sub> or %Si<sub>2</sub>H<sub>6</sub> increases. Comparison of  $\theta_V$  in dilutions of the SiH<sub>4</sub> plasma system, Figure 4.5c, shows  $\theta_V$  decreases as a function of increasing  $P$  and with decreasing %Ar. Surface scattering coefficients for SiH (not shown) are independent of plasma parameters (substrate temperature, feed gas composition, pressure, and applied rf power), with  $S \sim 0.05$  in all cases.<sup>4</sup>

**OH.** Internal and translational temperatures for OH radicals in a 100% H<sub>2</sub>O vapor plasma are shown in Figure 4.6.  $\theta_V$  values start ~2800 K at  $P = 30$  W and decrease with increasing  $P$ . In contrast,  $\theta_T$  and  $\theta_R$  have similar values that are considerably lower than  $\theta_V$  (~400 K) and are independent of  $P$ . Internal temperatures and  $\theta_T$  values for OH were also determined for mixed precursor systems, including 50:50 and 20:80 NH<sub>3</sub>/O<sub>2</sub> plasmas. Fig. 4.7 illustrates these values as a function of  $P$ , clearly demonstrating that  $\theta_V(\text{OH})$  for mixed precursor systems are at least 1.5 times less than  $\theta_V(\text{OH})$  for 100% H<sub>2</sub>O vapor plasmas, Fig. 4.6. Notably,  $\theta_V$  is slightly higher at all  $P$  for OH formed in the 50:50 NH<sub>3</sub>/O<sub>2</sub> plasma than in the 20:80 mixture. Comparatively, translational temperatures for OH in the 20:80 NH<sub>3</sub>/O<sub>2</sub> plasma only exceed those in the 50:50 mixture at  $P > 150$  W. Otherwise,  $\theta_T$  values are essentially identical for OH in both NH<sub>3</sub>/O<sub>2</sub> systems.  $\theta_R$  values appear to be largely independent of changing  $P$  and are similar (~400

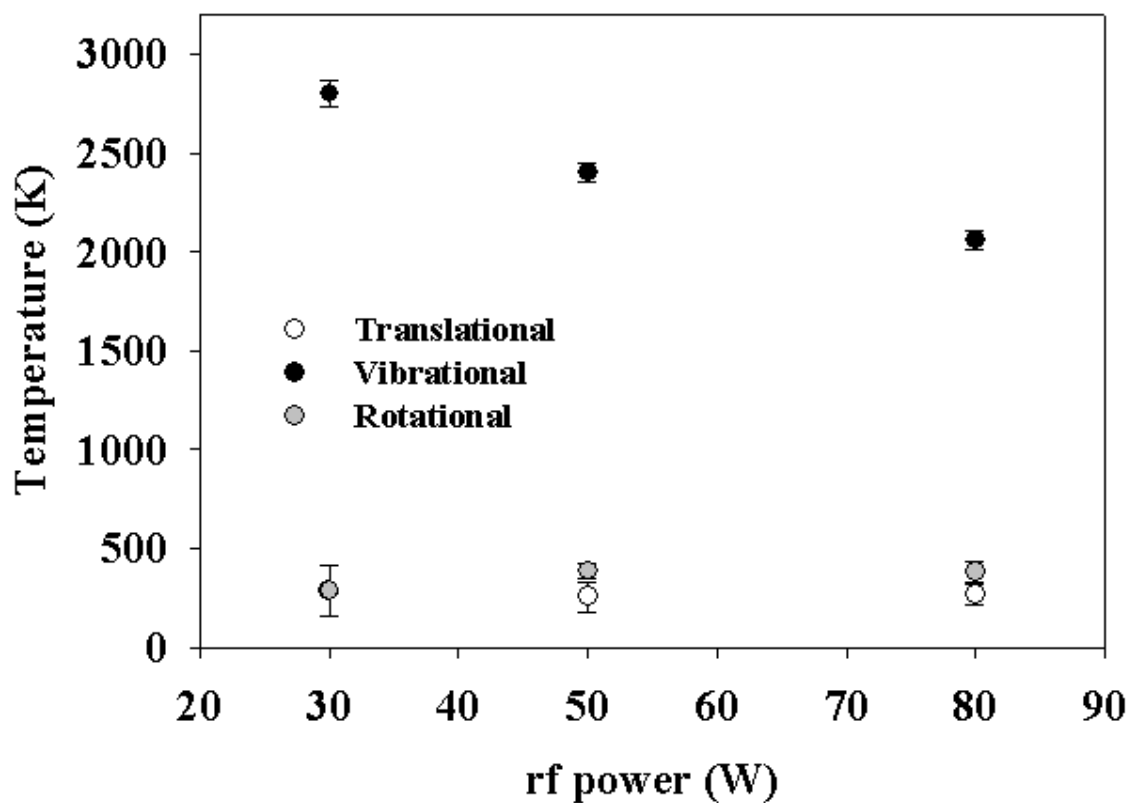


**Figure 4.6**  $\theta_V$  (black),  $\theta_T$  (white), and  $\theta_R$  (grey) for OH formed in a 100% H<sub>2</sub>O vapor plasma at  $P = 50$  W with a total system pressure of 50 mTorr.

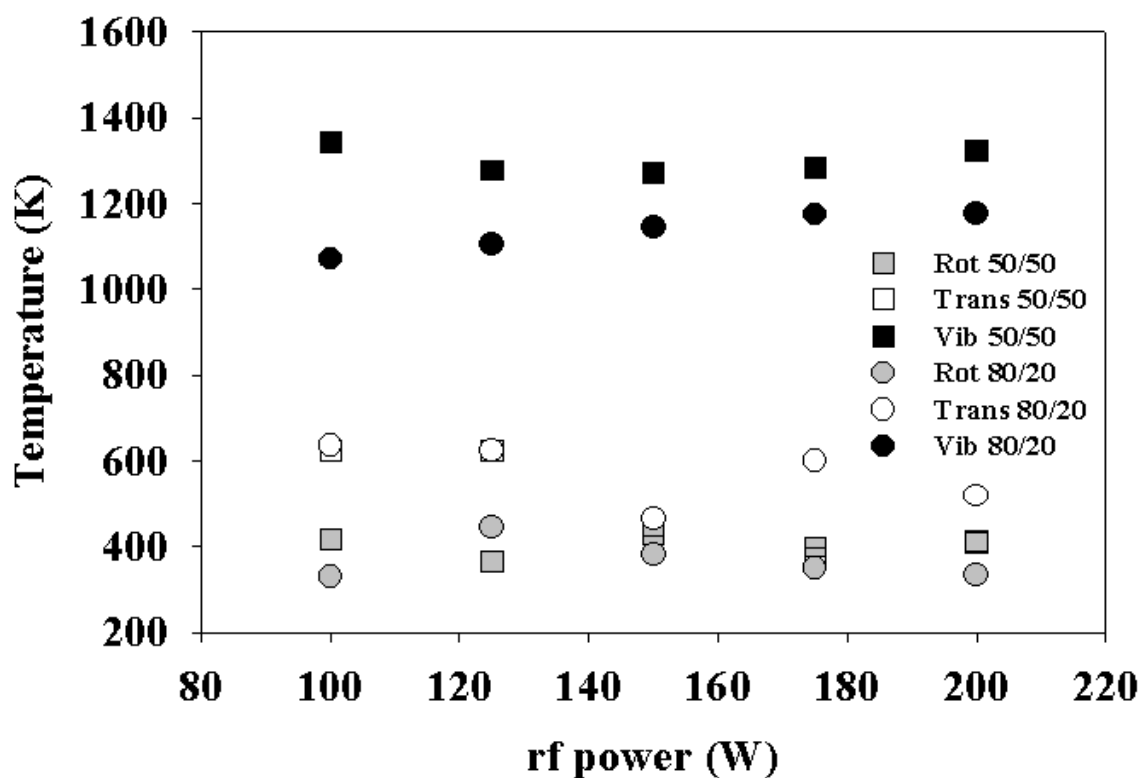


**Figure 4.7**  $\theta_V$  (black square/circle),  $\theta_T$  (white square/circle), and  $\theta_R$  (grey square/circle) for OH formed in 50:50 and 20:80  $\text{NH}_3/\text{O}_2$  plasmas. Squares represent the 50:50 mixture and circles represent the 20:80 mixture.

K) for OH in both mixtures. Note that these are also identical to those measured in the H<sub>2</sub>O plasmas.

**NH.**  $\theta_v$ ,  $\theta_T$ , and  $S$  values for NH formed in 100% NH<sub>3</sub> plasmas are plotted in Figure 4.8 as a function of  $P$ .  $\theta_v$  values increase from 4000 to 10,000 K over the  $P$  range 75-150 W, whereas  $\theta_R(\text{NH})$  remain constant ( $\sim 350$  K) and independent of  $P$ . In contrast to  $\theta_v$  trends,  $S(\text{NH})$  values are inversely related to  $P$ , declining from  $\sim 2.5$  to  $\sim 0.8$  over the  $P$  range 75-225 W. Comparison of these data to the internal and translational temperatures for NH from mixed precursor systems reveal contrasting results. Figure 4.9 shows that in the 50:50 NH<sub>3</sub>/O<sub>2</sub> mixture,  $\theta_v$  remains constant with increasing  $P$ , but decreases with  $P$  in the 20:80 mixture. Notably,  $\theta_T$  and  $\theta_R$  both equilibrate at  $\sim 360$  K, independent of  $P$ .

### 4.3 Discussion

Understanding how energy gets partitioned in complex systems such as plasmas is key to developing a detailed picture of the overall plasma chemistry. Exploring energy partitioning for a single molecule within a single plasma system provides only one piece of the puzzle. Clearly, more information can be gleaned by examining multiple molecules within the same plasma system, the same molecule within different plasma systems, and different molecules in different plasma systems. The data presented here for seemingly similar diatomic molecules formed in different plasma systems (e.g. CH and SiH in CH<sub>4</sub> and SiH<sub>4</sub> plasmas, respectively) as well as for the same molecule within multiple plasma systems (e.g. OH in H<sub>2</sub>O and NH<sub>3</sub>/O<sub>2</sub> plasmas) and for two molecules within the same plasma (e.g. OH and NH in NH<sub>3</sub>/O<sub>2</sub> plasmas) allows for a range of observations to be made. For example, one general observation is that  $\theta_v$  tends to exceed both rotational

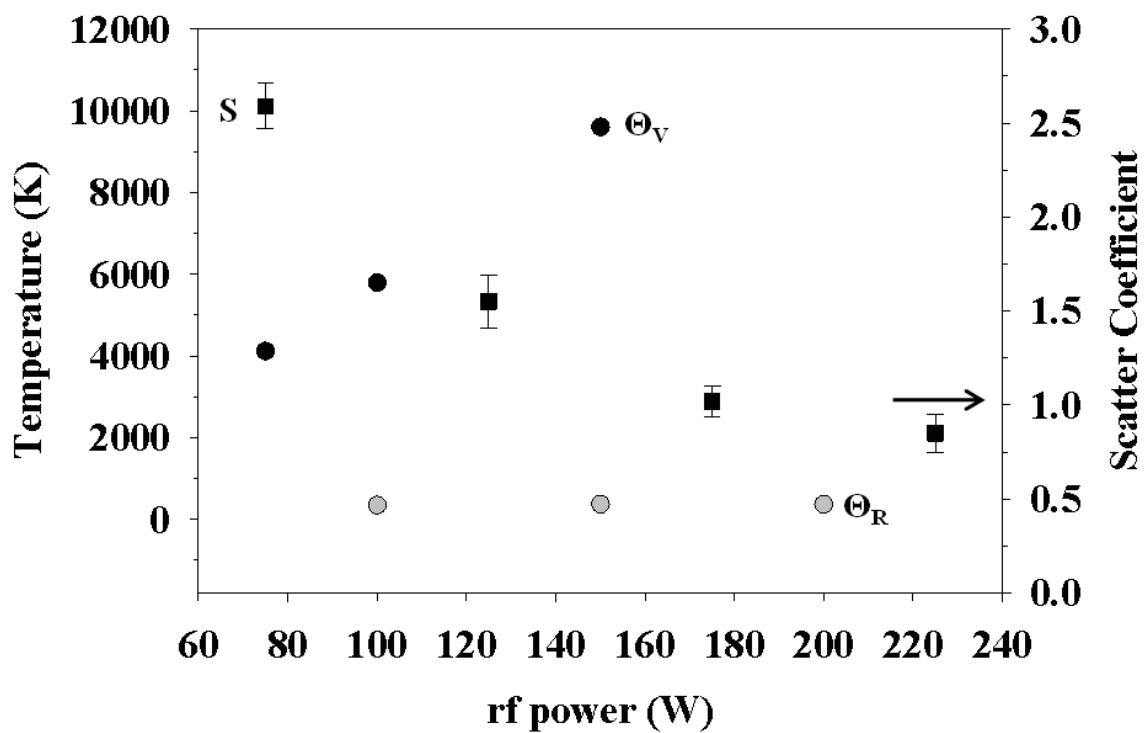


**Figure 4.8**  $\theta_V$  (black circles),  $\theta_R$  (grey circles), and scatter coefficients (black squares) for NH radicals formed in a 100%  $\text{NH}_3$  plasma as a function of applied rf power, with a total system pressure of 50 mTorr.

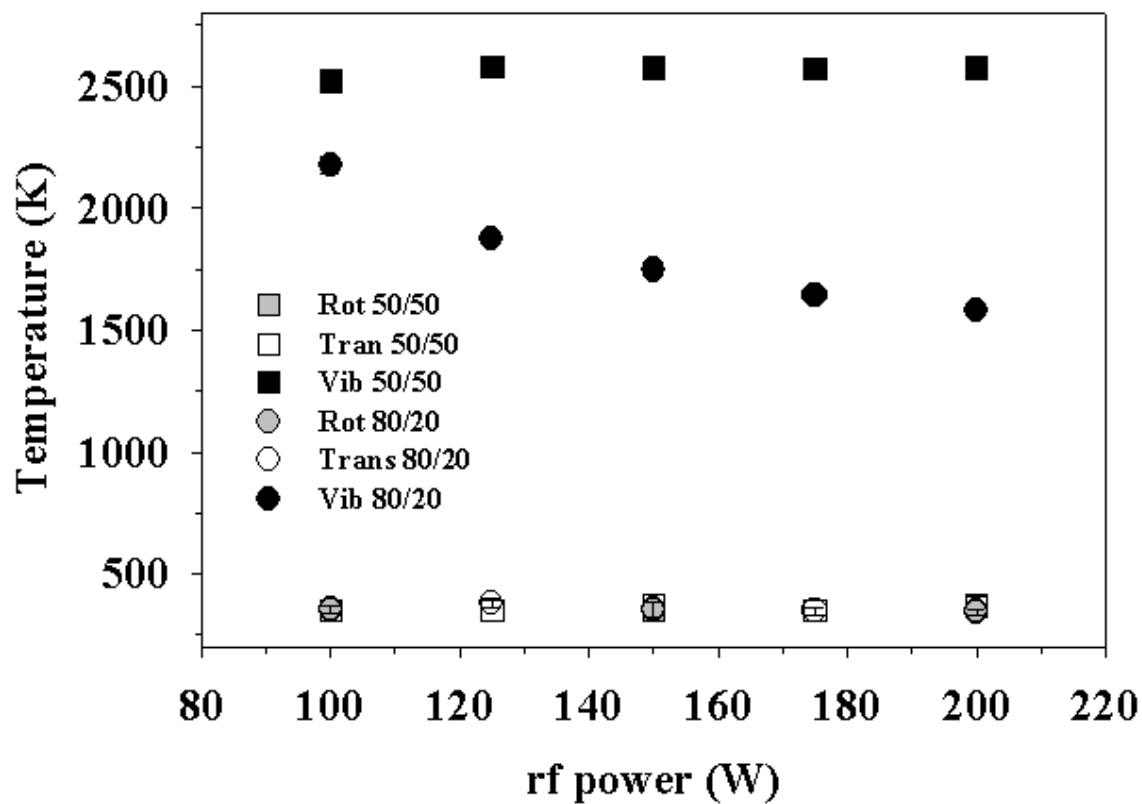


**Figure 4.9**  $\theta_V$  (black square/circle),  $\theta_T$  (white square/circle), and  $\theta_R$  (grey square/circle) for NH formed in 50:50 and 20:80  $\text{NH}_3/\text{O}_2$  plasmas. Squares represent the 50:50 mixture and circles represent the 20:80 mixture.

**Table 4.2**  $T_e$  (in eV) for selected plasma systems.<sup>a</sup>

<b>Applied rf Power (W)</b>	<b>CH<sub>4</sub> plasma <math>T_e</math></b>	<b>SiH<sub>4</sub><sup>b</sup> plasma <math>T_e</math></b>	<b>SiH<sub>4</sub><sup>c</sup> plasma <math>T_e</math></b>	<b>CH<sub>3</sub>OH plasma <math>T_e</math></b>	<b>H<sub>2</sub>O plasma <math>T_e</math></b>
10	-	2.24 ± 0.03	-	-	-
20	3.10 ± 0.09	2.40 ± 0.06	2.35 ± 0.03	-	-
40	-	2.30 ± 0.05	2.31 ± 0.05	-	-
60	2.86 ± 0.09	2.26 ± 0.04	2.28 ± 0.05	-	-
80	-	2.16 ± 0.03	2.33 ± 0.06	-	-
100	2.78 ± 0.09	-	-	4.27 ± 0.24	1.36 ± 0.02
140	2.83 ± 0.12	-	-	-	-
180	2.82 ± 0.12	-	-	-	-

<sup>a</sup>Calculated from Ar emission lines. Error represents the standard error calculated from the mean of three trials.

<sup>b</sup>40:60 SiH<sub>4</sub>/Ar plasma

<sup>c</sup>60:40 SiH<sub>4</sub>/Ar plasma

and translational temperatures for each of the systems studied here. Nonetheless, these temperatures are significantly lower than corresponding  $T_e$  values, Table 4.2. This is an expected result for non-thermal plasmas wherein species adhere to a classical energy-partitioning relationship. Further evaluation of the presented data shows more specific observations are revealed.

Temperatures for CH in CH<sub>4</sub>/Ar systems appear to be largely independent of changes in Ar concentration from 5-20% Ar in a 50 mTorr plasma with  $P = 180$  W, Fig. 4.4a. The exception here is that  $\theta_v$  increases slightly at %Ar  $\geq 15\%$ . Ostensibly, we might anticipate CH vibrational energy loss through collisions with Ar, but the behavior we observe likely results from fewer CH-CH collisions upon dilution with Ar. Indeed, the literature suggests that vibrational deactivation of CH<sub>x</sub> units is more probable on a per-collision basis through CH<sub>x</sub>-CH<sub>x</sub> collisions than through CH<sub>x</sub>-Ar collisions.<sup>14</sup> Furthermore, we obtain slightly higher  $\theta_v$  values for CH produced from higher pressure (i.e. 110 mTorr) CH<sub>4</sub> plasmas, wherein an increase in collision frequency ought to be commensurate with increased system pressure. Thus, the  $\theta_v(\text{CH})$  values reported here for plasmas that do not contain Ar reflect the lower limit of the vibrational temperature for the molecule.

In extending CH analyses to incorporate  $P$ -dependence, Fig. 4.4b, we observe that  $\theta_v$ ,  $\theta_T$ , and  $\theta_R$  do not change appreciably, nor do these values differ significantly from those depicted in Fig. 4.4a. Notably,  $\theta_R(\text{CH})$  values are particularly high ( $\sim 1500$  K) in all cases. Conventionally,  $\theta_R$  values are used as a metric for plasma gas temperature,  $T_g$ , as rotational equilibration tends to be a rapid process.<sup>15-18</sup> Previous studies suggest  $T_g$  should be at or near room temperature for the CH<sub>4</sub> plasma. As such, we speculate that these high

$\theta_R$  values result from excess rotational energy remaining after electron-impact dissociation of the methane precursor, as postulated by Luque and coworkers.<sup>19</sup>

Vibrational temperatures for SiH molecules depend upon both plasma feed gas composition and  $P$ , Fig. 4.5. For example,  $\theta_V(\text{SiH})$  in  $\text{SiH}_4$  plasmas, Fig. 4.5a, decreases with an increase in the argon fraction in the plasma. This contrasts with the  $\text{CH}_4/\text{Ar}$  system, in which we observed no dependence of  $\theta_V$  on argon addition. In the case of SiH, we are likely observing a trend relating to vibrational deexcitation of the molecule via Ar collision partners. Moreover, the decrease in  $\theta_V(\text{SiH})$  observed in  $\text{SiH}_4/\text{Ar}$  plasmas contrasts with the trend observed for SiH radicals in  $\text{Si}_2\text{H}_6/\text{Ar}$  plasmas, Fig. 4.5b, wherein vibrational temperatures are independent with respect to %Ar in the plasma. Although we have shown that relative ground state concentrations of SiH are similar,<sup>4</sup> actinometric OES data suggest that the relative excited state concentration of the molecule may be as much as three times higher in the  $\text{Si}_2\text{H}_6$  plasma as compared to the  $\text{SiH}_4$  system. As  $\theta_V(\text{SiH})$  values are similar at 0% Ar in both plasma systems, it would then follow that the apparent independence of  $\theta_V(\text{SiH})$  with respect to Ar addition in  $\text{Si}_2\text{H}_6/\text{Ar}$  plasmas is related to the higher amount of species present in the  $\text{Si}_2\text{H}_6/\text{Ar}$  plasma. Ultimately, we may simply be unable to observe the effect of vibrational deactivation by argon due to the large amount of SiH in the  $\text{Si}_2\text{H}_6/\text{Ar}$  system. The effect of varying  $P$  is evident in Fig. 4.5c, where  $\theta_V(\text{SiH})$  is indirectly proportional to  $P$  for each  $\text{SiH}_4/\text{Ar}$  system depicted. This general trend in SiH behavior as a function of  $P$  is corroborated by the results of Perrin and Delafosse.<sup>20</sup>

A disparity exists among the translational temperatures measured for SiH, depending upon the system in which the radical is formed. In particular, for  $\text{SiH}_4/\text{Ar}$  plasmas,

$\theta_T(\text{SiH})$  is constant, within error, with respect to Ar in the system, Fig. 4.5a, but decreases with increasing argon fraction in the  $\text{Si}_2\text{H}_6/\text{Ar}$  plasmas, Fig. 4.5b. We have previously concluded that this inconsistency is to the result of a higher efficacy of non-reactive collisional cooling in the latter system.<sup>9</sup> In all cases, the rotational temperatures for SiH thermalize at  $\sim 500$  K. These values follow with the expected results that the  $\theta_R$  values can be used to determine plasma gas temperature,  $T_g$ .

In considering the scatter coefficients for just the CH and SiH radicals, we have observed that both  $S(\text{CH})$  and  $S(\text{SiH})$  are independent of changing plasma parameters and lie collectively within the range of 0.01-0.05.<sup>4</sup> These  $S$  values are likewise independent of changes in  $\theta_V(\text{CH})$  or  $\theta_V(\text{SiH})$ , indicating that vibrational temperatures do not influence scatter. This contrasts sharply with our previously established results for radicals in other plasma systems, including SiF, NO, and CF, where we observe direct correlation between scatter coefficients and  $\theta_V$ .<sup>5</sup> Thus, internal energies do not account for the low scatter coefficients for CH and SiH. Rather, we propose that the reactivities of these molecules are heavily influenced by their electronic character, specifically the radical multiplicity. Both CH and SiH have doublet ground and first excited states, to which is attributed a significant propensity for reaction. Thus, when a CH or SiH radical interacts with a surface or deposited film, it tends not to scatter readily from the surface.

The  $T_e$  for  $\text{CH}_4$  plasmas decreases with increasing  $P$ , this affects  $k$  that in turn causes changes in  $\theta_V$ . The  $T_e$  for  $\text{SiH}_4/\text{Ar}$  plasmas at two different gas mixtures, 40:60 and 60:40, do not change with  $P$ , rendering  $k$  constant. Because our  $\theta_V$  temperatures change in the SiH systems and our  $\theta_R$  and  $\theta_T$  are significantly lower than the  $\theta_V$  temperature, we can conclude that the results obtained are related to changes in the  $e^-$  density that increases

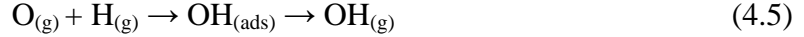
the number of collisions, and is not related to increases in the frequency of collisions that transfer energy.

Comparison of data obtained for CH radicals in both 50 and 110 mTorr CH<sub>4</sub> systems shows that  $\theta_R$  values are similar and independent of %Ar, whereas  $\theta_V$  increases in the 50 mTorr system and stays constant in the 110 mTorr system as a function of %Ar.  $\theta_T$  values are greater in the 110 mTorr system as compared to the 50 mTorr system. Both the 50 and 110 mTorr systems show  $\theta_V > \theta_T > \theta_R$  and their surface scattering coefficients are low, reflecting a high surface reactivity. For OH in a 100% H<sub>2</sub>O plasma,  $\theta_T$  and  $\theta_R$  are virtually identical and are independent of  $P$ . It is likely that these modes have thermalized to ~300 K and thus represent  $T_g$  for this system.  $\theta_V$  values are approximately an order of magnitude greater than the translational and rotational temperatures, indicating a preferential distribution of energy into the vibrational mode of the molecule. Nonetheless,  $\theta_V$  decreases steadily with  $P$ , which starkly contradicts results for other diatomic molecules, including NO, CF, and SiF. Here, we believe that highly vibrationally excited OH\* species simply dissociate as in reaction 4.2,<sup>21</sup> where either product can exist in an electronic excited state. Indeed, we see evidence from actinometric OES data that O\* and H\* signals both increase over OH\* as  $P$  is increased. The ramification of reaction 4.2 is that only the less vibrationally excited OH\* species remain intact and are thus used for calculations of vibrational temperatures. Ultimately, then this results in the apparent decrease in  $\theta_V(\text{OH})$  as a function of  $P$ .



Because the OH radical is a doublet hydride, we might expect to observe a high degree of surface reactivity (i.e.  $S \sim 0.05$ ). However, in contrast to both the CH and SiH

radicals discussed above,  $S(\text{OH})$  values measured for the  $\text{H}_2\text{O}$  plasma system are generally greater and  $\sim 0.50$ , regardless of changing plasma parameters. Notably, these values decrease to as low as 0.15 as substrate temperature ( $T_s$ ) is increased. We believe that some of the observed scatter for OH at  $T_s = 300$  K is a reflection of plasma-surface reactions that stimulate production of OH, as outlined in reactions 4.3 and 4.4. In the first



of these reactions, dissociation of the parent molecule at the surface results in formation of  $\text{OH}_{(\text{g})}$  which is present in the scatter signal but not in the incident plasma beam signal. In the second reaction, 4.4, surface hydroxyl groups already present on the substrate (i.e. from a surface oxide layer, such as  $\text{SiO}_2$ ) desorb during bombardment from energetic species such as ions or O radicals in the plasma. Finally, recombination of O and H plasma species at the surface and subsequent desorption of  $\text{OH}_{(\text{g})}$  can contribute to the increased scatter. Upon substrate heating, much of the surface hydroxyl groups are effectively removed, and as such, the contribution from reaction 4.4 diminishes substantially. Consequently, we believe that 4.4 plays the most significant role in dictating the scatter coefficient for the interaction of OH radicals with a room temperature substrate.

$\theta_v(\text{OH})$  as measured for the radical in  $\text{NH}_3/\text{O}_2$  plasmas are significantly lower than those values measured for the radical in 100%  $\text{H}_2\text{O}$  plasmas. Additionally,  $\theta_v(\text{OH})$  for  $\text{NH}_3/\text{O}_2$  systems appear to be independent of  $P$ , suggesting energy partitioning in the

molecule depends heavily upon the formation mechanism of OH. In H<sub>2</sub>O plasmas, direct formation of OH is achieved through a unimolecular decomposition reaction, whereas in the mixed precursor systems it can only be formed via bimolecular or recombination reactions. This may help explain why we see lower  $\theta_V$  temperatures for the mixed systems. During recombination or bimolecular collisions, energy can be lost or transferred, and that loss appears to occur preferentially via vibrational modes of the OH radicals. This is reinforced by the observation that little difference exists between the respective  $\theta_T(\text{OH})$  and  $\theta_R(\text{OH})$  values for H<sub>2</sub>O systems and the mixed NH<sub>3</sub>/O<sub>2</sub> plasma.

When we examine an alternate plasma system, CH<sub>3</sub>OH, wherein OH is also formed via unimolecular decomposition, we find that  $\theta_V(\text{OH})$  are similar to the mixed NH<sub>3</sub>/O<sub>2</sub> systems, ~1100 K. The difference in the CH<sub>3</sub>OH and the H<sub>2</sub>O  $\theta_V(\text{OH})$  can be attributed to differences in the way energy is distributed among vibrational modes. For example, unimolecular decomposition of a H<sub>2</sub>O molecule to form OH can result in the allocation of vibrational energy only to the O-H fragment since the remaining product is simply a hydrogen atom. Conversely, for OH production from CH<sub>3</sub>OH, vibrational energy can be transferred to either CH<sub>x</sub> (x = 1-3) or OH. Because CH<sub>x</sub> has a maximum of six normal modes of vibration, and OH has only one, we speculate that the distribution of energy necessarily favors the CH<sub>x</sub> fragment, resulting in lower observed  $\theta_V(\text{OH})$ .

The triplet radical, NH, appears to be formed with a high degree of vibrational energy in the 100% NH<sub>3</sub> plasma system, Fig. 4.8. As  $P$  increases,  $\theta_V(\text{NH})$  approaches 10<sup>4</sup> K, with the increase with  $P$  associated with increased energy deposition into vibrational modes. The rotational temperatures, on the other hand, equilibrate to the plasma gas temperature at ~300 K. Despite the increases in  $\theta_V(\text{NH})$  with  $P$ ,  $S(\text{NH})$  values for this

system decrease over a similar  $P$  range. We believe that highly vibrationally excited NH molecules interacting with a substrate abstract H from the surface and desorb as  $\text{NH}_2$ , as in reaction 4.6. Such production of  $\text{NH}_2$  is evidenced by high surface scattering coefficients for the molecule during  $\text{NH}_3$  plasma processing of substrates. The outcome of reaction 4.6 depletes NH in the scatter signal and leads to decreases in  $S(\text{NH})$  with  $P$ .



We can also study NH in the  $\text{NH}_3/\text{O}_2$  systems. Thermalization of translational and rotational temperatures appears to occur in both 20/80 and 50/50  $\text{NH}_3/\text{O}_2$  mixtures, Fig. 4.9. NH radicals formed in mixed precursor systems have significantly lower  $\theta_v$  than do those molecules formed in 100%  $\text{NH}_3$  plasmas, Fig. 4.8. In addition, increasing oxygen dilution results in decreased  $\theta_v(\text{NH})$ . Thus, we conclude that NH must lose significant amounts of vibrational energy to collisions. The decrease of  $\theta_v(\text{NH})$  with respect to  $P$  in the 20/80  $\text{NH}_3/\text{O}_2$  system, Fig. 4.9, mirrors the trend observed for OH in  $\text{H}_2\text{O}$ , Fig. 4.6. We assume a similar mechanism accounts for this, as vibrationally excited NH decomposes as  $P$  increases, leaving a population of NH in the gas-phase which has significantly lower vibrational energies. The already diluted NH signal decreases even more substantially, and we thus only observe moderately vibrationally excited molecules from which to calculate  $\theta_v(\text{NH})$ . In the 50/50  $\text{NH}_3/\text{O}_2$  plasma,  $S(\text{NH})$  values increased from  $\sim 1.1$  to  $\sim 1.5$  over the range  $P = 100\text{-}200$ .<sup>22</sup> These scatter values demonstrate the reverse trend from what was observed for a 100%  $\text{NH}_3$  plasma. Here, because there is essentially no variation in  $\theta_v(\text{NH})$  over the same range, Fig. 4.9, the change in scatter coefficient must arise from elsewhere. We believe that high levels of scatter (i.e.  $S > 1$ ) are at least partially a result of ion bombardment of passivating films and have shown

highly energetic ions can affect observed scatter significantly.<sup>6</sup> With NH scatter, we believe that ions, which tend to increase in average energy with increased  $P$ , from the  $\text{NH}_3/\text{O}_2$  system contribute to increasing  $S(\text{NH})$  as a function of  $P$ . Scatter values were not determined for the 20/80  $\text{NH}_3/\text{O}_2$  mixture due to poor NH signal in these systems.

Comparison of OH and NH formed in the mixed precursor systems, shows differences in  $\theta_V$  and  $\theta_T$ , whereas  $\theta_R$  for OH and NH are similar and as such, indicative of the gas temperature in all of these mixed precursor systems. Differences in  $\theta_V(\text{OH})$  and  $\theta_V(\text{NH})$  are expected for OH and NH due to their formation mechanisms. Because NH is formed through a unimolecular decomposition reaction and OH through a bimolecular recombination mechanism we expect  $\theta_V(\text{NH})$  to be higher than  $\theta_V(\text{OH})$ , as a distribution of vibrational energy will necessarily place some vibrational energy into the other species formed during the bimolecular recombination reactions that form OH. Indeed we observe this, as in Figures 4.7 and 4.9. Translational temperatures for these systems differ with  $\theta_T(\text{OH}) \sim 600$  K and  $\theta_T(\text{NH}) \sim 350$  K. The higher observed  $\theta_T(\text{OH})$  value is likely a result of OH gaining momentum through the collision(s) which occur to form the molecule to begin with. Indeed, in other systems in which OH must be formed through collisional processes (i.e. bimolecular reactions), such as the TEOS/ $\text{O}_2$  plasma, we see that the  $\theta_T(\text{OH})$  is likewise high at  $\sim 900$  K.

#### **4.4 Summary**

Vibrational, translational, and rotational temperature correlation with surface scatter coefficients for four diatomic hydride radical species was investigated. For all four molecules; CH, SiH, OH and NH the vibrational temperatures are significantly higher than both the translational and rotational temperatures. Previous results found that the

partitioning of energy into vibrational modes correlated with an increased propensity for scatter when a molecule interacted with a substrate.<sup>5</sup> However we found here that this was not the case, but that the likelihood of surface scatter is correlated more with the radicals electronic character and formation mechanisms. This data in combination with our previous studies<sup>5</sup> suggests that radical surface scatter coefficients are reliant upon the vibrational energy, electronic character, and formation mechanism of the radical. The addition of these studies has brought a clearer understanding to the gas-phase of plasmas and the probability of radicals to react with surfaces. The connection between internal and translational energies, electronic configuration, and surface reactivity of plasma species must be considered in the development of new and existing plasma applications.

## 4.5 References

- <sup>1</sup>N. Britun, M. Gaillard, A. Richard, Y. M. Kim, K. S. Kim, and J. G. Han, *J. Phys. D: Appl. Phys.* **40**, 1022 (2007).
- <sup>2</sup>A. Fridman, *Plasma Chemistry* (Cambridge University Press, New York, 2008).
- <sup>3</sup>K. H. A. Bogart, J. P. Cushing, and E. R. Fisher, *Journal of Physical Chemistry B* **101**, 10016 (1997).
- <sup>4</sup>W. M. M. Kessels, P. R. McCurdy, K. L. Williams, G. R. Barker, V. A. Venturo, and E. R. Fisher, *Journal of Physical Chemistry B* **106**, 2680 (2002).
- <sup>5</sup>M. F. Cuddy, K. J. Trevino, and E. R. Fisher, *J. Phys. Chem. A* **submitted** (2011).
- <sup>6</sup>D. Liu, I. T. Martin, J. Zhou, and E. R. Fisher, *Pure Appl. Chem.* **78**, 1187 (2006).
- <sup>7</sup>J. Zhou and E. R. Fisher, *Journal of Physical Chemistry B* **110**, 21911 (2006).
- <sup>8</sup>P. R. McCurdy, J. M. Truitt, and E. F. Fisher, *J. Vac. Sci. Technol. A* **17**, 2475 (1999).
- <sup>9</sup>J. Zhou, J. Zhang, and E. R. Fisher, *Journal of Physical Chemistry A* **109**, 10521 (2005).
- <sup>10</sup>E. R. Fisher, P. Ho, B. W. G., and R. J. Buss, *Journal of Physical Chemistry* **97**, 10287 (1993).
- <sup>11</sup>R. J. Buss, P. Ho, E. R. Fisher, and W. G. Breiland, *Material Research Society Symposium Proceedings* **334**, 51 (1994).
- <sup>12</sup>P. R. McCurdy, K. H. A. Bogart, N. F. Dalleska, and E. R. Fisher, *Rev. Sci. Instrum.* **68**, 1684 (1996).
- <sup>13</sup>K. H. A. Bogart, J. P. Cushing, and E. R. Fisher, *Chemical Physics Letters* **267**, 377 (1997).
- <sup>14</sup>D. J. Donaldson and S. R. Leone, *The Journal of Physical Chemistry* **91**, 3128 (1987).
- <sup>15</sup>Y. B. Golubovskii and V. M. Telezhko, *J. Appl. Spectrosc.* **39**, 999 (1983).
- <sup>16</sup>R. A. Porter and W. R. Harshbarger, *J. Electrochem. Soc.* **126**, 460 (1979).
- <sup>17</sup>G. P. Davis and R. A. Gottscho, *J. Appl. Phys.* **54**, 3080 (1983).
- <sup>18</sup>M. J. Schabel, V. M. Donnelly, A. Kornblit, and W. W. Tai, *J. Vac. Sci. Technol. A* **20**, 555 (2002).
- <sup>19</sup>J. Luque, M. Kraus, A. Wokaun, K. Haffner, U. Kogelschatz, and B. Eliasson, *Journal of Applied Physics* **93**, 4432 (2003).
- <sup>20</sup>J. Perrin and E. Delafosse, *J. Phys. D: Appl. Phys.* **13**, 759 (1980).
- <sup>21</sup>G. Gambus, P. Patino, and J. Navea, *Energ Fuel* **16**, 172 (2001).
- <sup>22</sup>D. Liu and E. R. Fisher, *Journal of Vacuum Science and Technology A* **25**, 368 (2007).

## CHAPTER 5

### ISOELECTRIC POINTS OF PLASMA MODIFIED AND AGED SILICON OXYNITRIDE SURFACES MEASURED USING CONTACT ANGLE TITRATIONS

This chapter contains data from a full published paper in the journal of *Surface and Interface Analysis*. Data were collected by Kristina J. Trevino with the exception of the x-ray photoelectron spectroscopy (XPS) data. Preliminary XPS results were published in Michelle M. Morgan's Masters thesis however the data presented here were recollected and analyzed by another graduate student, Jeffery C. Shearer. The manuscript was written by Kristina J. Trevino, Jeffery C. Shearer, and Ellen R. Fisher. These studies explore the relationships between surface isoelectric point, chemical composition, and aging effects of amorphous silicon oxynitride ( $\text{SiO}_x\text{N}_y$ ) treated with Ar,  $\text{H}_2\text{O}$  vapor, and  $\text{NH}_3$  inductively-coupled rf plasmas. The trends observed in isoelectric point and chemical changes upon aging for one month suggest that contact angle and composition are closely related, whereas the relationship between IEP and composition is not as directly correlated.

## 5.1 Introduction

Knowledge of both macroscopic and molecular level properties of thin film materials is critical to fully characterizing surfaces and understanding how these materials may be employed in a variety of processes. In particular, the acid-base properties of metal oxides and polymers can control adhesion properties between materials, electrical properties (i.e. electron transport), the physical structure of the material, and gas adsorption behavior. For example, electrostatic interactions can control the swelling and chain conformation in polymer chain assemblies (polymer brushes),<sup>1</sup> and the acid-base properties of metal oxides can control their adhesion to various polymers.<sup>2-4</sup> Indeed, many groups have explored improving adhesion between metals/metal oxides and polymers as these types of composite materials are critical for a range of applications including packaging and barrier coatings, biocompatible devices, and next generation solar cells.<sup>5-7</sup> At a fundamental level, characterizing interfaces between materials or between a material and its environment constitutes one of the most challenging aspects of materials science. Metal oxide surfaces have proven especially difficult in these types of studies as they are highly susceptible to many atmospheric reactions that can both alter the materials surface properties and increase contamination. Moreover, several studies have demonstrated that metal oxide surfaces are largely composed of hydroxyl groups,<sup>8,9</sup> the density of which can change dramatically depending on the ambient conditions (e.g. humidity).

Plasma surface modification has been successfully employed to improve adhesion between different types of materials.<sup>10,11</sup> One clear advantage that plasmas have for surface modification of polymers and metals is that plasma treatment generally affects only the outermost layer of the material being modified, but keeps the bulk properties

largely unchanged.<sup>10</sup> Plasma treatments can change the surface polarity, wettability and adhesive characteristics of both polymers and metal surfaces.<sup>11-14</sup> We have used plasma surface modification techniques to implant functional groups into polymeric membranes,<sup>14-17</sup> and to modify the surface of polyethylene fibers and other micro- and nano-structured materials via thin film deposition.<sup>13,15,18</sup>

One potential drawback to the plasma treatment of polymers and metal surfaces not always adequately addressed is dynamic changes that can occur over time after processing. Specifically, several studies have shown that the composition of plasma-modified surfaces can change with time.<sup>17,19,20</sup> This has been attributed to chain migration, surface reorganization and atmospheric oxidation in polymeric systems.<sup>20,21</sup> Polymer aging often results in hydrophobic recovery for surfaces that have been implanted with polar functional groups through plasma treatment. Aging of plasma-modified metal surfaces, however, has not been explored to a large extent in the literature. Presumably, aging effects in these systems would result in formation of surface carbides, nitrides, and sulfides for metal surfaces exposed to atmosphere following plasma treatment. One method for determining the extent of plasma surface modification for both polymers and metal surfaces is contact angle titration, which provides information on changes in hydrophilicity and surface charge state as a result of plasma treatment.<sup>8,22-24</sup>

Here, we investigated the plasma-surface treatment of amorphous silicon oxynitride ( $\text{SiO}_x\text{N}_y$ ) substrates. The goals of this work were to (1) measure the effect of plasma treatment on the isoelectric point of  $\text{SiO}_x\text{N}_y$ ; (2) to characterize the changes in surface chemistry resulting from each type of plasma treatment; and (3) to determine the

permanency of the treatment through aging studies. The plasmas investigated were all non-polymerizing, specifically Ar, H<sub>2</sub>O vapor, and NH<sub>3</sub>. Ar plasmas are effective at improving adhesion properties of a range of materials and also activate surfaces via formation of radical sites.<sup>25</sup> Water plasmas were chosen as a potentially amphoteric treatment (transferring either OH or H<sup>+</sup> groups, resulting in amphoteric surfaces), whereas NH<sub>3</sub> plasmas have been shown to implant amine functionalities into a variety of materials.<sup>14,16,17</sup> In addition to investigating effects of plasma modifying gas, we also examined the processing parameters of substrate location in the plasma and applied rf power.

## 5.2 Results

The SiO<sub>x</sub>N<sub>y</sub> substrates used were treated with three different plasma systems, 100% Ar, 100% H<sub>2</sub>O (g), and 100% NH<sub>3</sub>(g). The untreated and treated substrates were analyzed via CA titrations to establish hydrophilicity, hydrophobicity, IEP values, and surface charge states and with XPS to determine chemical composition and binding environments induced by the plasma treatments. The first three subsections here describe results for each plasma system and the final subsection describes SEM and OES analyses. All data for treated samples were compared to an untreated, as-received SiO<sub>x</sub>N<sub>y</sub> substrate, Figure 5.1a.

**Untreated SiO<sub>x</sub>N<sub>y</sub> and Ar plasma treatments.** Ar plasmas are used extensively to improve adhesion between layers and to create radical sites in polymer surfaces, thereby facilitating polymerization and other surface reactions. Here, we chose 100% Ar plasmas as a control system as they are expected to be relatively inert with respect to implantation of specific chemical functionality. Figure 5.2a shows CA titration data for the untreated

$\text{SiO}_x\text{N}_y$  substrate, which is relatively flat as a function of pH, exhibiting a contact angle of  $\sim 75^\circ$  for all CA solutions. This lack of dependence on pH suggests the untreated  $\text{SiO}_x\text{N}_y$  substrates are neither strongly acidic nor strongly basic. Indeed, attempts to fit these data with both second and third order polynomials were unsuccessful, further suggesting that the substrate is best described as amphoteric, meaning the surface can have both acidic and basic characteristics, or can be positively or negatively charged depending on the pH of its environment.

To our knowledge, there are no reported IEP values for  $\text{SiO}_x\text{N}_y$  substrates; however, given the mixed composition of the substrate, it is not surprising that the surface is neither clearly acidic, nor clearly basic. For comparison, literature values for the IEP of  $\text{SiO}_2$  are relatively acidic, in the range of 1.5-4.0, depending on the crystal type and formation method.<sup>26</sup> The reported IEP values for  $\text{Si}_3\text{N}_4$  are significantly more basic, and appear to depend heavily on material type (e.g. powder vs. thin film), formation mechanism, cleaning processes and extent of oxidation.<sup>27</sup> Jan and Raghavan reported IEP values for silicon nitride films produced via plasma enhanced chemical vapor deposition (PECVD) and low pressure CVD (LPCVD) as 3.5 to 5.3, depending on the cleaning process used.<sup>28</sup> Notably, the IEP value for  $\text{Si}_3\text{N}_4$  materials depends heavily on the extent of oxidation, as surface silanol groups are expected to exhibit acidic behavior, whereas surface silylamine groups would create a much more basic surface.<sup>27,29</sup>

In contrast to the untreated  $\text{SiO}_x\text{N}_y$  substrates, CA titration data for the Ar plasma treated substrates (fresh and aged) display clear dependence on pH, with maxima

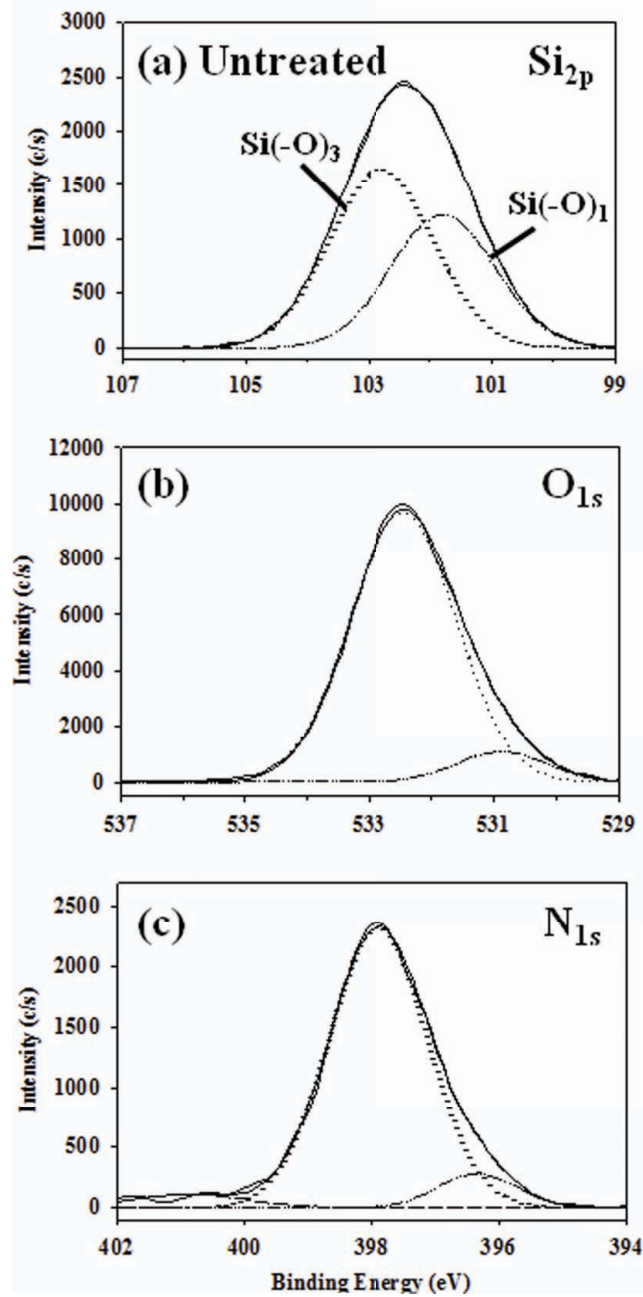


**Figure 5.1** High-resolution (a)  $\text{Si}_{2p}$ , (b)  $\text{O}_{1s}$ , and (c)  $\text{N}_{1s}$  XPS spectra for an untreated, "as received"  $\text{SiO}_x\text{N}_y$  substrate.

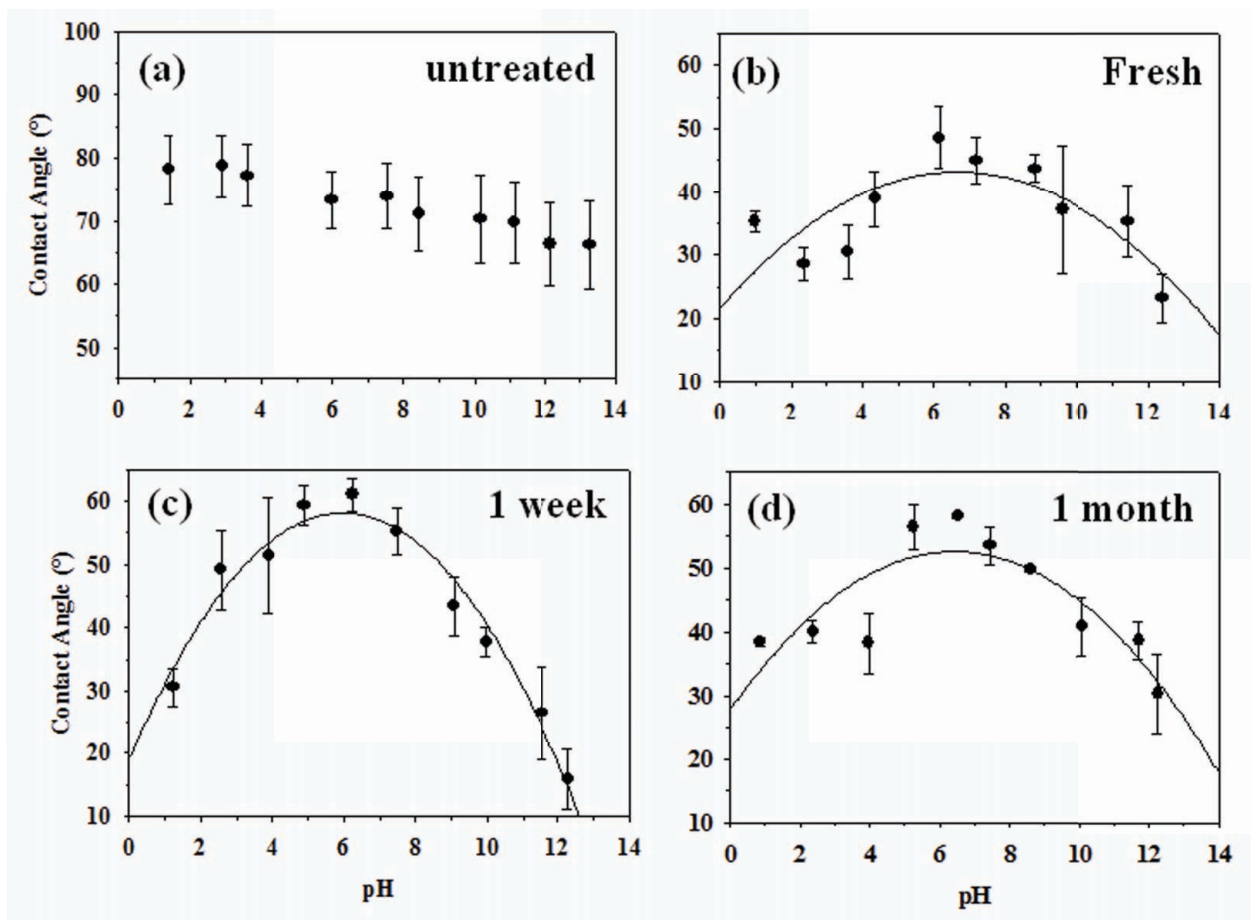


**Figure 5.2** Static contact angle titration data for (a) an untreated SiO<sub>x</sub>N<sub>y</sub> substrate; and SiO<sub>x</sub>N<sub>y</sub> substrates placed in the coil region of the plasma, treated with a 100% Ar plasma for 10 min with  $P = 50$  W and aged for (b) < 1 day (fresh); (c) 1 week; and (d) 1 month. The lines are second order polynomial fits to the data, yielding the IEP values in Table 5.1.

located at 5-7, Figures 5.2b-d. Figure 5.1 data were acquired for substrates positioned in the plasma coil with  $P = 50$  W; however, these data are representative of all substrates treated in Ar plasmas. There are two main observations to be made from these data. First,  $CA_{\max} = \sim 50^\circ$  for freshly treated and aged samples, which is significantly lower than that for the untreated substrate,  $CA = \sim 75^\circ$ . Moreover, this value does not change with aging of the samples. Second, unlike the untreated substrates, the CA titration data for treated  $SiO_xN_y$  substrates clearly display a maximum value, allowing the determination of an average IEP value of  $6.7 \pm 0.1$  for the freshly treated substrate, using a second order polynomial fit to the data. Both the 1 week and 1 month aged samples also display maxima, yielding average IEP values similar to the freshly treated substrates. Note that the IEP value does fluctuate significantly upon aging, suggesting a semi-permanent modification. The majority of substrates treated in Ar plasmas display the same general trend with respect to the IEP values determined from CA titration data, Table 5.1. The exception to this is the results for substrates placed 5 cm downstream from the coil with  $P = 150$  W. For these conditions, the IEP values steadily decline upon aging of the samples.

XPS elemental analysis of the untreated  $SiO_xN_y$  substrate revealed the expected amorphous content of oxygen, silicon, nitrogen, and carbon. Upon treatment with the 100% Ar plasmas, XPS analysis reveals minor changes in elemental composition of the surface for freshly treated samples. The most dramatic change occurs with surface carbon removal for substrates treated under the harshest plasma conditions (i.e. placement in the coil with  $P = 150$  W). As noted above, the interaction of Ar plasmas with the substrate preferentially removes adventitious carbon from the surface. As the

substrates age, the amount of carbon on the surface increases, in some cases reverting back to original “as received” values, presumably due to adventitious carbon accumulating on the surface. The N concentration also decreases upon treatment and shows no clear trend with time for the different treatment parameters. The Si and O percentages do not change appreciably upon treatment, regardless of the plasma parameters used.

To further explore possible changes in the binding environments in the  $\text{SiO}_x\text{N}_y$  substrates upon Ar plasma treatment, high-resolution  $\text{Si}_{2p}$  and  $\text{O}_{1s}$  XPS spectra were collected for fresh and aged  $\text{SiO}_x\text{N}_y$  substrates, Figure 5.3. As outlined above, the tetrahedral  $\text{Si}(\text{-O})_4$  silicon network binding environment was assigned to the highest energy peak at 103.3 eV. The other peak in this spectrum is located at 102.9 eV, yielding a  $\Delta = 0.4$  eV, and thus an assignment of  $\text{Si}(\text{-O})_3$ . Based on these assignments, the Ar plasma treated substrate is clearly much more oxidized than the untreated substrate, Figure 5.1a, which is consistent with the elemental composition data in Table 5.1. After the samples were aged, the spectra reveal greater quantities of Si exist in the lower oxidation environment of  $\text{Si}(\text{-O})_2$ . The  $\text{O}_{1s}$  spectra, Figures 5.2d-f, exhibit 2-3 binding environments, similar to what was observed for the untreated substrate. For the freshly treated substrate, the spectrum is dominated by the peak at 533.0 eV, corresponding to oxygen in a tetrahedral  $\text{SiO}_2$  network,<sup>30</sup> with a small contribution at 531.9 eV. This is consistent with the  $\text{Si}_{2p}$  spectrum that suggests the majority of the Si also exists within a  $\text{SiO}_2$  network. Upon aging, the  $\text{O}_{1s}$  spectra contain additional binding environments, mimicking the changes observed in the  $\text{Si}_{2p}$  spectra.

**Table 5.1** XPS elemental composition, IEP, and CA values for Ar plasma treated SiO<sub>x</sub>N<sub>y</sub> substrates<sup>a</sup>

Conditions	Age	% O	% Si	% N	% C	IEP	CA (°)
Untreated	—	41.7 ± 0.1	29.5 ± 0.2	14.5 ± 0.5	14.4 ± 0.6	amphoteric	73.6 ± 3.2
Coil, 50 W	Fresh	49.4 ± 0.4	32.5 ± 0.1	9.6 ± 0.4	8.6 ± 0.1	6.7 ± 0.1	43.2 ± 0.3
	1 week	48.3 ± 0.4	31.7 ± 0.9	9.2 ± 0.3	10.9 ± 0.8	6.0 ± 0.1*	58.1 ± 0.1*
	1 month	50.6 ± 0.4	28.8 ± 0.2	4.3 ± 0.2	16.4 ± 0.1	6.4 ± 0.1*	52.6 ± 0.3
Coil, 150 W	Fresh	62.6 ± 0.3	32.7 ± 0.1	2.0 ± 0.3	2.8 ± 0.5	7.0 ± 0.1	41.2 ± 0.4
	1 week	60.8 ± 1.1	32.3 ± 0.5	2.0 ± 0.1	5.0 ± 1.6	5.6 ± 0.1*	55.6 ± 0.3
	1 month	49.9 ± 0.5	30.7 ± 0.3	4.9 ± 0.1	14.5 ± 0.6	5.9 ± 0.1*	53.1 ± 0.2
5 cm, 50 W	Fresh	43.2 ± 0.1	32.7 ± 0.1	14.9 ± 0.1	9.3 ± 0.1	7.4 ± 0.1*	27.4 ± 0.3
	1 week	42.3 ± 0.4	31.5 ± 0.3	13.9 ± 0.4	12.4 ± 0.6	6.0 ± 0.1*	54.6 ± 0.4
	1 month	38.9 ± 8.8	25.5 ± 6.6	9.4 ± 3.2	26.4 ± 18.5	9.1 ± 0.4	48.1 ± 3.5
5 cm, 150 W	Fresh	53.3 ± 1.0	32.2 ± 0.0	9.8 ± 0.6	4.0 ± 0.3	7.1 ± 0.1*	37.6 ± 0.3
	1 week	52.7 ± 1.6	30.8 ± 0.3	9.0 ± 0.8	7.6 ± 0.5	5.8 ± 0.1*	45.0 ± 0.2
	1 month	41.9 ± 0.7	30.2 ± 0.7	11.1 ± 0.1	16.8 ± 1.6	4.7 ± 0.1	53.7 ± 0.3

<sup>a</sup>Error shown is 1 standard deviation of the mean unless otherwise indicated. Error listed as two standard deviations of the mean in indicated with an asterisk.

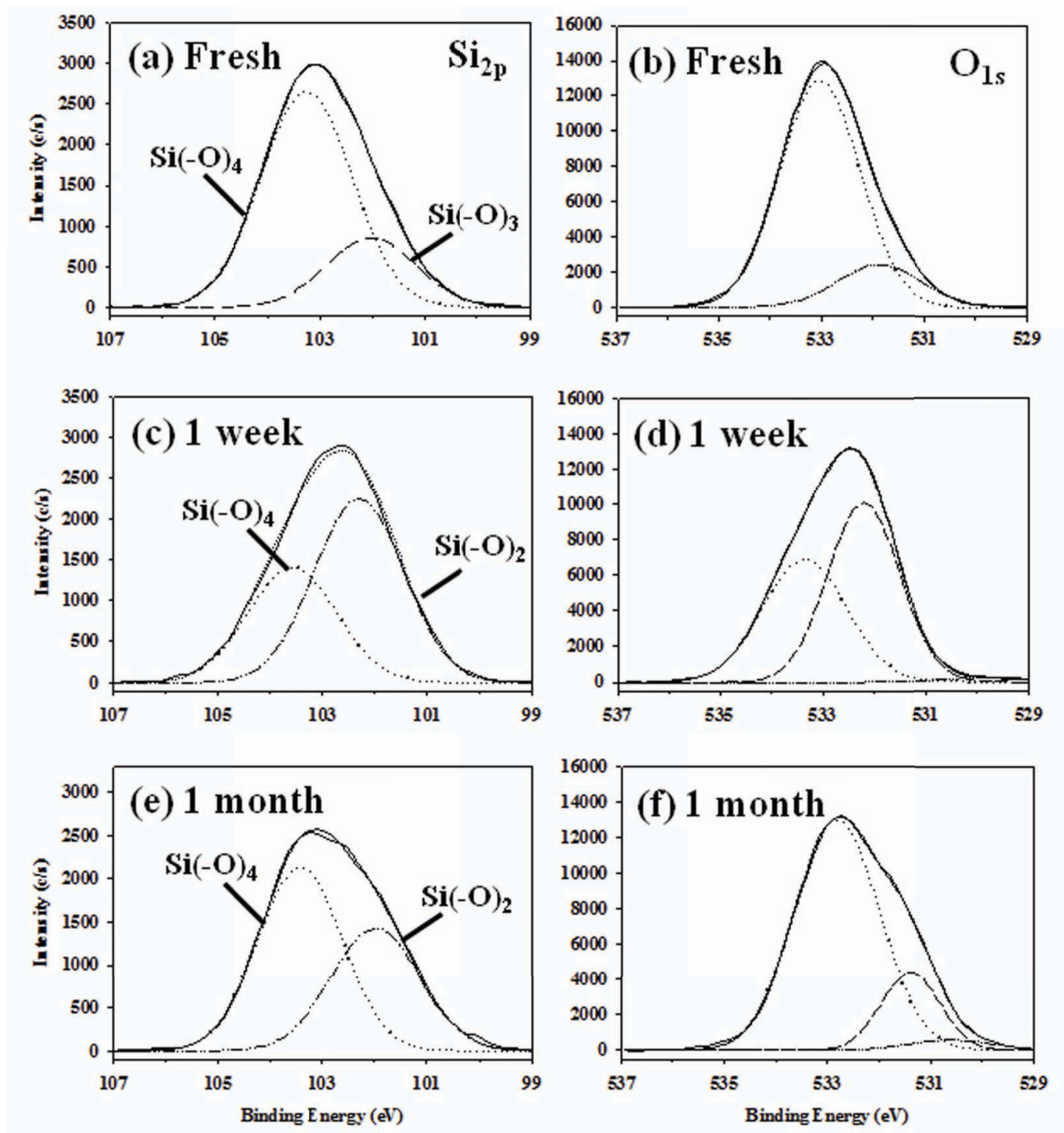


**Figure 5.3** High-resolution XPS  $\text{Si}_{2p}$  and  $\text{O}_{1s}$  spectra for  $\text{SiO}_x\text{N}_y$  substrates treated with a 100% Ar plasma for 10 min ( $P = 50$  W), immediately after treatment (fresh, panels a and b); 1 week after treatment (panels c and d); and 1 month after treatment (e and f).

**H<sub>2</sub>O (g) plasma treatments.** Figure 5.4 contains CA titration data and Si<sub>2p</sub> high resolution XPS spectra for SiO<sub>x</sub>N<sub>y</sub> substrates placed in the coil region of the plasma and treated with a 100% H<sub>2</sub>O (g) plasma ( $P = 150$  W). The CA titration data, Figures 5.4a-c, are representative of results from all of the H<sub>2</sub>O plasma treatments, regardless of  $P$  or position in the reactor. Similar to the Ar plasma, CAs for H<sub>2</sub>O plasma-treated samples were significantly lower ( $\sim 41^\circ$ ) than for the untreated substrates ( $\sim 75^\circ$ ), and again stayed relatively constant upon aging. These data also display clear maxima when fit with second order polynomials. Upon treatment, the average IEP value of the SiO<sub>x</sub>N<sub>y</sub> substrates, has increased to  $\sim 6$  and stays in the acidic range throughout the 1 month aging period. This is still considerably higher than that measured for the untreated SiO<sub>x</sub>N<sub>y</sub> substrates, and suggests a relatively permanent change to the surface charge character. Table 5.2 lists the XPS elemental composition data for 100% H<sub>2</sub>O vapor plasma-treated substrates. Similar to Ar plasma-treated substrates, the amount of carbon present on the substrate surface decreases upon treatment. Over the 1 month aging period, the carbon content increased, presumably from the accumulation of adventitious carbon. Likewise, the nitrogen content decreased upon treatment, but does not substantially recover during the aging period. The highest losses of nitrogen arise in samples that were treated with 150 W plasmas, regardless of location in the plasma. This suggests that the higher plasma power may be preferentially etching nitrogen from the surface. A similar preferential removal of nitrogen has been observed in plasma etching of gallium nitride materials.<sup>31</sup> The observation that the  $P = 150$  W plasma may be etching the substrate is substantiated by noting that the only samples that contained small amounts of sodium

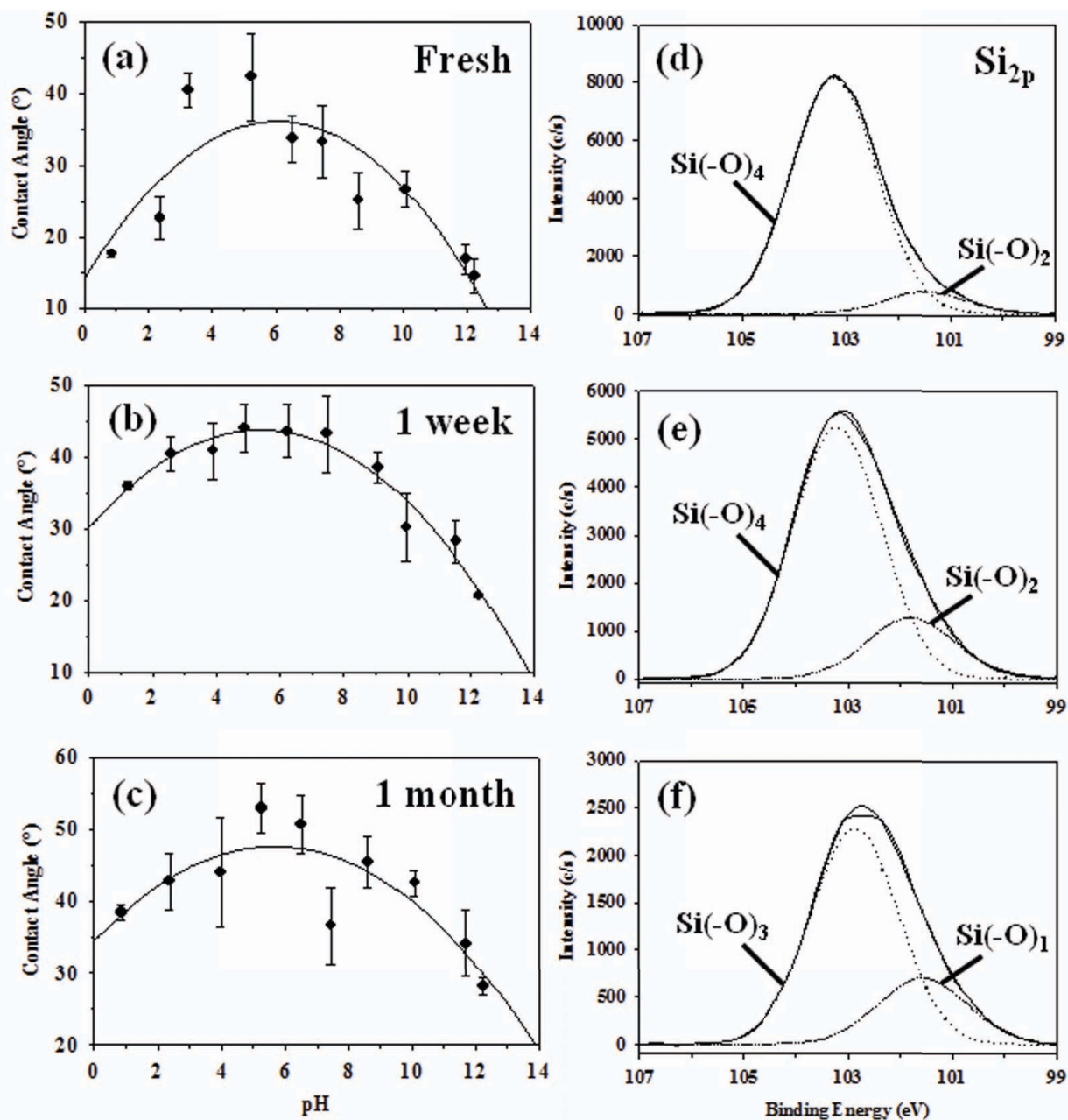


**Figure 5.4** Static contact angle titration data for a SiO<sub>x</sub>N<sub>y</sub> substrate placed in the coil region of a 100% H<sub>2</sub>O vapor plasma for 10 min ( $P = 150$  W) aged for (a) < 1 day (fresh); (b) 1 week; and (c) 1 month. The lines are second order polynomial fits to the data, yielding the IEP values reported in Table 5.2. Corresponding high-resolution Si<sub>2p</sub> XPS spectra for the same substrates are shown in panels d-f.

were those treated in the coil region with  $P = 150$  W. The sodium likely arises from etching of the walls of the glass reactor.<sup>32-34</sup>

For all substrates, the amount of oxygen increases upon treatment and does not change appreciably upon aging. Notably, the O/Si ratio for the untreated  $\text{SiO}_x\text{N}_y$  substrate is 1.4, for substrates treated in the  $P = 50$  W  $\text{H}_2\text{O}$  plasma, O/Si increases to  $\sim 1.6$ , regardless of position in the reactor, and decreases slightly upon aging. For substrates treated with  $P = 150$  W plasmas, however, the O/Si ratio is  $\sim 2.0$  for substrates placed directly in the coil and  $\sim 1.8$  for those placed 5 cm downstream from the coil. Although these values also decrease slightly upon aging, the observation that the O/Si ratio approaches that for  $\text{SiO}_2$  is a strong indicator that either nitrogen is being preferentially removed from the substrate or the walls of the glass reactor are being etched and redeposited on the substrates in plasmas with higher  $P$ .

Figures 5.4d-f show  $\text{Si}_{2p}$  high-resolution XPS spectra for substrates treated in the coil region of a 100%  $\text{H}_2\text{O}$  plasma ( $P = 150$  W). For the freshly treated substrate, the  $\text{Si}(-\text{O})_4$  moiety dominates the spectrum, with a small contribution from  $\text{Si}(-\text{O})_2$ , indicating a highly oxidized surface. Upon aging, the relative contributions of the  $\text{Si}(-\text{O})_4$  and  $\text{Si}(-\text{O})_2$  binding environments change slightly. After 1 month, however, the  $\text{Si}_{2p}$  peak has shifted appreciably, and the spectrum contains only contributions from  $\text{Si}(-\text{O})_3$  and  $\text{Si}(-\text{O})_1$  binding environments, similar to the untreated surface. For the aged material, however, elemental composition data show the surface carbon content increases by a factor of 3, Table 5.3. Notably, the  $\text{C}_{1s}$  spectrum for the aged surface (not shown) contains multiple binding environments assignable to C-C/C-H, -C-O, and  $-\text{C}=\text{O}$  moieties, indicating some

of the oxygen likely resides in a oxygenated hydrocarbon surface layer rather than the SiO<sub>2</sub> network.

**NH<sub>3</sub> Plasma Treatments.** CA titration data for NH<sub>3</sub> plasma treated SiO<sub>x</sub>N<sub>y</sub> substrates ( $P = 50$  W, 5 cm from the coil) are shown in Figure 5.5 along with the corresponding Si<sub>2p</sub> high resolution XPS spectra. Similar to results for the other two plasma systems, the CA<sub>max</sub> values measured for plasma treated samples were significantly lower than the untreated sample, Figures 5.5a-c. With the NH<sub>3</sub> plasma treatments, however, the CA<sub>max</sub> values decreased much more substantially to 30-40° for freshly treated substrates, Table 5.3. Upon aging, the contact angles stayed fairly constant, with the exception of that for substrates placed in the coil at  $P = 150$  W. The average IEP value for freshly treated substrates was slightly basic, which decreased after 1 week, but reverted back to the more basic value after 1 month, Table 5.3.

Elemental composition data for SiO<sub>x</sub>N<sub>y</sub> substrates treated with 100% NH<sub>3</sub> plasmas are also provided in Table 5.3. Results for this system look remarkably similar to those for the Ar plasma treatments with respect to changes in carbon content upon treatment and subsequent recovery due to adventitious carbon. Moreover, the Si and O content remains relatively stable upon treatment. In the NH<sub>3</sub> system, however, the nitrogen content of the samples is not depleted by plasma treatment. Indeed, for most conditions, the amount of nitrogen present at the surface does not change appreciably, as was observed in the H<sub>2</sub>O (g) plasma system. This may indicate plasma nitrogen replenishes surface nitrogen or that the NH<sub>3</sub> plasma does not promote etching. In a few samples, we observe incorporation of Na and trace amounts of F, which are likely due to etching of the reactor walls (Na) and residual fluorocarbon contamination in the system (F).

**Table 5.2** XPS elemental compositions, IEP, and CA values for H<sub>2</sub>O plasma treated SiO<sub>x</sub>N<sub>y</sub> substrates<sup>a</sup>

Conditions	Age	% O	% Si	% N	% C	IEP	CA (°)
Untreated	—	41.7 ± 0.1	29.5 ± 0.2	14.5 ± 0.5	14.4 ± 0.6	amphoteric	73.6 ± 3.2
Coil, 50 W	Fresh	53.2 ± 0.3	31.9 ± 0.1	9.2 ± 0.1	5.8 ± 0.6	5.9 ± 0.1*	27.7 ± 0.3
	1 week	51.5 ± 0.1	31.1 ± 0.1	9.2 ± 0.1	8.3 ± 0.1	5.5 ± 0.1	38.2 ± 0.2
	1 month	45.7 ± 0.9	29.4 ± 0.0	9.6 ± 0.5	15.5 ± 1.5	7.3 ± 0.1	40.4 ± 0.2
Coil, 150 W	Fresh <sup>b</sup>	60.0 ± 0.2	30.5 ± 0.4	2.7 ± 0.1	5.3 ± 0.4	6.0 ± 0.1*	38.7 ± 0.2
	1 week <sup>b</sup>	56.1 ± 0.6	27.9 ± 0.5	2.5 ± 0.3	10.7 ± 1.1	6.1 ± 0.1*	43.6 ± 0.2
	1 month	52.8 ± 0.9	28.3 ± 0.3	5.0 ± 0.3	13.9 ± 0.6	5.6 ± 0.1*	38.0 ± 0.2
5 cm, 50 W	Fresh	51.5 ± 0.1	31.2 ± 0.4	11.0 ± 0.1	6.4 ± 0.1	5.6 ± 0.1	49.0 ± 0.2
	1 week	49.8 ± 0.6	30.8 ± 0.2	10.7 ± 0.4	8.8 ± 1.1	6.3 ± 0.1*	39.0 ± 0.1
	1 month	44.5 ± 1.1	30.9 ± 0.4	11.6 ± 0.8	13.0 ± 2.3	7.0 ± 0.1*	40.0 ± 0.2
5 cm, 150 W	Fresh	58.1 ± 0.6	31.7 ± 0.6	6.8 ± 0.1	3.5 ± 1.3	5.6 ± 0.1*	38.1 ± 0.2
	1 week	55.2 ± 0.3	30.1 ± 0.1	6.8 ± 0.4	8.0 ± 0.7	6.2 ± 0.1*	39.5 ± 0.2
	1 month	49.7 ± 0.7	29.4 ± 0.0	7.9 ± 0.8	13.0 ± 0.1	7.4 ± 0.1*	37.7 ± 0.2

<sup>a</sup>Error shown is 1 standard deviation of the mean unless otherwise indicated. Error listed as two standard deviations of the mean is indicated with an asterisk. <sup>b</sup>Small amount of Na present, between 1.7 and 2.9 %

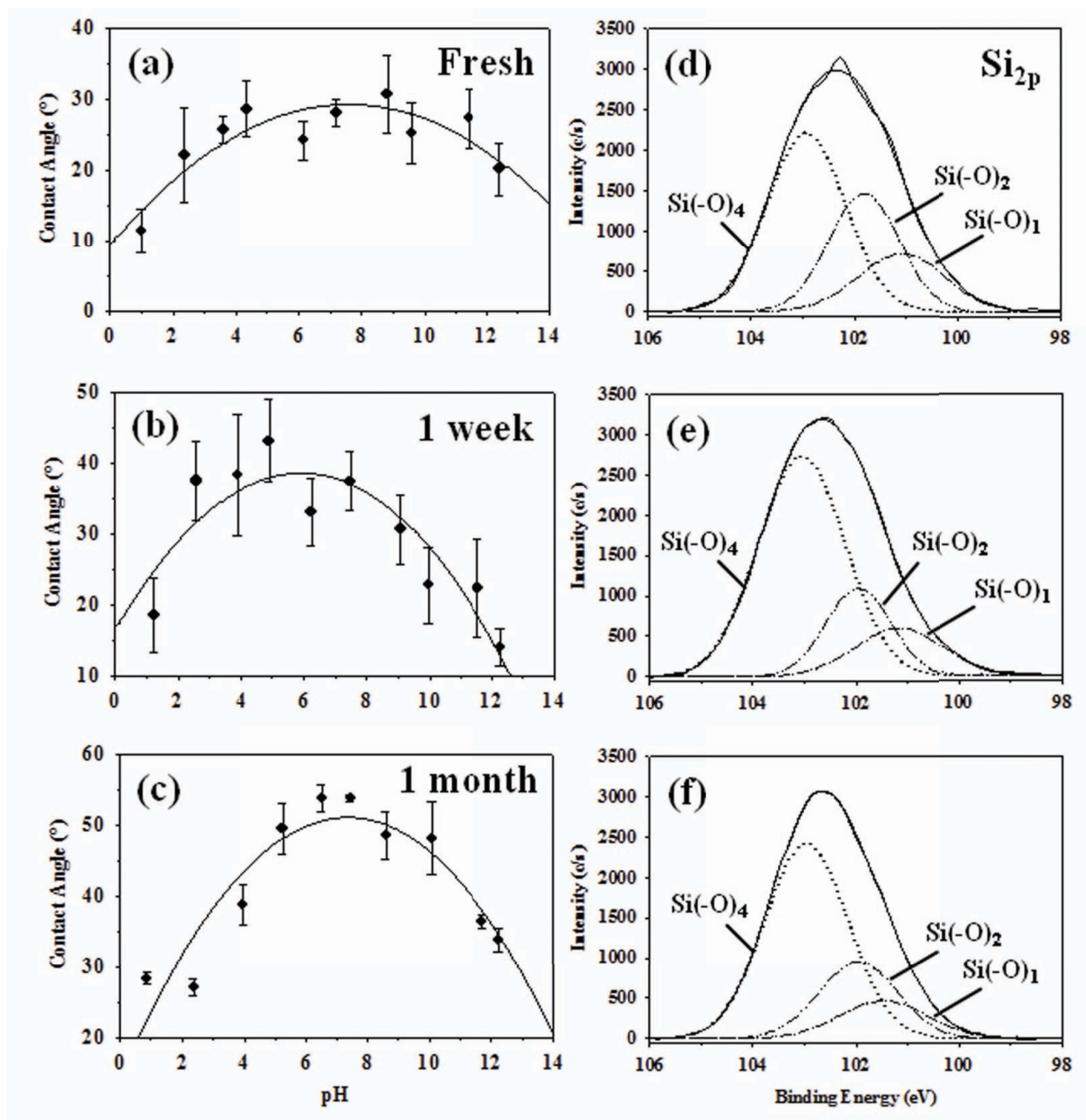


**Figure 5.5** Static contact angle titration data for a SiO<sub>x</sub>N<sub>y</sub> substrate placed 5 cm downstream from the coil and treated in a 100% NH<sub>3</sub> plasma for 10 min with  $P = 50$  W and aged for (a) < 1 day (fresh); (b) 1 week and (c) 1 month. The lines are second order polynomial fits to the data, yielding the IEP values in Table 5.3. Corresponding high-resolution Si<sub>2p</sub> XPS spectra for the same substrates are shown in panels d-f.

**Table 5.3** XPS elemental compositions, IEP, and CA values for NH<sub>3</sub> plasma treated SiO<sub>x</sub>N<sub>y</sub> substrates<sup>a</sup>

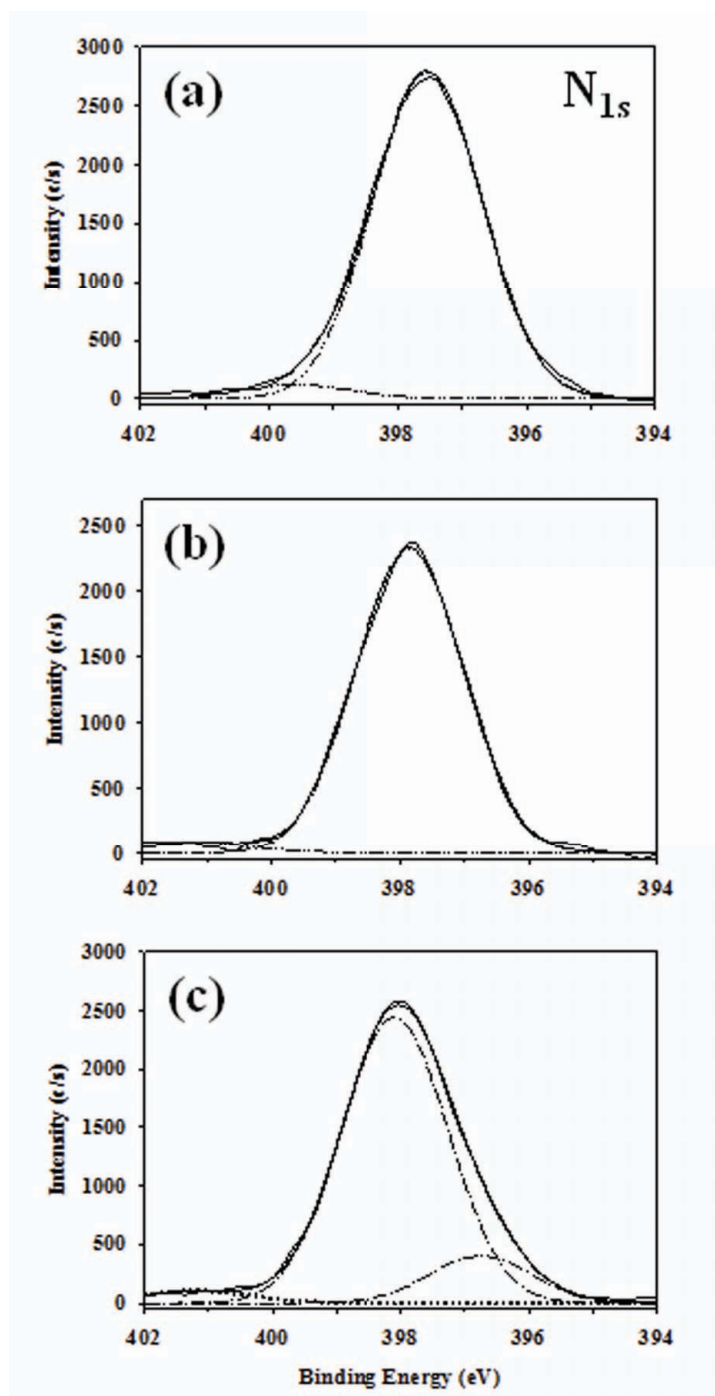
Conditions	Age	% O	% Si	% N	% C	IEP	CA (°)
Untreated	—	41.7 ± 0.1	29.5 ± 0.2	14.5 ± 0.5	14.4 ± 0.6	amphoteric	73.6 ± 3.2
Coil, 50 W	Fresh <sup>c</sup>	46.5 ± 1.5	32.7 ± 0.7	14.5 ± 0.8	5.4 ± 0.0	8.3 ± 0.1	36.5 ± 0.2
	1 week <sup>c</sup>	46.0 ± 2.3	31.9 ± 0.9	13.3 ± 2.3	8.7 ± 0.6	6.1 ± 0.1	36.6 ± 0.2
	1 month <sup>c</sup>	46.0 ± 1.5	28.1 ± 0.0	10.5 ± 0.1	15.2 ± 1.6	8.0 ± 0.1	41.7 ± 0.4
Coil, 150 W	Fresh <sup>b</sup>	48.7 ± 0.8	29.6 ± 0.5	11.0 ± 0.1	6.0 ± 0.4	7.6 ± 0.1	39.7 ± 0.2
	1 week <sup>b</sup>	47.8 ± 2.1	29.0 ± 0.1	11.1 ± 1.6	7.9 ± 3.3	6.4 ± 0.1 <sup>*</sup>	32.6 ± 0.2
	1 month <sup>b</sup>	46.5 ± 0.4	28.1 ± 0.6	10.8 ± 0.5	12.9 ± 0.1	7.3 ± 0.1 <sup>*</sup>	51.1 ± 0.2
5 cm, 50 W	Fresh <sup>d</sup>	48.7 ± 0.2	32.5 ± 0.1	13.6 ± 0.3	4.4 ± 0.1	6.5 ± 0.1 <sup>*</sup>	42.3 ± 0.1
	1 week <sup>c</sup>	48.6 ± 0.0	31.7 ± 0.5	12.7 ± 0.4	7.1 ± 0.8	6.6 ± 0.1 <sup>*</sup>	39.2 ± 0.2
	1 month <sup>c</sup>	47.9 ± 0.4	29.5 ± 0.2	11.6 ± 0.1	10.6 ± 0.5	5.6 ± 0.2	36.2 ± 0.3
5 cm, 150 W	Fresh <sup>c</sup>	45.2 ± 0.0	31.9 ± 0.1	15.8 ± 0.1	7.0 ± 0.1	7.6 ± 0.1 <sup>*</sup>	28.7 ± 0.2
	1 week <sup>c</sup>	43.5 ± 0.6	30.7 ± 0.5	14.8 ± 0.2	11.0 ± 0.9	7.2 ± 0.1 <sup>*</sup>	32.3 ± 0.2
	1 month <sup>c</sup>	43.7 ± 0.1	29.3 ± 0.3	14.5 ± 0.4	12.5 ± 0.7	4.3 ± 0.2	33.2 ± 0.1

<sup>a</sup>Error shown is 1 standard deviation of the mean unless otherwise indicated. Error listed as two standard deviations of the mean is indicated with an asterisk. <sup>b</sup>Small amount of Na present, between 1.8 and 4.9 %. <sup>c</sup>Small amounts of F present, 1% or less. <sup>d</sup>Contained ~1.5% F.

$\text{Si}_{2p}$  high resolution XPS spectra for  $\text{SiO}_x\text{N}_y$  substrates treated in a 100%  $\text{NH}_3$  plasma ( $P = 50$  W, 5 cm downstream) are shown in Figure 5.5. For both freshly treated and aged substrates, the three silicon binding environments present are  $\text{Si}(-\text{O})_4$ ,  $\text{Si}(-\text{O})_2$ , and  $\text{Si}(-\text{O})_1$ . After 1 week, the  $\text{Si}(-\text{O})_4$  binding environment increases significantly (from ~40% to 60%) and becomes the dominant moiety. Very little change is observed in the  $\text{Si}_{2p}$  spectra from 1 week to 1 month of aging. For consistency, we have made these peak assignments based on an oxidized silicon environment. Cova et al. have determined, however, that for  $\text{SiO}_x\text{N}_y$  substrates, up to 15  $\text{Si}_{2p}$  binding environments could exist, some of which are based on a fully nitrated material.<sup>35,36</sup> For example, the binding environment labeled as  $\text{Si}(-\text{O})_1$  in Figure 5.5f has the same binding energy as  $\text{Si}(-\text{N})_3$ , which may better reflect the actual surface composition for the  $\text{NH}_3$  plasma treated surfaces.

Given that the nitrogen content of the substrates remains high upon treatment in the  $\text{NH}_3$  plasmas, Table 5.3, we examined the  $\text{N}_{1s}$  high resolution XPS spectra for these materials, Figure 5.6. Spectra for freshly treated and 1 week aged substrates each contain two binding environments, with a dominant binding environment around 397.5 eV and small contributions from peaks at 399.6 (fresh) and 401.1 eV (1 week). After 1 month of aging, however, the  $\text{N}_{1s}$  spectrum looks similar to that for the untreated substrate, consistent with the compositional data in Table 5.3

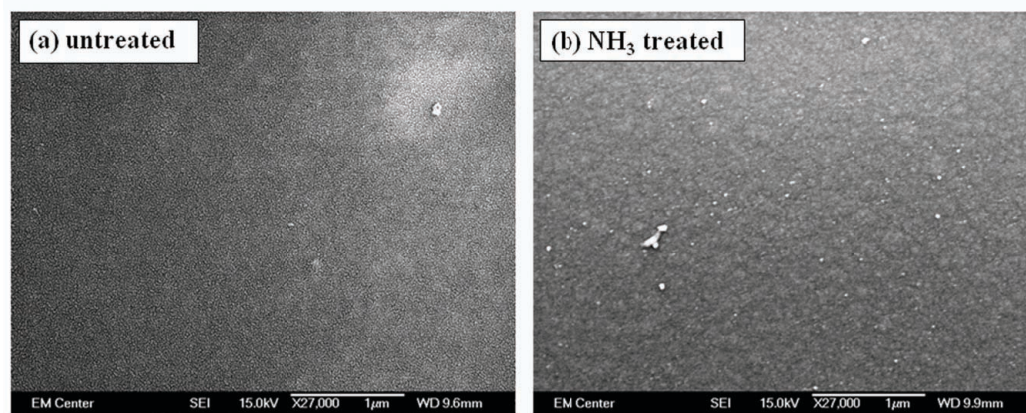
**Additional analyses.** SEM images of the untreated  $\text{SiO}_x\text{N}_y$  substrate and a substrate subjected to arguably the harshest conditions employed here, namely the 150 W  $\text{NH}_3$  plasma with the substrate placed in the coil region of the plasma, are shown in



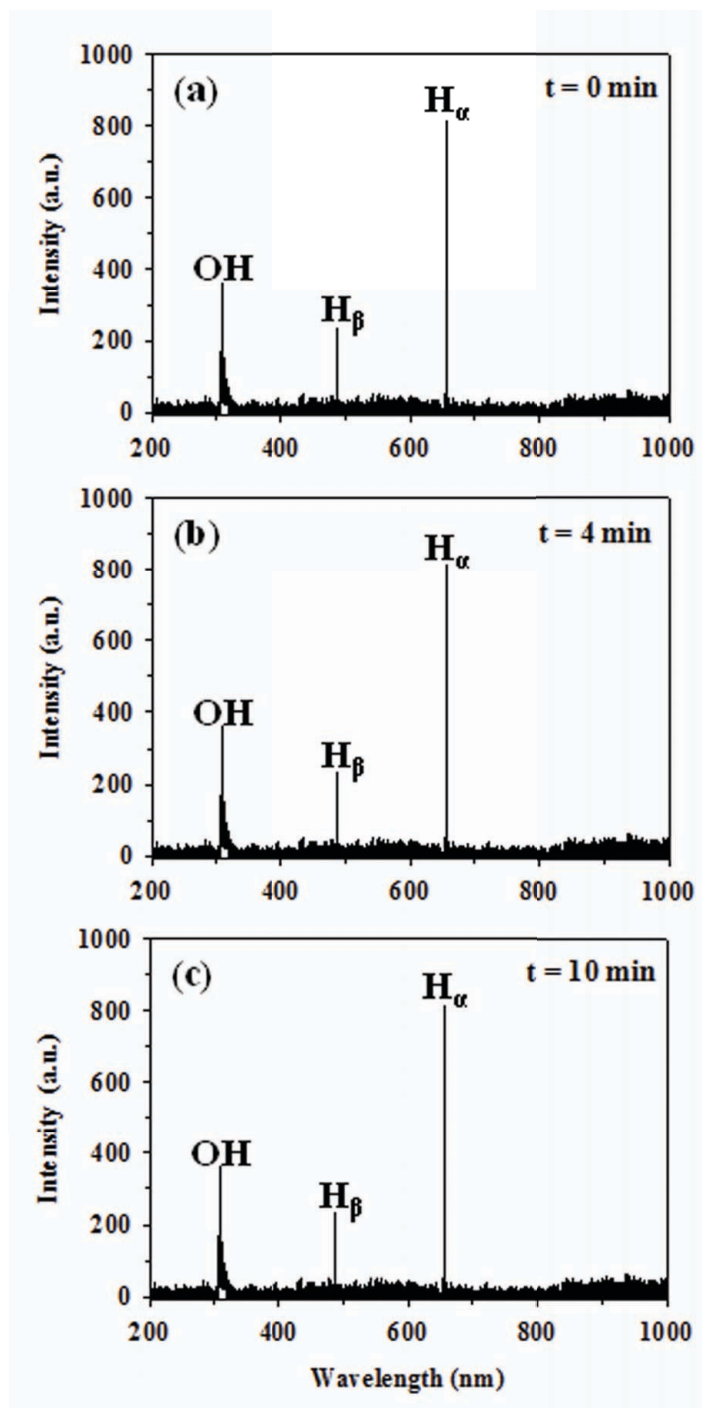
**Figure 5.6** High-resolution  $N_{1s}$  XPS spectra for  $SiO_xN_y$  substrates placed 5 cm downstream from the coil and treated with a 100%  $NH_3$  plasma for 10 min ( $P = 50$  W), followed by aging of (a) < 1 day (fresh); (b) 1 week; and (c) 1 month.

Figure 5.7. As can be seen from these images, the morphology of the substrate remains unchanged upon treatment, with no detectable pitting or craters on the surface, even at the highest magnifications. No physical damage was observed for any plasma system (Ar, H<sub>2</sub>O, and NH<sub>3</sub>), regardless of substrate location or applied rf power, suggesting the changes in CA data are the result of changes in surface composition and do not reflect changes in surface morphology.

To determine if the interaction of the plasma (specifically H<sub>2</sub>O) with the SiO<sub>x</sub>N<sub>y</sub> substrates resulted in substantial etching and thus formation of volatile products, we also examined the gas-phase chemistry using OES to probe the 100% H<sub>2</sub>O vapor plasma. For these measurements, we used the most intense conditions, with a substrate placed in the coil region and  $P = 150$  W. OES spectra, Figure 5.8, were collected essentially immediately after igniting the plasma, 4 min into the treatment time, and immediately prior to ending the experiment (i.e. 10 min). From the OES, the only species present arise from the dissociation of H<sub>2</sub>O (H<sub>α</sub> at 656.5 nm, H<sub>β</sub> at 486.1 nm, and OH at 308.9 nm); thus, we can conclude there are no contaminating species in the source gas. More importantly, we do not observe formation of atoms or molecules that might be attributed to removal of Si-containing surface species. This agrees nicely with the SEM results described above, specifically that no etching or other substantial physical damage is occurring during plasma treatment. These results also suggest the XPS elemental compositions measured (Tables 5.1-5.3) arise solely from the surface modification process, and not from physical sputtering and redeposition of the surface or the walls of the reactor.



**Figure 5.7** SEM images of (a) an untreated  $\text{SiO}_x\text{N}_y$  substrate; and (b) a  $\text{SiO}_x\text{N}_y$  substrate treated in the coil region of a 100%  $\text{NH}_3$  plasma ( $P = 150$  W). The scale bar represents  $1\mu\text{m}$ .



**Figure 5.8** OES data collected using a 100% H<sub>2</sub>O vapor plasma with a SiO<sub>x</sub>N<sub>y</sub> substrate placed in the coil region of the plasma and  $P = 150\text{W}$ . The spectra were acquired (a) immediately after plasma ignition; (b) after 4 min; and (c) at the end of the 10 min treatment time.

### 5.3 Discussion

Surface properties of materials control a wide range of processes, including particulate contamination, adhesion, heterogeneous catalysis, and corrosion. For many of these processes, it is a combination of properties that dictate the overall behavior of the surface. For metal and metal oxide surfaces, acid-base interactions (e.g. electron acceptor/donor reactions), surface charge, and oxide layer composition can control formation of electric double layers in solution as well as formation of air-induced oxides, and accumulation of particulates at solid-liquid interfaces.<sup>8,22,37</sup> Yet, understanding how surface properties such as contact angle, surface charge and composition are related to each other is a complex issue that is not easily deconstructed.

The results presented here for plasma treatment of an oxynitride surface examine the interplay between contact angle, surface charge (IEP), acid-base nature, and chemical composition along with the evolution of these surface properties over time. The three plasma treatments were chosen to explore the effects of (1) an inert gas treatment (100% Ar), wherein the expected chemical changes should be related primarily to physical interactions and/or exposure to atmosphere upon treatment; (2) a plasma system that is known to oxidize surfaces via the introduction of hydrophilic hydroxyl and carboxyl groups (100% H<sub>2</sub>O); and (3) a system that should serve to introduce hydrophilic basic (amine) groups (100% NH<sub>3</sub>). All three systems succeeded in lowering the contact angle of the SiO<sub>x</sub>N<sub>y</sub> substrates, clearly creating substantially more hydrophilic surfaces, with the greatest change occurring for NH<sub>3</sub> plasmas. The induced changes in CA in all systems can be considered semi-permanent at a minimum as they persisted over some period of time. In the Ar plasma system, the CA increases noticeably during the 1 month

aging period, but does not return to that of the untreated substrate. The change with time can be at least partially attributed to the return of adventitious surface carbon. In the other systems, the CA values do not change appreciably over time for most treatment conditions. This suggests the observed CA changes are primarily related to chemical changes in the surface as a result of plasma treatment.

The XPS data, Tables 5.1-5.3, support this hypothesis. For example, we employed cleaning methods that significantly altered the initial surface chemistry, but after treatment with a 100% H<sub>2</sub>O(g) plasma, the substrates had virtually the same chemical composition. Moreover, cleaned and “as received” samples were remarkably similar in chemical composition after H<sub>2</sub>O(g) plasma treatment, suggesting cleaning is not necessary to achieve the desired surface modification. Although cleaning could be seen as a more accurate representation of the SiO<sub>x</sub>N<sub>y</sub> surface, our results clearly show that regardless of the initial substrate, the plasma modification process controls the final chemistry. If plasma processes such as those described here were to be incorporated in commercial applications, the elimination of processing steps (such as cleaning) would be advantageous, as would be the ability to store samples under ambient conditions.

The primary effect of the Ar plasma treatment is removal of adventitious carbon and selective physical etching of surface nitrogen, Table 5.1. Moreover, samples treated under the mildest conditions (i.e. 5 cm downstream,  $P = 50$  W), arguably where the least amount of cleaning or etching would occur, indeed show the smallest change in carbon and nitrogen content. We also measured the most basic IEP values for substrates treated under these conditions, suggesting these surfaces have developed a more positive surface charge character. In contrast, the chemical changes induced by 100% H<sub>2</sub>O(g) and 100%

NH<sub>3</sub>(g) plasma treatments, Tables 5.2 and 5.3, generally appear to be more stable, with little changes in composition over the aging period. Likewise, the CA values do not change substantially with time. In many respects, the observed chemical changes upon treatment in these two systems were predictable based on previous studies.<sup>14,16,17</sup> Specifically, the H<sub>2</sub>O plasmas oxidize substrates and the NH<sub>3</sub> plasmas largely resulted in nitrogen-rich surfaces. Moreover, the lack of evidence in our SEM and OES data for physical sputtering of the reactor walls or substrates further substantiates that CA changes are related to chemical changes and not to morphological changes in the substrates.

As noted above, Chau and Porter<sup>8</sup> derived a relationship based on Young's equation and the related thermodynamics of surfaces and interfaces, determining there is a maximum in the CA (or minimum in  $\cos\theta$ ) at the point of zero surface charge, the IEP. Others have also used the surface IEP to establish the acid-base character of metal oxide surfaces in solution.<sup>2</sup> Specifically, if the excess surface charge is positive, the metal oxide acts as a base, whereas negative excess surface charge indicates an acidic surface. Here, this means that if the IEP value goes up, the surface charge character is becoming more positive, whereas a negative shift indicates an increase in negative surface charge character. For example, NH<sub>3</sub> plasma treatments should result in the introduction of positive surface charges, and a concomitant increase in IEP. If the treated samples aged via surface oxidation, we might then predict that the IEP values would decrease over time as a result of a variety of processes that could be occurring upon exposure to atmosphere. A cursory examination of the data presented in Tables 5.1-5.3 appears to support this hypothesis as the IEP values for the 1 month aged samples are all lower than those for freshly treated samples. If, however, we include both the Table 5.3 data for substrates

aged 1 week and the data from the other two plasma systems, Tables 5.1 and 5.2, our IEP values are much less well behaved than predicted.

To further explore this, we first consider only the results for freshly-treated substrates. In each plasma system, the IEP values for freshly treated  $\text{SiO}_x\text{N}_y$  substrates lie in relatively small ranges, regardless of the plasma conditions used. The small deviations in IEP values found immediately after plasma treatment suggest a similar amount of charge accumulation on the surface with a given plasma chemistry. In the  $\text{NH}_3$  system, note that the atomic compositions also are comparable for all freshly-treated substrates, Table 5.3. Although there is less agreement in the composition data for the other systems, these deviations may result from formation of a stable oxide with  $\text{H}_2\text{O}$  plasmas and the increase in selective removal of N in Ar plasmas at high  $P$ . Our initially treated substrates are not only consistent with the literature in terms of the surface charge character, IEP, and CA values but are also independent of  $P$  and position in the reactor.

Consideration of data for aged samples becomes much more complicated as many of the data sets do not show clear trends in IEP values. For example,  $\text{SiO}_x\text{N}_y$  substrates treated in the coil region of a 50 W  $\text{NH}_3$  plasma have an IEP value of  $\sim 8.3$  immediately after treatment. A week later, the IEP dropped appreciably, and after 1 month, the value returned to that of the freshly treated substrate. Such changes result from multiple, competing processes occurring upon exposure to atmosphere, including (a) oxidation, (b) migration or reorganization of charge on the surface, and (c) reactions of long-lived radicals in the treated material. Unfortunately, we could not find any literature studies that explored the effects of aging on surface composition or IEP values of plasma-treated metal oxides or nitrides. Numerous studies have, however, examined aging behavior of

plasma-treated polymers. Although perhaps not directly applicable, some insight into our  $\text{SiO}_x\text{N}_y$  results can be gained by comparison to these studies.

Tusek and co workers studied  $\text{NH}_3$  plasma treatment of polyamide 6 films using CA and zeta potential measurements.<sup>20</sup> They found the plasma treatment introduced a positive surface charge that resulted in a higher IEP value (5.6) than for the untreated polymer (4.2). Over time, the IEP decreased substantially to 4.9, although it did not return to the original value over 14 days. This change in IEP was attributed to a combination of the positively charged surface groups migrating into the bulk polymer and surface oxidation upon exposure to atmosphere. Likewise, Lappan et al. treated a fluorinated ethylene propylene material with  $\text{NH}_3$  plasmas and found the IEP increased from  $\sim 4.2$  to 6.5 upon treatment, and then decreased to  $\sim 5$  after aging for 28 days.<sup>19</sup> Their XPS data indicated the  $\text{NH}_3$  plasma defluorinated the surface and introduced both nitrogen (11%) and oxygen (7%) functionality, the latter from atmospheric oxidation or reactions with long-lived radicals in the treated material.

Canal et al.<sup>23</sup> examined plasma surface modification of polyamide with air,  $\text{H}_2\text{O}$ , and  $\text{N}_2$  plasmas using CA titrations over a nearly 80 day aging period. The untreated polymer exhibited an amphoteric surface, with little dependence on pH of the wetting solution, similar to what we observe for untreated  $\text{SiO}_x\text{N}_y$  substrates, Figure 5.1a. Upon exposure to the  $\text{H}_2\text{O}$  plasma, the CA titration data exhibited a maximum at a pH of  $\sim 4$ , comparable to our  $\text{H}_2\text{O}$  plasma treatment results, suggesting the  $\text{H}_2\text{O}$  plasma introduces negatively charged surface species. Upon aging, however, the observed IEP for treated polyamide surfaces increased dramatically, reaching a maximum of  $\sim 7$  after 77 days. In contrast, Canal et al. also found that polyamide exposure to  $\text{N}_2$  plasmas yielded an IEP of  $\sim 10$ .

Remarkably, this did not change appreciably over the extended aging period. These authors suggest several mechanisms to explain their observations including polymer dynamics, oxidation conditions, and surface contamination, but did not provide any chemical information on the surface composition. Thus, the relationship between changes in the IEP values and surface composition of the treated and aged samples was not fully explored.

As a final comparison to literature studies, Favia and coworkers examined flat graphite substrates treated with  $\text{NH}_3$ ,  $\text{O}_2$ , and  $\text{NH}_3/\text{O}_2$  plasmas using SEM, XPS, and CA titrations.<sup>24</sup> Their XPS elemental composition data clearly demonstrated the surface density of nitrogen atoms was directly proportional to the amount of  $\text{NH}_3$  in the feed gas and CA titration data revealed that the untreated substrates were amphoteric, with treated materials all exhibiting maxima at  $\text{pH} > 7$ . Unfortunately, these data were not interpreted using polynomial fits to expressly determine IEPs of the treated substrates. Nonetheless, their CA titration results are very similar to those discussed above for polymeric substrates and those obtained here for  $\text{SiO}_x\text{N}_y$  substrates. These literature studies and our results clearly suggest that exposure to  $\text{NH}_3$  plasmas introduces nitrogen moieties and a positive surface charge character, regardless of the substrate type.

Although aging of plasma-treated polymers has been discussed extensively in the literature, mechanisms for aging of these materials are not well understood. More importantly, no studies have explicitly examined the aging behavior of plasma-treated metal oxides. Moreover, most literature studies have focused on native or atmospherically-formed metal oxide layers on metals, not metal oxynitrides like  $\text{SiO}_x\text{N}_y$ . XPS data clearly show our substrates are highly amorphous with a minimal atmospheric

oxide layer. Thus, the complexity of our material complicates characterization of the aging process. As noted above, an array of reactions can occur after plasma treatment upon exposure to atmosphere. Our high-resolution Si<sub>2p</sub> XPS spectra, Figures 5.4 and 5.5 reveal at least two processes are transpiring, oxidation and the accumulation of adventitious carbon on the surface over time. Over the aging period, contributions from the highly oxidized Si(-O)<sub>4</sub> binding environment decrease and those from Si(-O)<sub>3-1</sub> environments increase.

Individually, oxidation and accumulation of carbon can each lead to a more positive or negative surface charge character depending on atmospheric conditions; humidity, temperature and sample storage conditions.<sup>9</sup> If these two processes are occurring simultaneously, they could combine either constructively or destructively to produce a surface with greater positive charge character, greater negative charge character, or a neutral character. Given the observed changes in IEP values for the majority of our plasma treatments, it is clear that the charge character is never completely neutralized, as this would result in the creation of an amphoteric surface. What could be occurring when IEP values do not follow a particular trend is that one process dominates during the initial 1 week aging period, and another dominates in the remaining 3 weeks of the 1 month aging period. In other words, initial exposure to the atmosphere results in oxidation of the surface and over time, formation of an adventitious carbon layer dominates. To complicate matters further, it is well known that plasma processing can introduce long-lived radical species that can continue to react over very long time periods (i.e. months).<sup>21,38</sup> Although polymer substrates are much more likely to undergo reorientation or migration, it is possible that surface moieties introduced into our SiO<sub>x</sub>N<sub>y</sub> substrates by

plasma treatments become displaced over time. This could occur through charge coupling with metal atoms in the bulk material.

Considering all the components of the surface properties simultaneously can be very difficult and somewhat inconclusive based on the array of reactions going on at the surface. Some broad generalizations can, however, be made about the relationships between the various surface properties studied here. Specifically, our results from Ar plasma treatments reveal that CA and composition are closely related, whereas the relationship between IEP and chemical composition is less clear. Note that the amorphous nature of the  $\text{SiO}_x\text{N}_y$  substrates is likely a causative agent. Had a more ordered or crystalline material been used, more conclusions on the relationship between the surface charge character and the corresponding composition could be drawn. Notably, the  $\text{H}_2\text{O}$  and  $\text{NH}_3$  plasmas which contain chemically-active species resulted in more permanent changes to the surface properties than Ar plasma treatment. Presumably, this is because covalently bound functional groups have been introduced into the surface layer of the material. In addition, our aging studies clearly demonstrate the need for these types of data when utilizing plasma surface modification methods for metal oxide surfaces.

#### **5.4 Summary**

We have treated  $\text{SiO}_x\text{N}_y$  substrates with three different non-polymerizing gases that effectively modify the surface in different ways. These chemistries induce changes in surface composition, acid/base surface character, surface charge (IEP), and  $\text{CA}_{\text{max}}$  values. Ar plasma treated substrates displayed more negative surface charge character than untreated surfaces. Because Ar plasmas do not explicitly implant functional groups,

these changes were not permanent over time. In contrast, the H<sub>2</sub>O and NH<sub>3</sub> plasmas created chemical changes in the SiO<sub>x</sub>N<sub>y</sub> surfaces, reflected in their IEP values. These changes were relatively permanent and could be ascribed to the formation of a stable SiO<sub>2</sub> surface in the H<sub>2</sub>O system and a nitrogen-rich surface in the NH<sub>3</sub> system. To further understand the surface chemistry of plasma treated metal oxides and their aging effects, ongoing studies in our laboratory are currently exploring IEP and aging of plasma-treated SiO<sub>2</sub> surfaces, including zeta potential measurements.

## 5.5 References

- <sup>1</sup>N. Houbenov, S. Minko, and M. Stamm, *Macromolecules* **36**, 5897 (2003).
- <sup>2</sup>E. McCafferty, *J. Adhesion Sci. Technol.* **16**, 239 (2002).
- <sup>3</sup>E. McCafferty and J. P. Wightman, *J. Adhesion Sci. Technol.* **13**, 1415 (1999).
- <sup>4</sup>E. McCafferty and J. P. Wightman, in *Apparent and Microscopic Contact Angles*, edited by J. Drelich, J. S. Laskowski, and K. L. Mittal (VSP, Utrecht, 2000), p. 149.
- <sup>5</sup>F. Arefi-Khonsari, J. Kurdi, M. Tatoulian, and J. Amouroux, *Surf. Coat. Technol.* **142**, 437 (2001).
- <sup>6</sup>N. De Vietro, P. Favia, F. Fracassi, and R. d'Agostino, *Plasma Process. Polym.* **7**, 582 (2010).
- <sup>7</sup>H. Ardelean, S. Petit, P. Laurens, P. Marcus, and F. Arefi-Khonsari, *Applied Surface Science* **243**, 304 (2005).
- <sup>8</sup>L.-K. Chau and M. D. Porter, *J. Colloid Interface Sci.* **145**, 283 (1991).
- <sup>9</sup>E. McCafferty and J. P. Wightman, *Surf. Interface Anal.* **26**, 549 (1998).
- <sup>10</sup>J. M. Grace and L. J. Gerenser, *J. Dispersion Sci. Technol.* **24**, 305 (2003).
- <sup>11</sup>E. M. Liston, L. Martinu, and M. R. Wertheimer, *J. Adhesion Sci. Technol.* **7**, 1091 (1993).
- <sup>12</sup>W. Birch, S. Mechken, and A. Carre, in *Surface Contamination and Cleaning; Vol. 1*, edited by K. L. Mittal (VSP, New York, 2003).
- <sup>13</sup>S. Debnath, R. Ranade, S. L. Wunder, G. R. Baran, J. Zhang, and E. R. Fisher, *J. Appl. Polym. Sci.* **96**, 1564 (2005).
- <sup>14</sup>K. R. Kull, M. L. Steen, and E. R. Fisher, *J. Membr. Sci.* **246**, 203 (2005).
- <sup>15</sup>M. L. Steen, W. C. Flory, N. E. Capps, and E. R. Fisher, *Chem. Mater.* **13**, 2749 (2001).
- <sup>16</sup>M. L. Steen, L. Hymas, E. D. Havey, N. E. Capps, D. G. Castner, and E. R. Fisher, *J. Membr. Sci.* **188**, 97 (2001).
- <sup>17</sup>M. L. Steen, A. C. Jordan, and E. R. Fisher, *J. Membr. Sci.* **204**, 341 (2002).
- <sup>18</sup>J. Zhou and E. R. Fisher, *J. Nanosci. Nanotechnol.* **4**, 539 (2004).
- <sup>19</sup>U. Lappan, M. Nitschke, D. Pleul, F. Simon, and S. Uhlmann, *Plasma Polym.* **6**, 211 (2001).
- <sup>20</sup>L. Tusek, M. Nitschke, C. Werner, K. Stana-Kleinschek, and V. Ribitsch, *Colloids Surf. A* **195**, 81 (2001).
- <sup>21</sup>T. R. Gengenbach, Z. R. Vasic, R. C. Chatelier, and H. J. Griesser, *J. Polym. Sci. A: Polym. Chem.* **32**, 1399 (1994).
- <sup>22</sup>M.-G. Barthes-Labrousse, *Vacuum* **67**, 385 (2002).
- <sup>23</sup>C. Canal, R. Molina, E. Bertran, and P. Erra, *J. Adhesion Sci. Technol.* **18**, 1077 (2004).
- <sup>24</sup>P. Favia, N. De Vietro, R. Di Mundo, F. Fracassi, and R. d'Agostino, *Plasma Process. Polym.* **3**, 66 (2006).
- <sup>25</sup>I. T. Martin, B. Dressen, M. Boggs, Y.-J. Liu, C. S. Henry, and E. R. Fisher, *Plasma Process. Polym.* **4**, 412 (2007).
- <sup>26</sup>G. A. Parks, *Chem. Rev.* **65**, 177 (1964).
- <sup>27</sup>R. M. Torres-Sanchez, A. B. Garcia, and A. M. Cesio, *J. Euro. Ceram. Soc.* **16**, 1127 (1996).
- <sup>28</sup>D. E. Jan and S. Raghavan, *J. Electrochem. Soc.* **141**, 2465 (1994).
- <sup>29</sup>J. Zhang, F. Ye, D. Jiang, and M. Iwasa, *Coll. Surf. A* **259**, 117 (2005).

- <sup>30</sup>*Handbook of X-ray Photoelectron Spectroscopy: A Reference Book of Standard Spectra for Identification and Interpretation of XPS Data; Vol.*, edited by J. Chastain and R. C. King, Jr. (Physical Electronics, Inc., Eden Prairie, MN, 1995).
- <sup>31</sup>C. R. Eddy, Jr. and B. Molnar, *J. Electronic Mater.* **28**, 314 (1999).
- <sup>32</sup>N. M. Mackie, D. G. Castner, and E. R. Fisher, *Langmuir* **14**, 1227 (1998).
- <sup>33</sup>N. M. Mackie, N. F. Dalleska, D. G. Castner, and E. R. Fisher, *Chem. Mater.* **9**, 349 (1997).
- <sup>34</sup>D. J. V. Pulsipher and E. R. Fisher, *Surf. Coat. Technol.* **203**, 2236 (2009).
- <sup>35</sup>P. Cova, S. Poulin, O. Grenier, and R. A. Masut, *J. Appl. Phys.* **97**, 073518 (2005).
- <sup>36</sup>P. Cova, S. Poulin, and R. A. Masut, *J. Appl. Phys.* **98**, 094903 (2005).
- <sup>37</sup>G. W. Simmons and B. C. Beard, *J. Phys. Chem.* **91**, 1143 (1987).
- <sup>38</sup>T. T. Wakida, Keiji; Tanaka, Itsuo; Takagishi, Toru, *Textile Res. J.* **59**, 49 (1989).

## CHAPTER 6

### COMPARING ISOELECTRIC POINT AND SURFACE COMPOSITION OF PLASMA MODIFIED NATIVE AND DEPOSITED SiO<sub>2</sub> FILMS USING CONTACT ANGLE TITRATIONS AND X-RAY PHOTOELECTRON SPECTROSCOPY

This chapter contains data from a manuscript submitted to the journal *Plasma Processes and Polymers*. Isoelectric point data were collected by Kristina J. Trevino, x-ray photoelectron spectroscopy data by Brendan D. Tompkins, and FTIR data by Jeffrey C. Shearer. The manuscript was written primarily by Kristina J. Trevino, Jeffrey C. Shearer, and Ellen R. Fisher, with editorial contributions from Brendan D. Tompkins. These studies examine the surface isoelectric point, contact angle, chemical composition, film growth method and aging effects of plasma-treated native and deposited SiO<sub>2</sub>. Samples were treated with two inductively-coupled rf plasma systems, Ar and H<sub>2</sub>O, to compare the differences in the surface characteristics listed above.

## 6.1 Introduction

Metal oxide semiconductor (MOS) technology relies heavily on silicon-based materials, including high quality insulating layers of  $\text{SiO}_2$ .<sup>1</sup> Traditionally, these  $\text{SiO}_2$  layers are grown using thermal processes or wet chemistry, although a range of methods are available, including electrochemical deposition, chemical vapor deposition (CVD), physical vapor deposition (PVD), molecular epitaxy, atomic layer deposition (ALD), and plasma-enhanced CVD (PECVD) using a variety of Si precursors.<sup>2-6</sup> Although new semiconducting materials such as GaN are being explored for next generation MOS devices,  $\text{SiO}_2$  remains the insulator of choice. In non-silicon based devices, however, the adhesion between  $\text{SiO}_2$  insulating layers and the underlying semiconductor becomes a critical factor in device performance. This is aggravated by the observation that metal oxide surfaces are highly susceptible to atmospheric reactions that can alter film chemistry.<sup>7,8</sup>

Other issues revolving around the  $\text{SiO}_2$  layers in microelectronic devices include diffusion of metal ions through insulating layers and formation of silicides at metal/oxide interfaces.<sup>6,9,10</sup> Often, Si layers in these devices may have a thin native oxide, which can also play a role in defect formation and adhesion between layers. Clearly, structural and electrical properties of  $\text{SiO}_2$  films can strongly influence the effectiveness of insulating and passivating layers and these characteristics are largely controlled by the method of preparation. Notably, plasma deposited films can often mimic the properties of materials grown either naturally (e.g. native oxides) or via other film deposition methods. Although film composition may be similar, there are other film properties that may depend heavily on the methodology used to deposit the material. Indeed, several studies have found that the density of the  $\text{SiO}_2$  layer as well as the continuity of the oxide network, defect density, and other structural properties can significantly affect the occurrence of deleterious events such as metal ion diffusion or silicide formation<sup>2,9</sup> In

addition, ion bombardment of SiO<sub>2</sub> layers has been shown to increase defect density through the creation of electron/hole pairs. Holes created in such a manner diffuse to the SiO<sub>2</sub>/Si interface, resulting in charge buildup at the interface.<sup>11</sup> Again, the rates of electron/hole pair formation, hole migration and recombination depend strongly on the method used to create the oxide layer. Thus, it is critical to develop a deeper understanding of the differences in surface and structural properties of oxide films formed using different methodologies as well as how these materials interact with surface modification strategies such as wet chemical and plasma processes.

Here, we investigated the plasma surface modification of relatively thin native silicon dioxide (nat-SiO<sub>2</sub>) and silicon dioxide films deposited from a hexamethyldisiloxane (HMDSO)/O<sub>2</sub> plasma (dep-SiO<sub>2</sub>). Specifically, we focused on (1) measuring the effect that different plasma treatments have on the surface isoelectric point (IEP) of the two oxides as a measure of the surface charge of the materials and (2) the changes in chemical composition induced by plasma exposure. This work extends our recent study of plasma modification of silicon oxynitride (SiO<sub>x</sub>N<sub>y</sub>) substrates treated in similar plasma systems, wherein we measured surface IEP values using three modification strategies.<sup>12</sup> In our previous study, we found that plasma treatments generally altered the amphoteric SiO<sub>x</sub>N<sub>y</sub> substrates into more neutral to basic surfaces (i.e. IEP ≥ 7), regardless of plasma chemistry. The two plasma systems studied here, 100% Ar and 100% H<sub>2</sub>O vapor, are known to modify the surface by creating active sites and implanting hydroxyl functional groups, respectively. IEP values were obtained via contact angle titration, which provides a measure of the acid-base properties of the untreated and treated SiO<sub>2</sub> substrates. Chemical composition data were acquired using x-ray photoelectron spectroscopy (XPS) and Fourier transform infrared spectroscopy (FTIR). In addition, both IEP and chemical composition data were tracked as a function of time after plasma

treatment to determine treatment stability. Significant differences in the effects of the two plasma treatments on nat- and dep-SiO<sub>2</sub> films were observed.

## 6.2 Results

As noted in the Introduction, this work extends our previous study of isoelectric points for plasma-treated Si-based materials.<sup>12</sup> Here, we have limited our study to the comparison of two types of SiO<sub>2</sub> substrates, nat-SiO<sub>2</sub> and dep-SiO<sub>2</sub> films. These materials were treated with two different plasma systems selected for their ability to create active sites in material surfaces (100% Ar) and to potentially create more hydrophilic surfaces (100% H<sub>2</sub>O vapor). Comparison of the two different forms of SiO<sub>2</sub> reveals differences in their structural and reactivity properties.

**Untreated nat-SiO<sub>2</sub> and Ar Plasma Treatments.** The CA titration data for untreated nat-SiO<sub>2</sub> substrates, Figure 6.1a, exhibit a clear dependence on pH and are readily fit with a second order polynomial. The resulting IEP of 3.9 indicates this is a fairly acidic surface. Additionally, the surface can be characterized as somewhat hydrophobic, with a CA<sub>max</sub> of ~62°. These values are consistent with literature values for SiO<sub>2</sub>, which range from 1.5-4.0 for the IEP,<sup>20,21</sup> and 40-55° for CA<sub>max</sub>.<sup>22-24</sup> For comparison, amorphous mixed oxide surfaces such as SiO<sub>x</sub>N<sub>y</sub> behave as amphoteric surfaces, with little to no CA dependence on pH, and have higher CA<sub>max</sub> values of ~75°.<sup>12</sup> Likewise, reported IEP values for Si<sub>3</sub>N<sub>4</sub> are more basic (3.5-5.3), and are highly dependent on preparation method as well as morphology.<sup>25-27</sup>

Ar plasma treatments create active radical sites on a range of surfaces, but little work has been done to characterize resulting changes in surface charge or composition.

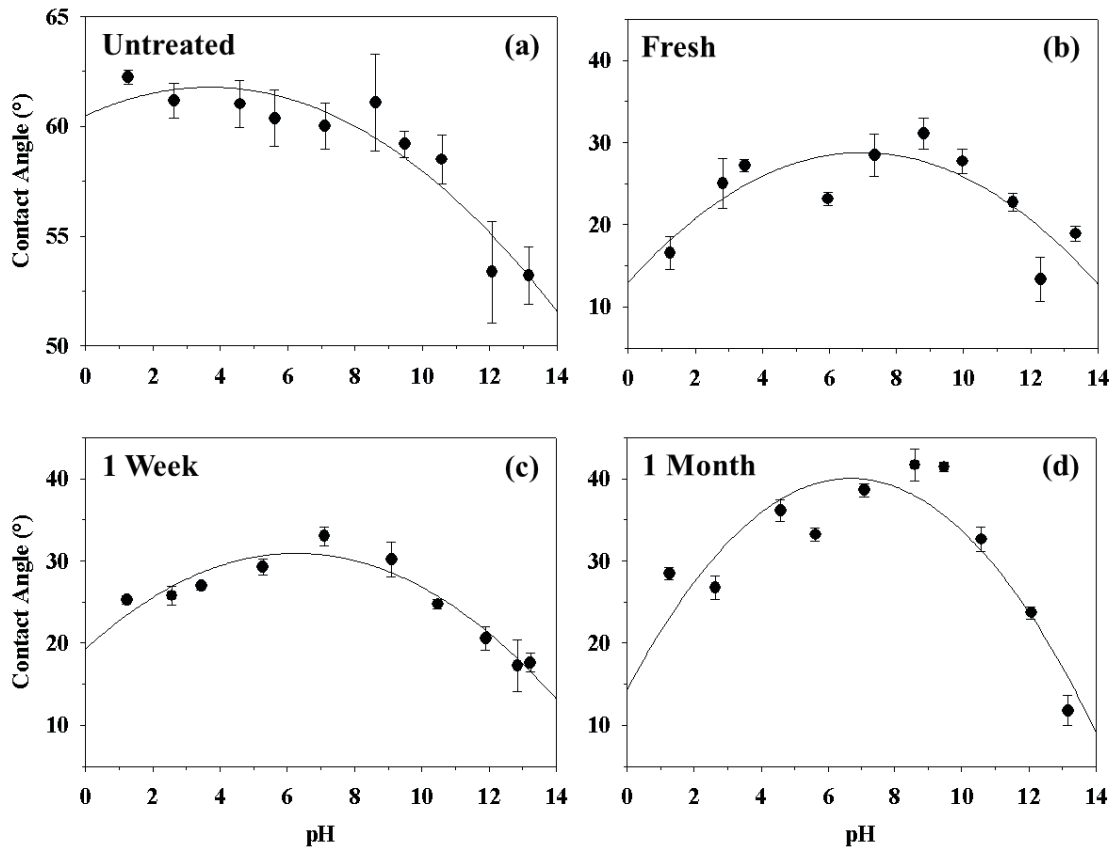


**Figure 6.1** CA titration data for nat-SiO<sub>2</sub> substrates: (a) untreated (IEP of  $3.89 \pm 0.13$ ); and treated with a 100% Ar plasma at 150 W in the coil (b) immediately after treatment; (c) 1 week after treatment; and (d) 1 month after treatment.

6.1b-d show CA titration data for a nat-SiO<sub>2</sub> substrate treated in the coil region of a 150 W 100% Ar plasma, which are representative of all nat-SiO<sub>2</sub> substrates treated with Ar plasmas, Table 6.1. In comparison to the untreated nat-SiO<sub>2</sub> substrate, the IEP for a freshly treated substrate shifts indicates a less acidic, essentially neutral surface, and the IEP remains reasonably constant over the 1 month aging period. Additionally, the second order polynomial fits to the data for the treated substrate reveal a more parabolic set of data points with clear maxima that are lower than that for the untreated nat-SiO<sub>2</sub>, with CA<sub>max</sub> ~29°. Notably, the CA<sub>max</sub> value for Ar plasma treated substrates rises to ~40° over the 1 month aging period, suggesting a semi-permanent wettability. Figure 6.2 shows SEM and AFM images of an untreated nat-SiO<sub>2</sub> substrate (Figs. 6.2a and 6.2b) and an aged, Ar plasma treated substrate (Figs. 6.2c and 6.2d). These images clearly demonstrate that the Ar plasma treatment does not significantly damage the surface, although a small degree of roughness is induced by the plasma treatment as the R<sub>rms</sub> values increase from 0.63 ± 0.03 nm for the untreated sample to 12.8 ± 0.8 nm for the treated sample. Despite this slight increase in roughness, the increased hydrophilicity suggests changes in the CA<sub>max</sub> values measured are a result of the chemical composition and not morphological changes to the surface.

High-resolution XPS spectra of the Si<sub>2p</sub> peak for untreated nat-SiO<sub>2</sub> substrates and nat-SiO<sub>2</sub> substrates treated with the same Ar plasma as above are shown in Figure 6.3. The Si<sub>2p</sub> region of the untreated nat-SiO<sub>2</sub> samples is composed of mostly Si<sup>0</sup> from the underlying substrate (67.5 ± 1.4%) with a smaller contribution from Si(-O)<sub>4</sub> (B.E. 103.8 eV, 32.5 ± 1.4%), Fig. 6.3a. Although nat-SiO<sub>2</sub> is expected to be approximately stoichiometric, the films are thin relative to the XPS sampling depth, resulting in a lower

**Table 6.1** Atomic concentrations, IEP, and CA for Ar plasma treated nat-SiO<sub>2</sub><sup>a</sup>

Conditions	Age	% C	% O	% Si	O/Si	IEP	CA <sub>max</sub> (°)
Untreated	—	12.1 ± 0.6	41.1 ± 0.2	46.7 ± 0.8	0.9 ± 0.1*	3.9 ± 0.1	61.6 ± 0.1
50 W Coil	Fresh	5.2 ± 0.8	60.8 ± 0.6	34.0 ± 0.4	1.8 ± 0.1*	8.0 ± 0.1*	28.5 ± 0.3
	1 week	7.6 ± 0.5	58.7 ± 0.5	33.8 ± 0.2	1.7 ± 0.1*	5.5 ± 0.2	25.1 ± 0.2
	1 month	15.3 ± 2.0	54.1 ± 1.6	30.5 ± 0.5	1.8 ± 0.1*	6.8 ± 0.1*	36.9 ± 0.2
50 W 5 cm	Fresh	7.0 ± 1.3	55.6 ± 0.9	37.4 ± 0.6	1.5 ± 0.1*	7.4 ± 0.1*	23.2 ± 0.2
	1 week	9.1 ± 1.8	54.4 ± 1.3	36.5 ± 0.6	1.5 ± 0.1*	6.4 ± 0.1*	26.0 ± 0.2
	1 month	17.4 ± 1.9	50.1 ± 1.3	32.5 ± 0.6	1.5 ± 0.1*	7.1 ± 0.1	35.6 ± 0.3
150 W Coil	Fresh	9.4 ± 0.5	50.2 ± 0.5	40.4 ± 0.2	1.2 ± 0.1*	7.0 ± 0.1	28.8 ± 0.2
	1 week	9.8 ± 0.2	49.6 ± 0.2	40.6 ± 0.1	1.2 ± 0.0	6.3 ± 0.1	31.0 ± 0.2
	1 month	17.0 ± 0.9	46.2 ± 0.3	36.8 ± 0.7	1.3 ± 0.1*	6.7 ± 0.1*	40.0 ± 0.2
150 W 5 cm	Fresh	9.1 ± 0.5	55.9 ± 0.4	34.9 ± 0.4	1.6 ± 0.1*	6.9 ± 0.1*	20.0 ± 0.1
	1 week	7.9 ± 1.7	56.8 ± 1.2	35.3 ± 0.5	1.6 ± 0.1*	5.8 ± 0.1	25.3 ± 0.1
	1 month	12.9 ± 0.4	53.3 ± 0.2	33.8 ± 0.3	1.6 ± 0.1*	6.9 ± 0.1*	38.3 ± 2.2

<sup>a</sup>Error shown is 1 standard deviation of the mean unless otherwise indicated. Error listed as two standard deviations of the mean is indicated with an asterisk.

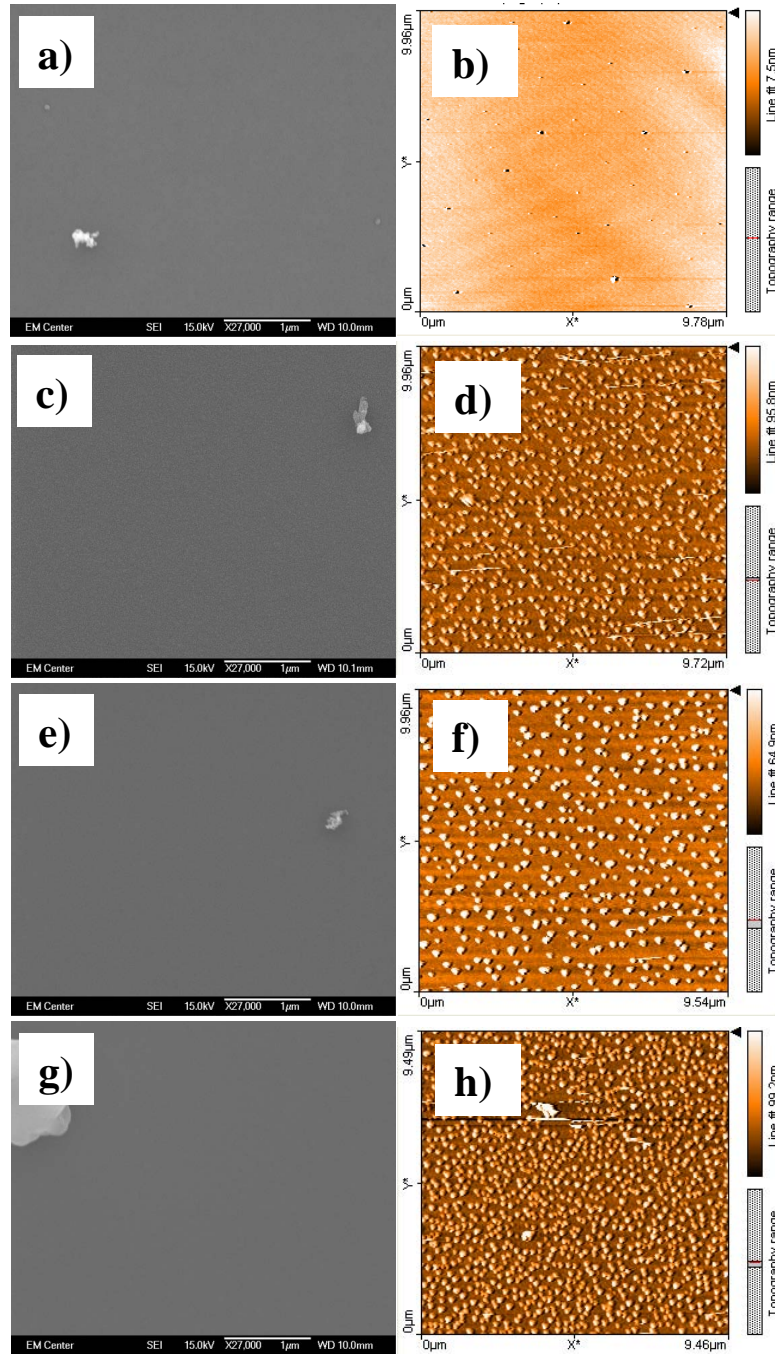


**Figure 6.2** SEM (left column) and AFM (right column) images for (a and b) untreated nat-SiO<sub>2</sub>; (c and d) 100% Ar plasma treated (150 W in the coil) nat-SiO<sub>2</sub>; (e and f) untreated dep-SiO<sub>2</sub>; and (g and h) 100% Ar plasma treated (150 W in the coil) dep-SiO<sub>2</sub> substrates.

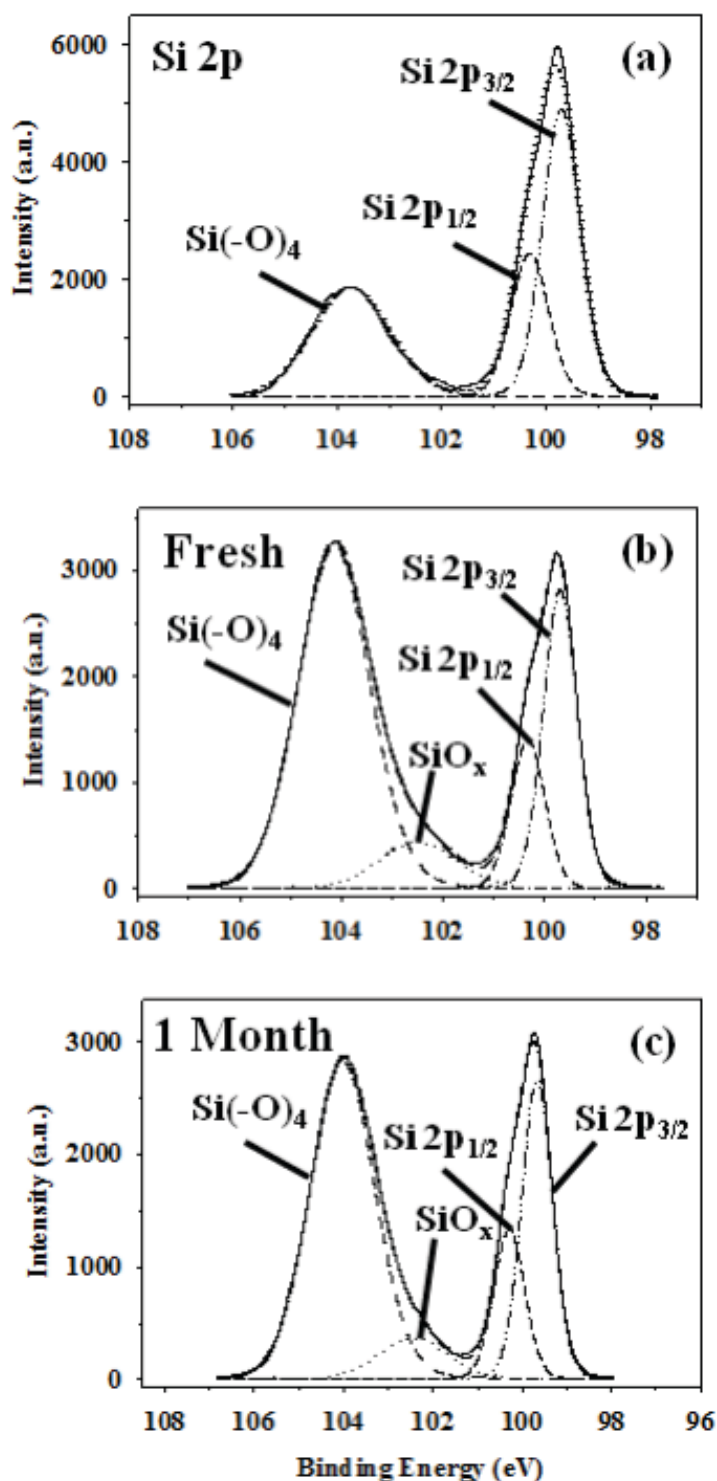


**Figure 6.3** High-resolution Si<sub>2p</sub> XPS spectra of (a) an untreated nat-SiO<sub>2</sub> substrate; and nat-SiO<sub>2</sub> substrates treated with a 100% Ar plasma at 150 W in the coil for 10 minutes (b) immediately after treatment; and (c) 1 month after treatment. The SiO<sub>x</sub> assignment corresponds to x = 1 and 2.

than stoichiometric O/Si ratio of  $\sim 0.9$ , Table 6.1, because the underlying Si substrate is also being sampled. An increase in the O/Si ratio occurs upon Ar plasma treatment, consistent with increasing surface oxidation/oxide layer thickness. This increase in the O/Si ratio remains nearly constant over the aging period, regardless of treatment conditions. Deconstruction of high resolution spectra for fresh substrates shows a much larger contribution from the oxide peak, which is a mixture of the  $\text{Si}(\text{-O})_4$  ( $56.7 \pm 0.6\%$ ) and reduced  $\text{Si}(\text{-O})_x$  ( $x = 1$  and  $2$ ,  $8.3 \pm 0.3\%$ ) binding environments, Fig. 6.3b. Generally, the amount of silicon found in an oxide environment increases with  $P$  and proximity to the coil, consistent with exposure to higher energy plasma species. As samples are aged, the contributions from different  $\text{Si}_{2p}$  binding environments are relatively constant, Fig. 6.4c.

Past studies have attempted to correlate surface acidity and basicity with shifts in XPS peaks associated with substrate film binding environments.<sup>21</sup> Small changes in the surface charging behavior during XPS analysis, which dictate shifts in the binding energy of chemical environments of a film, are believed to be sensitive to charged surface functional groups. This provides a potential connection between the IEP of a surface and the results of XPS analysis. We have attempted to test this by indexing our nat-SiO<sub>2</sub> spectra to the underlying  $\text{Si}^0$  chemical environment. Here, depth with respect to the charged surface isolates the silicon metal, allowing it to act as an internal standard. The nat-SiO<sub>2</sub> silicon oxide peak position ( $103.76 \pm 0.03$  eV) shifted to a higher binding energy upon treatment in an Ar plasma ( $104.13 \pm 0.05$  eV), reverting back to a lower binding energy during aging, regardless of processing conditions. Likewise, the  $\text{O}_{1s}$  binding energy also shifts to a higher energy upon treatment, going from 533.24 eV for

untreated nat-SiO<sub>2</sub> to 533.64 eV for the freshly treated substrate. One mechanism for relating XPS data and IEP seeks to correlate binding energy shifts in both the cation and O<sub>1s</sub> peaks for metal oxides.<sup>22</sup> This method involves two values, DM and DO, which are achieved using the following equations:

$$\text{DM (eV)} = \text{BE(cation)} - \text{BE(metal)}$$

$$\text{DO (eV)} = \text{BE(O}_{1s}\text{)} - 530.0 \text{ eV}$$

Delamar found that the sum of DM and DO are linearly correlated to the IEP values, with more basic substrates having a lower sum. In our work, DM for the untreated nat-SiO<sub>2</sub> is 3.76 and DO is 3.24, yielding a sum of 7.0 for a substrate that has an IEP of  $3.9 \pm 0.1$ . These values roughly agree with those obtained by Delamar for a SiO<sub>2</sub> substrate, 7.2 and 2.2, respectively. A similar analysis of plasma treated substrates, however, does not yield the linear relationship found by Delamar for metal oxide substrates. The values obtained for a nat-SiO<sub>2</sub> substrate treated in an Ar plasma (150 W, coil, fresh) are DM + DO = 7.8 and IEP =  $7.0 \pm 0.1$ , which is opposite of the trend found by Delamar. Thus, we do not believe our observed shifts in XPS binding energies are consistent enough to draw any meaningful conclusions merely from the XPS data. This observation is consistent with Mullins and Averbach who also acknowledge that use of such shifts in binding energy to ascribe absolute acidity/basicity to a surface is questionable.<sup>23,24</sup>

**Untreated dep-SiO<sub>2</sub> Substrates and Ar Plasma Treatments.** The dep-SiO<sub>2</sub> substrates exhibit an IEP of  $5.6 \pm 0.1$ , Fig. 6.4a, which is substantially higher than that for nat-SiO<sub>2</sub> (IEP ~ 3.9). In addition, the CA<sub>max</sub> for dep-SiO<sub>2</sub> is much lower (~40°) than that for nat-SiO<sub>2</sub> (~60°), but agrees well with literature reports of SiO<sub>2</sub> films deposited from atmospheric tetraethoxysilane (TEOS) plasmas under high flow conditions.<sup>16</sup> This

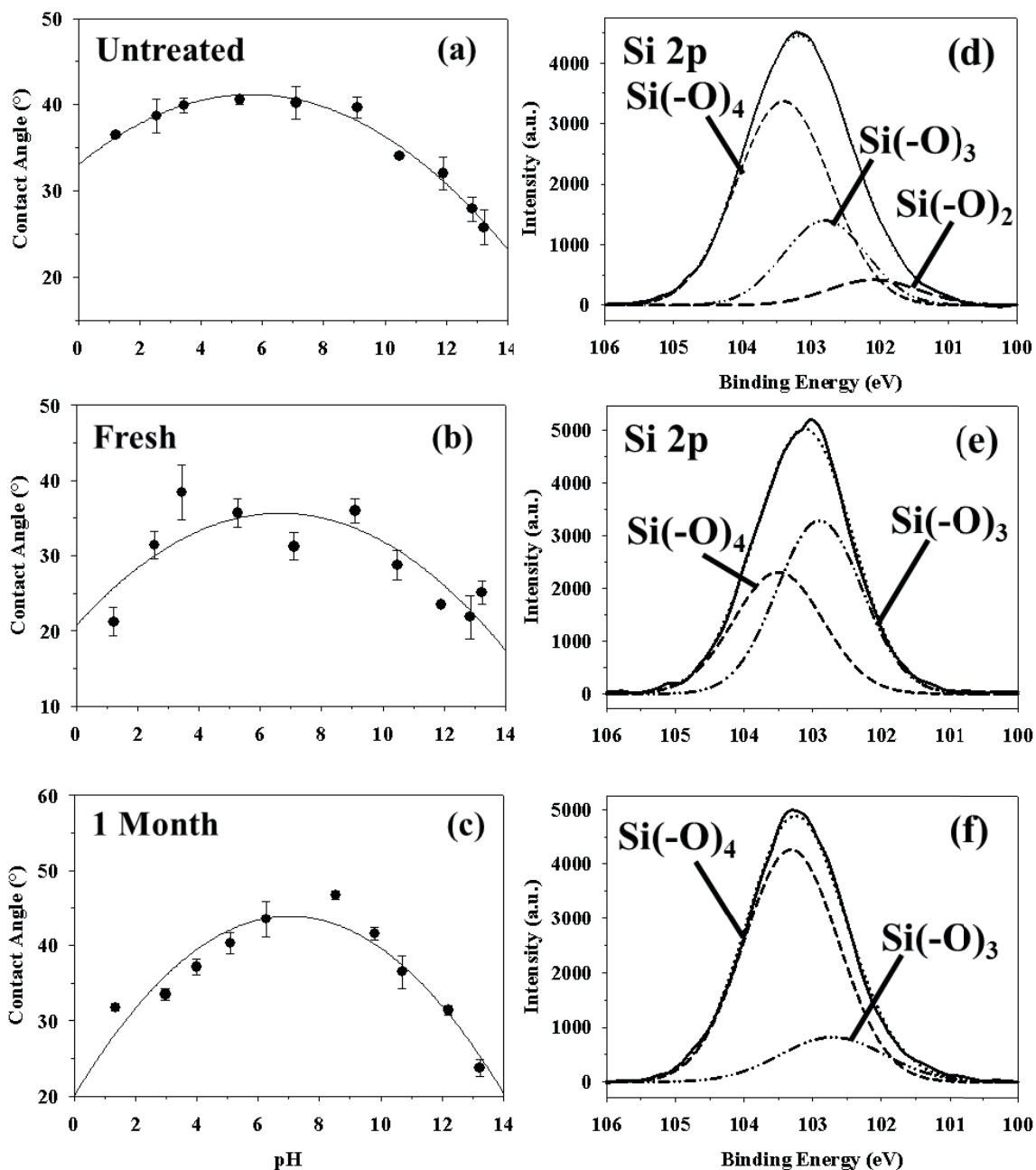


**Figure 6.4** Contact angle titration data for (a) dep-SiO<sub>2</sub> and dep-SiO<sub>2</sub> substrates treated with a 100% Ar plasma at 150 W, in the coil both (b) freshly treated and (c) 1 month aged. Corresponding high-resolution Si<sub>2p</sub> XPS spectra for the same substrates are shown in panels d-f, respectively. SEM images for untreated and 100% Ar plasma treated dep-SiO<sub>2</sub> substrates are shown as insets in panels (a) and (c), respectively.

suggests the dep-SiO<sub>2</sub> surface is negatively charged, an acidic substrate with somewhat different surface characteristics than nat-SiO<sub>2</sub>. Interestingly, IEP values for dep-SiO<sub>2</sub> substrates treated in Ar plasmas are similar to those for nat-SiO<sub>2</sub> substrates treated under the same conditions, Fig. 6.1. More importantly, the IEP values for dep-SiO<sub>2</sub> substrates do not change dramatically upon treatment or over time. Average IEPs for all Ar plasma treated dep-SiO<sub>2</sub> substrates fall in the 6.5-7.5 range with few exceptions, Table 6.2. In contrast, CA<sub>max</sub> values for Ar plasma treated dep-SiO<sub>2</sub> substrates remain relatively close to that for the untreated material (~40°). The SEM and AFM images shown in Figs. 6.2e-h reveal the dep-SiO<sub>2</sub> substrate ( $R_{\text{rms}} = 13.4 \pm 0.3$  nm) is somewhat rougher than the nat-SiO<sub>2</sub> substrate, but that little increase in roughness occurs at the plasma surface interface as  $R_{\text{rms}} = 19.5 \pm 1.5$  nm for the Ar plasma treated dep-SiO<sub>2</sub> surface; thus, similar to results for the nat-SiO<sub>2</sub> substrates, changes in CA<sub>max</sub> values are representative of changes in chemical composition of the surface, not in morphology.

Elemental composition results for untreated and Ar plasma treated dep-SiO<sub>2</sub> films are presented in Table 6.2. The elemental composition of the untreated dep-SiO<sub>2</sub> films deposited in the coil is consistent with previously reported results.<sup>25,26</sup> High resolution Si<sub>2p</sub> spectra for untreated and 100% Ar plasma treated dep-SiO<sub>2</sub> films are shown in Figs. 6.4d-f. Untreated dep-SiO<sub>2</sub> films contain Si(-O)<sub>4</sub> (62.8 ± 4.6%), Si(-O)<sub>3</sub> (28.6 ± 4.1%) and Si(-O)<sub>2</sub> (8.65 ± 0.5%), also consistent with previously reported results.<sup>25,26</sup> After treatment, the Si<sub>2p</sub> binding environment comprises Si(-O)<sub>4</sub> (41.0 ± 5.4%) and Si(-O)<sub>3</sub> (59.0 ± 5.4%). After 1 month, the binding environment breakdown shifts to Si(-O)<sub>4</sub> (77.2 ± 7.3%) and Si(-O)<sub>3</sub> (22.8 ± 7.3%), suggesting the film oxidizes further as it ages after plasma treatment. It is relevant to note here that the Si<sub>2p</sub> binding environment of a fully

**Table 6.2** Atomic concentrations, IEP, and CA for Ar and H<sub>2</sub>O plasma treated dep-SiO<sub>2</sub><sup>a</sup>

Conditions	Age	% C	% O	% Si	O/Si	IEP	CA <sub>max</sub> (°)
Untreated dep-Coil	Fresh	15.3 ± 0.3	55.6 ± 0.1	29.1 ± 0.3	1.9 ± 0.1*	5.6 ± 0.1*	41.2 ± 0.1
	1 week	14.3 ± 1.3	56.0 ± 1.6	29.7 ± 0.4	1.9 ± 0.1*	2.1 ± 1.4	58.5 ± 0.2
	1 month	16.1 ± 3.3	54.1 ± 2.3	29.9 ± 1.1	1.8 ± 0.1	2.7 ± 0.4	56.4 ± 0.2
50 W Coil Ar	Fresh	12.4 ± 0.3	56.6 ± 0.5	31.0 ± 0.2	1.8 ± 0.1*	6.5 ± 0.1	30.7 ± 0.2
	1 week	14.5 ± 0.7	55.4 ± 0.6	30.1 ± 0.5	1.8 ± 0.1*	7.5 ± 0.1	37.4 ± 0.2
	1 month	13.3 ± 1.4	57.5 ± 1.0	29.2 ± 0.9	2.0 ± 0.1*	7.0 ± 0.1*	38.1 ± 0.2
150 W Coil Ar	Fresh	12.7 ± 0.8	56.7 ± 0.6	30.7 ± 0.2	1.9 ± 0.1*	6.7 ± 0.1	35.7 ± 0.2
	1 week	14.2 ± 1.9	56.0 ± 1.5	29.9 ± 0.5	1.9 ± 0.1*	7.2 ± 0.1*	37.6 ± 0.4
	1 month	13.1 ± 0.7	56.5 ± 0.3	30.4 ± 0.4	1.9 ± 0.1*	7.0 ± 0.1*	43.9 ± 0.2
50 W Coil H <sub>2</sub> O	Fresh	13.3 ± 0.2	56.5 ± 0.3	30.2 ± 0.4	1.9 ± 0.1*	7.0 ± 0.2	21.8 ± 0.1
	1 week	12.5 ± 2.5	57.1 ± 1.7	30.3 ± 0.9	1.9 ± 0.1*	7.1 ± 0.1	25.8 ± 0.2
	1 month	14.7 ± 0.9	56.0 ± 0.5	29.3 ± 0.4	1.9 ± 0.1*	7.4 ± 0.1*	38.7 ± 0.2
150 W Coil H <sub>2</sub> O	Fresh	13.9 ± 0.7	55.7 ± 0.8	30.4 ± 0.2	1.8 ± 0.1*	5.8 ± 0.2	31.0 ± 0.2
	1 week	13.6 ± 1.0	56.1 ± 0.7	30.3 ± 0.4	1.9 ± 0.1*	6.6 ± 0.1	42.7 ± 0.2
	1 month	13.8 ± 1.8	55.9 ± 1.4	30.3 ± 0.4	1.9 ± 0.1*	7.1 ± 0.1*	49.3 ± 0.2

<sup>a</sup>Error shown is 1 standard deviation of the mean unless otherwise indicated. Error listed as two standard deviations of the mean is indicated with an asterisk.

oxidized SiO<sub>2</sub> surface with no contaminants, would theoretically have 100% of the Si in an Si(-O)<sub>4</sub> environment.

**H<sub>2</sub>O Plasma Treatments.** CA titration data for untreated nat-SiO<sub>2</sub> and for nat-SiO<sub>2</sub> substrates treated with a 100% H<sub>2</sub>O vapor plasma, Figure 6.5, yield higher IEP values for treated substrates. This trend is seen for nearly all H<sub>2</sub>O (g) plasma treated nat-SiO<sub>2</sub> substrates, Table 6.4. H<sub>2</sub>O (g) plasmas are expected to implant -OH functionality,<sup>27,28</sup> thereby creating more hydrophilic surfaces. Accordingly, CA<sub>max</sub> measurements for treated nat-SiO<sub>2</sub> substrates are nearly all more hydrophilic than those for untreated nat-SiO<sub>2</sub> (~62°). Although CA<sub>max</sub> values creep upward somewhat during the aging period, Table 4, they do not revert back to the original value of the untreated substrate, regardless of treatment conditions.

Elemental analysis results for H<sub>2</sub>O plasma treated nat-SiO<sub>2</sub> samples, Table 6.3, show similar trends to those found with Ar plasma treatments (Table 6.1). With the exception of one set of conditions (150 W, 5 cm downstream), the surface carbon content decreases slightly upon initial plasma treatment and subsequently increases as the sample is aged. This behavior is typically attributed to changes in adventitious surface carbon. The oxygen concentrations of the freshly treated samples increase compared to the untreated sample, consistent with the oxidizing nature of H<sub>2</sub>O plasmas. As the samples age, the O/Si ratio is the same within experimental error, indicating the oxide films stabilize quickly and do not continue to change over time.

High-resolution Si<sub>2p</sub> spectra for nat-SiO<sub>2</sub> treated with a H<sub>2</sub>O vapor plasma, Figure 6.6 show similar binding environments to those found in spectra of Ar plasma treated nat-

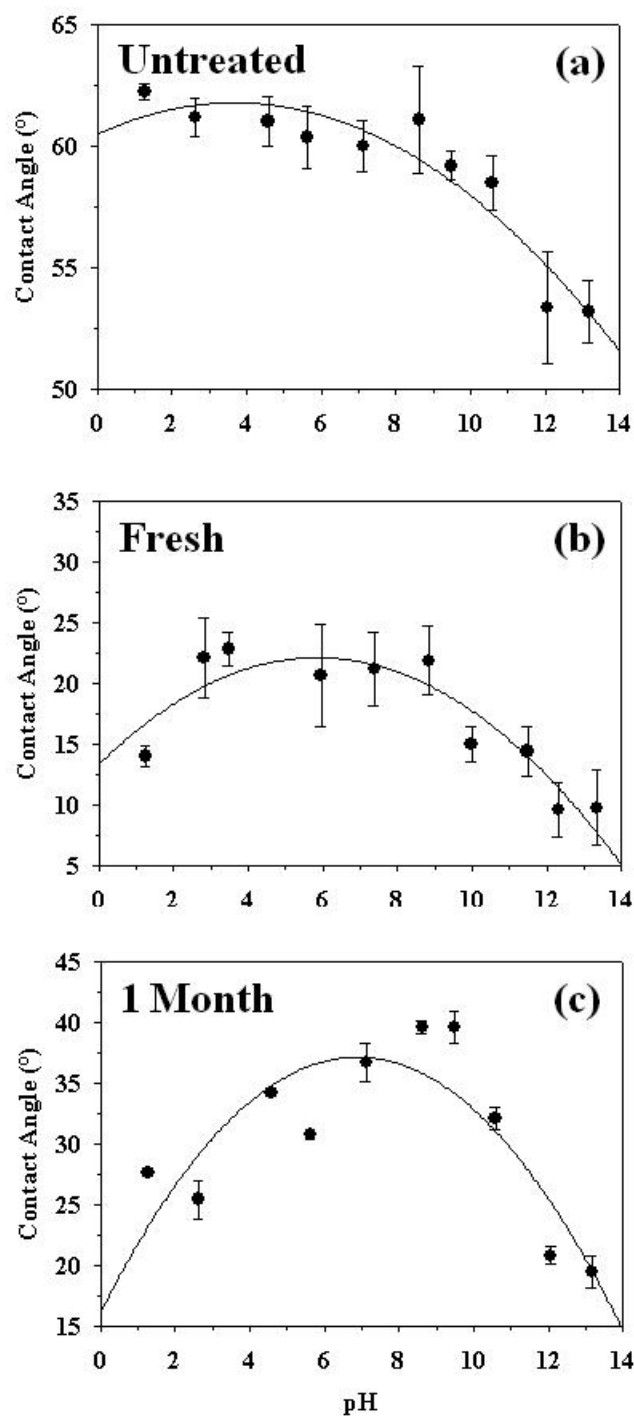


**Figure 6.5** Contact angle titration data for (a) an untreated nat-SiO<sub>2</sub> substrate; and for nat-SiO<sub>2</sub> substrates treated with a 100% H<sub>2</sub>O vapor plasma at 50 W in the coil, (b) immediately after treatment; and (c) 1 month after treatment. The untreated nat-SiO<sub>2</sub> exhibits an IEP of  $3.9 \pm 0.1$  and an average CA of  $61.6 \pm 0.1$ .

**Table 6.3** Atomic concentrations, IEP, and CA for H<sub>2</sub>O plasma treated nat-SiO<sub>2</sub><sup>a</sup>

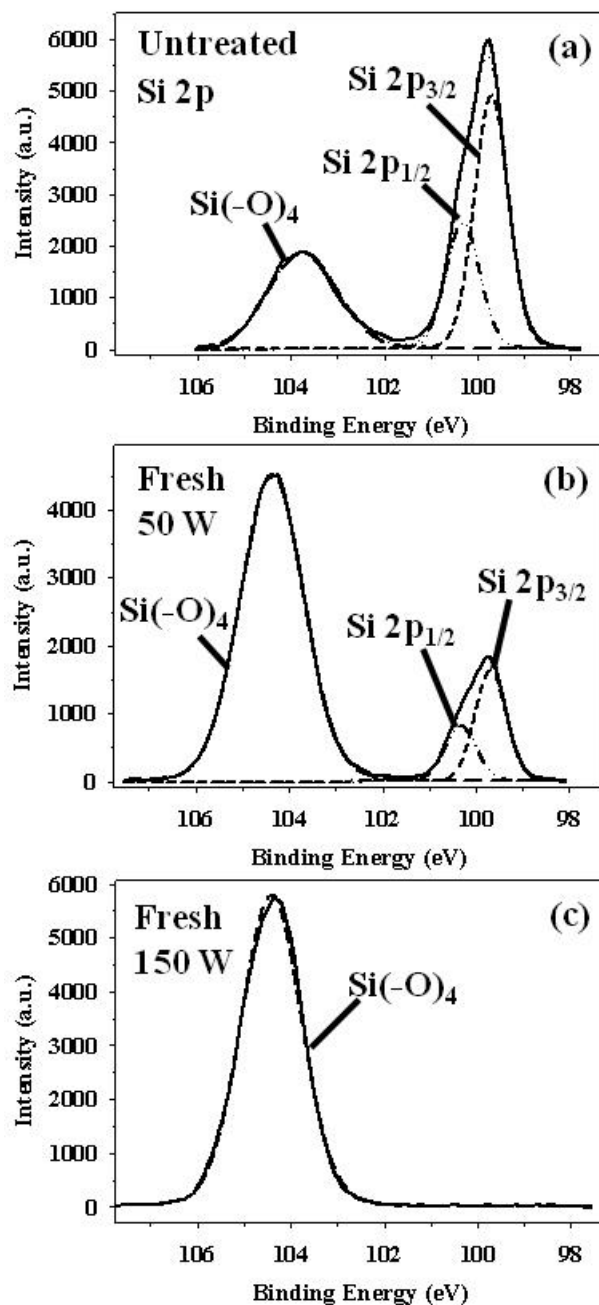
Conditions	Age	% C	% O	% Si	O/Si	IEP	CA <sub>max</sub> (°)
Untreated	—	12.1 ± 0.6	41.1 ± 0.2	46.7 ± 0.8	0.9 ± 0.1*	3.9 ± 0.1	61.6 ± 0.1
50 W Coil	Fresh	8.6 ± 0.8	57.4 ± 0.8	34.0 ± 0.7	1.7 ± 0.1*	5.6 ± 0.1	22.1 ± 0.2
	1 week	7.3 ± 0.2	58.6 ± 0.4	34.1 ± 0.3	1.7 ± 0.1*	4.3 ± 0.2	23.6 ± 0.1
	1 month	15.7 ± 0.5	53.7 ± 0.4	31.0 ± 0.3	1.7 ± 0.1*	6.9 ± 0.1	37.1 ± 0.2
50 W 5 cm	Fresh	10.2 ± 0.6	53.6 ± 0.7	36.2 ± 0.1	1.5 ± 0.1*	1.3 ± 0.4	85.4 ± 0.6
	1 week	8.3 ± 1.5	53.4 ± 0.6	38.4 ± 1.0	1.4 ± 0.1*	7.2 ± 0.1	26.9 ± 0.2
	1 month	14.6 ± 1.3	51.0 ± 0.8	34.4 ± 0.5	1.5 ± 0.1*	8.4 ± 0.1	46.6 ± 0.2
150 W Coil	Fresh	9.3 ± 0.7	59.5 ± 0.5	31.2 ± 0.4	1.9 ± 0.1*	6.7 ± 0.1*	31.9 ± 0.2
	1 week	7.0 ± 0.4	60.8 ± 0.4	32.3 ± 0.5	1.9 ± 0.1*	5.3 ± 0.1	34.5 ± 0.1
	1 month	14.9 ± 0.7	56.2 ± 0.2	29.9 ± 0.5	1.9 ± 0.1*	6.4 ± 0.1	42.3 ± 0.2
150 W 5 cm	Fresh	12.9 ± 0.2	57.0 ± 0.2	30.0 ± 0.2	1.9 ± 0.1*	4.6 ± 0.3	21.7 ± 0.2
	1 week	7.5 ± 0.1	60.5 ± 0.2	32.0 ± 0.2	1.9 ± 0.1*	5.7 ± 0.1	24.5 ± 0.2
	1 month	13.1 ± 0.7	57.2 ± 0.3	29.7 ± 0.5	1.9 ± 0.1*	6.5 ± 0.1*	39.0 ± 0.2

<sup>a</sup>Error shown is 1 standard deviation of the mean unless otherwise indicated. Error listed as two standard deviations of the mean is indicated with an asterisk.

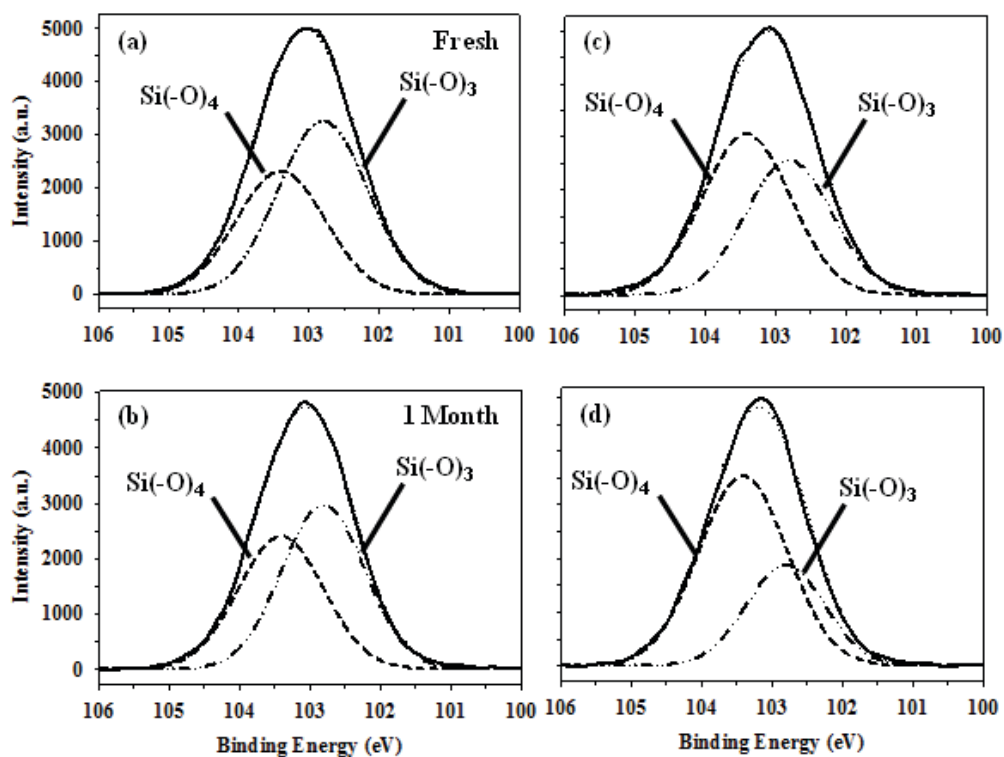
SiO<sub>2</sub>. Comparison of spectra for the untreated and fresh surfaces, Figs. 6.6a and 6.6b, reveals a significant increase in the Si(-O)<sub>4</sub> binding environment (76.2 ± 2.3%) upon treatment. Similar results are found with all H<sub>2</sub>O plasma treatment conditions, although increasing plasma power and proximity to the coil region leads to increased oxidization. The extreme of this trend is demonstrated by samples treated at 150W in the coil region which no longer have a measurable Si<sup>0</sup> peak, Fig. 6.6c.

Figure 6.7 compares high-resolution Si<sub>2p</sub> XPS spectra for fresh and 1 month aged dep-SiO<sub>2</sub> substrates treated with a 100% H<sub>2</sub>O vapor plasma. Deconstruction of the Si<sub>2p</sub> spectra for H<sub>2</sub>O (g) plasma treated dep-SiO<sub>2</sub> samples indicates the silicon is in a slightly more oxidized binding environment, than when treated with the Ar plasma. The best fits for these spectra were found using two peaks, consistent with Si(-O)<sub>3</sub> and Si(-O)<sub>4</sub> binding environments. IEP results are similar to dep-SiO<sub>2</sub> substrates treated with Ar plasmas, Table 6.3; CA<sub>max</sub> values decrease upon treatment and eventually revert back to the untreated value of ~40° after 1 month. This is true for all of the dep-SiO<sub>2</sub> substrates treated with 100% H<sub>2</sub>O plasmas, suggesting that the plasma treatment-imposed changes are not entirely permanent. Similar to the Ar plasma treated dep-SiO<sub>2</sub> samples, the surface composition changes very little upon H<sub>2</sub>O plasma treatment, Table 6.3, and stays approximately constant as the samples are aged though 1 month.

**FTIR Analysis.** To explore the possibility of OH incorporation on the surface of the dep-SiO<sub>2</sub> substrates, SiO<sub>2</sub> films were deposited on KBr pellets and analyzed using FTIR spectroscopy. Figure 6.8 shows FTIR spectra of an untreated dep-SiO<sub>2</sub> film, substrates freshly treated with 100% Ar and 100% H<sub>2</sub>O (g) plasmas, and a substrate aged 1 month



**Figure 6.6** High-resolution Si<sub>2p</sub> XPS spectra for (a) an untreated nat-SiO<sub>2</sub> substrate; and freshly-treated nat-SiO<sub>2</sub> substrates exposed to 100% H<sub>2</sub>O (g) plasmas with (b)  $P = 50$  W; and (c)  $P = 150$  W. Additional treatment conditions for both plasma treatments were 100 mTorr system pressure and treatment time of 10 min with substrates placed in the coil.



**Figure 6.7** High-resolution  $\text{Si}_{2p}$  XPS data for dep- $\text{SiO}_2$  substrates treated with a 100%  $\text{H}_2\text{O}$  vapor plasma at (a) and (b) 50 W; and at (c) and (d) 150 W in the coil. Freshly treated samples are shown in panels (a) and (c), corresponding 1 month data are shown in panels (b) and (d).

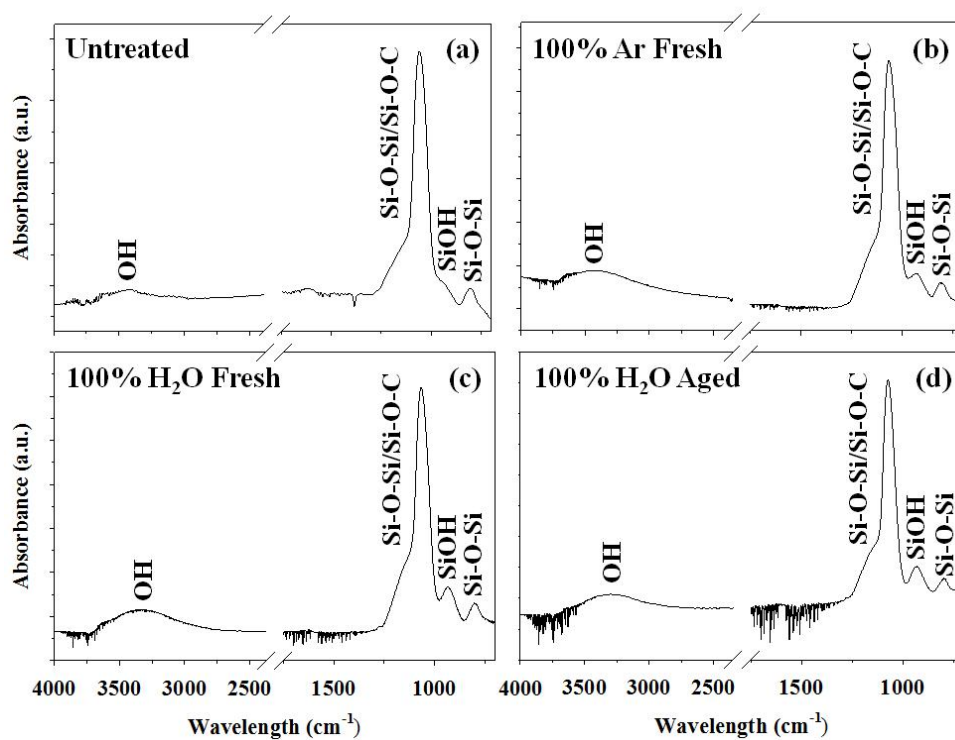


**Figure 6.8** FTIR spectra of dep-SiO<sub>2</sub> substrates for (a) untreated; (b) freshly treated with a 100% Ar plasma; (c) freshly treated with a 100% H<sub>2</sub>O (g) plasma; and (d) the substrate shown in panel (c) aged 1 month after treatment. Plasma treated substrates were placed in the coil with  $P = 150$  W and 10 min treatment time.

spectra for dep-SiO<sub>2</sub> films is the absorbance band at 1080 cm<sup>-1</sup> (Si-O-Si/Si-O-C asymmetric stretch), our primary focus is the broad Si-OH stretch centered around 3300 cm<sup>-1</sup> and Si-OH bend at ~930 cm<sup>-1</sup>. The most notable change upon plasma treatment is the growth of the Si-OH stretch at 3300 cm<sup>-1</sup>. This is mirrored with the enhancement and increased resolution of the Si-OH shoulder around 930 cm<sup>-1</sup>, regardless of the plasma treatment. Notably, the Si-OH peaks are enhanced more upon treatment with 100% H<sub>2</sub>O (g) plasmas and these enhancements are retained over the 1-month aging period. This result is supported by the XPS compositional data that show little change in the O/Si ratio upon aging and by O<sub>1s</sub> high resolution spectra that contain a second binding environment attributable to O-C/O-H moieties.

### **6.3 Discussion**

Accurate characterization of surface and interfacial properties of materials is critical to the development and application of a range of materials from polymers to semiconductors to metal oxides. Understanding how surface properties change as a result of synthesis method used (e.g. PECVD, sputter coating, native oxide), exposure to irradiation, or various surface modification strategies also represents an important problem in materials surface and interfacial science. As discussed extensively in our previous study of the effects of plasma treatments on the isoelectric points of SiO<sub>x</sub>N<sub>y</sub> substrates,<sup>12</sup> surface properties such as IEP (surface charge), CA, and surface composition are intricately interwoven and their interplay is not easily deconstructed. Here, we continue to explore the effects of plasma treatment on these intertwined properties, but also include the additional parameter of SiO<sub>2</sub> film formation method.

As noted in the Introduction, nat-SiO<sub>2</sub> and dep-SiO<sub>2</sub> could nominally be perceived as the same material, but the results presented here suggest there are subtle differences in surface properties that ultimately affect their response to plasma treatment. If we first examine the untreated surfaces, we find that the IEP and CA<sub>max</sub> values are significantly different between the two materials, with the nat-SiO<sub>2</sub> substrates exhibiting a much more acidic IEP, but a 20° higher contact angle than the dep-SiO<sub>2</sub> substrates, Tables 6.2 and 6.3. Both plasma treatments, however, appear to initially affect the substrates in a similar manner, resulting in shifts to more basic IEP values and concomitant decreases in CA<sub>max</sub> under all treatment conditions. Interestingly, the change in IEP value ( $\Delta$ IEP) upon plasma treatment is very different for the two materials and for the two plasma treatments. Specifically,  $\Delta$ IEP for nat-SiO<sub>2</sub> substrates treated with Ar plasmas is ~3-4, whereas  $\Delta$ IEP = 2-3 for the dep-SiO<sub>2</sub> films under the same conditions. In contrast, using the H<sub>2</sub>O plasma treatments, we observe very similar  $\Delta$ IEP values for both materials, with  $\Delta$ IEP ~ 0.5-2.5 under most treatment conditions. The difference between the two plasma systems likely arises because the H<sub>2</sub>O (g) plasma system is known to both create active sites on surfaces as well as implant functional groups (e.g. -OH), whereas the Ar plasma simply creates active sites on the surface that can then further react upon exposure to atmosphere. Thus, the Ar plasma surface modification is going to be more or less effective, depending on the ability of the generated plasma species to interact with the substrate being modified. For example, plasma treatment of polymers tends to be much more invasive than treatment of harder surfaces such as metals.<sup>33</sup> Likewise, as there is little control over the density and type of atmospheric species available for any specific

experimental run, the ultimate changes imparted to the surface could differ widely from substrate to substrate.

All substrates were stored in closed petri dishes throughout the 1 month aging period in an effort to limit post treatment contamination yet maintain the ability to store samples under ambient conditions. Use of a more controlled environment such as a dessicator for storage could, however, have even further minimized effects of aging. Our results do, however, indicate the H<sub>2</sub>O plasma treatments have more stable results on the nat- and dep-SiO<sub>2</sub> substrates than the Ar plasma treatments. For example, the nat-SiO<sub>2</sub> substrates have a larger oxygen incorporation following H<sub>2</sub>O plasma treatment, resulting in lower CA<sub>max</sub> values that remain stable upon aging. Oxygen incorporation such as this was somewhat anticipated based on previous results for H<sub>2</sub>O plasma treatment of polymeric membranes<sup>31,32</sup> and our SiO<sub>x</sub>N<sub>y</sub> study.<sup>12</sup> Overall, the nat-SiO<sub>2</sub> surfaces treated with H<sub>2</sub>O plasmas are more stable than those treated with Ar plasmas.

Along these lines, the stability of the plasma treatment appears to be at least somewhat dependent on the type of SiO<sub>2</sub> being treated. With the nat-SiO<sub>2</sub> substrates, the IEPs are relatively stable over the one month aging period for the majority of processing conditions. The least stable nat-SiO<sub>2</sub> surfaces (with respect to IEP) appear to be those treated in the coil at 50 W, regardless of plasma system. These systems also display the largest variability in carbon content, with values ranging from ~5% to ~17%, depending on the aging period and the plasma system. The increase in carbon over time can be at least partially attributed to the return of adventitious surface carbon. This change in surface carbon is generally reflected in surface hydrophobicity, with higher carbon content resulting in higher CA<sub>max</sub> values. In contrast, the dep-SiO<sub>2</sub> substrates treated in

either plasma system do not display significant changes in IEP values or chemical composition upon aging, Table 6.3. Indeed, for most processing conditions, the IEP values are either the same within experimental error or vary less than  $\pm 0.5$  upon aging. Moreover, the O/Si ratio for films treated with either plasma system is the same within experimental error, regardless of treatment parameters. Similarly, the carbon content for all of the treated dep-SiO<sub>2</sub> substrates is roughly the same, ~12-15%, suggesting that the carbon is likely incorporated in the dep-SiO<sub>2</sub> film<sup>17</sup> and is not merely adventitious surface carbon that returns upon aging.

The CA<sub>max</sub> values for the dep-SiO<sub>2</sub> substrates do change as the treated samples age, with somewhat higher CA<sub>max</sub> being measured after the full 1 month aging period. In general, this type of “hydrophobic recovery,” especially with polymeric materials, is thought to occur via rearrangement, migration, or burying of polar surface atoms into the bulk material to decrease surface energy.<sup>30,31</sup> Although these exact mechanisms may not be realistic for metal oxide materials, it is instructive to use them as a basis for understanding what is occurring with our materials. For the dep-SiO<sub>2</sub> substrates, the presence of absorbance bands attributable to OH (arguably the most polar surface group in these materials) in the FTIR spectra does not appear to track with the CA<sub>max</sub> measurements. For all samples, the intensity of OH absorbance bands in the FTIR spectra increased upon plasma treatment with both 100% H<sub>2</sub>O (g) and Ar plasma treatments, reflected in lower CA<sub>max</sub> values for freshly treated substrates. The OH signal does not, however appreciably change over the 1-month aging period, but CA<sub>max</sub> increases. This suggests that the OH functionality exists throughout the bulk of the material, not just at the surface of the film. Further evidence that “burial” or rearrangement or migration of

polar groups is not feasible with these materials.

The observation that plasma-treated dep-SiO<sub>2</sub> substrates are more stable over time than the nat-SiO<sub>2</sub> substrates could be the result of a number of factors. First, the dep-SiO<sub>2</sub> substrates may have experienced some ambient heating during the deposition process, thereby effectively annealing these materials. Previous work in our laboratory suggests that ambient substrates can reach temperatures over 60 °C in as little as 10 min.<sup>32</sup> A range of SiO<sub>2</sub> deposition studies in our laboratory have demonstrated that films deposited at 100 °C can be significantly different compositionally, depending on the precursor used.<sup>25,26,33,34</sup> Second, the dep-SiO<sub>2</sub> films were produced in the coil region of the plasma reactor, exposing them to higher levels of ion bombardment, which can result in elimination of defects created as a result of strain in the SiO<sub>2</sub> network, this can be likened to the observed increase in crosslinking in polymeric films formed in ion-rich environments.<sup>35-37</sup> Materials that have fewer defects are less susceptible to aging effects.<sup>31</sup>

A third contributing factor is that the dep-SiO<sub>2</sub> films are relatively thick (~100 to 300 nm)<sup>25,26</sup> in comparison to the nat-SiO<sub>2</sub> films. Consequently, during plasma exposure, it is more likely that ions interacting with the nat-SiO<sub>2</sub> films could penetrate through the oxide layer to the underlying substrate. As noted in the introduction, high energy electrons can ionize atoms in oxides, creating electron-hole pairs. Hole/pair creation is aided by the defects present at the interface as a result of oxygen vacancies and lattice mismatch.<sup>11</sup> Notably, there is a relatively high density of defects at the interface between Si and its native oxide.<sup>38</sup> In general, the fewer defects that are present, the more stable the surface/interface. Given that the dep-SiO<sub>2</sub> films are relatively thick, they are likely to be more stable to effects of ionizing radiation and charged species interactions. This may

be why we see formation of a relatively thick (i.e. >10 nm) oxide layer when the nat-SiO<sub>2</sub> substrates are exposed to the 150 W plasma, Fig. 7c, as opposed to the 50 W plasma, Fig. 7b. As a final note here, it is well known that during oxidation, Si atoms can be emitted from the growing SiO<sub>2</sub>/Si interface and diffuse into the oxide layer to relieve strain. Thus, oxidation occurs at the oxide/Si interface,<sup>39</sup> resulting in multilayer oxide formation.<sup>40,41</sup>

Increased ion bombardment could aid this process by disrupting Si-Si bonds at the interface for the nat-SiO<sub>2</sub> substrates. Again, the much thicker dep-SiO<sub>2</sub> substrates are much less likely to be susceptible to this as ions are much less likely to penetrate to the underlying Si interface. Moreover, penetration of ions to the Si interface is potentially being prevented due to the strained nature of the dep-SiO<sub>2</sub> oxide surface.

#### **6.4 Summary**

This work focused on the surface isoelectric points, contact angles and chemical composition of two different types of SiO<sub>2</sub> surfaces treated in two non-polymerizing plasmas that effectively modify the surface in different ways. These chemistries induce changes in surface composition, acid/base surface character, surface charge (IEP), and CA<sub>max</sub> values. With both substrates, the changes induced by the H<sub>2</sub>O plasma appear to be more permanent than those imparted by the Ar plasma treatments. This is most likely because the Ar plasma primarily creates active surface sites whereas the H<sub>2</sub>O plasma imparts OH functionality. The most stable responses, however, arise for the dep-SiO<sub>2</sub> substrates rather than the nat-SiO<sub>2</sub> materials. This result is attributable to the mechanisms for formation of the dep-SiO<sub>2</sub> substrates and the relative thickness of the films. The results presented here suggest that plasma-based surface modification strategies can be effective methods to permanently alter the surface charge of metal oxides.

## 6.5 References

- <sup>1</sup>E. Fazio, F. Monforte, F. Neri, F. Bonignore, G. Curro, M. Camalleri and D. Cali, J. Electrochem. Soc. **155**, G1 (2008).
- <sup>2</sup>V. V. Balashev, V. V. Korobtsov, T. A. Pisarenko and E. A. Chusovitin, Phys. Solid State **51**, 601 (2009).
- <sup>3</sup>K. W. Goynes, A. R. Zimmerman, B. L. Newalkar, S. Komarneni, S. L. Brantley and J. Chorover, J. Porous Mater. **9**, 243 (2002).
- <sup>4</sup>S. Brahma and S. A. Shivashankar, Thin Solid Films **518**, 5905 (2010).
- <sup>5</sup>J. van den Brand, P. C. Snijders, W. G. Sloof, H. Terryn and J. H. W. de Wit, J. Phys. Chem. B **108**, 6017 (2004).
- <sup>6</sup>S. Witanachchi, H. Weerasingha, H. A. Mourad and P. Mukherjee, Physica B **405**, 208 (2010).
- <sup>7</sup>L.-K. Chau and M. D. Porter, J. Colloid Interface Sci. **145**, 283 (1991).
- <sup>8</sup>E. McCafferty and J. P. Wightman, Surf. Interface Anal. **26**, 549 (1998).
- <sup>9</sup>H. Dallaporta, M. Liehr and J. E. Lewis, Phys. Rev. B **41**, 5075 (1990).
- <sup>10</sup>G. W. Simmons and B. C. Beard, J. Phys. Chem. **91**, 1143 (1987).
- <sup>11</sup>J. R. Schwank, M. R. Shaneyfelt, D. M. Fleetwood, J. A. Felix, P. E. Dodd, P. Paillet and V. Ferlet-Cavrois, IEEE Trans. Nucl. Sci. **55**, 1833 (2008).
- <sup>12</sup>K. J. Trevino, J. C. Shearer, P. R. McCurdy, S. E. Pease-Dodson, C. C. Okegbe and E. R. Fisher, Surf. Interface Anal. in press (2011)
- <sup>13</sup>K. H. A. Bogart, N. F. Dalleska, G. R. Bogart and E. R. Fisher, J. Vac. Sci. Technol. A **13**, 476 (1995).
- <sup>14</sup>N. M. Mackie, N. F. Dalleska, D. G. Castner and E. R. Fisher, Chem. Mater. **9**, 349 (1997).
- <sup>15</sup>K. J. Trevino and E. R. Fisher, Plasma Process. Polym. **6**, 180 (2009).
- <sup>16</sup>J. C. Shearer, M. J. Fisher, D. Hoogeland and E. R. Fisher, Appl. Surf. Sci. **256**, 2081 (2010).
- <sup>17</sup>D. S. Wavhal, J. Zhang, M. L. Steen and E. R. Fisher, Plasma Process. Polym. **3**, 276 (2006).
- <sup>18</sup>E. McCafferty and J. P. Wightman, J. Colloid Interface Sci. **194**, 344 (1997).
- <sup>19</sup>G. A. Parks, Chem. Rev. **65**, 177 (1964).
- <sup>20</sup>E. McCafferty, J. Adhesion Sci. Technol. **16**, 239 (2002).
- <sup>21</sup>G. A. Parks and P. L. De Bruyn, J. Phys. Chem. **66**, 967 (1962).
- <sup>22</sup>M. B. Ali, F. Bessueille, J. M. Chovelon, A. Abdelghani, N. Jaffrezic-Renault, M. A. Maaref and C. Martelet, Mat. Sci. Eng. C **28**, 628 (2008).
- <sup>23</sup>D. P. Dowling, A. Ramamoorthy, M. Rahman, D. A. Mooney and J. M. MacElroy, Plasma Process. Polym. **6**, S483 (2009).
- <sup>24</sup>S.-H. Yang, C.-H. Liu, C.-H. Su and H. Chen, *Thin Solid Films* **2009**, 517, 5284.
- <sup>25</sup>D. E. Jan and S. Raghavan, J. Electrochem. Soc. **141**, 2465 (1994).
- <sup>26</sup>M. C. Poon, C. W. Kok, H. Wong and P. J. Chan, Thin Solid Films **4620463**, 42 (2004).
- <sup>27</sup>R. M. Torres-Sanchez, A. B. Garcia and A. M. Cesio, J. Euro. Ceram. Soc. **16**, 1127 (1996).
- <sup>28</sup>M.-G. Barthes-Labrousse, Vacuum **67**, 385 (2002).
- <sup>29</sup>W. M. Mullins and B. L. Averbach, Surf. Sci. **206**, 29 (1998).

- <sup>30</sup>W. M. Mullins and B. L. Averbach, *Surf. Sci.* **206**, 41 (1998).
- <sup>31</sup>M. L. Steen, L. Hymas, E. D. Havey, N. E. Capps, D. G. Castner and E. R. Fisher, *J. Membr. Sci.* **188**, 97 (2001).
- <sup>32</sup>M. L. Steen, A. C. Jordan and E. R. Fisher, *J. Membr. Sci.* **204**, 341 (2002).
- <sup>33</sup>C. I. Butoi, M. L. Steen, J. R. D. Peers and E. R. Fisher, *Journal of Physical Chemistry B* **105**, 5957 (2001).
- <sup>34</sup>L. Tusek, M. Nitschke, C. Werner, K. Stana-Kleinschek and V. Ribitsch, *Colloids Surfaces A* **195**, 81 (2001).
- <sup>35</sup>T. R. Gengenbach, Z. R. Vasic, R. C. Chatelier and H. J. Griesser, *J. Polym. Sci. A: Polym. Chem.* **32**, 1399 (1994).
- <sup>36</sup>J. M. Stillahn and E. R. Fisher, *J. Phys. Chem. C* **113**, 1963 (2009).
- <sup>37</sup>K. H. A. Bogart, S. K. Ramirez, L. A. Gonzales, G. R. Bogart and E. R. Fisher, *J. Vac. Sci. Technol. A* **16**, 3175 (1998).
- <sup>38</sup>J. Zhang, D. S. Wayhal and E. R. Fisher, *J. Vac. Sci. Technol. A* **22**, 201 (2004).
- <sup>39</sup>C. I. Butoi, N. M. Mackie, L. J. Gamble, D. G. Castner, A. M. Miller, J. E. Barnd and E. R. Fisher, *Chem. Mater.* **12**, 2014 (2000).
- <sup>40</sup>N. M. Mackie, D. G. Castner and E. R. Fisher, *Langmuir* **14**, 1227 (1998).
- <sup>41</sup>D. J. Cole, M. C. Payne and L. C. Ciacchi, *Surf. Sci.* **601**, 4888 (2007).
- <sup>42</sup>M. Uematsu, H. Kageshima and K. Shiraishi, *Comp. Mater. Sci.* **24**, 229 (2002).
- <sup>43</sup>H. Watanabe, K. Kato, T. Uda, K. Fujita and M. Ichikawa, *Phys. Rev. Lett.* **80**, 345 (1998).
- <sup>44</sup>L. C. Ciacchi and M. C. Payne, *Phys. Rev. Lett.* **95**, 196101 (2005).

## **CHAPTER 7**

### **SURFACE CHARACTERIZATION OF RF PLASMA TREATED ZEOLITE X**

In this chapter, preliminary data for the surface modification of zeolite X using fluorocarbon (FC) plasmas are presented. These data are part of a larger project focused on development of a new rotating drum reactor. Specifically, the experiments presented here were designed to test the new reactor's efficacy with respect to total surface area modification and to determine if any structural damage was incurred by the zeolites as a result of this new reactor design. Although similar reactor systems have been described in the literature for the treatment of metal oxides and polymer beads, the plasma treatment of zeolites has not yet been explored using a rotating drum reactor.

## 7.1 Introduction

Zeolites can be both naturally and artificially produced, and both types have been used extensively in three key applications: as adsorbents, as catalysts, and for ion-exchange.<sup>1</sup> Two common forms of zeolites are Zeolite X and Zeolite Y. Zeolite X is used primarily for ion-exchange purposes because of the low amounts of Si present in the material. It is Al rich, with  $\text{Si/Al} \leq 2$ ,<sup>2,3</sup> and contains the highest cation exchange properties of all zeolites. In addition, Zeolite X has the highest overall net negative charge on its surface, rendering it hydrophilic.<sup>2,3</sup> It was used exclusively until Breck and coworkers reported on the synthesis of Zeolite Y, which contained intermediate amounts of Si,  $2 < \text{Si/Al} \leq 5$ , and retained a decreased cation content, making the material more hydrophobic.<sup>2,3</sup> Additionally, Zeolite Y is thermally stable and retains its chemical structure in acids.<sup>2,3</sup> Both Zeolite X and Zeolite Y have similar large pore sizes of 8 – 12 Å. Surface and interior modification of these zeolites has been widely studied because of their adsorbent properties, their vast ion exchange applications, and their varying degrees of negative or positive surface charge.<sup>2,4,5</sup>

Currently, the majority of zeolites are chemically altered by aqueous solutions to afford the desired surface properties.<sup>6,7</sup> These methods are undesirable, however, because of the large production of waste and lack of structural stability that some zeolites, Zeolite X in particular, have in certain solutions. Alternatively, plasma modification presents an ideal methodology to create tailored surface properties because minimal amounts of waste are produced from surface treatments and they have the ability to fine tune surface treatments for specific surface functionality. Plasmas also enable surfaces to be treated at a range of parameters that can essentially control when structural damage will and will

not occur. We have seen this specifically in our lab with the treatment of polysulfone membranes with H<sub>2</sub>O plasmas.<sup>8</sup> At low rf powers, pressures, and treatment time, surface modification occurred with no structural damage to the membrane. At higher rf powers degradation of the membrane occurred. Two studies by Yamazaki and coworkers employed capacitively-coupled parallel plate plasma discharges for the modification of zeolite H-Y with CF<sub>4</sub>.<sup>9,10</sup> In these studies, the structure of the zeolite was thought to have been altered by the replacement of -OH groups with -CF<sub>3</sub> and -F groups as seen by TG/DTA-MASS spectrometry, thereby creating a more hydrophobic surface. Unfortunately, the hydrophilicity of the surface of the zeolite before and after treatment was not explicitly tested. Additional x-ray diffraction data did reveal that the zeolites crystal structure collapsed at rf powers  $\geq 75$  W.

Because the goal of Yamazaki and coworkers was to incorporate -CF<sub>3</sub> and -F groups into the surface of Zeolite Y a CF<sub>4</sub> plasma was most likely used for the treatment because of its known ability to etch and imbed F atoms into the surface of materials. This is the likely reason that they saw damage to their crystal structure. Here, we explored CF<sub>4</sub> and larger FC monomers because surface properties change with changes in F/C ratios in the precursor. In general the higher the F/C ratio is for the feed gas, the more likely etching will occur over film deposition.<sup>11</sup> Hence, CF<sub>4</sub> plasmas are excellent systems for etching. Because of the large amount of F that is produced in a 100% CF<sub>4</sub> plasma, etching will outweigh deposition under most conditions. However, during the etching process a thin passivation layer forms on the surface of the material to regulate interaction of the surface with reactants and other high-energy species. Passivation layers are thin CF<sub>x</sub> polymer layers, < 10 nm thick, that form as a result of the competition between etching and film

deposition in fluorocarbon plasmas.<sup>12</sup> C<sub>2</sub>F<sub>6</sub> plasmas have a lower F/C ratio than CF<sub>4</sub> and this promotes the deposition of passivation layers, although etching can dominate under some conditions. For a 100% C<sub>2</sub>F<sub>6</sub> plasma, deposition will dominate unless additional gases are added to the system (e.g. O<sub>2</sub>) or if *P* is relatively high.<sup>11</sup> The largest FC monomer used in this research, C<sub>3</sub>F<sub>8</sub>, was chosen due to its lower F/C ratio which shifts the plasma regime almost exclusively to film deposition.<sup>11</sup> The easy formation of CF<sub>2</sub> and CF<sub>3</sub> species from C<sub>3</sub>F<sub>8</sub> plasmas leads to deposition of reasonably thick FC films, although film deposition rate depends on plasma parameters.<sup>13</sup>

This chapter presents preliminary results on the plasma treatment of Zeolite X with three different FC precursors (CF<sub>4</sub>, C<sub>2</sub>F<sub>6</sub>, and C<sub>3</sub>F<sub>8</sub>) in a rotating drum reactor newly created in our laboratories. Previous studies in the Fisher group have plasma treated uniquely shaped materials, wherein commercially-obtained nanoparticles were suspended in methanol, and then applied to Si substrates prior to plasma treatment.<sup>14</sup> We are currently exploring the viability of completely coating individual, unsupported particles through the use of a rotating drum reactor that has been shown in the literature to coat metal oxide materials<sup>15,16</sup> and polymer beads<sup>17</sup>. Zeolites are one particle type that could benefit from having a reactor wherein the particles are rotating and dropping through the ionized gas. Specifically, we are interested in discerning whether the rotating reactor provides a rational approach to complete surface modification of high surface area particles and differences that FC monomers have on these materials. X-ray photoelectron spectroscopy (XPS) data provides analysis of surface fluorination and morphological changes resulting from plasma processing are revealed with scanning electron microscopy (SEM).

## 7.2 Reactor Design

Zeolite modification experiments were performed in a home-built ICP rotating drum reactor, Figure 7.1. The reactor consists of two glass tubes (50 mm i.d.) joined by an o-ring (58 mm i.d., 3.5 mm cross-section) to allow access to the interior of the reactor. The main barrel of the reactor is ~380 mm long. The interior of the reactor contains a rotating drum that is ~102 mm in length with an inner diameter of ~44 mm. Attached to the rotating drum is an arm that extends into the gas inlet stem on the reactor that allows the drum to stay centered in the reactor, on the opposite end of the drum is a glass joint 57 mm in length that is attached to a second glass rod, 330 mm long. This longer glass rod is attached to an electric powered motor that allows the inner drum to be rotated; zeolites in these experiments were rotated at a rate of 19 rpm.

## 7.3 Results/Discussion

**Untreated Zeolite X.** Figures 7.2a and 7.2b shows two SEM images of untreated Zeolite X. Particles are uniform in size (~500  $\mu\text{m}$ ) and are indistinguishable from one another. To highlight different features of the material, Figure 7.2a emphasizes the zeolite pores, whereas Figure 7.2b shows the complete zeolite particles. High-resolution  $\text{C}_{1s}$  XPS data, Figure 7.2c, for untreated Zeolite X suggests the surface consists of carbon bound in environments corresponding to C-C/C-H, C-O-H/C-O-C, and C=O (~284.4, ~286, and ~288.5 eV, respectively). Because zeolites are very porous with high surface area, the adsorption of atmospheric carbon containing species on the surface (i.e. “adventitious carbon”) is expected. XPS compositional analysis data of the untreated zeolites, Table 7.1, reveals the Si/Al ratio is ~7.0, which suggests a Si rich zeolite. This indicates that

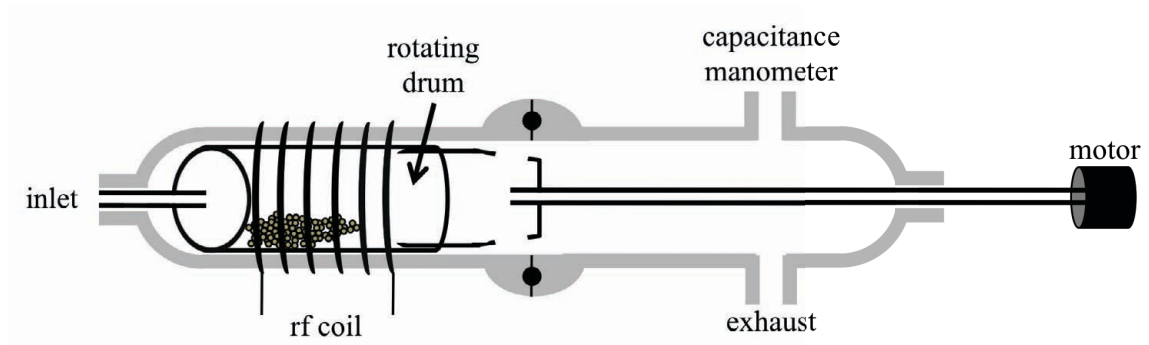


**Figure 7.1** Cross-sectional schematic of the rotating drum reactor used for zeolite modification.

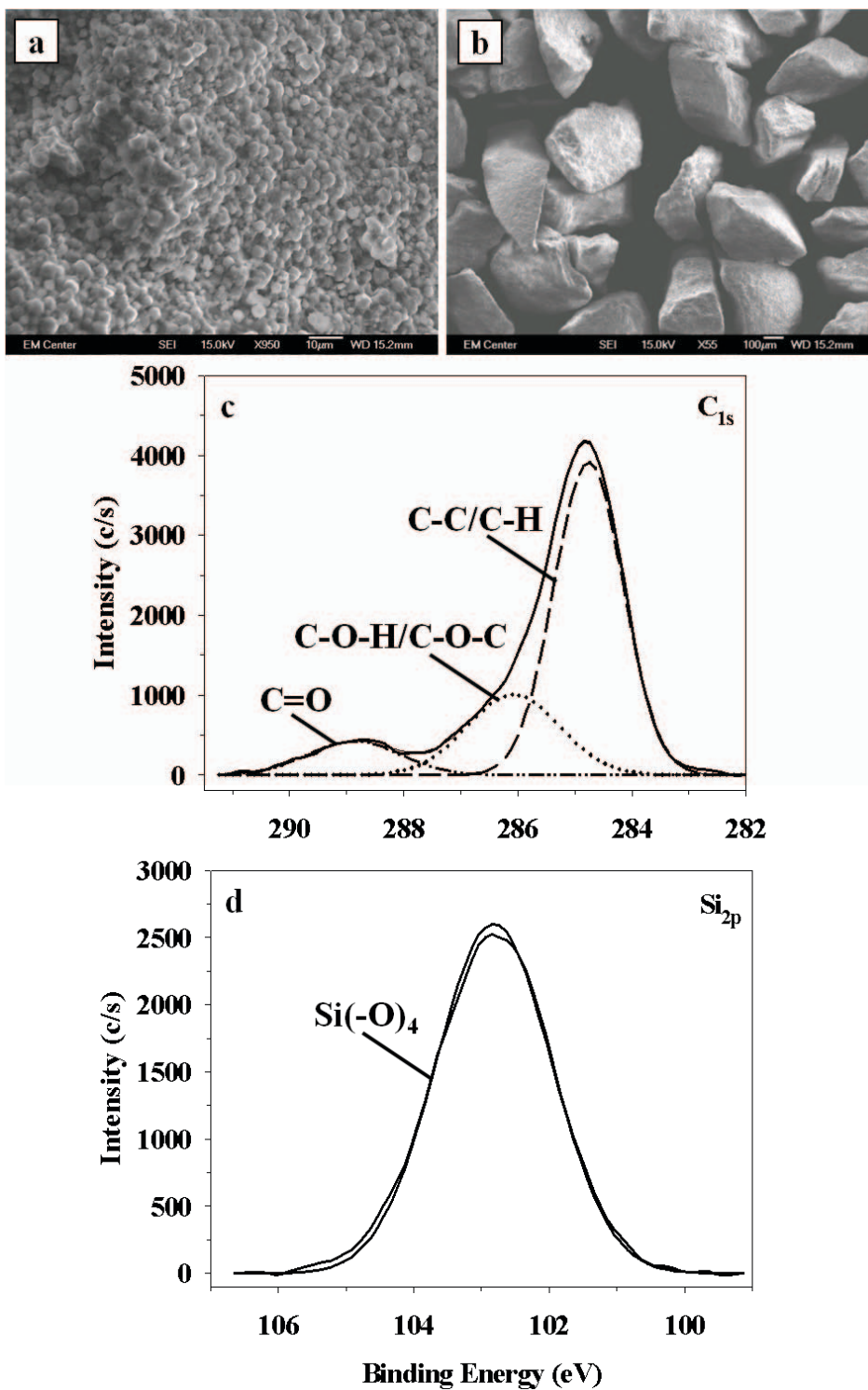


**Figure 7.2** SEM images of untreated Zeolite X at magnifications (a) 950x and (b) 55x. Corresponding high-resolution XPS spectra are also shown for (c)  $C_{1s}$  and (d)  $Si_{2p}$  binding environments.

**Table 7.1** XPS elemental compositions for untreated zeolites, along with plasma treated zeolites and Si substrates. Specific sampling sites are representative of the specific data shown in Figures 7.3-7.5.

Plasma Treatment	%O	%Si	%C	%F	%Al
Untreated	60.5 ± 3.3	19.3 ± 1.6	18.8 ± 5.5	-	2.7 ± 0.5
100% CF <sub>4</sub> spot 1	28.0	12.8	4.9	54.3	-
100% CF <sub>4</sub> spot 2 <sup>a</sup>	26.2	9.5	3.8	48.5	4.4
100% C <sub>2</sub> F <sub>6</sub> spot 1 <sup>b</sup>	27.0	7.3	32.9	21.7	4.2
100% C <sub>2</sub> F <sub>6</sub> spot 2 <sup>c</sup>	25.4	6.7	34.9	25.8	5.2
100% C <sub>3</sub> F <sub>8</sub> spot 1 <sup>d</sup>	18.2	7.7	22.4	45.9	0.6
100% C <sub>3</sub> F <sub>8</sub> spot 2 <sup>e</sup>	19.4	4.4	19.2	50.9	0.7
100 % C <sub>3</sub> F <sub>8</sub> coil* <sup>f</sup>	3.5 ± 1.0	8.9 ± 3.2	29.6 ± 6.5	57.8 ± 3.3	-
100% C <sub>3</sub> F <sub>8</sub> 14 cm*	-	-	34.4 ± 4.9	65.3 ± 4.3	-

<sup>a</sup>contains 7.5 % Mg

<sup>b</sup>contains 3.2 % Mg and 3.7% Na

<sup>c</sup>contains 2.0 % Mg

<sup>d</sup>contains 4.4 % Mg

<sup>e</sup>contains 3.5 % Mg

<sup>f</sup>contains 1.4 ± 0.4 % Na

\*Si substrates

this particular sample may be Zeolite Y, regardless of the designation provided by the manufacturer, as zeolites with  $\text{Si}/\text{Al} \geq 5$  are generally considered to be of the Y type. This is further substantiated by high-resolution  $\text{Si}_{2p}$  XPS data, Fig. 7.2d, which shows one primary Si binding environment (at  $\sim 103$  eV), corresponding to an inorganic  $\text{SiO}_2$  silicon network.<sup>18</sup> The O/Si ratio for this sample is  $\sim 3.1$ , the theoretical value for a pure  $\text{Si}(-\text{O}_4)$  environment (e.g. a 100% tetrahedral  $\text{SiO}_2$  network) is  $\sim 2$ . Note that some of the oxygen present in the sample is likely bound to the small amount of Al in the zeolites.

**100%  $\text{CF}_4$  treated Zeolite X.** As mentioned above the primary use of  $\text{CF}_4$  plasmas is the etching of materials with a resulting passivation layer. The passivation layer on the sample can be analyzed for composition with XPS and for thickness with ellipsometry. We have previously measured passivation layer deposition rates of  $1.23 \text{ \AA}/\text{min}$  at 50 W and  $1.35 \text{ \AA}/\text{min}$  at 150 W using  $\text{CF}_4$  plasmas.<sup>19</sup> Zeolite treatment with a 100%  $\text{CF}_4$  plasma ( $P = 50 \text{ W}$ ) shows little change in the particle morphology, Figures 7.3a and 7.3b, compared to the untreated zeolites. Inspection of the higher magnification image reveals, however, the presence of a slight film on the zeolite. Figures 7.3c and 7.3d, contain high-resolution  $\text{C}_{1s}$  XPS data for two sampling sites on the sample treated in the 100%  $\text{CF}_4$  plasma. Interestingly, the two spectra shown in these figures are significantly different from each other, indicating that a non-uniform surface treatment has occurred. The first sampling site (Figure 7.3c) shows the deconstructed  $\text{C}_{1s}$  binding environment containing contributions from C-C/C-H, C-O-H/C-O-C, and O-C=O/C-CF moieties at 284.6, 286.4, and 289.0 eV, respectively. The presence of the -C-CF binding environment is clear evidence that the plasma has altered the surface chemistry of the zeolite in some way. The similarity between the binding environments present in the second sampling location

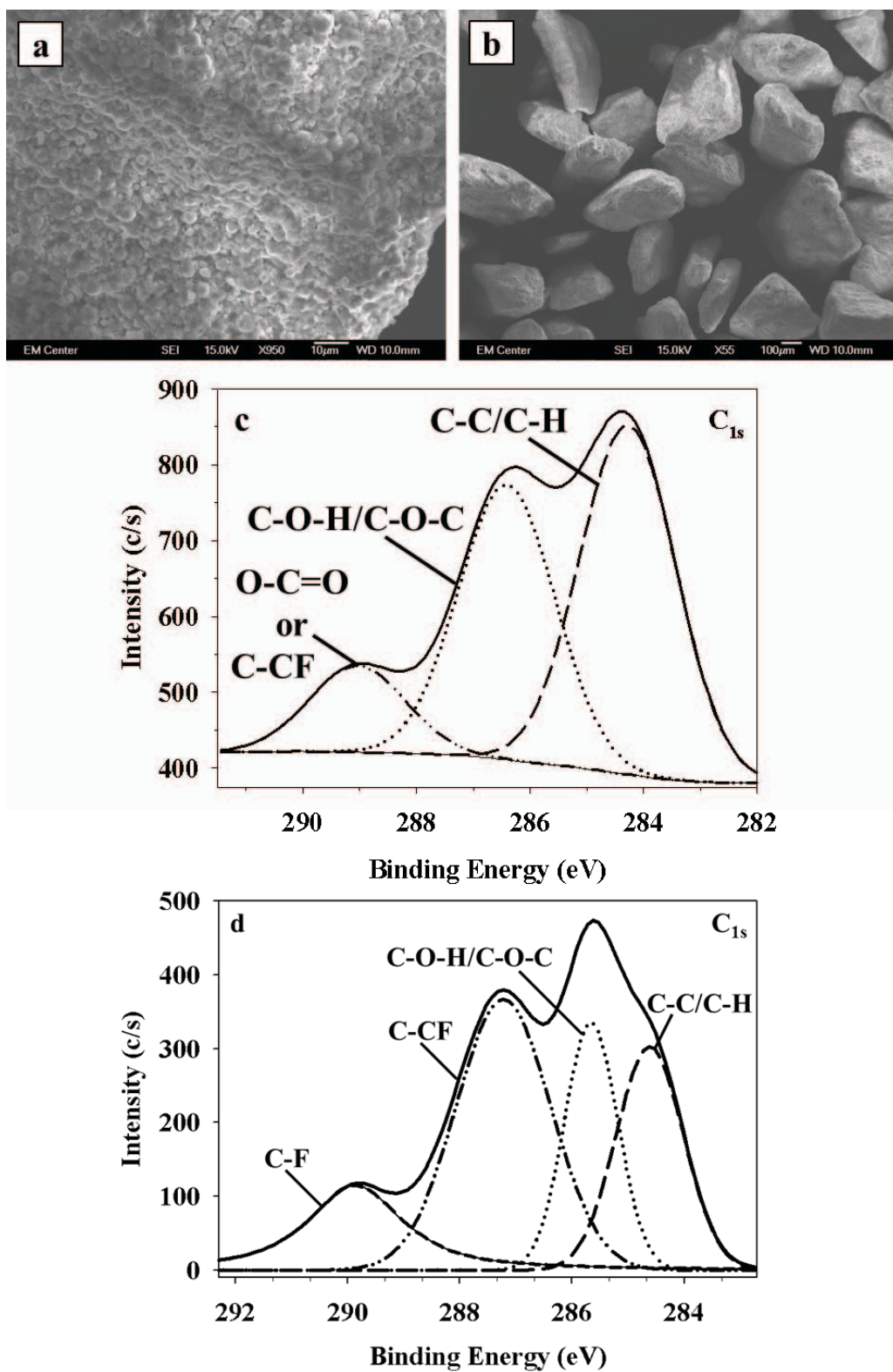


**Figure 7.3** SEM images of 100% CF<sub>4</sub> plasma treated Zeolite X at magnifications (a) 950x and (b) 55x. High-resolution C<sub>1s</sub> XPS spectra are shown in (c) and (d) for two different sampling locations on the zeolite surface.

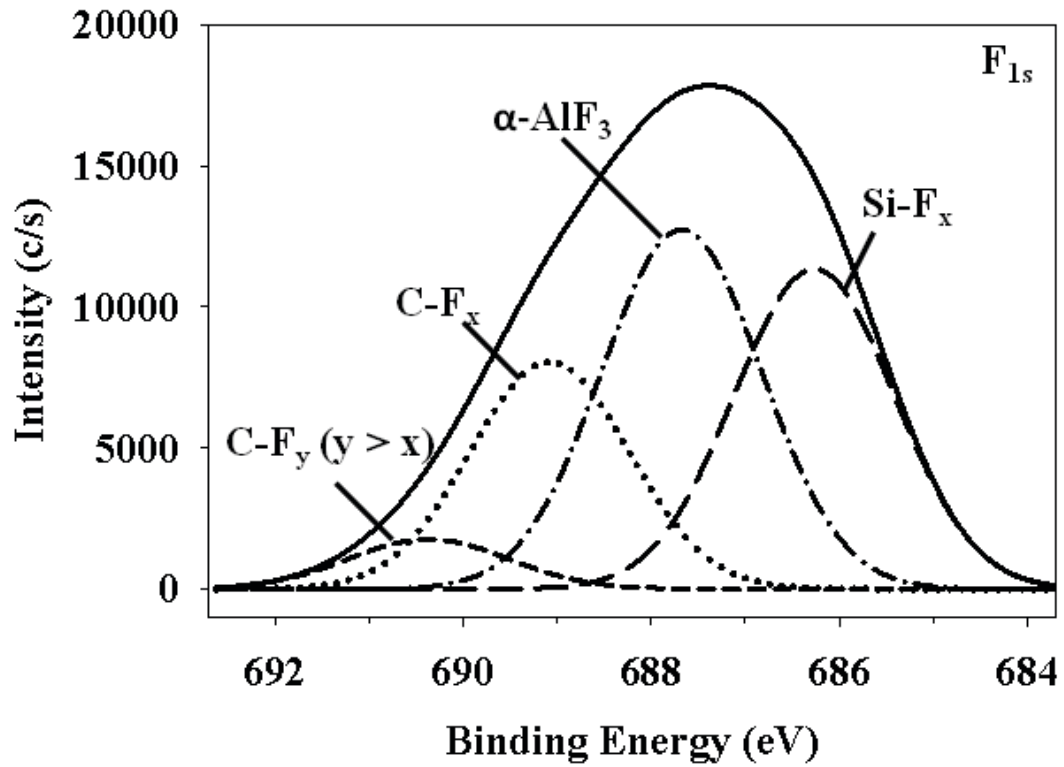


**Figure 7.4** High-resolution  $F_{1s}$  XPS spectra for  $CF_4$  plasma treated zeolites.

and the untreated zeolites (albeit in different proportions) clearly indicates incomplete plasma deposition over the entire sample. For this analysis site, the C-C/C-H binding environment along with additional contributions from C-O-H/C-O-C and C=O/C-CF (285 and 287 eV, respectively) are observed. Although significant ion bombardment takes place within the coil region of the reactor, which can impede deposition, any contributions from F seen on the zeolite surface are from F species implanted in the surface of the zeolite or from the formation of a passivation layer containing F. Binding environments in Figure 7.4 suggest that F is embedding itself in the zeolite with the presence of  $\text{Si-F}_x$  and  $\alpha\text{-AlF}_3$ . Additionally, two peaks are seen that suggest F incorporation in the adventitious carbon present on the surface of the zeolite or a thin passivation layer.

The significant difference in the surface properties revealed for the two sampling sites on the zeolite, Figure 7.3, is attributed to a combination of the reactor design as well as the placement of the zeolites on Si wafers for XPS analysis. Samples were treated while the reactor was rotating, thereby causing the particles to repeatedly drop through the partially ionized gas. This method is expected to equally expose all of the zeolite surfaces to the reactive species in the plasma. To eliminate sampling bias, treated zeolites were randomly taped onto XPS and SEM stubs for analysis without regard to the position in the reactor from which they were collected. We therefore conclude that uniform treatment is not being achieved under these conditions. One possible explanation is that the plasma glow is not concentrated inside the rotating drum, but on the outside between the reactor walls and the rotating drum. Thus, the sample is not uniformly exposed to plasma species responsible for FC plasma surface modification.

**100% C<sub>2</sub>F<sub>6</sub> plasma treatment.** Previous results in our lab have shown that C<sub>2</sub>F<sub>6</sub> plasmas deposit relatively thin amorphous FC films, which can still be considered as passivation layers. The highest deposition rate occurs when substrates are placed directly in the coil region of the reactor. Furthermore, as the applied rf power increases, the deposition rate decreases, e.g. at  $P = 50$  W the deposition rate is 7.40 Å/min, whereas at  $P = 150$  W, the deposition rate is 1.83 Å/min.<sup>19</sup> With C<sub>2</sub>F<sub>6</sub> plasmas, the inherent competition between deposition and etching can be controlled by deliberate choice of plasma parameters such as substrate position, applied rf power, and total reactor pressure. Figure 7.5 shows SEM images of 100% C<sub>2</sub>F<sub>6</sub> plasma treated zeolites and corresponding high-resolution C<sub>1s</sub> XPS spectra. Figures 7.5 a and 7.5b reveal cracks on the plasma treated zeolite surface, not present on the untreated samples, Figure 7.2. Higher magnification images indicate a thin film/thick passivation layer has been deposited on the zeolite particles. XPS elemental composition suggests an organic carbon containing film or FC film has been deposited on the surface, as there are significantly lower concentrations of Si on the surface. The observation that both Si and Al are still present in the composition data, Table 7.1, suggests the film is relatively thin (i.e. less than the sampling depth of XPS <~10 nm) as these elements are likely being detected from the underlying zeolite material. The high-resolution C<sub>1s</sub> XPS binding environments, Figures 7.5c and 7.5d, supports this hypothesis as these data appear to have a more oxidized film containing contributions from C, F, and O coating the zeolite particles. Additional, high-resolution F1s XPS data are shown in Figure 7.6 and show that F is incorporating itself in to the zeolites surface with the presence of the SiF<sub>x</sub> and  $\alpha$ -AlF<sub>3</sub> peak. The two C-F peaks at 689 and ~690 eV also reveal the presence of a thin passivation layer.

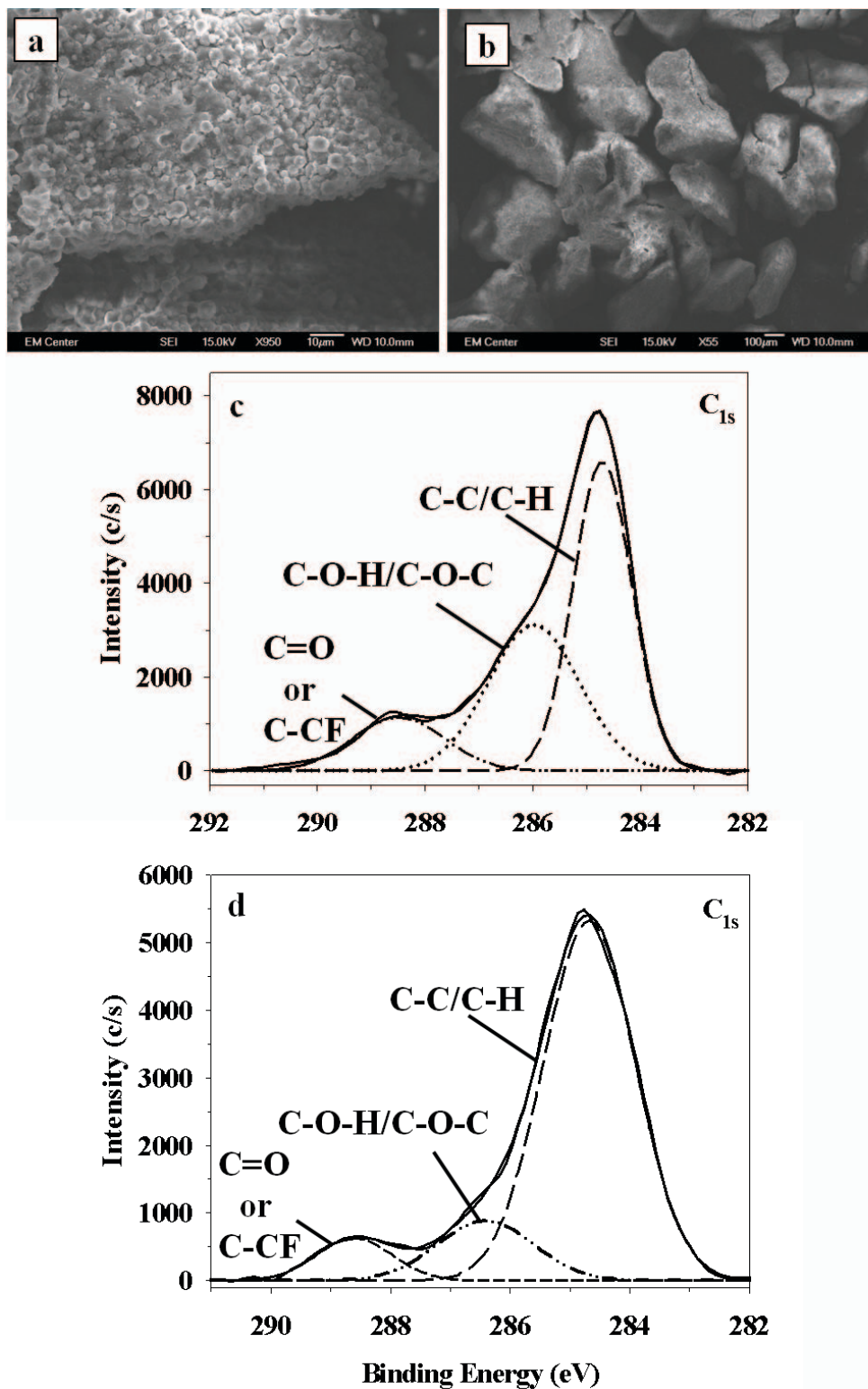


**Figure 7.5** SEM images of 100% C<sub>2</sub>F<sub>6</sub> plasma treated Zeolite X at magnifications (a) 950x and (b) 55x. Corresponding high-resolution C<sub>1s</sub> XPS spectra for two different sampling locations are shown in (c) and (d).

As with the  $\text{CF}_4$  plasma treated zeolites, different sampling sites on the zeolite surface reveal different surface compositions. Deconstructing the  $\text{C}_{1s}$  spectrum in Figure 7.4c, indicates a similar surface composition as the untreated zeolites. Small contributions from C-F are, however, observable in the spectrum, suggesting that F is present in the deposited film or passivation layer. Further high-resolution XPS analysis of a second site on the same sample, Figure 7.4d, shows a similar amount of F with  $\text{C}_{1s}$  binding environments similar to the first site. The notable differences in the two spots lie mainly in the relative intensities of C-C/C-H to C-O-H/C-O-C. This again can be attributed to the reactor's design. The idea that the plasma is not coming in full contact with the zeolites inside the rotating drum results in random plasma treatment and in turn gives different intensities of binding environments and small amounts of FC incorporation in the zeolites. We would expect based on the morphological and compositional data, along with previous results in our lab, that higher FC incorporation would occur on the zeolites when placed in the coil region of the reactor.<sup>13</sup>

**100%  $\text{C}_3\text{F}_8$  plasma treated Zeolite X.** One of the main differences of  $\text{C}_3\text{F}_8$  plasmas and  $\text{C}_2\text{F}_6$  plasmas is that  $\text{C}_3\text{F}_8$  exhibits higher deposition rates as samples are moved farther downstream from the coil region and as rf powers are increased, e.g. deposition rate at  $P = 30$  W is  $\sim 40$  Å/min and at  $P = 50$  W it is  $\sim 90$  Å/min.<sup>13</sup> Figures 7.7a and 7.7b show two SEM images for 100%  $\text{C}_3\text{F}_8$  plasma treated zeolites. Visually, the treated zeolites are quite similar to untreated zeolites, Figure 7.2. Although portions of the zeolite surface appear to be clumped together in some areas, they do not have coating patches and cracks like the  $\text{C}_2\text{F}_6$  plasma treated zeolites. However, at the lower magnification the zeolites look similar to the  $\text{C}_2\text{F}_6$  plasma treated zeolites with large cracks. These visual

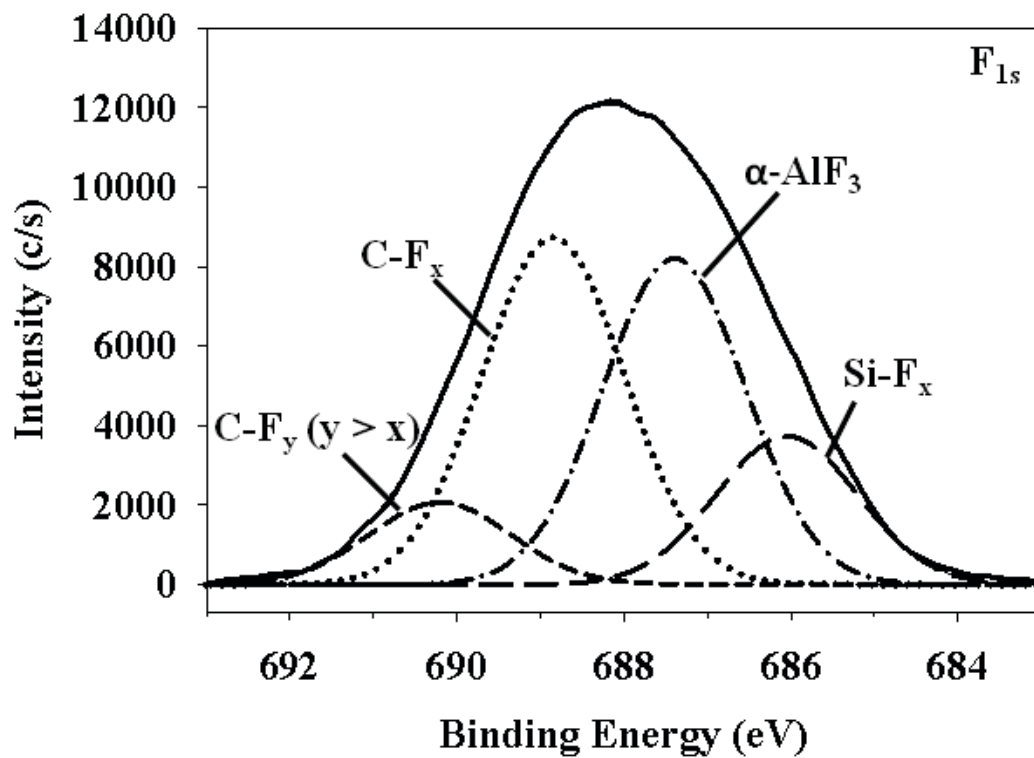


**Figure 7.6** High-resolution  $F_{1s}$  XPS spectra for  $C_2F_6$  plasma treated zeolites.

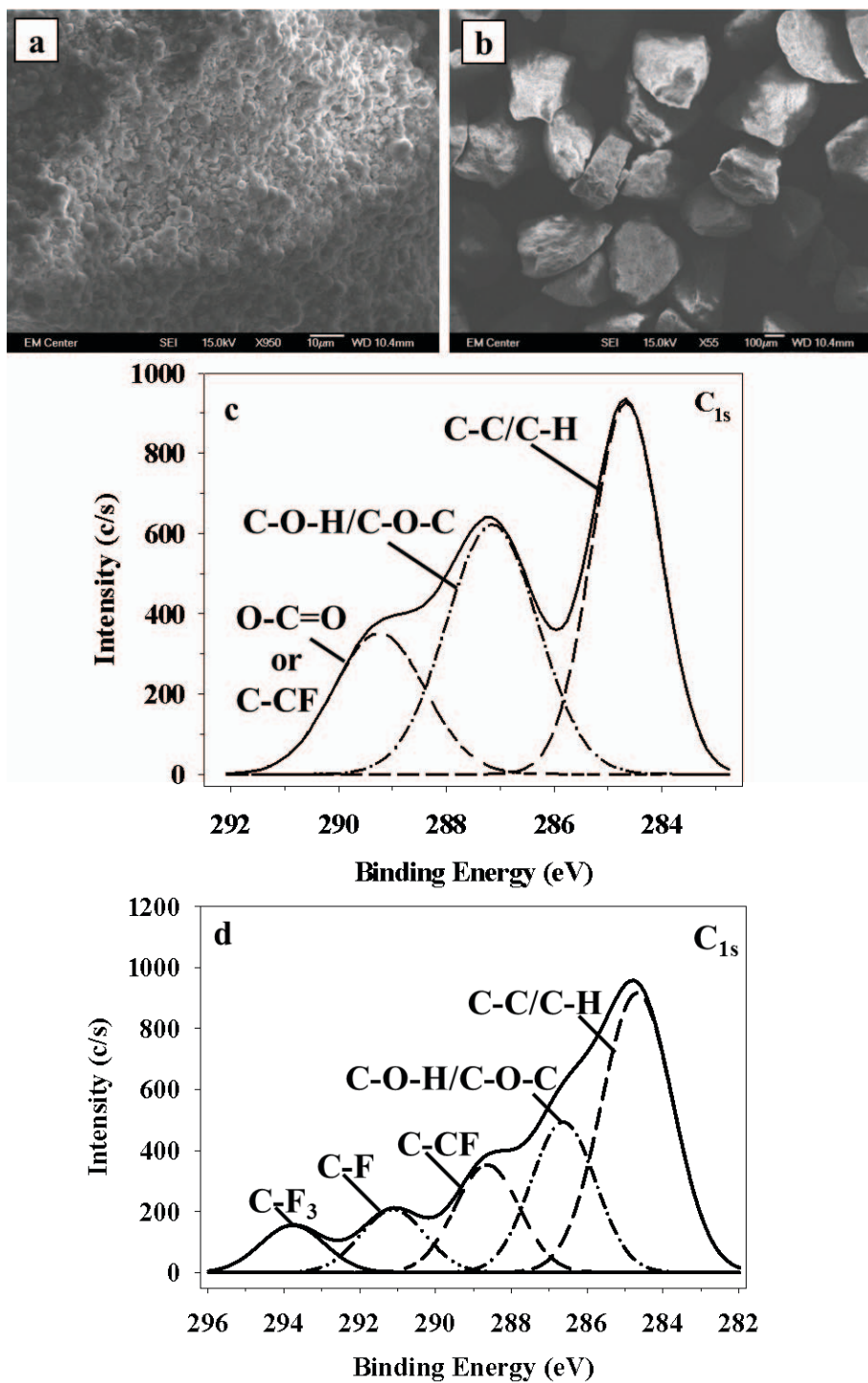


**Figure 7.7** SEM images of 100%  $C_3F_8$  plasma treated Zeolite X at magnifications (a) 950x and (b) 55x. Corresponding high-resolution  $C_{1s}$  XPS spectra are shown for two different sampling locations in (c) and (d).

defects could indicate that a FC film was deposited on the zeolites. Surface composition data, Table 7.1, show a large amount of F (~50%) and similar amounts of C to the untreated sample (~20%). We would expect to see an increase in both the F and C% if we were depositing a FC film. This suggests that the FC film we deposited is thin or we are seeing a thick passivation layer based on the decreased amount of Si in these samples relative to the untreated values. We measure substantial differences in XPS spectra collected at different locations on the zeolite, Figures 7.7c and 7.7d. Carbon is incorporated in the formation of a FC passivation layer or a thin film on the surface in some areas of the zeolites, Fig. 7.7c, as opposed to others (Fig 7.7d). The first sampling site, Fig 7.7c, reveals similar binding environments to the C<sub>2</sub>F<sub>6</sub> treated zeolite surface. A second location, Fig. 7.7d, reveals a FC film prevalent by the low intensity C-CF, CF<sub>3</sub> and CH<sub>2</sub>-CF<sub>2</sub> peaks at ~287, ~293 and ~290 eV, respectively. The differences in these two specific sampling sites can be attributed to one of two things (1) a thin FC film is being deposited because the sample is placed in the coil region and not downstream from the coil (2) or because of the reactor design, inconsistencies in the plasma exposure are resulting in different chemical functionalities on the surface.

**100% C<sub>3</sub>F<sub>8</sub> plasma treated silicon wafer.** To verify that the inconsistent data obtained for plasma treated zeolites were a result of a poor reactor design (for the use of treating zeolite particles), a Si wafer was placed in the drum reactor treated with a 100% C<sub>3</sub>F<sub>8</sub> plasma ( $P = 50$  W, in coil region) at a stationary position in the coil. XPS data show that the Si wafer treated in the reactor drum had only  $4.9 \pm 0.3$  % F on its surface, less than any of the measured F atom concentrations from the FC plasma treatments made on zeolite surfaces. This suggests that the sample is not being directly exposed to the plasma.

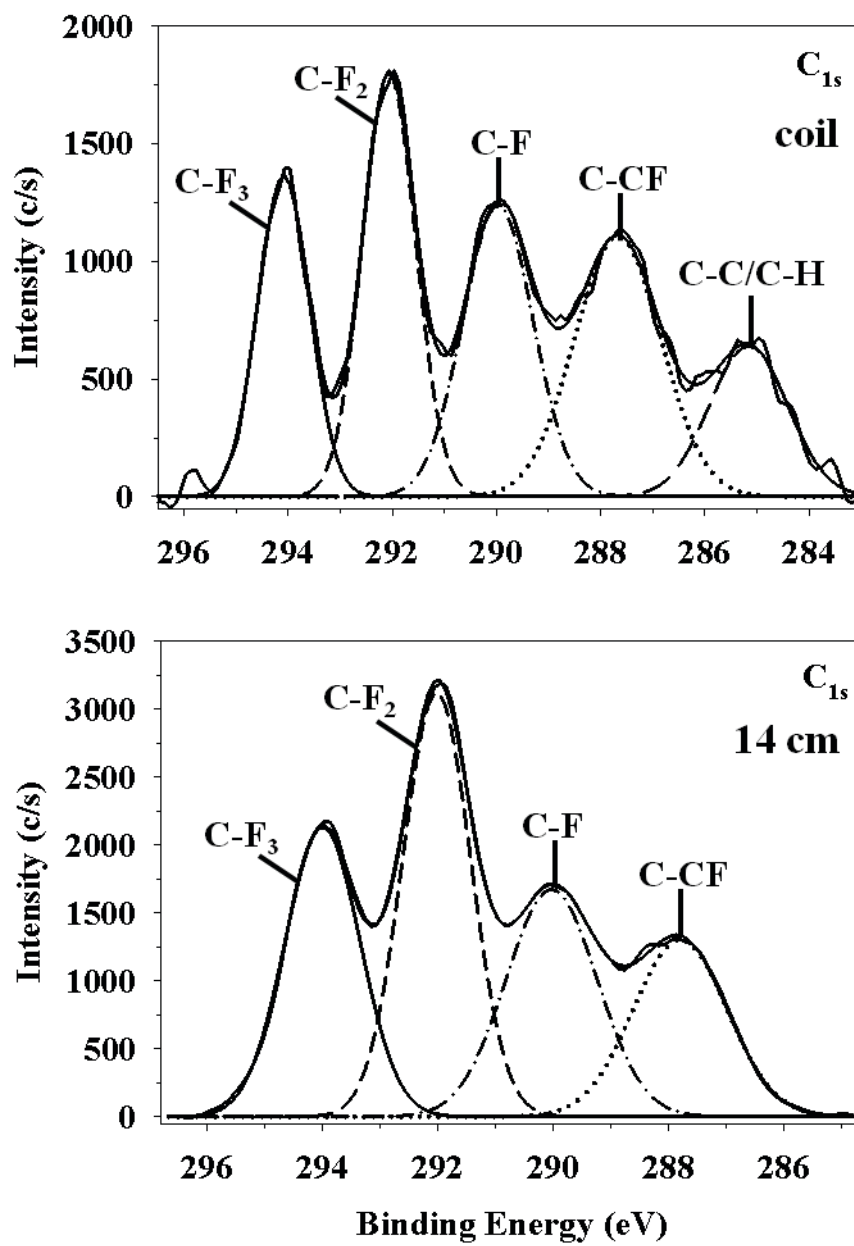


**Figure 7.8** High-resolution  $C_{1s}$  XPS spectrum of 100%  $C_3F_8$  plasma treated Si wafers (a) in the coil and (b) 14 cm downstream from the coil.

For further confirmation of the differences we see in sampling sites, Si wafers placed in the coil region and at 14 cm downstream from the coil (not placed in the rotating drum) were treated with a 100% C<sub>3</sub>F<sub>8</sub> plasma. High-resolution C<sub>1s</sub> XPS data, Fig. 7.8, confirm that a FC film was deposited. Spectra for substrates placed in the coil region, Fig. 7.8a, exhibit five primary binding environments (C-C/C-H, -C-CF, -CF, -CF<sub>2</sub>, and -CF<sub>3</sub>). This is confirmed through the elemental composition data, Table 7.1, which show low percentage of Si and O. Substrates deposited 14 cm downstream from the coil region exhibit four binding environments (C-CF, C-F, C-F<sub>2</sub>, and C-F<sub>3</sub>) that are typical for this type of plasma polymer.<sup>20</sup> Elemental composition data in Table 7.1 shows increasing percentages of both C and F and decreasing amounts of Si and O as the substrate position moved away from the coil region. This suggests that in the coil region of the reactor, a competition between deposition and etching is occurring resulting in thinner films, and more deposition occurs further downstream from the coil at 14 cm as expected. These binding environments results were the same at all sampling sites further confirming that the confinement of the plasma is not exclusively in the rotating drum, but between the rotating drum and the reactor walls as well. This explains why we see inconsistent surface compositions for all FC plasma treated zeolites.

#### **7.4 Summary and Future Work**

This work explored the surface modification of zeolite X in the coil region of a new rotating drum reactor with CF<sub>4</sub>, C<sub>2</sub>F<sub>6</sub> and C<sub>3</sub>F<sub>8</sub> plasma systems. Clearly these studies are in its early stages with only a few groups performing research on plasma modification of zeolite materials. Thus, the overarching goals of this research were to plasma treat the total surface area of the zeolites, ideally using a new rotating drum reactor while not

damaging the zeolites surface. To fully satisfy the first goal of completely modifying the surface of the zeolites, modification to the rotating drum reactor design is necessary. Containment of the plasma glow inside the rotating drum is vital to the success of this surface modification procedure. To achieve this, the rotating drum, Fig. 7.1, should incorporate holes at the downstream end to allow for plasma species to easily flow through the rotation chamber and react with the zeolites. Additionally, the position of the rotating drum must be adjustable relative to the coil region. This will ensure that the precise chemistry of surface modification or film deposition can be controlled. The second goal of preventing plasma damage to the zeolites was much more easily achieved. The data presented here show the plasma treatments used did not appreciably damage the surface of the zeolites. Moreover there was some evidence of FC coatings forming on the zeolites using the  $C_2F_6$  and  $C_3F_8$  plasma treatments. Coatings of this nature were not discussed by Yamazaki and coworkers and they did not present any morphological data. Without these critical pieces of information, it is virtually impossible to make any meaningful comparisons to previous work on these systems. To change a zeolites' surface to be more hydrophobic, it would be desirable to change the surface functional groups without depositing a thick coating that could change the other properties of the zeolites. For example, deposition of blanket-like coatings could cover the zeolites pores, thereby decreasing their efficacy as adsorbants.

Once the rotating reactor design is optimized, further studies can be performed to better classify the hydrophilic/hydrophobic nature of the zeolite surface and to determine the mechanisms necessary to facilitate the replacement of  $-OH$  groups on the surface of the zeolites. The first potential study involves analyzing the zeta potentials of untreated

zeolites, 100% C<sub>3</sub>F<sub>8</sub> plasma treated zeolites, and 100% NH<sub>3</sub> plasma treated zeolites using an Anton Parr electrokinetic analyzer. These measurements will provide the isoelectric point of these materials and subsequently the surface charge can be calculated. Untreated zeolites are expected to have an acidic surface based on their overall net negative charge. Treating zeolites with both 100% C<sub>3</sub>F<sub>8</sub> and 100% NH<sub>3</sub> plasmas should shift the overall surface charge to a net positive resulting from the replacement of surface –OH groups with –CF<sub>x</sub> species or –NH<sub>x</sub> groups.<sup>18</sup> These modified surfaces could also be analyzed with infrared (IR) spectroscopy. If the –OH groups were in fact being replaced, IR spectra would show a reduction in the –OH stretch and an increase in –CF<sub>x</sub> and –NH stretches from both the C<sub>3</sub>F<sub>8</sub> and NH<sub>3</sub> plasma treated zeolites.

## 7.5 References

- <sup>1</sup>C. Otero Arean, *Zeolites and Intrazeolite Chemistry: Insights from Infrared Spectroscopy* Vol. 22 (Overseas Publishers Association 2000).
- <sup>2</sup>*Handbook of Zeolite Science and Technology* (Marcel Dekker, Inc, New York, 2003).
- <sup>3</sup>A. A. G. Tomlinson, *Modern Zeolites: Structure and Function in Detergents and Petrochemicals*, Vol. 3 (Trans Tech Publications, New York, 1998).
- <sup>4</sup>H. Arai and M. Machida, *Catal. Today* **22**, 97 (1994).
- <sup>5</sup>T. Montanari, I. Salla, and G. Busca, *Microporous Mesoporous Mater.* **109**, 216 (2008).
- <sup>6</sup>A. K. Ghosh and R. A. Kydd, *Zeolites* **10**, 766 (1990).
- <sup>7</sup>E. Y. Hwang, J. R. Kim, J. K. Choi, H. C. Woo, and D. W. Park, *J. Anal. Appl. Pyrolysis* **62**, 351 (2002).
- <sup>8</sup>M. L. Steen, L. Hymas, E. D. Havey, N. E. Capps, D. G. Castner, and E. R. Fisher, *Journal of Membr. Sci.* **188**, 97 (2001).
- <sup>9</sup>K. Nishihara, K. Furukawa, H. Ijiri, and S. Yamazaki, *Trans. Mater. Res. Soc. Jpn* **26**, 1201 (2001).
- <sup>10</sup>S. Yamazaki, T. Nishimura, K. Furukawa, H. Ijiri, and K. Tsutsumi, *Zeolites* **135**, 1718 (2001).
- <sup>11</sup>R. d'Agostino, F. Cramarossa, F. Fracassi, and F. Illuzzi, *Plasma Deposition, Treatment, and Etching of Polymers* (Academic Press, INC., San Diego, 1990).
- <sup>12</sup>D. Zhang and M. J. Kushner, *J. Vac. Sci. Technol. A* **19**, 524 (2001).
- <sup>13</sup>I. T. Martin, G. S. Malkov, C. I. Butoi, and E. R. Fisher, *J. Vac. Sci. Technol. A* **22**, 227 (2004).
- <sup>14</sup>J. C. Shearer, M. J. Fisher, D. Hoogeland, and E. R. Fisher, *Appl. Surf. Sci.* **256**, 2081 (2010).
- <sup>15</sup>D. Kim, J. Kang, and K. Kim, *J. Ind. Eng. Chem.* **16**, 997 (2010).
- <sup>16</sup>A. Nasonova, H. C. Pham, D. Kim, W. Kim, T. Charinpanitkul, and K. Kim, *Journal Nanosci. Nanotechnol.* **11**, 1323 (2011).
- <sup>17</sup>D. Kim, H. C. Pham, and K. Kim, *Surf. Rev. Lett.* **17**, 329 (2010).
- <sup>18</sup>K. J. Trevino, J. C. Shearer, B. D. Tompkins, and E. R. Fisher, *Plasma Process Polym*, Submitted for Publication (2011).
- <sup>19</sup>M. F. Cuddy and E. R. Fisher, not published.
- <sup>20</sup>M. F. Cuddy and E. R. Fisher, *J. Appl. Phys.* **108**, 03303 (2010).

## CHAPTER 8

### DEPOSITION OF a-CN<sub>x</sub> MATERIALS IN BrCN PLASMAS: FILM CHARACTERIZATION IN SUPPORT OF MECHANISMS FOR ADHESION BEHAVIOR

This chapter contains data from manuscript accepted by the Journal *ACS Applied Materials and Interfaces* and was written by Joshua M. Stillahn, Kristina J. Trevino, and Ellen R. Fisher. The major contribution made to this work by K. J. Trevino was X-ray photoelectron spectroscopy (XPS) data, which are presented in this chapter are complementary to data published previously in Joshua M. Stillahn's dissertation. The data presented here provide insight into the relationship between film composition and delamination of materials deposited in BrCN-containing plasmas. Delamination is thought to be the result of humidity, film stress, hydrocarbon species, and Br content in the film. These factors are discussed in relation to composition studies using XPS.

## 8.1 Introduction

Advanced materials systems, such as ultralarge scale integrated circuits, various protective coatings, solar cells, and magnetic memory devices rely on multilayer devices integrating different types of materials. As such, a key factor in the efficacy of these systems and devices is the robustness of film-substrate and film-film interfaces, specifically with respect to mechanical properties.<sup>1-3</sup> In particular, films that undergo thermal changes, radiation exposure, or ion bombardment can deform, crack, or delaminate from the underlying substrate causing device failure. In addition, diffusion of reactive molecules such as water or ions can also result in delamination or cracking.<sup>3-5</sup> Often, protective coatings as well as dielectric materials in integrated circuits are formed using plasma-enhanced chemical vapor deposition (PECVD), a method that has numerous advantages, but that also often exposes the film to a range of high energy species that can ultimately contribute to mechanical failure of the resulting material. Thus, examination of the mechanical performance and reliability of film/substrate interfaces created via PECVD is an important component of understanding the entire plasma deposition process.

Deposition of a-CN<sub>x</sub> films in PECVD systems have largely focused on mixed precursor systems, such as CH<sub>4</sub>/N<sub>2</sub>, which allow independent control over C and N densities in the gas phase. Previous results from our lab highlight the relatively high surface reactivity of CN radicals in CH<sub>4</sub>/N<sub>2</sub> discharges,<sup>6</sup> but the chemical complexity of these mixed systems limits the confidence with which contributions of CN radicals to the deposition process can be established. To alleviate some of this ambiguity, surface

interactions of CN from both  $\text{CH}_3\text{CN}$ <sup>7</sup> and  $\text{BrCN}$ <sup>8</sup> suggest surface reactions favor the incorporation of CN during film deposition.

The BrCN plasma system presents an interesting opportunity to further expand on single precursor studies. BrCN is also well-suited to the reductionist approach we have taken to studying a-CN<sub>x</sub> systems as it allows observation of CN radical behavior in the absence of other depositing species, such as H or CH<sub>x</sub> species. Because CN is the primary deposition species in BrCN discharges, it becomes feasible to deposit a-CN<sub>x</sub> materials that do not contain hydrogen. Such films have been shown to exhibit substantially different microstructures and mechanical properties,<sup>12-15</sup> thereby creating a possible link between the molecular level plasma chemistry and possible performance and reliability issues with a-CN<sub>x</sub> films. Notably, films without hydrogen are predominately obtained by sputtering graphite in a N<sub>2</sub> atmosphere, and reports of the formation of H-free a-CN<sub>x</sub> by PECVD are few.<sup>15,16</sup>

This chapter presents results from a-CN<sub>x</sub> depositions in systems containing BrCN. Adhesion of the deposited film to the underlying substrate has been shown to delaminate when exposed to atmosphere and become visibly rougher. These results were observed with optical micrographs and scanning electron microscopy images. The root cause of these results is due to atmospheric humidity, the films stress, hydrocarbon species, and Br content in the film. With the aid of x-ray photoelectron spectroscopy (XPS) we can gain a greater insight to the incorporation of CN and additional chemical composition of these films after deposition prior to delamination.

## 8.2 Results/Discussion

Delamination behavior such as that observed in our 100% BrCN plasma systems has been reported in the deposition of carbon nitride<sup>17</sup> and boron nitride materials,<sup>4</sup> with an emphasis on the role of humidity and material stresses in delamination. Peponas et al. employed infrared absorption spectroscopy (IRAS) measurements to hypothesize that delamination involves chemical reactions between H<sub>2</sub>O and isocyanate (R-C=N=O) groups at the film-substrate interface.<sup>18</sup> Although this type of absorption spectroscopy constitutes a bulk characterization technique and thus does not provide conclusive evidence of interfacial reactions, the data show that the process of delamination is not simply a mechanical phenomenon, but involves chemical changes as well.

Another notable aspect of both the boron nitride and carbon nitride studies is that they involve materials deposited by sputter coating; our observation of the same behavior in PECVD systems suggests there are some basic chemical similarities between films deposited with the two deposition methods. Interestingly, however, we do not observe delamination of films deposited in 100% CH<sub>3</sub>CN plasmas, Figure 8.1a. These films have a uniform appearance throughout the field of view, whereas the film deposited in a 100% BrCN plasma very clearly has delaminated from the substrate, Figure 8.1b.

Chemical characterization of the films produced in our plasmas was pursued with Fourier transform infrared (FTIR) spectroscopy and XPS. The FTIR spectra for films deposited on KBr pellets in 100% CH<sub>3</sub>CN and 100% BrCN plasmas, Figure 8.2,

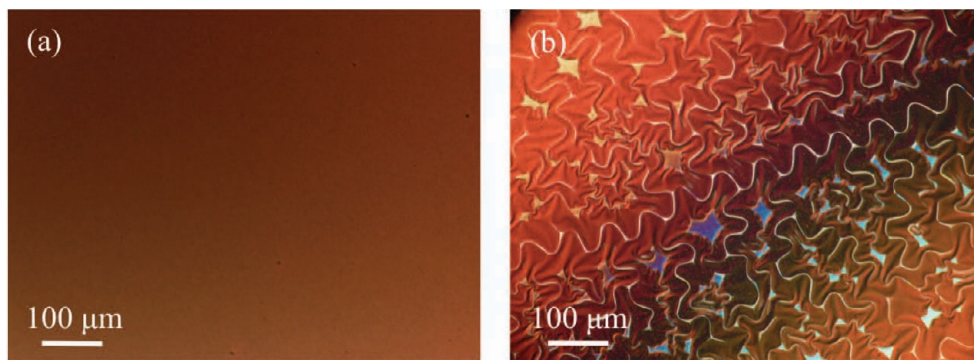


**Figure 8.1** Phase contrast microscope images of films deposited for 20 min in (a) 100%  $\text{CH}_3\text{CN}$  and (b) 100%  $\text{BrCN}$  plasmas. In each case, total gas pressure = 100 mTorr and rf power = 50 W.

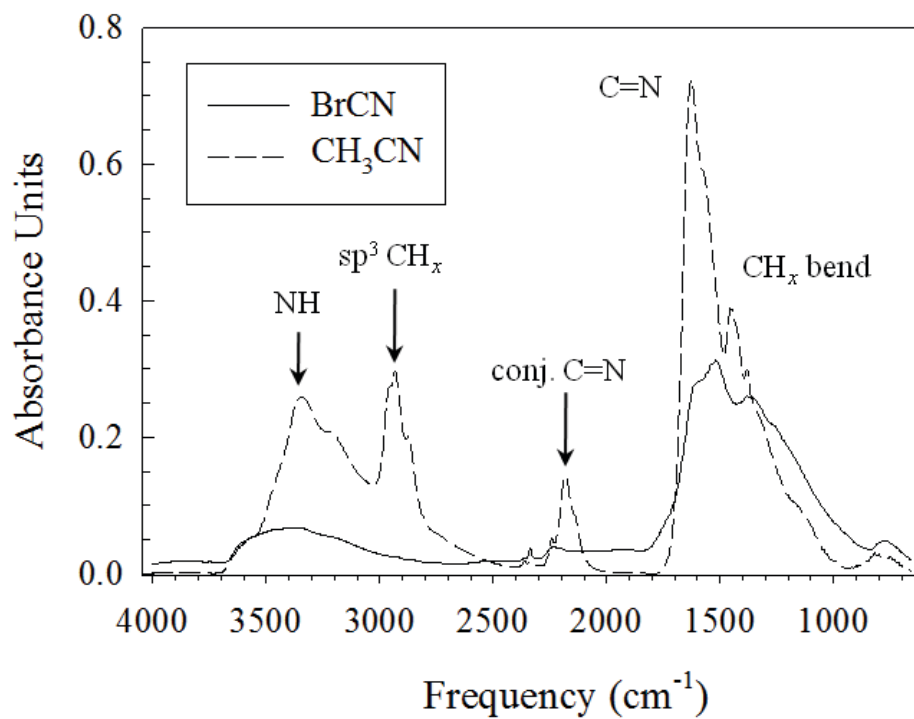


**Figure 8.2** Corrected transmission FTIR spectra of film deposited for one hour on a KBr substrate in 100% BrCN (solid line) and 100% CH<sub>3</sub>CN (dashed line) plasmas.

show absorption features in the region of  $1500\text{ cm}^{-1}$  and are assigned to C=N stretching and  $\text{CH}_x$  bending modes. A broad absorption band centered near  $3400\text{ cm}^{-1}$  is visible in both spectra, though more well-defined absorption bands somewhat obscure this feature in the spectrum of the film deposited from a 100%  $\text{CH}_3\text{CN}$  plasma. We assign this peak to C=NH, but it has been associated with OH stretching in the work of Benlahsen and coworkers.<sup>18</sup> Further studies are needed to resolve this discrepancy, but this spectral feature may prove useful in understanding the effects of  $\text{H}_2\text{O}$  on delamination behavior. The absence of sharp NH and  $\text{sp}^3\text{ CH}_x$  stretching modes in the BrCN films is not surprising, as we do not expect to have hydrogen in the discharge. The lack of conjugated C=N absorption in the BrCN film is notable, however, as this is indicative of differences in the microstructure of the two films. Note also that the absorption spectrum shown in Figure 8.2 for the film deposited in a BrCN plasma was measured after the films had buckled, and may not accurately portray the composition and structure of the as deposited material.<sup>18</sup> Subsequent investigation of film delamination focused on establishing fundamental connections between the behavior of films deposited in the different plasma systems. As the composition and morphology of pressed KBr pellets can be unpredictable, Si wafers were used as substrates for the remainder of the studies.

High-resolution  $\text{C}_{1s}$  XPS spectra for films deposited on Si substrates in 100% BrCN and 100%  $\text{CH}_3\text{CN}$  plasmas are shown in Figure 8.3. The  $\text{C}_{1s}$  spectrum for films deposited in 100% BrCN plasmas, Figure 8.3a, exhibits three major peaks at 285.0 eV, 287.0 eV, and 288.9 eV, designated as C-C/C-H, C=N ( $\text{sp}^2$  carbon), and C-N ( $\text{sp}^3$  carbon), respectively. Although the same peaks appear in the spectrum for the film deposited in

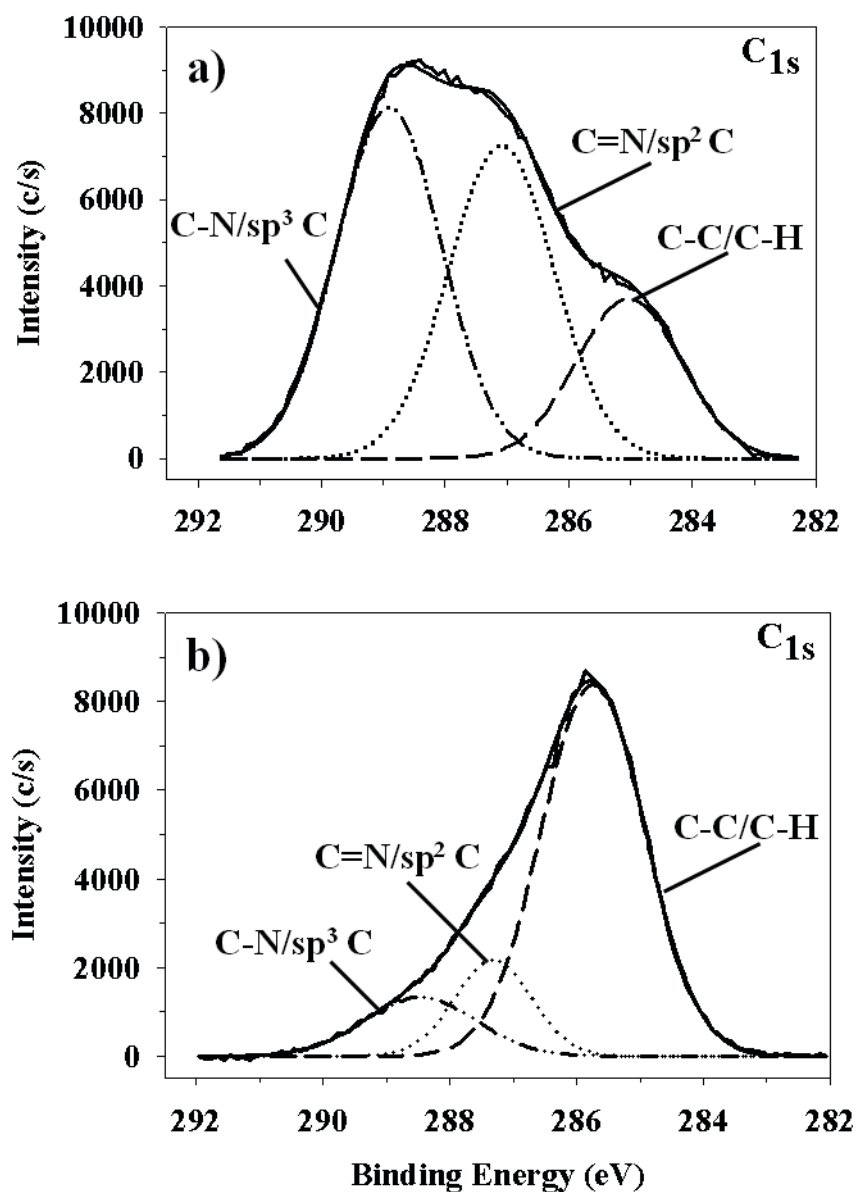


**Figure 8.3** High-resolution  $C_{1s}$  XPS spectra for a film deposited in (a) 100% BrCN and (b) 100%  $CH_3CN$  plasmas. Both spectra are for freshly deposited samples and contain three binding environments: C-C/C-H (long dash), C=N,  $sp^2$  carbon (dotted line), and C-N,  $sp^3$  carbon (dash-dot-dot). Plasma conditions were: 100 mTorr and 50W for 40 minutes.

100% CH<sub>3</sub>CN, Figure 8.3b, their respective contributions to the total peak area differ dramatically. Specifically, films deposited in 100% BrCN plasmas have a larger fraction of sp<sup>2</sup> and sp<sup>3</sup> carbon, which has been identified as contributing to delamination in a-CN<sub>x</sub> films.<sup>5,19</sup> XPS elemental analysis, Table 8.1, reveals these films contain small amounts of oxygen; thus, the two peaks assigned to C=N and C-N could also contain C=O and C-O moieties as contributions from oxygen-containing species are not resolvable from those of nitrogen-containing species.

Films deposited from BrCN plasmas also include small but significant levels of bromine, Table 8.1. Figure 8.4 contains the high resolution Br<sub>3d</sub> XPS spectrum for a film deposited from 100% BrCN. There are four different binding environments, suggesting bromine is incorporated in these films in different forms. Notably, the largest peak at ~70.8 eV can be attributed to bromine covalently bonded to carbon.<sup>20</sup> The smaller peak at higher binding energies (72.2 eV) likely corresponds to oxybrominated derivatives (BrO<sub>x</sub><sup>-</sup>) as these are the only species with higher binding energies than covalently bound bromine. The two peaks at 69.3 and 68.2 are assigned to bromide (Br<sup>-</sup>) species, most likely in the form of physisorbed BrH, and C-Br<sub>2</sub> surface charge transfer complexes, respectively.<sup>20</sup> Given the relatively high contributions from bromine not covalently bound to carbon, we anticipate that heating or prolonged exposure to atmosphere could decrease or eliminate the bromine from these films.

One possible reason for why film adhesion differs so dramatically between BrCN and CH<sub>3</sub>CN discharges is that the films deposited in BrCN plasmas are less cross-linked (i.e., have a higher density of terminating functional groups) than films deposited in CH<sub>3</sub>CN discharges. To mirror the gas phase composition in CH<sub>3</sub>CN discharges, CH<sub>4</sub> was

**Table 8.1** XPS percent composition and C/N ratios for freshly treated and aged samples

		<b>%C</b>	<b>%N</b>	<b>%O</b>	<b>%Br</b>	<b>%Au</b>	<b>C/N</b>
<b>100% BrCN</b>	Fresh	42.0 ± 3.2	35.1 ± 4.0	12.5 ± 0.0	6.7 ± 1.3	3.7 ± 1.0	0.8 ± 0.2
	Aged	55.8 ± 2.0	30.0 ± 1.9	8.0 ± 0.3	-	6.2 ± 0.4	0.5 ± 0.1
<b>100% CH<sub>3</sub>CN</b>	Fresh	64.4 ± 1.9	19.6 ± 1.3	9.2 ± 1.2	-	6.8 ± 2.0	0.3 ± 0.0
	Aged	59.5 ± 1.1	21.0 ± 1.0	15.0 ± 2.2	-	4.5 ± 0.3	0.4 ± 0.0
<b>50:50 BrCN/CH<sub>4</sub></b>	Fresh	61.2 ± 1.5	2.5 ± 1.1	9.2 ± 1.3	-	4.6 ± 1.0	0.4 ± 0.0
	Aged	66.3 ± 3.3	11.3 ± 2.7	18.3 ± 0.2	-	4.1 ± 1.0	0.4 ± 0.1
<b>100% BrCN:N<sub>2</sub> plasma treated</b>	Fresh	39.1 ± 1.3	36.9 ± 1.5	13.5 ± 2.0	6.9 ± 1.6	3.7 ± 0.8	1.1 ± 0.1

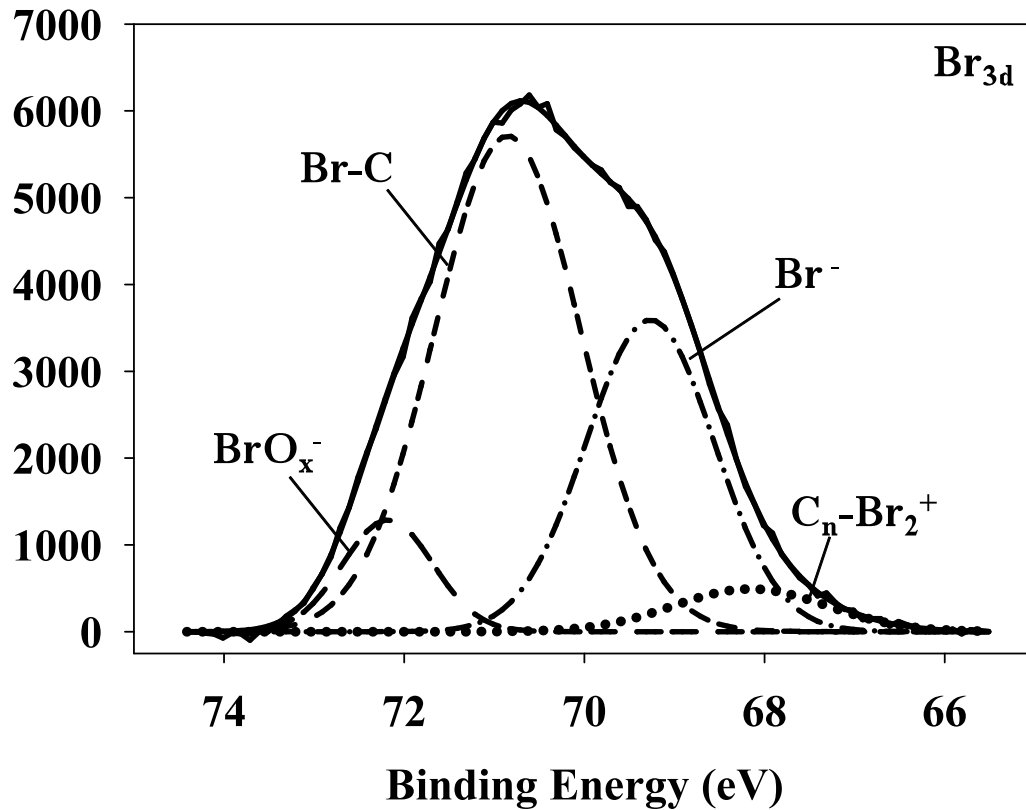


**Figure 8.4** High-resolution Br<sub>3d</sub> XPS spectrum for a film freshly deposited in a 100% BrCN plasma, containing four binding environments: BrO<sub>x</sub><sup>-</sup> (medium dash); Br covalently bonded to carbon (short dash); Br<sup>-</sup> (dash-dot); and C<sub>n</sub>-Br<sub>2</sub><sup>+</sup> (dotted). Plasma conditions were: 100 mTorr, 50 W for 40 minutes.

added to the BrCN systems, thereby adding a purely hydrocarbon (i.e.  $\text{CH}_x$ ) component to the flow. In addition to changes associated with the co-deposition of  $\text{CH}_x$  and CN species in BrCN/ $\text{CH}_4$  discharges, we anticipated that the presence of atomic H might also favor increased cross-linking during deposition. This idea is supported by mechanistic studies of diamond-like carbon (DLC) deposition by Von Keudell and coworkers<sup>21</sup> who found that atomic H can abstract terminating H atoms from the surface of a growing film to create active sites. The presence of these active sites promotes cross-linking as additional precursors (particularly  $\text{CH}_3$ ) arrive at the DLC film growth front. The observation of  $\text{CH}_x^+$  and  $\text{H}^*$  in  $\text{CH}_3\text{CN}$  plasmas<sup>7</sup> along with the abundance of unsaturated  $\text{C}\equiv\text{N}$  bonds would favor such a mechanism in a- $\text{CN}_x$  deposition as well. Indeed, the same strategy was shown by Kim et al. to improve the adhesion of carbon-containing boron nitride (BN:C) materials obtained by PECVD, with reductions in both the compressive stress of the material and its susceptibility to humidity.<sup>22</sup>

A high-resolution  $\text{C}_{1s}$  XPS spectrum for a film deposited from a 50:50 BrCN/ $\text{CH}_4$  plasma is shown in Figure 8.5. This spectrum is very similar to that collected for the film deposited from 100% BrCN, Figure 8.3a. The primary difference is that the C-C/C-H peak in the film deposited from the BrCN/ $\text{CH}_4$  plasma is significantly higher than the same peak in the film deposited from 100% BrCN. This suggests BrCN/ $\text{CH}_4$  films would also be unstable with respect to delamination. Figure 8.6 contains an optical micrograph of a film deposited in a plasma containing equal partial pressures of BrCN and  $\text{CH}_4$ , clearly showing delamination has occurred. This indicates that even with additional hydrocarbon, the resulting film remains porous enough to allow diffusion of water vapor

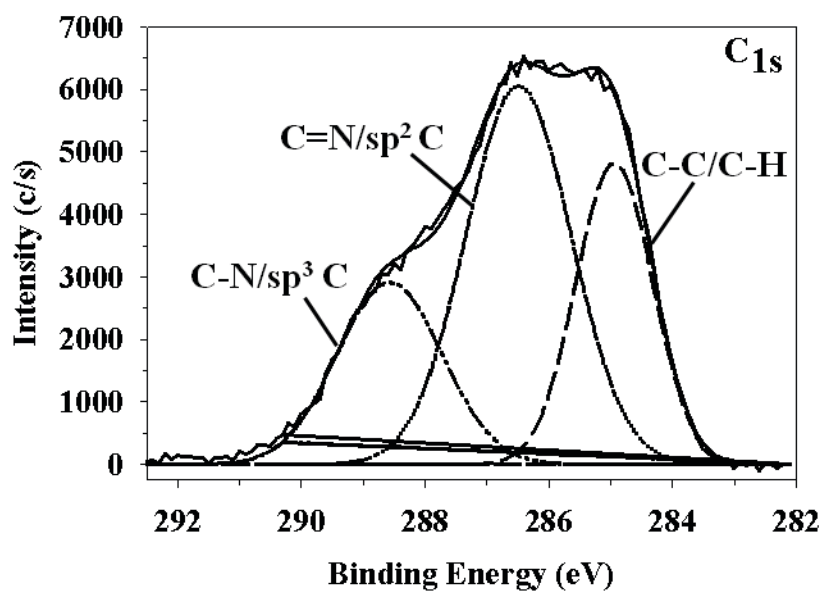


**Figure 8.5** High-resolution C<sub>1s</sub> XPS spectra for a film deposited in a 50:50 BrCN/CH<sub>4</sub> plasma. The spectrum is for a freshly deposited sample and contains three binding environments: C-C/C-H (long dash), C=N, sp<sup>2</sup> carbon (dotted line), and C-N, sp<sup>3</sup> carbon (dash-dot-dot). Plasma conditions were: 100 mTorr and 50W for 20 minutes.

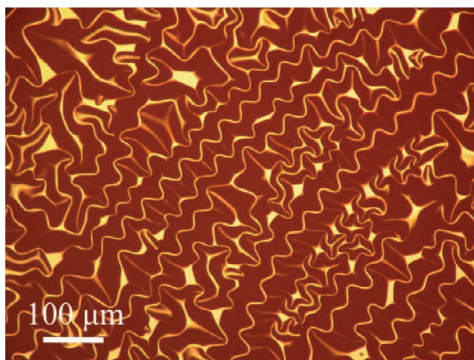


**Figure 8.6** Phase contrast microscope image of a film deposited for 40 min in a 50:50 BrCN/CH<sub>4</sub> plasma. The total gas pressure = 100 mTorr and rf power = 50 W.

to the interface. Such images suggest that the presence of hydrocarbons and atomic H does not sufficiently alter the deposition chemistry so as to prevent film delamination.

Given that our a-CN<sub>x</sub> films are susceptible to humidity, an additional factor to consider is possible effects of aging. Figure 8.7 shows XPS high-resolution C<sub>1s</sub> spectra for aged films deposited in the three plasma systems: 100% BrCN, 100% CH<sub>3</sub>CN, and 50:50 BrCN/CH<sub>4</sub>. Comparison of C<sub>1s</sub> spectra for aged and fresh samples reveals that aging dramatically changes the binding environment in the films. For the films deposited from plasmas containing BrCN, we see a sharp increase in the C-C/C-H peak, which is likely the result of adventitious carbon being incorporated during the aging period, Table 8.1. In contrast, the C<sub>1s</sub> binding environments in the film deposited from CH<sub>3</sub>CN have shifted from primarily C-C/C-H to sp<sup>2</sup> and sp<sup>3</sup> carbon bonded to nitrogen and/or oxygen. We also measure a concomitant increase in both nitrogen and oxygen content, Table 8.1. Thus, these films appear to oxidize with time, whereas the films deposited from BrCN systems do not. Notably, the aged film deposited from the 100% BrCN plasma does not contain any Br, consistent with our analysis of the Br<sub>3d</sub> spectrum for the fresh films.

To explore the hypothesis that Br-content is responsible for the delamination of our films, mixtures of gases were used according to a simple model that allows for variation of the effective Br-content in the gas phase. Specifically, the precursors CH<sub>3</sub>CN, BrCN, and CH<sub>4</sub> were each considered in terms of the number of equivalents of Br, CH<sub>x</sub>, and CN they contribute to the discharge. High resolution C<sub>1s</sub> XPS spectra for the different amounts of CH<sub>3</sub>CN, BrCN, and CH<sub>4</sub> are shown in Figure 8.8 and reveal that films deposited in 1:1:1 and 14:43:43 CH<sub>3</sub>CN/BrCN/CH<sub>4</sub> mixtures resemble those

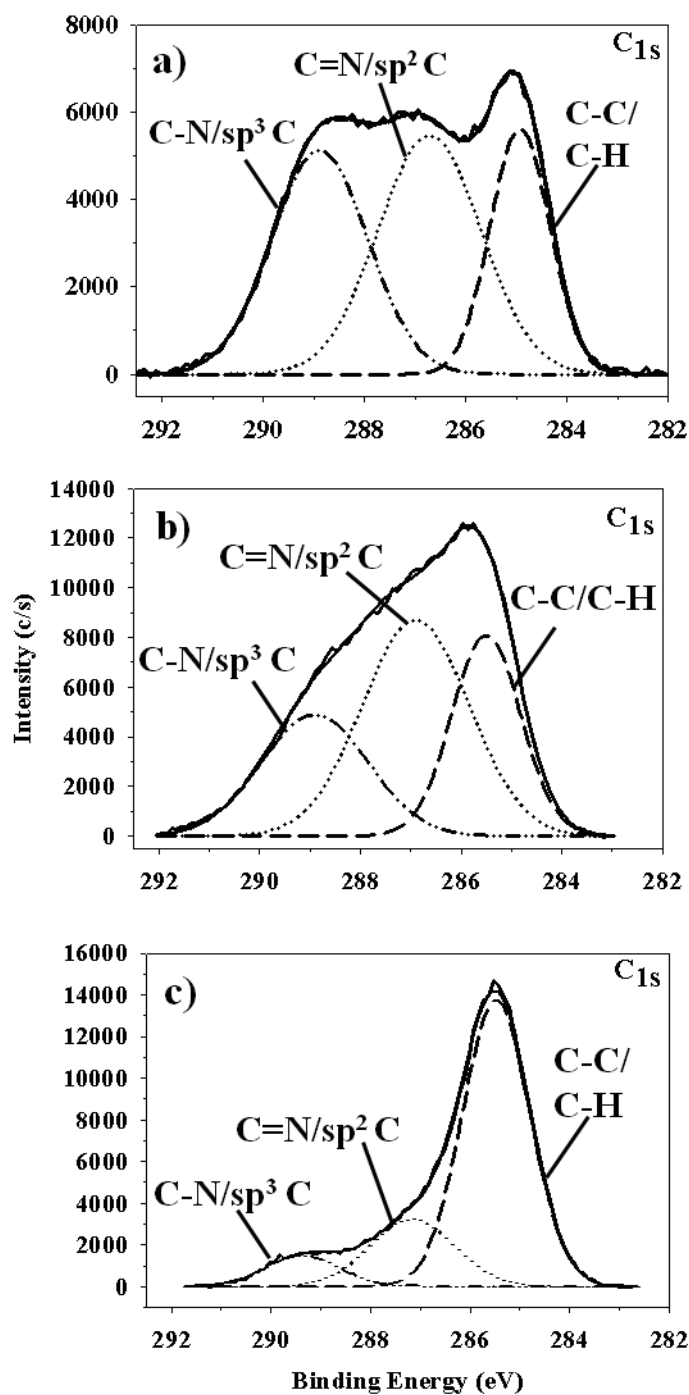


**Figure 8.7** High-resolution  $C_{1s}$  XPS spectra for films deposited in (a) 100% BrCN; (b) 100% CH<sub>3</sub>CN; and (c) a 50:50 BrCN/CH<sub>4</sub> plasma. The spectra are for aged samples (2-9 months) and contain three binding environments: C-C/C-H (long dash), C=N,  $sp^2$  carbon (dotted line), and C-N,  $sp^3$  carbon (dash-dot-dot). Plasma conditions: 100 mTorr and 50 W; BrCN and CH<sub>3</sub>CN were run for 40 minutes and the BrCN/CH<sub>4</sub> mixture was run for 20 minutes.

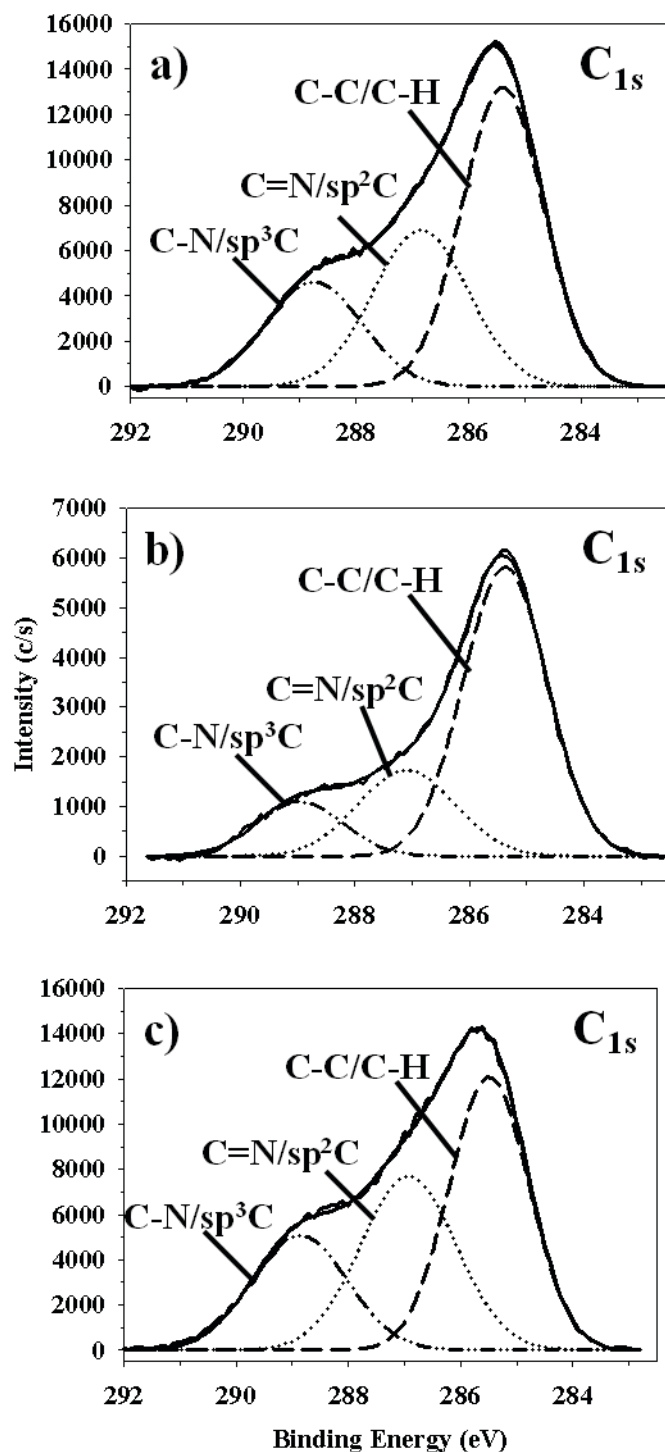


**Figure 8.8** High-resolution  $C_{1s}$  XPS spectra for films deposited in (a) 1:1:1; (b) 14:43:43; and (c) 3:1:1  $CH_3CN/BrCN/CH_4$  plasmas. The spectra are for fresh samples and contain three binding environments: C-C/C-H (long dash), C=N,  $sp^2$  carbon (dotted line), and C-N,  $sp^3$  carbon (dash-dot-dot). Plasma conditions: 100 mTorr and 50 W; plasma mixture was run for 20 minutes.

deposited in the 50/50 BrCN/CH<sub>4</sub> plasma, Figure 8.7c, whereas films deposited in the 3:1:1 CH<sub>3</sub>CN/BrCN/CH<sub>4</sub> gas mixture resemble those deposited in 100% CH<sub>3</sub>CN plasmas, Figure 8.7b.

### 8.3 Summary

In this work, the chemical composition of a-CN<sub>x</sub> films deposited in plasma discharges containing BrCN was explored. Attempts to understand the behavior of film delamination were examined with XPS and supportive results were acquired. In the 100% CH<sub>3</sub>CN plasmas we found that carbon was present in both sp<sup>2</sup> and sp<sup>3</sup> hybridized states, suggesting this may be contributing to the observed film delamination. In films deposited from 100% BrCN plasmas, small amounts of Br were present that disappeared over time, indicating accumulation of adventitious carbon. In our mixed precursor systems, 50:50 BrCN/CH<sub>4</sub> for example, film XPS results were similar to those found for films deposited from 100% BrCN plasmas, suggesting that delamination would occur. Adhesion of an a-CN<sub>x</sub> film to a Si substrate can be maintained, however, when the effects of Br addition are attenuated (e.g. by additional hydrocarbon content in the plasma) even under humid conditions as evidenced by optical micrographs and XPS data.

### 8.3 References

- <sup>1</sup>L. L. Mishnaevsky and D. J. Gross, *Int. Appl. Mech* **40**, 140 (2004).
- <sup>2</sup>A. R. Shugurov and A. V. Panin, *Phys. Mesomech* **13**, 79 (2010).
- <sup>3</sup>T. S. Kim and R. H. Dauskardt, *IEEE Trans. Device Mater. Reliab.* **9**, 509 (2009).
- <sup>4</sup>J. Moller, D. Reiche, M. Bobeth, and W. Pompe, *Surf. Coating Technol.* **150**, 8 (2002).
- <sup>5</sup>M. Lejeune, M. Benlahsen, and P. Lemoine, *Solid State Commun.* **135**, 434 (2005).
- <sup>6</sup>D. Liu and E. R. Fisher, *J. Vac. Sci. Technol. A* **25**, 368 (2007).
- <sup>7</sup>J. M. Stillahn and E. R. Fisher, *J. Phys. Chem. C* **113**, 1963 (2009).
- <sup>8</sup>J. M. Stillahn and E. R. Fisher, *J. Phys. Chem. A* **114**, 5287 (2010).
- <sup>9</sup>H. Ito, Y. Ozaki, K. Suzuki, and T. Kuchitsu, *J. Chem. Phys.* **96**, 4195 (1992).
- <sup>10</sup>H. F. I. Schaefer and T. G. Heil, *J. Chem. Phys.* **54**, 2573 (1971).
- <sup>11</sup>H. Ito, N. Ito, T. Takahashi, H. Takamatsu, D. Tanaka, and H. Saitoh, *Jpn. J. Appl. Phys. Part I* **39**, 1371 (2000).
- <sup>12</sup>J. M. Mendez, A. Gaona-Couto, S. Muhl, and S. J. Jimenez-Sandoval, *J. Phys.: Condensed Matter* **11**, 5225 (1999).
- <sup>13</sup>N. Hellgren, M. P. Johansson, B. Hjorvarsson, E. Broitman, M. Ostblom, B. Liedberg, L. Hultman, and J. E. Sundgren, *J. Vac. Sci. Technol. A* **18**, 2349 (2000).
- <sup>14</sup>P. Hammer, N. M. Victoria, and F. Alvarez, *J. Vac. Sci. Technol. A* **16**, 2941 (1998).
- <sup>15</sup>M. Ricci, M. Trinquocoste, F. Auguste, R. Canet, P. Delhaes, C. Guimon, G. Pfister-Guillouzo, B. Nvesten, and J. P. Issi, *J. Mater. Res.* **8**, 480 (1993).
- <sup>16</sup>H. Saitoh, H. Takamatsu, D. Tanaka, N. Ito, S. Ohshio, and H. Ito, *J. Appl. Phys. Part I* **39**, 1258 (2000).
- <sup>17</sup>S. Peponas, M. Guedda, and M. Benlahsen, *Solid State Commun.* **146**, 78 (2008).
- <sup>18</sup>S. Peponas, M. Benlahsen, and M. Guedda, *J. Appl. Phys.* **106**, 013525 (2009).
- <sup>19</sup>S. Peponas, M. Guedda, and M. Benlahsen, *Appl. Surf. Sci.* **255**, 8706 (2009).
- <sup>20</sup>E. Papirer, R. Lacroix, J. B. Donnet, G. Nanse, and P. Fioux, *Carbon* **32**, 1342 (1994).
- <sup>21</sup>A. Von Keudell, T. Schwarz-Selinger, and W. Jacob, *J. Appl. Phys.* **89**, 2979 (2001).
- <sup>22</sup>K. B. Kim and S. H. Kim, *J. Vac. Sci. Technol. A* **18**, 900 (2000).

## **CHAPTER 9**

### **RESEARCH SUMMARY AND PERSPECTIVES**

This final chapter describes the research advancement in the areas of gas-phase chemistry, plasma surface modification, and plasma enhanced chemical vapor deposition. The benefits of the previous chapters allowed us to gain a better understanding of the plasma processes that are occurring in the gas-phase for a collection of plasma precursors as well as insight to the plasma modification of metal oxides surfaces and the film properties of deposited a-CN<sub>x</sub>. The end of this chapter considers additional areas of study that would prove useful for the advancement of related plasma research.

## 9.1 Research Summary

The understanding of complex plasma systems and their use for surface modification and deposition is a never-ending task. The many available gaseous precursors and the large selection of plasma systems allows for plasma research to be a viable and desirable option for a variety of material processing. Here, we have studied the gas phase of plasma systems to gain further insight to the processes that affect plasma surface modifications. Additionally, we have worked on projects that are both traditional and non-traditional as far as plasma surface interactions are concerned. The gas-phase properties studied in this dissertation included the breakdown and remediation of artificially contaminated wastewater and the measurement of internal and kinetic temperatures of plasma species in a collection of plasma systems. Plasma surface processing in this dissertation was fundamentally focused on surface modification, but contributions to plasma deposition were also discussed. Surface modification was explored for metal oxides through their isoelectric points (IEP) and surface functionality. The plasma treatment of Zeolite X was also examined to determine functional group incorporation and surface damage. Plasma deposition studies focused on the creation of amorphous carbon nitride ( $a\text{-CN}_x$ ) films. All of the above analyses aim at increasing our understanding of plasma systems or exploring new uses for plasmas with a non-traditional approach.

Qualitative measurement of the gas phase species in artificially contaminated water samples with methanol and methyl *tert*-butyl ether (MTBE) displayed that inductively coupled-plasma (ICP) systems can be used for the breakdown and remediation of organic contaminants in water. The presence of excited state species generated from the dissociation of the parent molecule (detected using optical emission spectroscopy (OES)),

indicated our plasma systems were indeed decomposing the organic contaminants. Additional mass spectrometry (MS) data showed that recombination of these species was not occurring, but oxidation was further reducing their hazardous nature. These results were encouraging as the study of water remediation with other plasma systems are complicated by plasma instabilities and water remediation volume.<sup>1,2</sup> The reactions that occurred in the gas phase were clearly dominated by the plasma parameters and species present in the plasma.

The internal and kinetic temperatures and the surface reactivity of radical species in the gas phase were examined to gain insight into the energetics of molecules formed in our plasmas. Specifically CH, SiH, OH, and NH were studied in single and mixed precursor systems to determine the relationship if any to their internal and kinetic temperatures and corresponding surface scatter coefficients. For both CH and SiH we found that surface scatter coefficients correlate to the electronic state of the radical as opposed to the internal or translational temperatures. NH and OH exhibit different results that suggest their mechanisms of formation and dispersion of energy directly affect their surface scatter coefficients. The reported surface scatter coefficients provided knowledge of the chemistry resulting from plasma-surface interactions and optimization parameters to allow for tailoring processes to a given application.

The change in metal oxide surface charge was studied by the plasma treatment of  $\text{SiO}_x\text{N}_y$ , native  $\text{SiO}_2$  (nat- $\text{SiO}_2$ ), and deposited  $\text{SiO}_2$  (dep- $\text{SiO}_2$ ) substrates using Ar,  $\text{H}_2\text{O}$ , and  $\text{NH}_3$  plasmas. Contact angle (CA) data along with x-ray photoelectron spectroscopy (XPS) data revealed that shifts in the surface charge had occurred based on the measured IEP values and changes in the surface functionality initially after plasma treatment and

over time. We found that depending on the plasma precursor and the plasma parameters used the IEP shifted to a more acidic/basic surface. These results were critical because few literature reports exist for measurements of IEP and surface change on plasma-treated metals, in comparison to those available for polymers,<sup>3,4</sup> glass,<sup>5</sup> and powders.<sup>6</sup> Due to the efficiency of plasmas, their uses can lead to exploration of non-traditional applications; once proved effective, however, they can quickly become the primary methodology used for materials processing.

One example of a non-traditional use of plasmas is the surface modification of zeolites. We found that surface modification of Zeolite X is achievable through the use of rf plasma discharges. In addition to the surface treatment, we have introduced a new rotating drum reactor that will, when perfected, essentially provide overall plasma surface treatment to zeolites. The basis of this reactor design stems from literature reports on the treatment of zeolites occurring in capacitively coupled plate reactors.<sup>7,8</sup> The preliminary results presented in this dissertation not only suggest plasma treatment was possible in the rotating reactor with all three fluorocarbon plasmas, but these treatments did impart any apparent damage to the zeolite surface. Unfortunately, however, the zeolites were not uniformly treated in our new reactor. Proposed future studies to resolve this issue will be discussed in detail in Section 9.2.

The final work in this dissertation focused on understanding the delamination of a-CN<sub>x</sub> films deposited from single source and mixed precursor systems. The data presented herein were a continuation of earlier studies that attributed the delamination of these films to humidity, film stress, hydrocarbon species, and Br content in the film. The XPS data acquired on fresh and aged samples further supported these results with the

observation of C<sub>1s</sub> binding environments that promote delamination. Analysis of aged samples indicated the likelihood of film delamination.

## 9.2 Future Work

The research presented in this dissertation explored a selection of gas-phase chemistry and plasma processing techniques. Future studies for the majority of the reported projects are discussed in detail below. The collection of additional energy partitioning data for radials presented in Chapter 4 are limited in scope as inclusion of translational temperatures for all species would allow for greater insight on gas-phase and gas-surface interactions. Ultimately, collection of additional internal and kinetic temperature data for additional plasma species could increase our growing database of information on how energy is partitioned in plasmas, what effect internal energy has on surface reactivity, and how radical and electron temperatures are related. All of these are aspects of plasma chemistry that are not fully developed or understood.

The IEP studies of metal oxides in Chapters 5 and 6 were performed using contact angle titration data. An additional potential avenue for exploration extends these studies by the addition of zeta potential measurements on the same surfaces. These measurements would bolster our reported IEP values, and may be a more reliable method for surface charge characterization. Currently reported IEP values of surfaces in the literature are determined from either zeta potential measurements<sup>9</sup> or advancing and receding contact angle measurements.<sup>3,4</sup> Additionally, the IEP values reported here were for metal oxide surfaces treated with neutral and basic precursors. To further add to this study, acidic precursors should be tested to differentiate between the three types of precursors. Moving to the treatment of polymeric surfaces with an eye toward

understanding IEP and surface charge would also be an interesting path to pursue as polymer adhesion to metals is reliant on the acidic/basic nature of the polymer.<sup>10</sup> One follow up experiment would examine the adhesion behavior of polymers deposited on plasma treated metal oxides surfaces. Comparison to untreated surfaces would determine if polymer adhesion increases or decreases when in contact with a specifically charged surface.

The project that shows the greatest potential for vast exploration is the plasma treatment of zeolites. First, a new reactor design or modifications to the existing reactor must be developed. This is necessary to ensure that the plasma glow is located within the rotating drum where the material to be treated is placed so that a more effective and uniform plasma treatment can occur. Second, the position of the rotating drum must be adjustable relative to the coil region. This would allow for control of the overall plasma process occurring in the system, surface etching, film deposition, and surface modification. Finally, a more complete examination of the effects of plasma parameters on the overall plasma treatment should be performed. For example, increasing the applied rf power could produce thinner films and increasing reactor pressure or drum rotation speed would likely result in thicker deposited films.<sup>11</sup> These parameters are important to consider when plasma treating the zeolites with fluorocarbons because too thick of films could mask the pores of the material.

The research presented in this dissertation focused on gaining information for a wide selection of plasma chemistry including the gas-phase of plasma systems and how plasma species affect different materials. As a result these projects lend appreciable information to fundamental plasma questions and potential use for real world applications.

### 9.3 References

- <sup>1</sup>D. C. Johnson, D. S. Dandy, and V. A. Shamamian, *Water Res.* **40**, 311 (2006).
- <sup>2</sup>S. Manolache, E. B. Somers, A. C. L. Wong, V. Shamamian, and F. Denes, *Environ. Sci. Technol.* **35**, 3780 (2001).
- <sup>3</sup>E. McCafferty and J. P. Wightman, *J. Colloid Interface Sci.* **194**, 344 (1997).
- <sup>4</sup>E. McCafferty and J. P. Wightman, *J. Adhesion Sci. Technol.* **13**, 1415 (1999).
- <sup>5</sup>W. Birch, S. Mechken, and A. Carre, in *Surface Contamination and Cleaning; Vol. 1*, edited by K. L. Mittal (VSP, New York, 2003).
- <sup>6</sup>N. De Vietro, P. Favia, F. Fracassi, and R. d'Agostino, *Plasma Processes Polym.* **7**, 582 (2010).
- <sup>7</sup>S. Yamazaki, T. Nishimura, K. Furukawa, H. Ijiri, and K. Tsutsumi, *Zeolites* **135**, 1718 (2001).
- <sup>8</sup>K. Nishihara, K. Furukwa, H. Ijiri, and S. Yamazaki, *Trans. Mater. Res. Soc. Jpn* **26**, 1201 (2001).
- <sup>9</sup>D. Tebee, R. Thull, and U. Gbureck, *Biomed. Eng. Online* **6** (2007).
- <sup>10</sup>E. McCafferty and J. P. Wightman, in *Apparent and Microscopic Contact Angles*, edited by J. Drelich, J. S. Laskowski, and K. L. Mittal (VSP, Utrecht, 2000), p. 149.
- <sup>11</sup>D. Kim, J. Kang, and K. Kim, *J. Ind.Eng. Chem.* **16**, 997 (2010).

## APPENDIX A: Sample cleaning methods for $\text{SiO}_x\text{N}_y$ and nat- $\text{SiO}_2$ substrates

For the  $\text{SiO}_x\text{N}_y$ , nat- $\text{SiO}_2$ , and dep- $\text{SiO}_2$  substrate experiments samples were used “as received” as one of the goals of our work was to minimize processing steps. To determine if surface contamination significantly affected our results substrates ( $\text{SiO}_x\text{N}_y$  and nat- $\text{SiO}_2$ ) were “cleaned” using one of three methods: (1) an HF dip; (2) a 100% Ar plasma, or (3) a 100%  $\text{O}_2$  (Airgas, 99.99%) plasma to elucidate issues associated with possible contaminants on the “as received” samples. The HF dip involved dipping the substrates in a 50:1 diluted solution of hydrofluoric acid and 100% DI water for 15 sec followed by a 1 min rinse in DI water.<sup>1</sup> This procedure is known to remove the thin silicon dioxide layer on Si wafers. Both the Ar and  $\text{O}_2$  plasma cleaning treatments were implemented at 100 mTorr for 10 minutes with  $P = 150$  W, with substrates in the coil region. These conditions are expected to remove foreign debris and adventitious carbon and nitrogen from the surface.

Isoelectric points (IEP), contact angle max values ( $\text{CA}_{\text{max}}$ ), and x-ray photoelectron spectroscopy (XPS) elemental analyses for as-received substrates are listed in Table A.1 for  $\text{SiO}_x\text{N}_y$  and Table A.2 for nat- $\text{SiO}_2$  along with results for substrates cleaned with one of the above three methods. Elemental composition data for the  $\text{SiO}_x\text{N}_y$  substrates show that the two plasma cleaning processes remove significant amounts of both carbon and nitrogen from the metal oxide surfaces, leaving essentially a  $\text{SiO}_x\text{N}_y$  or  $\text{SiO}_2$  surface. In contrast, the HF dip process effectively removes oxygen from the surface, but leaves the carbon content virtually intact. The HF dipped nat- $\text{SiO}_2$  substrate showed contrasting results to the  $\text{SiO}_x\text{N}_y$ , the amount of oxygen is significantly reduced while the carbon content increases significantly. The IEP for the nat- $\text{SiO}_2$  is higher than

**Table A.1** XPS elemental compositions, IEP, and CA values for cleaned SiO<sub>x</sub>N<sub>y</sub> substrates

<b>Process</b>	<b>% O</b>	<b>% Si</b>	<b>% N</b>	<b>% C</b>	<b>IEP</b>	<b>CA<sub>max</sub> (°)</b>
Untreated	41.7 ± 0.1	29.5 ± 0.2	14.5 ± 0.5	14.4 ± 0.6	amphoteric	73.6 ± 3.2
HF Dip	31.6 ± 0.9	33.7 ± 0.3	33.7 ± 0.3	13.1 ± 0.2	amphoteric	67.0 ± 0.7
Ar	62.6 ± 0.3	32.7 ± 0.1	2.0 ± 0.3	2.8 ± 0.5	6.9 ± 0.1	41.2 ± 0.4
O <sub>2</sub>	58.7 ± 1.2	32.7 ± 0.6	2.6 ± 0.4	5.9 ± 1.9	5.4 ± 0.1	45.4 ± 0.2
Untreated:H <sub>2</sub> O	60.0 ± 0.2	30.5 ± 0.4	2.7 ± 0.1	5.3 ± 0.4	6.0 ± 0.1*	38.7 ± 0.2
HF:H <sub>2</sub> O	55.3 ± 1.4	31.5 ± 0.8	7.0 ± 0.5	6.1 ± 1.1	5.5 ± 0.1	31.5 ± 0.2
Ar:H <sub>2</sub> O	57.2 ± 1.0	33.6 ± 0.3	4.7 ± 0.6	6.5 ± 2.1	5.4 ± 0.1	44.0 ± 0.1
O <sub>2</sub> :H <sub>2</sub> O	54.0 ± 0.7	32.7 ± 0.6	1.0 ± 0.6	10.6 ± 0.7	4.6 ± 0.1*	39.1 ± 0.1

Error listed as two standard deviations of the mean is indicated with an asterisk.

**Table A.2** XPS elemental compositions, IEP, and CA values for cleaned nat-SiO<sub>2</sub> substrates

<b>Conditions</b>	<b>% O</b>	<b>% Si</b>	<b>% N</b>	<b>% C</b>	<b>IEP</b>	<b>CA (°)</b>
Untreated	41.1 ± 0.2	46.7 ± 0.8	--	12.1 ± 0.1	3.9 ± 0.1	61.6 ± 0.1
HF Dip	13.5 ± 1.1	65.2 ± 1.3	--	21.3 ± 2.2	5.8 ± 0.1	87.5 ± 0.1
Ar	53.9 ± 0.3	35.9 ± 0.8	4.7 ± 1.0	5.5 ± 1.5	7.0 ± 0.1	28.8 ± 0.2
O <sub>2</sub>	62.6 ± 0.5	34.3 ± 0.5	--	4.1 ± 0.6	8.1 ± 0.1	54.0 ± 0.2
Untreated:H <sub>2</sub> O	59.5 ± 0.5	31.2 ± 0.4	--	9.3 ± 0.7	6.7 ± 0.1*	31.9 ± 0.2
HF:H <sub>2</sub> O	63.4 ± 0.2	28.0 ± 0.6	--	8.7 ± 0.4	7.5 ± 0.1*	42.5 ± 0.1
Ar:H <sub>2</sub> O	59.8 ± 0.7	25.4 ± 0.7	5.7 ± 0.1	9.0 ± 0.3	10.0 ± 0.3	30.0 ± 0.3
O <sub>2</sub> :H <sub>2</sub> O	59.7 ± 0.7	21.8 ± 1.1	9.4 ± 1.2	9.2 ± 0.7	7.4 ± 0.1*	43.4 ± 0.2

Error listed as two standard deviations of the mean is indicated with an asterisk.

the untreated substrate ( $3.9 \pm 0.1$ ), but is still in the acidic IEP range at  $5.8 \pm 0.1$ . Following treatment with a high  $P$   $H_2O$  (g) plasma all surfaces ( $SiO_xN_y$  and nat- $SiO_2$ ) display nearly identical surface composition suggesting the  $H_2O$  plasma treatment nullifies the effects of substrate cleaning. Likewise, the IEP and  $CA_{max}$  values for the cleaned and  $H_2O$  plasma treated surfaces are very similar, regardless of cleaning method, Table A.1 and A.2. With the exception of the HF dipped substrate followed by a  $H_2O$  plasma treatment, a decrease in the  $CA_{max}$  is seen due to the addition of OH on the surface from the  $H_2O$  plasma. More importantly, the composition, IEP, and CA results for cleaned substrates subjected to a  $H_2O$  plasma are comparable to those for “as received” substrates treated in a  $H_2O$  plasma system suggesting the cleaning procedure does not influence the effects of plasma treatment on the surface.

Notably, cleaning methods such as those employed here could also activate surface sites or cause rearrangements in the structure and binding environments of surfaces. This can be seen in the high-resolution  $Si_{2p}$  XPS spectra for untreated and plasma-cleaned  $SiO_xN_y$  (Figure A.1) and nat- $SiO_2$  (Figure A.2) substrates. The HF dip process dramatically reduces the prevalence of a tetrahedral  $Si(-O)_4$  network present on the surface of the nat- $SiO_2$ , Figure A.2b, when compared to the untreated spectrum in Figure A.1a and A.2a. Although the removal of surface oxides is expected with an HF dip, the cleaning procedure did not remove a significant amount of surface carbon from the  $SiO_xN_y$  or nat- $SiO_2$  substrate, Table A.2. Compared to untreated substrates (Figure A.1a and A.2a), the  $Si_{2p}$  spectra for substrates cleaned with one of the two plasma-based methods exhibit a higher degree of oxidation in a tetrahedral silicon network. The compositional data as well as the IEP and  $CA_{max}$  data for “as received” substrates treated

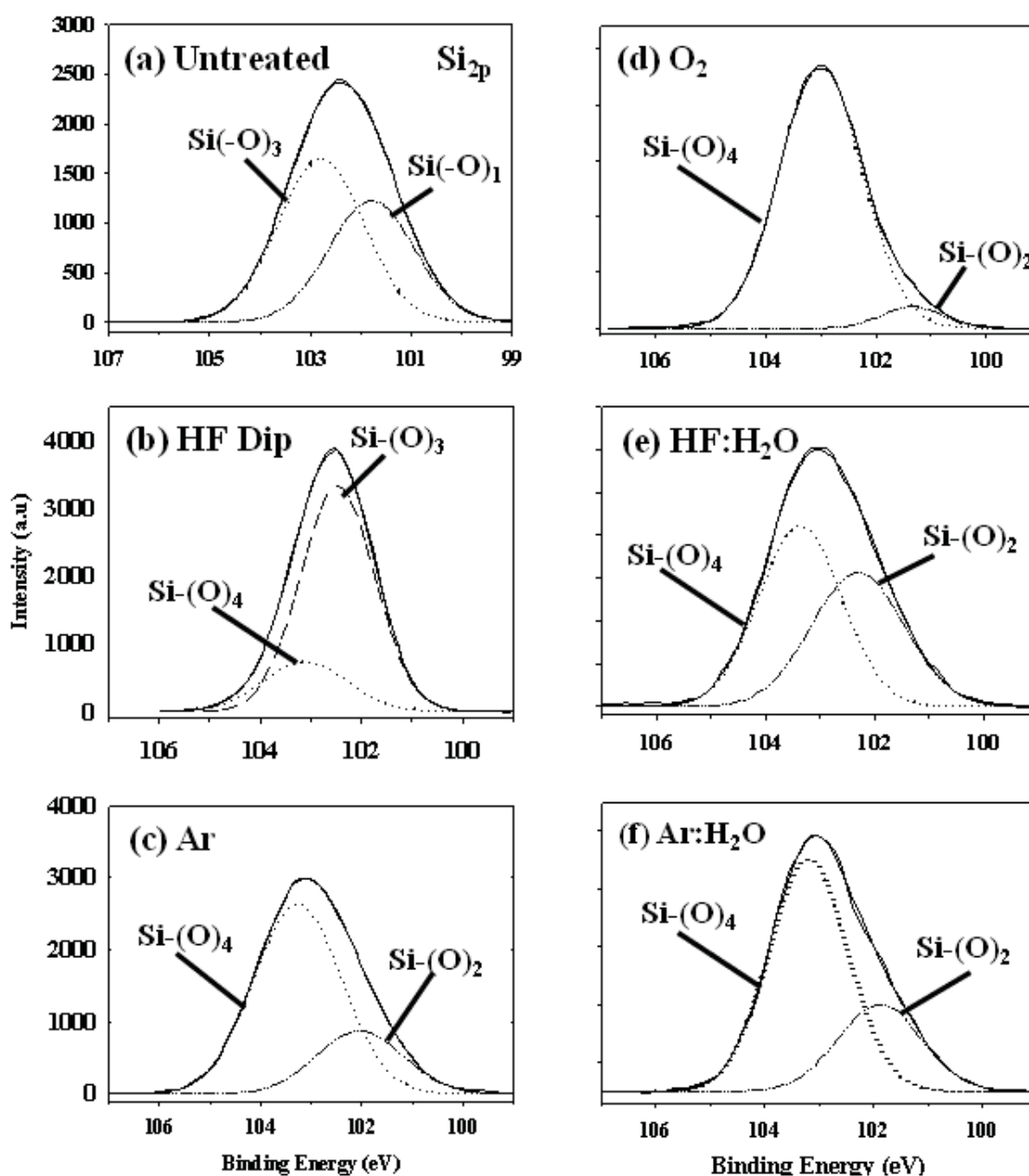


**Figure A.1** XPS  $\text{Si}_{2p}$  high-resolution spectra for an (a) untreated  $\text{SiO}_x\text{N}_y$  substrate and substrates having undergone an (b) HF dip; (c) 100% Ar plasma cleaning; (d) 100%  $\text{O}_2$  plasma cleaning; (e) HF dip followed by a 100%  $\text{H}_2\text{O}$  plasma treatment; and (f) Ar plasma cleaning followed by a 100%  $\text{H}_2\text{O}$  plasma treatment. Cleaning plasmas were run for 10 minutes at 100 mTorr with  $P = 150$  W, with substrates in the coil. The  $\text{H}_2\text{O}$  plasma treatments were conducted under the same conditions.

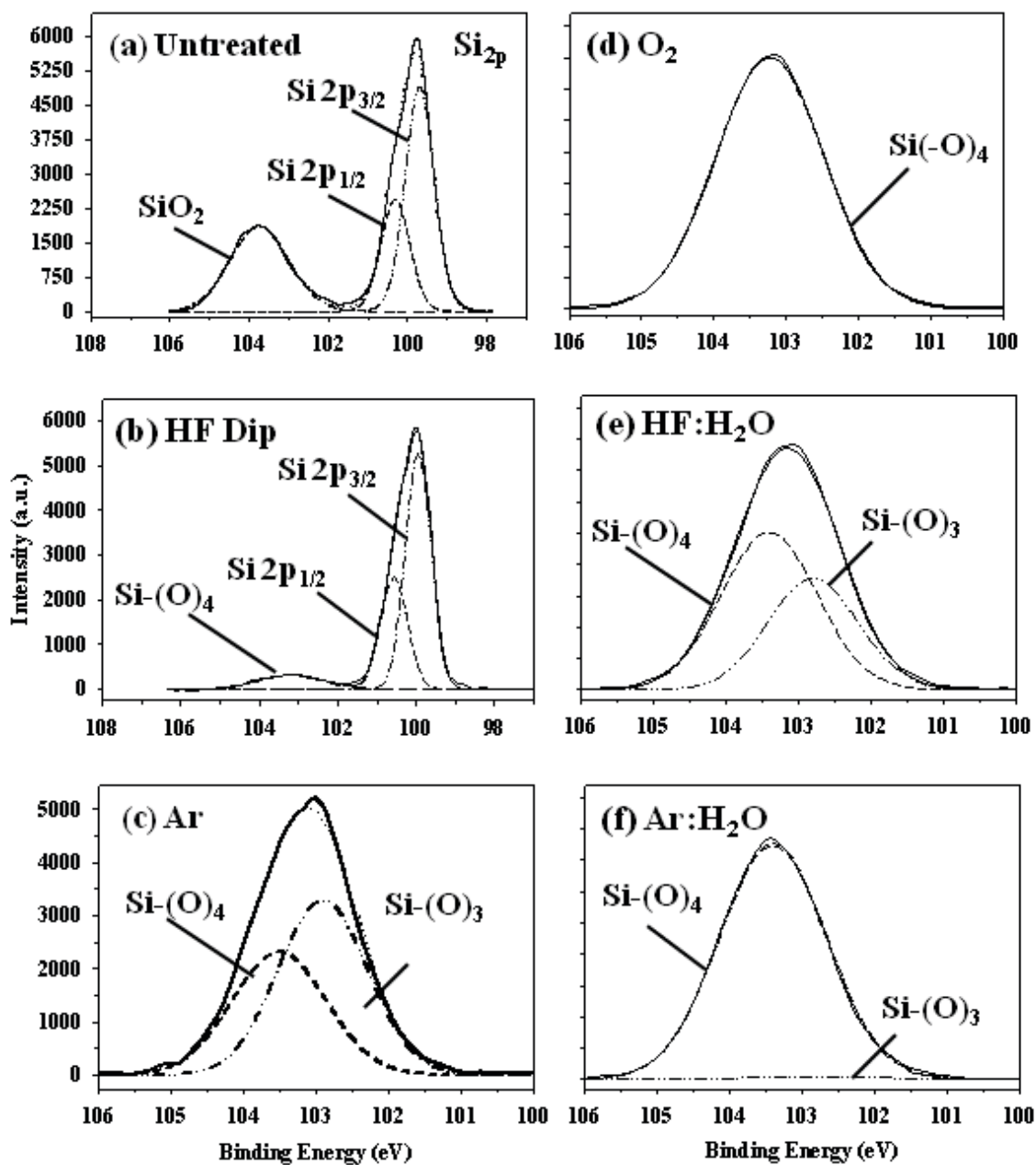


**Figure A.2** High-resolution Si<sub>2p</sub> XPS spectra for an (a) untreated nat-SiO<sub>2</sub> substrate and substrates having undergone the following treatments: (b) HF dip; (c); 100% Ar plasma cleaning; (d) 100% O<sub>2</sub> plasma cleaning; (e) HF dip followed by a 100% H<sub>2</sub>O plasma treatment; and (f) Ar plasma cleaning followed by a 100% H<sub>2</sub>O plasma treatment. Cleaning plasma parameters were: 100 mTorr for 10 minutes with  $P = 150\text{W}$ , with substrates placed in the coil. The subsequent H<sub>2</sub>O plasma treatments were conducted at the same conditions.

in one of the three plasma systems do not differ appreciably from the results for cleaned substrates that are then treated in one of our plasmas. Thus, the data presented on metal oxide treated substrates was collected using “as received” substrates that were not subjected to any cleaning prior to plasma treatment. This minimized our sample prep time, eliminated a step in the surface modification process, and also created a consistency in making comparisons between untreated and treated substrates, as plasma processes (such as cleaning) could activate surface sites and cause surface atom rearrangement.

### **References**

<sup>1</sup>W. Kern and D. A. Puotinen, *RCA Rev.* **31**, 187 (1970).